

FLUIDS ENGINEERING DIVISION

Editor
J. KATZ (2009)

Assistant to the Editor
L. MURPHY (2009)

Associate Editors
M. J. ANDREWS (2009)
E. M. BENNETT (2012)
S. L. CECCIO (2009)
D. DRIKAKIS (2012)
P. DURBIN (2012)
I. EAMES (2010)
C. HAH (2010)
T. J. HEINDEL (2011)
J. KOMPENHANS (2009)
YU-TAI LEE (2009)
J. A. LIBURDY (2011)
R. MITTAL (2010)
T. J. O'HERN (2009)
N. A. PATANKAR (2011)
H. PEERHOSSAINI (2011)
U. PIOMELLI (2010)
Z. RUSAK (2010)
D. SIGINER (2009)
M. STREMLER (2012)
M. WANG (2011)
St. T. WERELEY (2011)
Y. ZHOU (2009)

PUBLICATIONS COMMITTEE
Chair, **B. RAVANI**

OFFICERS OF THE ASME
President, **THOMAS M. BARLOW**
Executive Director, **THOMAS G. LOUGHLIN**
Treasurer, **T. D. PESTORIUS**

PUBLISHING STAFF
Managing Director, Publishing
P. DI VIETRO
Manager, Journals
C. MCATEER
Production Coordinator
A. HEWITT

Transactions of the ASME, Journal of Fluids Engineering (ISSN 0098-2202) is published monthly by The American Society of Mechanical Engineers, Three Park Avenue, New York, NY 10016. Periodicals postage paid at New York, NY and additional mailing offices.

POSTMASTER: Send address changes to Transactions of the ASME, Journal of Fluids Engineering, c/o THE AMERICAN SOCIETY OF MECHANICAL ENGINEERS, 22 Law Drive, Box 2300, Fairfield, NJ 07007-2300. CHANGES OF ADDRESS must be received at Society headquarters seven weeks before they are to be effective. Please send old label and new address.

STATEMENT from By-Laws. The Society shall not be responsible for statements or opinions advanced in papers or printed in its publications (B7.1, Par. 3). COPYRIGHT © 2009 by the American Society of Mechanical Engineers. Authorization to photocopy material for internal or personal use under those circumstances not falling within the fair use provisions of the Copyright Act, contact the Copyright Clearance Center (CCC), 222 Rosewood Drive, Danvers, MA 01923, tel: 978-750-8400, www.copyright.com. Request for special permission or bulk copying should be addressed to Reprints/Permission Department, Canadian Goods & Services Tax Registration #126148048.

RESEARCH PAPERS

Flows in Complex Systems

- 031101 Transient Simulation of the Aerodynamic Response of a Double-Deck Bus in Gusty Winds
Hassan Hemida and Siniša Krajnović
- 031102 Assessment Measures for Engineering LES Applications
I. Celik, M. Klein, and J. Janicka

Fundamental Issues and Canonical Flows

- 031201 Slip-Flow Pressure Drop in Microchannels of General Cross Section
M. Bahrami, A. Tamayol, and P. Taheri
- 031202 Long-Wave Instabilities in a Non-Newtonian Film on a Nonuniformly Heated Inclined Plane
I. Mohammed Rizwan Sadiq and R. Usha
- 031203 Effect of Geometrical Parameters on Vortex-Induced Vibration of a Splitter Plate
T. Pärssinen, H. Eloranta, and P. Saarenrinne

Multiphase Flows

- 031301 Modeling of Cavitation Bubble Dynamics in Multicomponent Mixtures
Si Huang and A. A. Mohamad
- 031302 Parameters for Assessing Oil Reservoir Water Flooding Additives
Nico Reuvers and Michael Golombok
- 031303 Improvements of Particle Near-Wall Velocity and Erosion Predictions Using a Commercial CFD Code
Yongli Zhang, Brenton S. McLaury, and Siamack A. Shirazi
- 031304 Modeling the Onset of Gas Entrainment in a Single Downward Discharge From a Stratified Gas-Liquid Region With Liquid Crossflow
R. C. Bowden and I. G. Hassan

2006 FREEMAN SCHOLAR LECTURE

- 031801 Swimming and Flying in Nature—The Route Toward Applications: The Freeman Scholar Lecture
Promode R. Bandyopadhyay

TECHNICAL BRIEFS

- 034501 Hot-Wire Anemometry for Velocity Measurements in Nanopowder Flows
Sergey P. Bardakhanov and Sang W. Joo
- 034502 Effects of Jet Obliquity on Hydraulic Jumps Formed by Impinging Circular Liquid Jets on a Moving Horizontal Plate
R. P. Kate, P. K. Das, and Suman Chakraborty

(Contents continued on inside back cover)

This journal is printed on acid-free paper, which exceeds the ANSI Z39.48-1992 specification for permanence of paper and library materials. ©™
♻️ 85% recycled content, including 10% post-consumer fibers.

034503 Perspective: Validation—What Does It Mean?
Patrick J. Roache

The ASME Journal of Fluids Engineering is abstracted and indexed in the following:

Applied Science & Technology Index, Chemical Abstracts, Chemical Engineering and Biotechnology Abstracts (Electronic equivalent of Process and Chemical Engineering), Civil Engineering Abstracts, Computer & Information Systems Abstracts, Corrosion Abstracts, Current Contents, Ei EncompassLit, Electronics & Communications Abstracts, Engineered Materials Abstracts, Engineering Index, Environmental Engineering Abstracts, Environmental Science and Pollution Management, Excerpta Medica, Fluidex, Index to Scientific Reviews, INSPEC, International Building Services Abstracts, Mechanical & Transportation Engineering Abstracts, Mechanical Engineering Abstracts, METADEX (The electronic equivalent of Metals Abstracts and Alloys Index), Petroleum Abstracts, Process and Chemical Engineering, Referativnyi Zhurnal, Science Citation Index, SciSearch (The electronic equivalent of Science Citation Index), Shock and Vibration Digest, Solid State and Superconductivity Abstracts, Theoretical Chemical Engineering

Transient Simulation of the Aerodynamic Response of a Double-Deck Bus in Gusty Winds

Hassan Hemida
e-mail: hemida@chalmers.se

Siniša Krajnović

Division of Fluid Dynamics,
Department of Applied Mechanics,
Chalmers University of Technology,
SE-41296 Gothenburg, Sweden

The purpose of the research reported in this paper was to investigate the aerodynamic response of a double-deck bus in gusty winds using a detached-eddy simulation (DES). The bus was subjected to three different scenarios of wind gusts: gust in a wind tunnel, gust in a natural wind, and gust behind the exit of a tunnel. The proposed scenarios of gusts are in the time domain and take into account the dynamic behavior of natural winds. The Reynolds number of the flow, based on the time-averaged speed of the side wind and a reference length of $\sqrt{0.1}$ m, was 1.3×10^6 . Detailed transient responses of the aerodynamic coefficients and flow structures were investigated. Good agreement was found between the DES results and the available experimental data. A comparison between the influence of the different gust scenarios on the aerodynamic coefficients shows that the gust behind the exit from a tunnel has a stronger influence on the aerodynamics than the other gust scenarios. Moreover, the influence of the gusts on the time history of aerodynamic coefficients is found to be limited to the period of the gust.
[DOI: 10.1115/1.3054288]

Keywords: DES, side wind, vehicle aerodynamics, flow structures, unsteady flow

1 Introduction

A bus in motion experiences different aerodynamic forces and moments. These aerodynamic forces and moments are large when the bus is subjected to a side wind. The natural side wind has a transient behavior, meaning that it varies in both time and space. This variation is due to the turbulence behavior of the natural wind. In some extreme cases, the wind changes its speed rapidly to form a gust. In this particular case, the natural side wind may influence both the stability of the bus and the ride comfort of the passengers. In other cases, when a bus travels in a tunnel and no overtaking takes place, the influence of side winds is small. Once the bus leaves the tunnel it might encounter a strong wind from a side to form a gust in space that might also be variable in time. The influence of gusts is of a great concern in bus aerodynamics. The expected sudden change in forces and moments acting on a bus is believed to be a reason for several bus accidents. In November 1998, between Enköping and Sala in Sweden, a bus turned over and six people were killed. The Swedish accident investigation board concluded that the probable cause of the crash was the large lateral wind force that, in combination with a slippery road surface, made the coach impossible to steer the front wheels as they lost the necessary road grip [1]. In October 1995, a bus with 41 passengers went off the road in a high side wind and rolled over. The accident occurred when the bus was driving north alongside a narrow fjord in the northwest of Iceland. This resulted in two passengers being killed and leaving the others with minor to severe injuries [2].

Many researchers have investigated the steady side wind around vehicles. Some research has addressed the stability of high speed trains subjected to steady side winds [3–8]. Some other research has addressed the steady side wind flow around road vehicles [9–12]. However, few investigations have been made to study the influence of gusty wind on vehicles. The period during which a gust is effective and strong is normally less than 3 s. In

some extreme cases, it might extend to more than 10 s [13]. This makes it difficult to investigate the aerodynamics of a real vehicle in gusty wind. Instead, numbers of wind tunnel investigations have been carried out in the past four decades to quantitatively measure the aerodynamics of vehicles in gust. Some EU projects have been initiated in recent years to study the influence of gusts on vehicles [13–15]. Ryan and Dominy [16] experimentally investigated the wake behind a passenger car subjected to a cross wind gust. The aerodynamics of the Maglev train in gust were also experimentally investigated by Howell [17]. He found that the aerodynamic coefficients for the Maglev train are similar to those of a planar track except for the side force coefficient. Because of the difficulties of modeling the natural gust, few numerical simulations are found in the literature. Clarke and Filippone [18] numerically studied the aerodynamics of two vehicles in overtaking. Their study was limited to two-dimensional models. Some other reports in the literature dealt with analytical investigation of the gust response (Filippone [19], Patrick and Christophe [20], and Baker [21]). Cheli et al. [22] used a generic model for the aerodynamic forces caused by a gust to analytically study the dynamic response of a heavy vehicle. The side wind on buses has recently been given great attention since several vehicle accidents have been traced to side wind, especially when it is accompanied with a gust [23–25]. The aerodynamic response during the gust is not properly investigated in the literature, however. A suitable wind gust model for numerical investigation that takes into account the dynamic behavior of a typical gust is also lacking in literature to the knowledge of the authors.

In this paper, we propose a mathematical model for three different scenarios of gusts in the time domain. The flow around a double-deck bus model subjected to the proposed scenarios of gusts was computed using detached-eddy simulation (DES). The bus is a 1/10 model of the type Scania K112 TL. A high level of complexity was maintained in the geometry, especially in the underbody, to simulate realistic flow conditions. To validate the method, the flow around a bus subjected to a 30 deg side wind yaw angle was computed and compared with experimental data. The Reynolds number of the flow, based on the speed of the relative side wind and a reference length of $\sqrt{0.1}$ m, is 1.3×10^6 .

Contributed by the Fluids Engineering Division of ASME for publication in the JOURNAL OF FLUIDS ENGINEERING. Manuscript received May 19, 2008; final manuscript received October 20, 2008; published online February 4, 2009. Assoc. Editor: Ugo Piomelli.

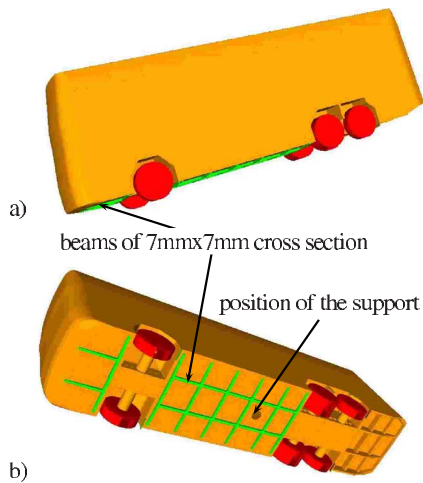


Fig. 1 The shape of the bus model: (a) view from the side and front and (b) view from the bottom of the bus showing the beams, wheels, and axles

The transient response of the aerodynamic coefficients to the gusty wind is investigated, and a concrete conclusion is drawn at the end of the paper.

2 Setup and Boundary Conditions

The model has some geometrical details underneath the bus, such as wheels, beams, and axles, as shown in Fig. 1. This model was used for the experimental investigation of the sensitivity of side winds for the range of yaw angles between -95 deg and $+95$ deg [26]. The experiment was performed at two different Reynolds numbers, 1.3×10^6 and 1.6×10^6 , based on the speed of the side wind and a reference length of $\sqrt{0.1}$ m. The experiment proved that the aerodynamic coefficients are Reynolds number independent or, in other words, the effect of the Reynolds number is very low. The height of the bus is $H=400$ mm and the length is $L=1190$ mm, while its width at the widest part is $W=300$ mm. To simulate the underbody of the real bus, pipes 12 mm in diameter are drilled in the chassis of the bus to connect the two sides of the wheelhouses. These pipes allow the air to pass from one side to the other. The model was mounted on the floor of the wind tunnel, as shown in Fig. 2. The cross section of the wind tunnel is circular with a diameter of 3600 mm, as shown in Fig. 2(a). The center of the model is lowered 300 mm from the center of the tunnel to reduce the blockage ratio. The distance between the inlet section of the wind tunnel and the front face of the bus is $8H$ in our simulation, which is about $2H$ longer than that of the experiment. The purpose of this longer distance is to make sure that the inlet pressure is not influenced by the model. This constraint is essential for numerical stability. The boundary layer thickness on the floor, which was measured in the experimental work at the model reference point (midway between the front and second axles), was 37 mm. It was measured while the model was not mounted in the channel. This boundary layer thickness was used to estimate the upstream length of the no-slip floor in the computational domain. The remaining length of the upstream floor is used as the slip floor (see Fig. 2(b)), where no boundary layer is formed. This setup is used to validate the numerical method with the available experimental data and to investigate the influence of gusts on aerodynamic coefficients in the case of a wind tunnel in which the bus is standing still. For the investigation of wind gust in the case of a moving bus in open air or at the exit of a tunnel, a similar computational domain with a rectangular cross section instead of a circular one is used.

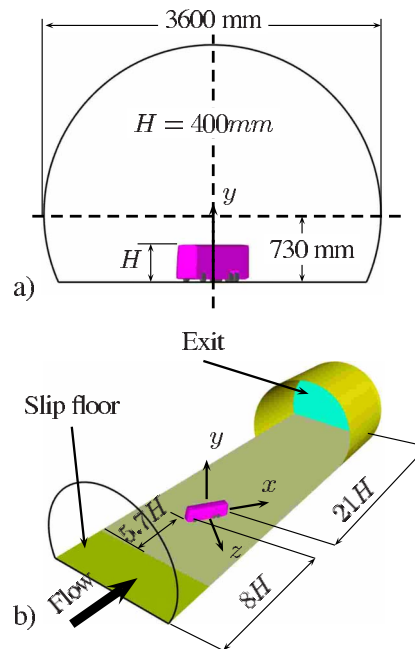


Fig. 2 Computational domain: (a) cross section of the tunnel and (b) dimensions of the computational domain

A uniform inlet velocity, constant in time, with a 0.25% turbulent intensity was used at the inlet of the domain. Wall function boundary conditions were used on the model, floor, and wind tunnel walls. This boundary condition has been implemented in FLUENT 6.3 to switch between the linear viscous layer law and the turbulent logarithmic wall law based on the resolution normal to the wall, y^+ . In the case of $y^+ < 11.5$, it uses the linear sublayer law to calculate the shear stress at the first cell close to the wall, and a pure no-slip boundary condition is retained. In the case of $y^+ > 30$, the standard wall function is used to calculate the shear stress at the first cell close to the wall based on the turbulent logarithmic wall law. On the other hand, if $11.5 < y^+ < 30$, then some kind of blending between the linear law and the logarithmic law is used to find the shear stress at the first cell close to the wall. For more details on the form of blending, the reader can consult the FLUENT manual [27] or Kader [28]. An outlet boundary condition is used at the exit of the domain.

3 Numerical Method

The closure model in our DES is based on a modification of the Spalart–Allmaras one-equation model [29]. The standard Spalart–Allmaras model solves a transport equation for a modified eddy viscosity. The length scale used in this model is the distance between the center of the computational cell and the nearest wall. The modification to the Spalart–Allmaras model to obtain the DES formulation is a redefinition of the minimum wall distance, d , with a new length scale, $d = \min(d, C_{DES}\Delta)$, where Δ is the local maximum grid spacing in all three directions. Near solid boundaries, Δ is larger than d , the standard Spalart–Allmaras model is recovered, and the flow is predicted from the Reynolds-averaged equations. Far from walls, $\Delta < d$, and a balance between the production and destruction terms in the model equation shows that the definition of the closure model is similar to the Smagorinsky expression for the eddy viscosity in the “large-eddy simulation (LES) region” [30]. The length scale redefinition increases the magnitude of the destruction term in the Spalart–Allmaras model, drawing down the eddy viscosity and allowing instabilities to develop, creating a cascade down to the grid scale as in classical LES. A constant value of 0.65 was used for the model coefficient, C_{DES} . Constantinescu and Squires [30] showed that the Spalart–

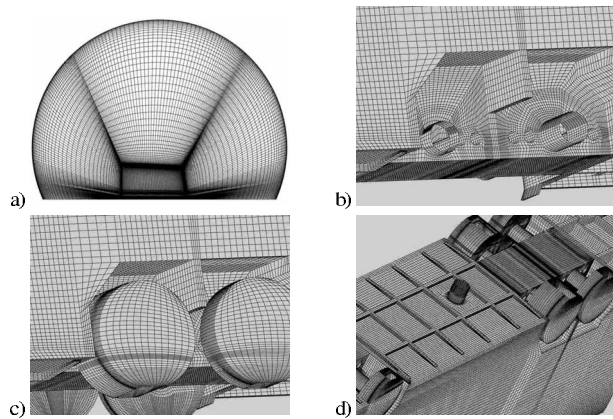


Fig. 3 The computational mesh: (a) the mesh at the inlet plane, (b) the mesh around the axles, (c) the mesh around the wheels, and (d) the mesh around the beams and the support

Allmaras model is very sensitive to the value of its coefficient, C_{DES} , and the optimum value that retains results similar to those of the LES is 0.65.

The ICEM-CFD package was used to generate a hexahedral mesh around the model. To investigate the influence of the mesh resolution on the results, we made two computations on two different meshes with different numbers of cells. The fine mesh consists of about 7×10^6 cells, while the coarse mesh consists of about 4×10^6 cells. The topology of each mesh consists of O-grid, C-grid, and H-grid topologies. Figure 3(a) shows the shape of the fine mesh at the inlet of the computational domain. It consists of a C-grid shape starting from the floor on one side of the bus and ends on the floor on the other side of the bus. Using a C-grid topology in this part of the domain enables good quality cells close to the wind tunnel wall. This also helped to make finer meshes close to the model surface and close to the wind tunnel surface, which is a requirement for using no-slip boundary conditions on both surfaces. The mesh under the bus and around the wheels is very complex. It consists of a combination of C-grid, O-grid, and H-grid topologies. The grid topology around the axles and the wheels of the bus is mainly of the C-grid type, while the grid topology in the part between the axles and the floor is of the H-grid type. These topologies are connected with O-grids in the small pipes connecting the two sides of the wheelhouses, as shown in Fig. 3(b). The momentum equation was discretized using a second-order bounded central difference scheme, while the transport equation for the turbulent viscosity in the Spalart–Allmaras model was discretized using a first-order upwind scheme. Time discretization was approximated using the second-order Crank–Nicolson scheme. The solution is initialized everywhere by the inlet velocity. A constant time step, $\Delta t = 0.0001$ s, is used during the entire simulation. The Courant–Friedrichs–Levy (CFL) number based on this time step, the inlet velocity, and the height of the bus, H , is more than 1.0 in 122 cells for the fine mesh, with a maximum value of 3.0. On the other hand, it is more than 1.0 in 64 cells in the case of the coarse mesh, with a maximum value of about 2.0. The mean value of the CFL number in the whole domain is about 0.5 for the fine mesh, while it is lower than 0.45 for the coarse mesh. The time history of the aerodynamic coefficients and the residual of all the turbulent variables were monitored in each time step during the simulation. Fully developed turbulent flow was obtained in the domain after about 7000 time steps. In each time step, the maximum residual of each turbulent equation was converged to 10^{-4} .

4 Validation of the Numerical Method

To validate our transient numerical method, a DES was made of the flow around the bus in the experimental wind tunnel for com-

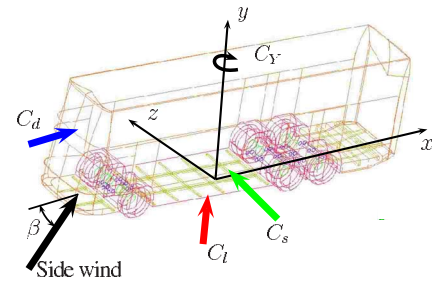


Fig. 4 Conventional directions for the aerodynamic coefficient with respect to the side wind direction

parison with the experimental data. The bus was subjected to a steady side wind with a 30 deg yaw angle with respect to the relative side wind. The fine and coarse meshes were used in the simulations. The time-averaged flow is obtained using 42,000 time steps, or a 4.2 s total sampling time.

The conventional directions for the drag force coefficient, C_d , the lift force coefficient, C_l , the side force coefficient, C_s , and the yaw moment coefficients, C_y , are shown in Fig. 4. The reference point of C_y is located at the floor between the front and the back axles at the center of the supporting cylinder.

The time-averaged values of the aerodynamic coefficients obtained from our simulations are shown in Fig. 5. This figure also shows the minimum and maximum peaks of the aerodynamic coefficients during the sampling time. All the aerodynamic coefficients are normalized with the density of the air, $\rho = 1.16$ kg/m³, the free stream velocity, $U_\infty = 57$ m/s, the reference area, $A = 0.1$ m², and a reference length of 1 m. Figure 5 also shows the experimental values of the aerodynamic coefficient at the range of yaw angles, β , of -95 deg to $+95$ deg. The computed values of the time-averaged C_s and C_y agree well with the experimental values, as shown in Figs. 5(c) and 5(d). Some discrepancies were found between the computed time-averaged value of C_d and the experimental value. On the other hand, the difference in C_l between the simulation and the experiment is relatively large, as shown in Fig. 5(b). However, the measured values are located between the maximum and minimum peaks for the computed aerodynamic coefficients. In the experiment, the model rotated around the support cylinder at a constant rate of 1 deg/s. The aerodynamic coefficients were computed using 100 samples at each angle. The model rotated in a constant angular velocity, meaning that the 100 samples were not taken at a fixed yaw angle. The flow around the model, especially in the wake behind the bus, is not stationary, which raises a question about the credibility of the experimental C_d . Figure 5 shows that the curves obtained from the experiment are not symmetric around the zero yaw angle. This means that the continuous rotation of the model has some influence on the measured values. The C_d , which depends on the wake structure (the contribution of the friction drag is relatively small compared with the pressure drag), seems to be strongly affected by the rotation of the model. Moreover, the model in the experiment was raised 5 mm from the floor to allow its vibration and to prevent any contribution of the friction between the wheels and the floor in the aerodynamic coefficients. In our numerical simulations, the 5 mm distance between the wheels and the road is not used in order for the flow conditions on the road to be correct. The discrepancy in C_l can be traced to this 5 mm clearance and to the possible vibration of the model in the experiment. These vibrations might change the incidence angle of the oncoming air with respect to the bottom surface of the bus and hence the value of C_l . The minimum surface pressure is found on the lee side face of the bus, close to the leading edge, while the highest pressure is found on the area between the front face of the bus and the upstream side face of the bus. The largest time-averaged pressure on the lee side face is confined to between the front wheel and the back

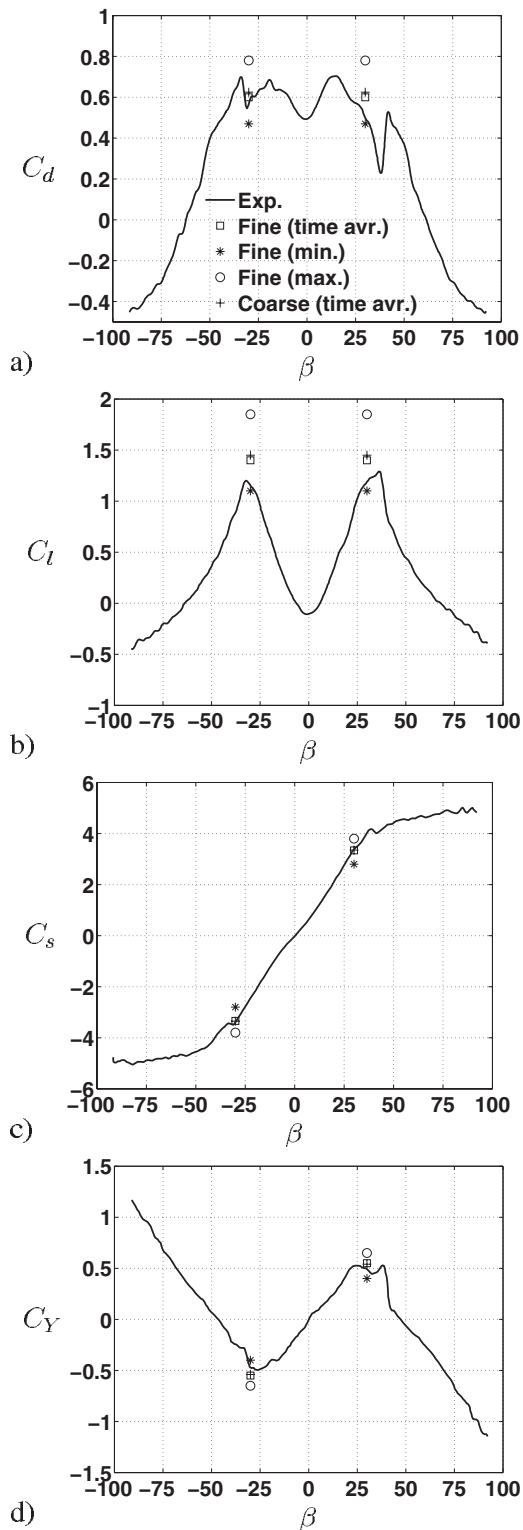


Fig. 5 Comparison of the DES aerodynamic coefficients and the experiment: (a) drag coefficient, (b) lift coefficient, (c) side force coefficient, and (d) yaw moment coefficient

wheel in the middle of the height of the bus. Moreover, regions of high and low pressures are found on the top side face.

Figure 5 shows the time-averaged values of the aerodynamic coefficients obtained from the coarse and fine meshes. The results from the coarse mesh coincide with those from the fine mesh for both C_s and C_Y . It can be seen in Fig. 5 that the C_d and C_l

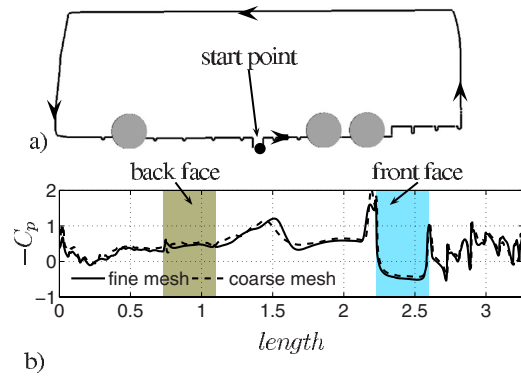


Fig. 6 Local pressure coefficient: (a) the line along which the pressure coefficient is drawn showing the starting point and (b) the pressure coefficient against the length of the line

obtained from the coarse mesh are in good agreement with those obtained from the fine mesh simulation. Figure 6(b) shows further comparison between the results obtained from the fine and coarse meshes in terms of the time-averaged local pressure coefficient, C_p , plotted along a line drawn at the middle of the bus at $z=0$ (shown in Fig. 6(a)). All the results reported here are from the fine simulation unless otherwise stated.

5 Mathematical Model for a Wind Gust

The existing unsteady gust scenarios are not satisfactory for a better description of the real gust in the time domain. Some scenarios have been used in some of the EU projects [13–15] that are based on a sudden change in the wind speed. The wind speed was steady without any perturbations that account for the transient behavior of the natural wind during the gust. The wind tunnel scenarios used in the existing experimental work are more realistic, but there is still no mathematical model for these scenarios suitable for any future numerical investigations. The mathematical model proposed in the present paper is a combination of damping, saturation, and sinusoidal functions. The amplitude of the damping function gives the maximum gust speed. The sinusoidal function has different frequencies to control the perturbations of the gust. Finally, the purpose of the saturation function is to limit the speed of the wind behind the gust. An equation for a gust model in a stationary wind tunnel takes the following form:

$$V(t) = V_{\text{mean}} + F_1 F_2 + F_3 F_4 \quad (1)$$

Here, F_1 , F_2 , F_3 , and F_4 are defined as

$$F_1 = A_1 t e^{-A_2 t} \quad (2)$$

$$F_2 = \sin(w_1 t) \quad (3)$$

$$F_3 = (A_3 + A_4 t) e^{A_5 t} \sin(w_2 t) \quad (4)$$

and

$$F_4 = \sin(w_2 t) \quad (5)$$

The constants A_1 – A_5 , w_1 , and w_2 in Eqs. (1)–(5) are the model constants, which can be adjusted to change the gust profile. V_{mean} in Eq. (1), is the time-averaged velocity of the side wind.

Figure 7(a) shows the gust profile obtained from Eq. (1) using the values in Table 1. The gust profile used for the natural wind is shown in Fig. 7(b). This profile assumes a sudden gust hitting the side of a bus moving in still air. The yaw angle of the effective side wind takes the same profile as the gust. The variation in the yaw angle is also shown in Fig. 7(b). The mathematical model that describes this particular gust scenario takes the following form:

$$V(t) = G_1 + G_2 + G_3 \quad (6)$$

Here G_1 , G_2 , and G_3 are defined as

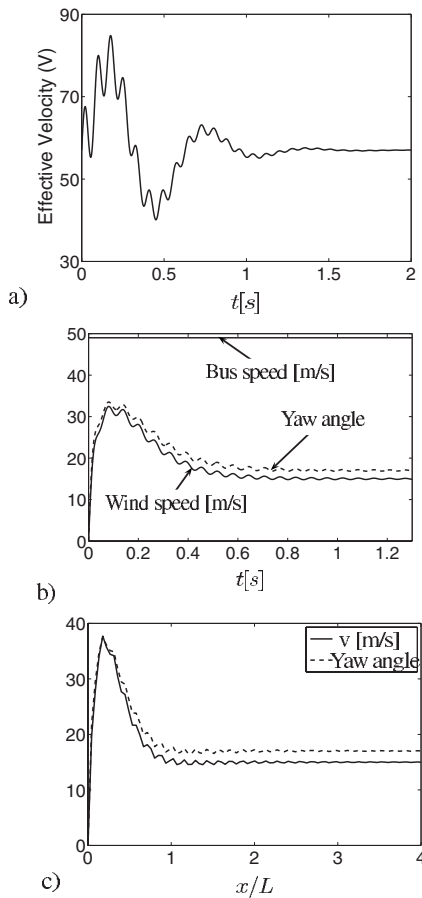


Fig. 7 Scenarios for wind gusts: (a) gust for wind tunnel simulation, (b) gust for open air simulation, and (c) gust at the exit of a tunnel

$$G_1 = B_1 t e^{-B_2 t} \quad (7)$$

$$G_2 = V_s \operatorname{erf}(B_3 t) \quad (8)$$

and

$$G_3 = B_4 e^{B_5 t} \sin(\Omega t) \quad (9)$$

The values of the constants in Eqs. (6)–(9) used to draw the profile in Fig. 7(b) are shown in Table 2.

The gust profiles shown in Figs. 7(a) and 7(b) represent a gust that might occur in a wind in a time shorter than 1 s. It is possible to extend the gust over a longer time by adjusting the model constants. The third gust scenario is the gust that might exist at the exit of a tunnel (shown in Fig. 7(c)). The mathematical model for this profile can be achieved by adjusting the constants in Eqs. (6)–(9), and the coordinate system here is space instead of time. The profile shown in Fig. 7(c) starts with zero velocity at the exit of the tunnel to simulate the no-slip boundary. There is also a

sudden increase in the gust velocity close to the exit of the tunnel due to a compression of the flow stream lines coming around the mountain in which the tunnel is located. After about one bus length away from the tunnel, the side wind speed approaches a steady constant value.

6 Results

6.1 Gust in a Wind Tunnel. The gust profile shown in Fig. 7(a) is applied as an inlet boundary condition at the wind tunnel inlet instead of a steady side wind. The model is yawed by 30 deg to the direction of the flow. In this simulation, the model is stationary with a stationary floor and nonmoving wheels. The yaw angle is kept constant, while the side wind speed is changed according to the gust profile in Fig. 7(a). The steady value of the side wind speed is 57 m/s, which gives the same Reynolds number as the constant side wind simulation. Since the model is stationary and the yaw angle is constant, the gust simulation is equivalent to changing the Reynolds number in the wind tunnel for the side wind flow around a bus at a 30 deg yaw angle. The computational domain, mesh resolution, and boundary conditions are identical to those used in the steady side wind simulation. The only difference is the inlet boundary condition, which varies in time, that represents the gust model. Figure 8 shows the aerodynamic coefficients: C_d (Fig. 8(a)), C_s (Fig. 8(b)), and C_Y (Fig. 8(c)). Here, the aerodynamic coefficients are scaled with a constant reference velocity of 57 m/s. The values of the time-averaged aerodynamic coefficients behind the gust (after about 1.5 s from the onset of the gust) are the same as the values of the aerodynamic coefficients in the case of steady side wind. It can also be noticed in Fig. 8 that C_s and C_Y follow a trend similar to that of the gust, while C_d is different. The minimum value of C_d is found at the first minimum peak in the gust profile (at $t \approx 0.05$ s from the start of the gust). Moreover, the drag coefficient shows a transient behavior during the gust.

C_s follows the same trend as the gust, where its maximum value occurs when the gust has a maximum speed, and its minimum value occurs at the same time as the minimum gust speed. On the other hand, C_Y shows a phase difference from the imposed gust profile in terms of the minimum and maximum peaks. The maximum and minimum velocities of the gust are approximately at 0.2 s and 0.45 s from its start, respectively, while the minimum and maximum values of C_Y are at 0.21 s and 0.4 s, respectively. This difference is due to the contribution of the drag force in the yaw moment.

For a further understanding of the influence of gust on the aerodynamic coefficients, the instantaneous velocity is used to scale the aerodynamic coefficients instead of a constant velocity. The results are shown in Fig. 9. As expected, the time-averaged values do not change with a change in the Reynolds number, as the gust does. On the other hand, the transient effect is clear in all of the coefficients during the effect of the gust. This is shown as a large variation between the maximum and minimum peaks of the aerodynamic coefficients. When the value of the gust changes at the minimum velocity ($t \approx 0.4$ – 0.5), there is a large variation in the aerodynamic coefficients, especially the yaw moment coefficient, meaning that the flow and the pressure fields change dramatically

Table 1 Values of the constants in Eqs. (1)–(5) that give the gust profile in Fig. 7(a)

Constants	V_{mean}	A_1	A_2	A_3	A_4	A_5	w_1	w_2
Values	57	300	5	10	10	3.5	10	80

Table 2 Values of the constants in Eqs. (6)–(9) that give the gust profile in Fig. 7(b)

Constants	B_1	B_2	B_3	B_4	B_5	Ω
Values	450	10	15	1.5	2	100

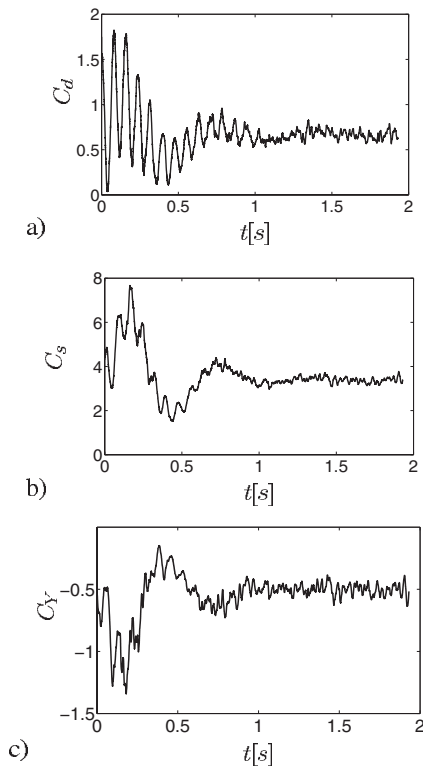


Fig. 8 Gust in a wind tunnel. Aerodynamic response during the gust time normalized by the steady side wind velocity: (a) drag coefficient, (b) side force coefficient, and (c) yaw moment coefficient.

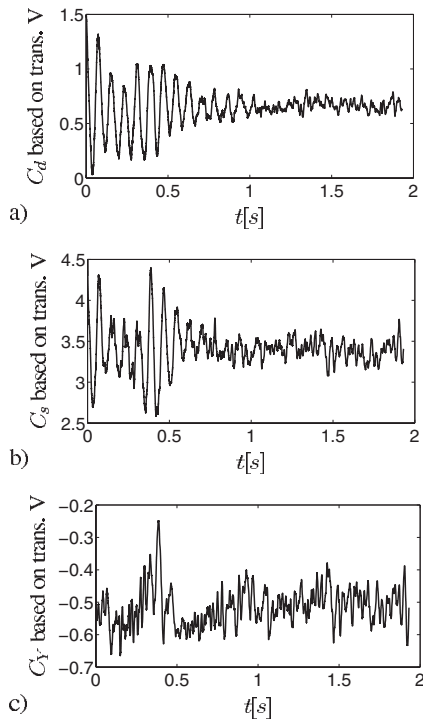


Fig. 9 Gust in a wind tunnel. Aerodynamic response during the gust time normalized by transient side wind velocity: (a) drag coefficient, (b) side force coefficient, and (c) yaw moment coefficient.

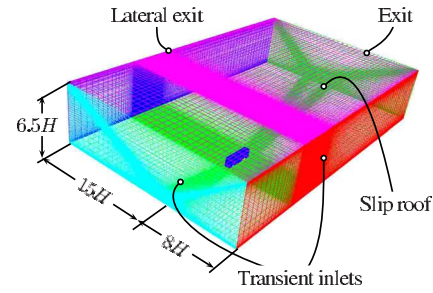


Fig. 10 Surface mesh in the computational domain of the open air and exit of tunnel simulations

during this transient period. The value of C_Y at $t \approx 0.4$ s is 0.25, which is half that of the time-averaged one. At the same instant, the value of C_s changes from 4.4 to 2.6 in about 0.05 s.

6.2 Bus on Road Influenced by a Gust. In this simulation, the flow around a bus in motion in a natural gust is obtained using DES. The bus moves at a velocity of 49 m/s. Here, the wheels of the bus are rotating. The computational domain is a box with a rectangular cross section, as shown in Fig. 10. The sides of the bus are kept parallel to the sides of the computational domain. This configuration of the computational domain makes it possible to set boundary conditions suitable for a natural wind. A slip boundary condition is used on the roof of the computational domain. An outflow boundary is used in two places on the boundaries: on the exit and on the downstream side of the computational domain. The floor moves with a speed equal to the speed of the bus. The transient profile of the gust is imposed at the inlet section and on the upstream side of the computational domain. A no-slip boundary condition combined with wall functions is used at the bus wall. The gust hits the entire bus at the same time, meaning that there is no spatial distribution of the gust on the surface of the bus. As shown in Fig. 10, a constant distance is maintained between the model and both the inlet section and the upstream side of the domain, which is equal to $8H$. This distance proved to be sufficient for computational stability and ensured that the pressure at the inlet plane is not influenced by the model.

Figure 11 shows the aerodynamic coefficients: C_d , C_l , and C_Y in the case of a bus subjected to the natural gust scenario, shown in Fig. 7(b). The C_d is reduced sharply with an increasing speed of the gust. On the other hand, both C_l and C_Y increase suddenly from zero values, when there is no side wind, to their peaks, when the gust has its maximum value. The maximum gust speed is at $t \approx 0.08$ s from the start of the gust, as shown in Fig. 7(b). At this instant, the values of the C_l and C_Y are 2.5 and -1.2 , respectively. The C_l follows the same trend as the gust, while C_d shows a different behavior. There is an overshoot in the value of the C_d between $t \approx 0.2$ and $t \approx 0.3$. The C_d also oscillates once the gust passes its peak, as shown in Fig. 11(a). As a result of this, there are also some oscillations on the C_Y at the same period of time, as shown in Fig. 11(c).

6.3 Bus at the Exit of a Tunnel. In this part of the work, the gust at an exit of a tunnel is simulated around the same bus model, as described in Sec. 2. The gust profile is shown in Fig. 7(c). The length of the effective gust is about one bus length, starting at the exit of the tunnel. The gust starts with zero velocity, which simulates the no-slip condition at the tunnel exit. The same computational domain that was used for the simulation of the gust in the natural wind simulation is used in this simulation. The bus moves with a constant velocity, and the wheels are allowed to rotate. To simulate the gust at the exit of the tunnel, the boundary condition is fixed in space and the whole computational domain moves with a speed equal to the speed of the bus. In other words, the computational domain is fixed in space and the gust profile is moved on

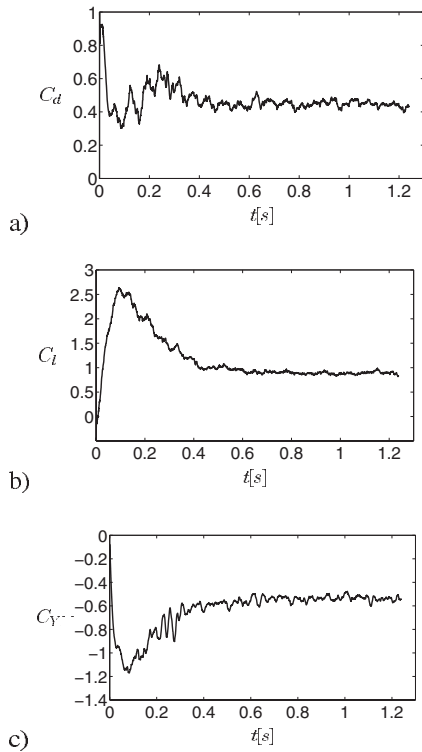


Fig. 11 Open air gust. Aerodynamic response during the gust time normalized by the speed of the bus: (a) drag coefficient, (b) lift coefficient, and (c) yaw moment coefficient.

the boundary of the domain. An outlet boundary condition is employed at the exit of the computational domain. The boundary conditions used in FLUENT at outflow boundaries satisfy a zero diffusion flux for all flow variables normal to the boundary and an overall mass balance correction. A slip boundary condition is applied on the top side of the computational domain in order to simulate the roof of the tunnel in the case when the bus is inside the tunnel and to simulate the outside condition in the case when the bus is outside the tunnel. The floor moves with a speed equal to the speed of the bus in the direction of the bus movement. The inlet section and the two sides of the computational domain are subjected to the gust profile. Here, the boundary conditions are variable in both time and space to simulate the movement of the bus as well as the gust profile, as shown in Fig. 12.

Figure 13 shows the force coefficients when the bus exits the tunnel. The aerodynamic coefficients are drawn against the distance from the exit of the tunnel, x , scaled by the length of the bus, L .

The aerodynamic coefficients show large oscillations inside the tunnel. These oscillations are damped out when the bus approaches the tunnel exit. C_d oscillates between 0.3 and 0.7 inside the tunnel. C_l oscillates between -0.5 and 0, while large oscillations are found for C_s , which oscillates between -1 and 1.5. These oscillations in the aerodynamic coefficients are caused by the differences in the flow structures around the bus in time. Figure 14 shows the flow structures at two instants at which the bus is inside the tunnel by means of the isosurface of the positive second invariant of the velocity gradient. These two instants correspond to a maximum and a minimum value of C_s inside the tunnel. The large value of C_s corresponds to a large separation and hence large vortices on the negative z face of the bus, as shown in Fig. 14(a). In contrast, the low value of C_s corresponds to large separations on the positive z face of the bus.

The flow structures, shown in Fig. 14, fluctuate on both sides of the bus and are related to the separation on the roof of the bus, as

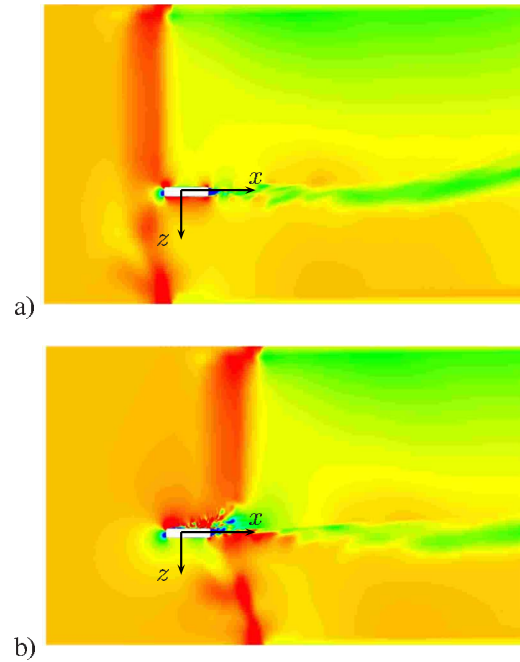


Fig. 12 Gust at the exit of a tunnel. Horizontal plane at the mid height of the bus colored by velocity magnitude.

shown in Fig. 15. The flow separates at the front edge of the roof side face to form large unsteady structures that have their axis parallel to the edge of separation. Due to the unsteadiness of these structures, they move toward one of the sides of the bus, causing a massively separated flow that influences the pressure field. Fig-

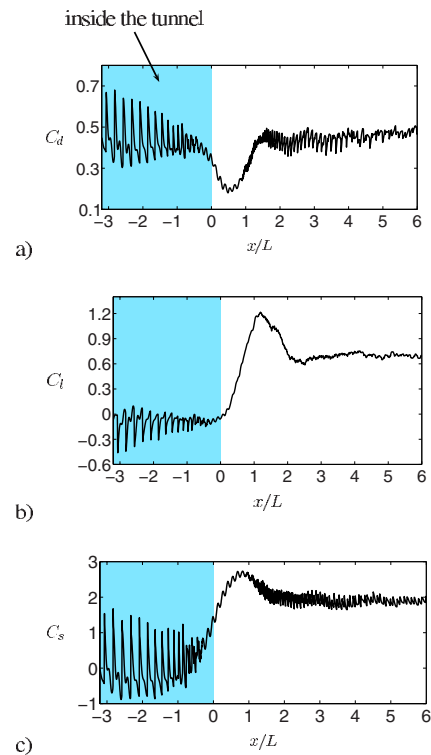


Fig. 13 Gust at the exit of the tunnel. Aerodynamic response of the bus during the gust normalized by the speed of the bus: (a) drag coefficient, (b) lift coefficient, and (c) side force coefficient.

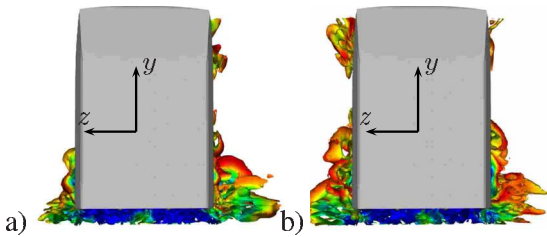


Fig. 14 Instantaneous flow structures around the sides of the bus in a tunnel. (a) and (b) show snapshots at different instants. The view is from the rear of the bus.

Figure 15(a) shows a snapshot of the flow structures on the top side face when these structures move toward the negative z face of the bus. This snapshot corresponds to a large side force. Figure 15(b) shows a different snapshot of the flow structures where the large structures move toward the positive z face of the bus. This snapshot corresponds to the low value of C_s .

Once the bus starts to exit the tunnel, at $x/L=0$, the oscillations damp out, and a large change in the aerodynamic coefficients starts to build up. C_d decreases, and its minimum value is found at $x/L \approx 0.5$, as shown in Fig. 13(a). The maximum value of C_l is at $x/L \approx 1.0$ (i.e., when the bus is completely outside the tunnel). The maximum value of C_s is found at $x/L \approx 0.75$ (i.e., when only one-third of the bus is still in the tunnel). The aerodynamic coefficients oscillate due to the transient effect of the gust when the bus is completely outside the tunnel (at $x/L \approx 1.5$). These oscillations disappear when the bus is at $x/L \approx 5.0$.

Figures 16(a)–16(c) show the pitching moment, C_p , the rolling moment, C_R , and the yaw moment coefficients, C_Y , respectively. Similar to the force coefficients, the moment coefficients show large oscillations inside the wind tunnel. The oscillations of C_Y are smaller than the oscillations of the other two moment coefficients. The peak values of C_Y and C_R are found at $x/L \approx 0.75$. This is in agreement with the position at which the side force is maximum. This means that the side force has a stronger contribution in the rolling and yaw moments than the other two aerodynamic forces: the drag and the lift. C_p is generally small compared with the other moment coefficients. Figure 16(a) shows that C_p has a be-

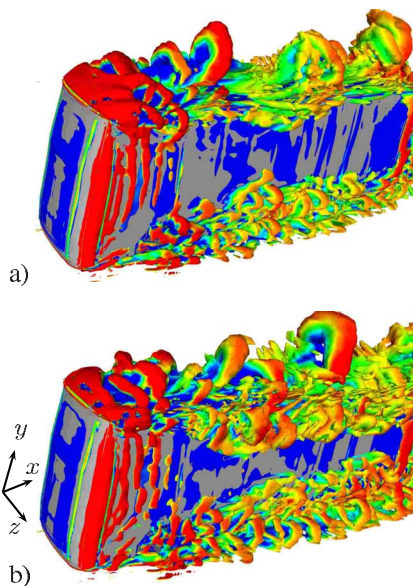


Fig. 15 Instantaneous flow structures on the top and side faces of the bus. (a) and (b) show snapshots at different instants.

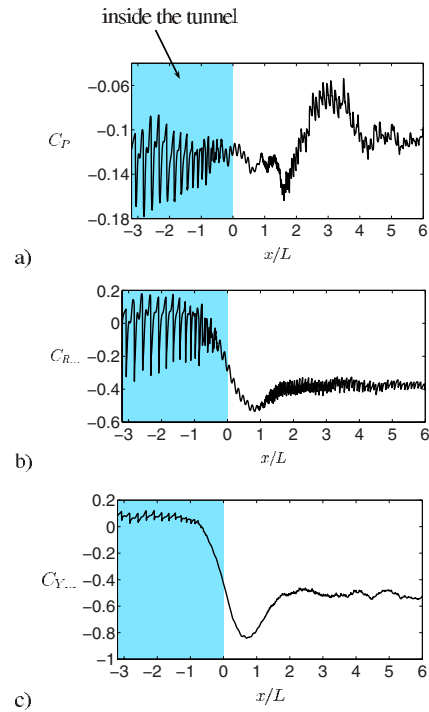


Fig. 16 Gust at the exit of a tunnel. Aerodynamic moment response of the bus during the gust normalized by the speed of the bus and one unit length: (a) pitching moment coefficient, (b) rolling moment coefficient, and (c) yaw moment coefficient.

havior very sensitive to the transient gust when the bus leaves the tunnel. The minimum value is observed at $x/L \approx 1.5$, and the maximum value is seen at $x/L \approx 3.0$. C_p stabilizes when the bus is at a distance of about five bus lengths from the exit of the tunnel.

6.4 Transient Effect. In the case of a gust in open air and a gust at the exit of a tunnel, the resultant gust velocity is chosen to give a Reynolds number similar to that of the steady side wind simulation at a yaw angle of 30 deg. This makes it possible to compare the aerodynamic coefficients obtained from the different simulations when the yaw angle is 30 deg. Table 3 summarizes the different aerodynamic coefficients obtained from the DES simulations. The values of these coefficients are based on the resultant side wind speed and a constant reference area of 0.1 m². In the case of the aerodynamic moments, a constant reference length of 1 m is used. In the case of a transient gust in a wind tunnel, the yaw angle is constant while the wind speed is variable in time. The Reynolds number based on the velocity of the gust matches the Reynolds number for the simulation of the steady side wind at 0.3 s and 0.7 s from the start of the gust. The aerodynamic coefficients obtained from the DES at these particular instants are reported in Table 3.

Table 3 shows that time-averaged values of the aerodynamic coefficients obtained from the wind tunnel simulations are not influenced by the gust. The differences here are the minimum and maximum values, which are related to the transient effect of the gust. The minimum value of C_d in the wind tunnel simulation corresponds to the first minimum peak of the gust. Although the minimum gust velocity, which occurs at about 0.5 s from the start of the gust, is about 40% lower than the first maximum peak of the velocity, C_d is not at its minimum at this instant. The reason for this is the time required for the flow around the bus to respond to the gust. The drag is based on the flow structures at the front and the back of the bus. The structures of the flow in these two regions depend on the history of the velocity of the gust before the gust reaches its minimum velocity. In contrast, the values of C_s and C_Y depend mainly on the flow in the upstream and lee side

Table 3 Values of aerodynamic coefficients of the bus at 30 deg yaw angle, obtained from different simulations

Coefficient	Wind tunnel steady wind			Wind tunnel transient wind					Open air	Exit of tunnel
	min	max	mean	min	max	mean	0.3 s	0.7 s		
C_d	0.47	0.78	0.6	0.1	1.3	0.6	0.25	0.85	0.3	0.2
C_l	1.2	1.8	1.4	-	-	-	-	-	2.5	1.2
C_s	2.9	3.9	3.5	2.6	4.4	3.5	2.7	4	-	2
C_Y	0.42	0.65	0.52	0.24	0.67	0.52	0.35	0.65	1.1	0.8
C_R	-	-	-	-	-	-	-	-	-	0.13
C_P	-	-	-	-	-	-	-	-	-	0.5

flows. The flow structures on the lee side of the bus are less sensitive to the change in the gust velocity. This is why the minimum and maximum values of C_s and C_Y correspond to the minimum and maximum velocities of the side wind. This behavior can be seen in Fig. 8 in conjunction with Fig. 7(a). This transient effect can also be recognized in the values of the aerodynamic coefficients at the two positions, where the Reynolds number and yaw angle are similar to those in the case of the steady side wind: at 0.3 s and 0.7 s from the start of the gust. The value of C_d at the first time position is lower than the minimum value in the case of the steady side wind, while its value at the second time position is larger than the maximum value in the case of the steady side wind. A similar behavior can also be seen for C_s and partially for C_Y . The first time position corresponds to a lower aerodynamic coefficient, while the second time position corresponds to a higher value. The difference in these values at the two time positions is because the time velocity gradient is negative at the first time position, while it is positive at the second time position. As mentioned above, the values in Table 3 of the aerodynamic coefficients in the case of open air and in the case of exit from a tunnel correspond to a yaw angle of 30 deg, which gives a Reynolds number similar to that of the steady side wind Reynolds number. As can be seen in Table 3, these values are completely different from those of the steady side wind.

7 Conclusion

A DES of a typical double-deck bus under the influence of windy gusts is presented. The mesh dependency of the results is examined by making two computations on two different meshes with different numbers of nodes. The time-averaged aerodynamic coefficients were obtained from the coarse and fine meshes and compared with experimental values. The side force and yaw moment coefficients agree well with the experimental values, while some discrepancies were found for the lift and drag force coefficients. In all cases, the measured values of the aerodynamic coefficients are between the minimum and maximum values of the computed coefficients during the sampling time.

The DES results are also presented for the flow around the double-deck bus in three different gust scenarios: a gust in a wind tunnel, a gust in natural open air, and a gust when the bus exits a tunnel. The simulations show that the aerodynamic coefficients fluctuate strongly inside the tunnel. The unsteady flow structures around the bus contribute to these oscillations. The time-averaged values of the aerodynamic coefficients behind the gust were found to be unaffected by the gust and to approach the values of the aerodynamic coefficients in the case of a steady side wind. For the same Reynolds number and yaw angle, the transient aerodynamic coefficients are different depending on whether the bus is influenced by a gust or a steady side wind. In the case of gust affecting a stationary model in the wind tunnel simulation, the aerodynamic coefficients oscillate strongly during the gust, and the unsteady behavior of the flow appears in a large oscillation in the transient aerodynamic coefficients. The study of the gust at the exit of a tunnel showed that the bus is most resistant to C_P .

Each computation presented in this paper was made using 20 processors. The Linux cluster is a 4 Xeon 5160 (Woodcrest) 3 GHz core (dual core), 4 Gbyte random access memory with MPI over a gigabit Ethernet. The total resources used are about 40,800 wall time hours.

Acknowledgment

This work was supported by the Swedish Agency for Innovation System (VINNOVA), Bombardier Transportation, and Scania. The computer time at the Swedish National Infrastructure for Computing (SNIC) resources (High Performance Computing Center North, HPC2N, National Supercomputer Center in Sweden, NSC, and Center for Scientific Computing at Chalmers, C3SE) is gratefully acknowledged. The authors would like to thank Professor Lars Davidson for valuable discussions.

References

- [1] SHK, 2001, "Fire in a Coach After a Traffic Accident on Highway 70, Fjärdhundra, C län, 21st November 1998," Swedish Accident Investigation Board (SHK), Report No. 2001:04.
- [2] Sigbjörnsson, R., and Snæbjörnsson, J. T., 1998, "Probabilistic Assessment of Wind Related Accidents of Road Vehicles: A Reliability Approach," *J. Wind. Eng. Ind. Aerodyn.*, **74–76**, pp. 1079–1090.
- [3] Chiu, T. W., and Squire, L. C., 1992, "An Experimental Study of the Flow Over a Train in a Crosswind at Large Yaw Angles Up to 90°," *J. Wind. Eng. Ind. Aerodyn.*, **45**, pp. 47–74.
- [4] Suzuki, M., Tanemoto, K., and Maeda, T., 2003, "Aerodynamic Characteristics of Train/Vehicles Under Cross Winds," *J. Wind. Eng. Ind. Aerodyn.*, **91**, pp. 209–218.
- [5] Baker, C. J., Jones, J., Lopez-Calleja, F., and Munday, J., 2004, "Measurements of the Cross Wind Forces on Trains," *J. Wind. Eng. Ind. Aerodyn.*, **92**, pp. 547–563.
- [6] Baker, C. J., 2003, "Some Complex Applications of the Wind Loading Chain," *J. Wind. Eng. Ind. Aerodyn.*, **91**, pp. 1791–1811.
- [7] Hemida, H., and Krajnović, S., 2008, "LES Study of the Influence of a Train Nose Shape on the Flow Structures Under Cross-Wind Conditions," *ASME J. Fluids Eng.*, **130**(9), p. 091101.
- [8] Krajnović, S., Georgii, J., and Hemida, H., 2008, "DES of the Flow Around a High-Speed Train Under the Influence of Wind Gusts," Seventh International ERCOFTAC Symposium on Engineering Turbulence Modelling and Measurements, ETMM7, Amathus, Cyprus, Jun. 4–6.
- [9] Esra, O., and Bedii, O., 2004, "Turbulent Structure of Three-Dimensional Flow Behind a Model Car: Exposed to Crosswind," *J. Turbul.*, **5**, pp. 1–18.
- [10] Hucho, W. H., and Sovran, G., 1993, "Aerodynamics of Road Vehicles," *Annu. Rev. Fluid Mech.*, **25**, pp. 485–537.
- [11] Baker, C. J., and Reynolds, S., 1992, "Wind-Induced Accidents of Road Vehicles," *Accid. Anal. Prev.*, **24**(6), pp. 559–575.
- [12] Kobayashi, T., and Kitoh, K., 1983, "Cross-Wind Effects and the Dynamics of Light Cars," *Int. J. Veh. Des.*, Special Publication **SP3**, pp. 142–157.
- [13] Diedrichs, B., 2005, "Computational Methods for Crosswind Stability of Railway Trains," Division of Railway Technology, Department of Mechanical Engineering, Royal Institute of Technology, Sweden, Stockholm, Report.
- [14] Matschke, G., 2001, "Sicherheitsnachweis bei seitenwind," Deutsche Bahn AG, Konzernrichtlinie 401, Version 03.2001.
- [15] DEUFRAKU Project, 2004, "Side Wind Behaviour of Rail Vehicles (Project No. 19p0056b)," <http://www.transport-research.info/web/projects/>
- [16] Ryan, A., and Dominy, R. G., 2000, "Wake Surveys Behind a Passenger Car Subjected to a Transient Cross-Wind Gust," SAE Paper No. 2000-01-0874.
- [17] Howell, J. P., 1986, "Aerodynamic Response of MAGLEV Train Models to a Crosswind Gust," *J. Wind. Eng. Ind. Aerodyn.*, **22**, pp. 205–213.
- [18] Clarke, J., and Filippone, A., 2007, "Unsteady Computational Analysis of Vehicle Passing," *ASME J. Fluids Eng.*, **129**, pp. 359–367.
- [19] Filippone, A., 2003, "Unsteady Gust Response of Road Vehicles," *ASME J.*

Fluids Eng., **125**, pp. 806–812.

- [20] Patrick, G., and Christophe, N., 2004, “Contribution to the Analysis of Transient Aerodynamic Effects Acting on Vehicles,” SAE Paper No. 2004-01-1311.
- [21] Baker, C. J., 1991, “Ground Vehicles in High Cross Winds, Part II: Unsteady Aerodynamic Forces,” *J. Fluids Struct.*, **5**, pp. 91–111.
- [22] Cheli, F., Belforte, P., Melzi, S., Sabbioni, E., and Tomasini, G., 2006, “Numerical-Experimental Approach for Evaluating Cross-Wind Aerodynamic Effects on Heavy Vehicles,” *Veh. Syst. Dyn.*, **44**, pp. 791–804.
- [23] Juhlin, M., 2005, “A Study on Crosswind Sensitivity of Buses,” thesis for Licentiate of Engineering, Department of Aeronautical and Vehicle Engineering, The Royal Institute of Technology (KTH), Sweden.
- [24] Petzäll, J., Torlund, P. A., Falkmer, T., Albertsson, P., and Björnsting, U., 2008, “Aerodynamic Design of High-Sided Coaches to Reduce Cross-Wind Sensitivity, Based on Wind Tunnel Tests,” *Int. J. Crashworthiness*, **13**, pp. 158–194.
- [25] Hemida, H., and Krajnović, S., 2007, “DES of the Flow Around a Realistic Bus Model Subjected to a Side Wind With a 30° Yaw Angle,” Fifth IASME/WSEAS International Conference on Fluid Mechanics and Aerodynamics, Athens, Greece, Aug. 25–27.
- [26] Per-Åke, T., 1999, “Experimentell undersökning av sidvindskänsligheten hos en modell av en tvåvåningsbuss i FFA:s vindtunnel LT1,” Report No. FFA TN 2000-05, in Swedish.
- [27] 2008, FLUENT6.3 Manual, <http://www.cranfield.ac.uk/cww/ccdocs/documentation/fluvent/fluvent6.3/>
- [28] Kader, B., 1981, “Temperature and Concentration Profiles in Fully Turbulent Boundary Layers,” *Int. J. Heat Mass Transfer*, **24**(9), pp. 1541–1544.
- [29] Shur, M., Spalart, P. R., Strelets, M., and Travin, A., 1999, “Detached-Eddy Simulation on an Airfoil at High Angle of Attack,” *Engineering Turbulence Modelling and Experiments 4*, W. Rodi and D. Laurence, eds., Elsevier, New York, pp. 669–678.
- [30] Constantinescu, G. S., and Squires, K. D., 2003, “LES and DES Investigations of Turbulent Flow Over a Sphere at $Re=10,000$,” *Flow, Turbul. Combust.*, **70**, pp. 267–298.

Assessment Measures for Engineering LES Applications

I. Celik

Department of Mechanical and Aerospace
Engineering,
West Virginia University,
Morgantown, WV 26505
e-mail: ismail.celik@mail.wvu.edu

M. Klein

e-mail: kleinm@ekt.tu-darmstadt.de

J. Janicka

e-mail: janicka@ekt.tu-darmstadt.de

Energy and Power-Plant Technology (EKT),
Department of Mechanical Engineering,
Technical University of Darmstadt,
Darmstadt 64287, Germany

Anticipating that large eddy simulations will increasingly become the future engineering tool for research, development, and design, it is deemed necessary to formulate some quality assessment measures that can be used to judge the resolution of turbulent scales and the accuracy of predictions. In this context some new and refined measures are proposed and compared with those already published by the authors in the common literature. These measures involve (a) fraction of the total turbulent kinetic energy, (b) relative grid size with respect to Kolmogorov or Taylor scales, and (c) relative effective subgrid/numerical viscosity with respect to molecular viscosity. In addition, an attempt is made to segregate the contributions from numerical and modeling errors. Proposed measures are applied to various test cases and validated against fully resolved large eddy simulation and/or direct numerical simulation whenever possible.

[DOI: 10.1115/1.3059703]

Keywords: quality assessment measures, LES, modeling and numerical errors, LES quality

1 Introduction

The objective of this paper is to formulate several indicators of large eddy simulation (LES) quality in terms of both numerical and model accuracies. Numerical accuracy concerns primarily grid resolution, and model accuracy refers to how good a certain subgrid scale (sgs) (or subfilter scale (sfs)) model performs compared with “true” direct numerical simulation (DNS) and/or experimental data. Since in most applications the filtering process is convoluted with numerical discretization errors, it is difficult to segregate these factors. This is the reason for seeking some verifiable measures that could be used as indicators of numerical and/or modeling errors in LES.

Before discussing measures for LES quality assessment, one has to distinguish two approaches to deal with the unknown correlation $u_i u_j$ appearing in the filtered Navier–Stokes equations (Lund [1]):

$$\overline{u_i u_j} = \overline{u_i} \overline{u_j} + (\overline{u_i u_j} - \overline{u_i} \overline{u_j}) \quad (1)$$

$$\overline{u_i u_j} = \overline{u_i} \overline{u_j} + (\overline{u_i u_j} - \overline{u_i} \overline{u_j}) \quad (2)$$

The terms in the parentheses are the unknown sgs stress tensor τ_{ij} . If Eq. (1) is used, a closed equation for $\overline{u_i}$ is obtained, provided a model for τ_{ij} is supplied. This equation requires no explicit filtering during the solution process. If Eq. (2) is used, one obtains again a closed equation, but this time with an additional explicit filtering operation applied to the nonlinear term. Therefore we call the first approach implicit filtering and the second approach explicit filtering (note that Sagaut [2] used the terminology double and triple decompositions). Both approaches have several advantages and disadvantages which will not be discussed here. However, there is a specific issue that is important with respect to the definition of errors and their quantification. In the context of explicit filtering, the filter width and the grid size can be changed independently in order to separate both error contributions, and as a consequence, a grid independent solution can be achieved. If the

implicit approach is used, the only reference to the filter is through the filter width Δ appearing, for example, in the well-known Smagorinsky model,

$$\tau_{ij} - \frac{1}{3} \tau_{kk} \delta_{ij} = -2(C_s \Delta)^2 |\overline{S}_{ij}| \overline{S}_{ij} \quad (3)$$

Therefore, the definition of filter width is to some extent arbitrary. However, for several reasons it is reasonable to identify filter width with grid spacing. As a result, there is no such thing as grid independent LES since such LES tends toward the DNS if the grid is refined. This has implications for the definition of error contributions, as discussed below. Geurts and Fröhlich [3] and Meyers et al. [4] adopted a third point of view, which should not be confused with the explicit filtering approach. They interpreted the product $(C_s \Delta)$ as the effective filter controlling the smoothness of the LES solution. Increasing the grid resolution while keeping the effective filter width constant leads to an exact solution for the “Smagorinsky fluid,” which is not necessarily also an accurate approximation to filtered DNS.

All the above interpretations lead to different definitions of modeling and numerical errors. Assuming the existence of a grid independent LES, the numerical error ε_{num} and modeling error ε_{mod} of a quantity φ are typically defined as (e.g., see Vreman et al. [5])

$$\varepsilon_{\text{num}}(\varphi) = \varphi_{\text{fine grid LES}} - \varphi_{\text{LES}} \quad (4)$$

and

$$\varepsilon_{\text{mod}}(\varphi) = \varphi_{\text{filtered DNS}} - \varphi_{\text{fine grid LES}} \quad (5)$$

The total error, which depends in this definition on the filter, is then given by

$$\varepsilon_{\text{tot}}(\varphi) = \varepsilon_{\text{num}}(\varphi) + \varepsilon_{\text{mod}}(\varphi) = \varphi_{\text{filtered DNS}} - \varphi_{\text{LES}} \quad (6)$$

Meyers et al. [4] used a similar definition; however, the modeling error is defined with respect to the DNS rather than the filtered DNS, and the true LES solution has to be understood in the sense of the exact solution for the Smagorinsky fluid. In implicit LES, there is no such thing as grid independent LES as mentioned above and consequently, Eqs. (4) and (5) cannot be used to define the modeling error. In this context, the numerical error and the modeling error have to be understood with a more philosophical thinking as the error contribution due to numerical representation (discretization) and modeling errors representing the shortcomings of the sgs model to represent flow physics on this particular grid

Contributed by the Fluids Engineering Division of ASME for publication in the JOURNAL OF FLUIDS ENGINEERING. Manuscript received January 31, 2007; final manuscript received October 17, 2008; published online February 9, 2009. Assoc. Editor: Rajat Mittal. Paper presented at the 2006 ASME Fluids Engineering Division Summer Meeting and Exhibition (FEDSM2006), Miami, FL, July 17–20, 2006.

with respect to the DNS (see also Klein [6], Freitag and Klein [7], and Celik et al. [8]).

We emphasize the fact that in many engineering LES applications of practical interest, numerical errors, such as phase/dispersion, amplitude/dissipation, and aliasing errors, are present. Of these, numerical dissipation is particularly important since it implicitly affects the apparent Reynolds number of the flow, which is the primary scaling factor in viscous fluid flow. When Reynolds number is modified, flow regimes could change, hence making it difficult to compare LES results with experiments and/or DNS. To illustrate the consequences of numerical errors more, we give below some examples from the literature.

According to Ghosal [9], the finite difference error is proportional λ^q , where λ is the wave number in the spectral space and the exponent q is independent, while the constant of proportionality is a weak function, of the numerical scheme. Chow and Moin [10] examined Ghosal's [9] conclusions for a more realistic flow field. They reported that the filter size should be at least twice as large as the grid size for a sixth order Padé scheme and four times the grid spacing for a second order scheme in order to ensure that the subgrid forcing terms are larger than the numerical error. This is nearly impossible to achieve for engineering LES applications. Also Vreman et al. [5,11] showed that even with higher order methods, the numerical dissipation can be as large as, and may have the opposite sign as, the sgs contribution, thus canceling each other. Meyers et al. [4] applied Richardson extrapolation to DNS to demonstrate the sensitivity of the Taylor microscale to grid size. Therefore grid convergence studies should be applied on most sensitive flow parameters to quantify discretization error.

In a recent study by You et al. [12], it is clearly demonstrated in the context of a linear two-dimensional convection-diffusion equation without any source term that mesh nonuniformity and skewness affect the phase and amplitude errors as well as the temporal stability of the numerical schemes used. They concluded that on a uniform skewed mesh, the commonly used central differencing scheme exhibits "large numerical dissipation in the low Reynolds number cases while numerical dispersion is a major concern at the high Reynolds number cases. The amplification error and resulting numerical instability are further enhanced if mesh skewness is coupled with mesh stretching." Given that controlling the mesh skewness and stretching is not trivial in simulations of flows with complex geometries, such as flow past an array of circular cylinders in heat exchangers, it can be concluded that the solution will be polluted by all types of numerical errors in engineering applications of LES.

Figures 1(a)–1(c) illustrate various consequences of mesh size on LES results. Figure 1(a) depicts the mean velocity profile from channel flow simulations ($Re_\tau=180$) at three different grid sizes with a grid coarsening factor of 2. The results on the finest grid correspond to DNS; the medium and coarse grid simulations correspond to LES without a subgrid scale model. Figure 1(b) shows the energy spectrum for these three simulations together with the channel flow LES results at considerably higher Reynolds number ($Re_\tau=1500$), where a Smagorinsky model has been used. It is important to note that the high Reynolds number channel flow LES was performed on a rather coarse grid in order to illustrate clearly the effect of an apparent dissipation range, which can occur in practical LES applications as a result of interacting numerical, modeling, and grid cutoff errors. A similar plot in the context of isotropic decaying turbulence can be found in Geurts and Fröhlich [3]. The energy spectra calculated on the coarse grid with and without the sgs model show approximately the same cutoff frequency and the same slope in the "apparent" dissipation range. Figure 1(c) shows the turbulent kinetic energy along the axis of a plane jet obtained from DNS at four different Reynolds numbers together with one LES simulation, using the Smagorinsky model, at the same Reynolds number. While these DNS calculations show

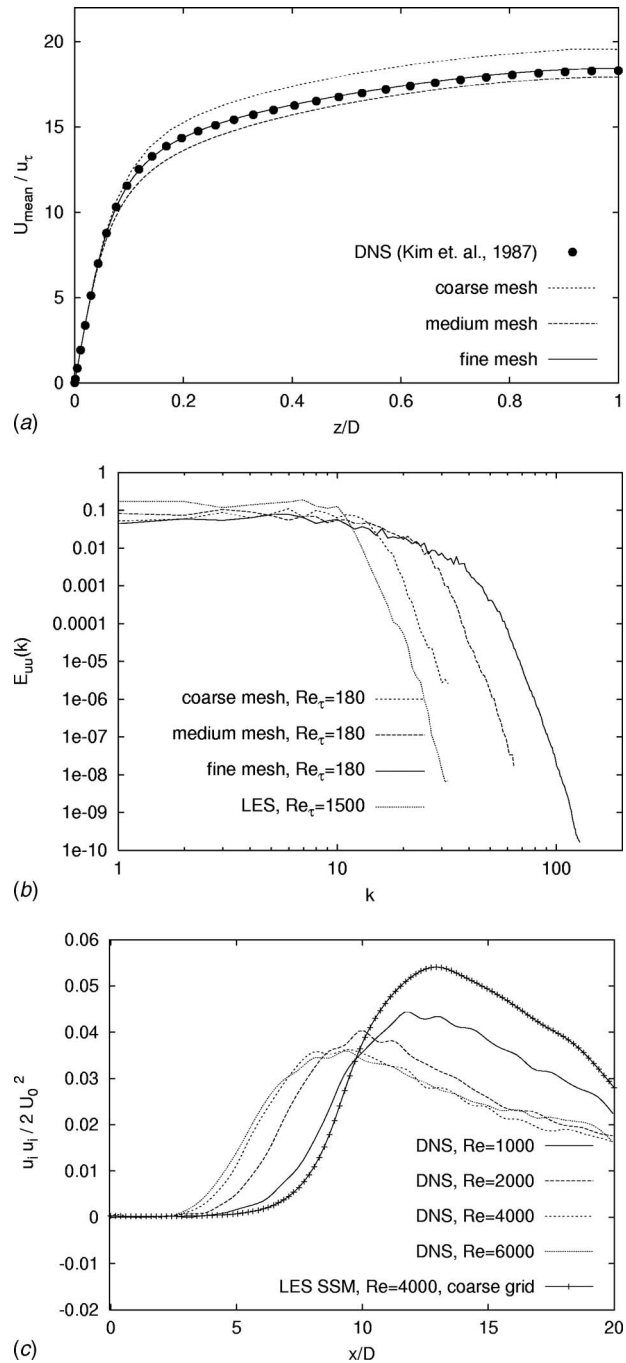


Fig. 1 Effect of mesh size on simulation results: (a) channel flow mean velocity profiles on different meshes, (b) energy spectra for the channel flow calculations, (c) turbulent kinetic energy from DNS and LES of a plane jet plotted at different Reynolds numbers along the centerline of the jet (Klein [6] and Klein et al. [13]). Note that the channel flow simulations by Klein were performed using a second order central differencing scheme on a staggered grid with a grid stretching factor of approximately 1.05 in the wall-normal direction without any local coordinate transformation.

that as the Reynolds number decreases the transition point moves downstream, the LES calculations with the same Re as in DNS predicts a retarded transition in a plane jet.

These apparent mismatches in Reynolds number scaling may be due to a combination of numerical errors, grid filter errors, and modeling errors. The interaction of these three apparent filters may cause the spectrum to decay steeply at a wave number where

there is an inertial range in the corresponding DNS. Hence, it is crucial to devise a method to analyze the relative contributions of numerical and modeling errors.

Moreover, if the numerical contribution indeed leads to a decrease in effective Reynolds number, as the authors suspect to be the case in many applications, then it becomes necessary to have a measure of the numerical viscosity present in the calculations so that proper assessment of flow regimes and, hence, a fair comparison can be made of simulations and experiments.

It should be mentioned that symmetric schemes are strictly dispersive although most multipurpose computational fluid dynamics (CFD) codes do not even run stable with a purely central symmetric scheme. Further, a symmetric scheme becomes asymmetric if applied to a nonuniform grid, resulting in a first order dissipation error. It is, however, also important to note that accurate numerical schemes can be designed based on central differencing schemes on staggered grids using coordinate transformation, provided special attention is given to grid skewness and stretching effects along with the preservation of global conservation properties for the numerical scheme (see, e.g., You et al. [12,14]). Such schemes are, however, rarely implemented in commercial CFD codes.

1.1 Overview of Methods. Roache [15] gave the following taxonomy for obtaining information for error estimates, which have been used in the context of Reynolds-averaged Navier-Stokes (RANS) simulations but are in principle also applicable to LES:

1. auxiliary algebraic evaluations on the same grid
2. additional solutions of the governing equations on other grids
3. additional solutions of the governing equations on the same grid
4. auxiliary partial differential equation (PDE) solutions on the same grid

This paper focuses on methods that can be used with any CFD code, which is not the case for methods belonging to category 4. The rest of the paper is organized as follows.

In Sec. 2, we start with some concepts that can be applied as a single grid estimator (category 1). An example of a two grid estimator (category 2) is the large eddy simulation index of quality (LES_IQ) suggested by Celik et al. [16] in Sec. 3. The systematic grid and model variation (SGMV) proposed by Klein [6] is a combination of methods belonging to categories 2 and 3 and requires three simulations on two different grids (see Sec. 4). Although three (or more) grid studies would be desirable in calculating the observed order of the numerical or modeling error rather than using their theoretical values, such an approach seems to be impractical for engineering applications. Section 5 discusses the estimation of turbulence quantities and scaling exponents relevant to error estimation. Sections 6 and 7 contain applications of the proposed method followed by conclusions and recommendations in Sec. 8.

2 Single Grid Estimators

Geurts and Fröhlich [3] proposed to use the activity parameter s to qualify LES results,

$$s = \frac{\langle \varepsilon_{ij} \rangle_{\text{turb}}}{\langle \varepsilon_{ij} \rangle_{\text{lam}} + \langle \varepsilon_{ij} \rangle_{\text{turb}}} \quad (7)$$

where ε denotes dissipation rate.

The modified activity parameter proposed by Celik et al. [16] reads

$$s^* = \frac{\langle v_l \rangle + \langle v_{\text{num}} \rangle}{\langle v_l \rangle + \langle v_{\text{num}} \rangle + v} = \frac{v_{l,\text{eff}}}{v_{l,\text{eff}} + v} \quad (8)$$

Alternative measures are the relative Kolmogorov scale index

$$\text{LES_IQ}_\eta = \frac{1}{1 + \alpha_\eta \left(\frac{h}{\eta_{\kappa,\text{eff}}} \right)^m} \quad (9)$$

the relative sgs-viscosity index

$$\text{LES_IQ}_v = \frac{1}{1 + \alpha_v \left(\frac{\langle v_{\text{eff}} \rangle}{v} \right)^n} \quad (10)$$

and the relative resolved turbulent kinetic energy (tke) content

$$\frac{k_{\text{res}}}{k_{\text{tot}}} = \frac{k_{\text{res}}}{k_{\text{res}} + k_{\text{sgs}} + |k_{\text{num}}|} \quad (11)$$

Here $\alpha_\eta = \alpha_v = 0.05$, $m = 0.5$, $n = 0.53$, $v_{\text{eff}} = v_{\text{sgs}} + v_{\text{num}} + v$, $v_{\text{sgs}} = (C_s \Delta)^2 \bar{S}$, and $v_{\text{num}} = C_v h \sqrt{k_{\text{num}}}$. If k_{num} is not known, an approximate estimate could be used such as that given by Eq. (28). Strictly speaking m and n are functions of Reynolds number, and the values given here are calibrated ones (see Celik et al. [16]). The effective (or the apparent) Kolmogorov scale is a scale that is estimated from numerically computed values since the actual one is not known. See the discussion below for some estimates.

The effective quantities denoted by subscript “eff” should ideally include the effect of numerical dissipation as well as the filter size, Δ . In all of these formulas, there is at least one parameter that is difficult to estimate: the Kolmogorov scale in Eq. (9), v_{num} in Eqs. (8) and (10), and k_{num} in Eq. (11) (or C_n in Eq. (28)). Empirical equations are suggested in the later sections for approximation of these quantities.

3 LES_IQ

An example of a two grid estimator (category 2) is the LES_IQ suggested by Celik et al. [16],

$$\text{LES_IQ}_k = 1 - \frac{|k_{\text{tot}} - k_{\text{res}}|}{k_{\text{tot}}} \quad (12)$$

When the filter length, Δ , is different from the grid size, h , and the order of the numerical scheme, p , is also different from the filtering effect, q , then it is postulated that

$$k_{\text{tot}} - k_{\text{res}} = k_{\text{eff,sgs}} = ah^p + b\Delta^q \quad (13)$$

To determine all the five unknowns above, namely, k_{tot} , a , b , p , and q , one needs five calculations; this is not a practical option. If we assume $p=q$ and use implicit filtering, i.e., $\Delta = \text{const} \times h$, then

$$k_{\text{tot}} - k_{\text{res}} = k_{\text{eff,sgs}} = a_k h^p \quad (14)$$

Now there are only three unknowns, and these can be determined from three calculations on significantly different but geometrically similar grids, as it is done for RANS calculations. If three grid calculations become too expensive, then one can use the theoretical order of the scheme; if that is not known, one can assume $p=2$ based on the arguments put forward by Celik et al. [16]. Results from the current study (see Sec. 5) show that p can change over a wide range and $p=2$ seems to be good as an average value.

When Eq. (12) is applied to transitional flows such as the plane jet flow shown in Fig. 1(c), it may result in unreasonable indices (Celik et al. [8]) in the laminar flow regimes. Correction for laminar flow regions is necessary where LES_IQ has no real meaning. There, it should be allowed to go to zero smoothly. This is done by introducing an empirical laminar flow correction factor

$$f_{\text{lam}} = 0.5(1 + \tanh\{\beta[\text{Re}_{\text{tr}}^{0.5} - C_{sl} \text{Re}_{\text{tr-crt}}^{0.5}]\}) \quad (15a)$$

where Re_{tr} is an estimated effective turbulence Reynolds number defined as

$$\text{Re}_{\text{tr}} = \frac{\left(\frac{2}{3}k_{\text{tot}}\right)^{1/2} \ell}{v_{\text{eff}}} \quad (15b)$$

with an appropriate length scale.

This function tends to zero for turbulence Reynolds numbers $\text{Re}_{\text{tr}} \ll \text{Re}_{\text{tr-crt}}$, and it has the value of 0.5 at $\text{Re}_{\text{tr}} = C_{\text{sl}}^2 \text{Re}_{\text{tr-crt}}$; $C_{\text{sl}} = \sqrt{2}$ and $\text{Re}_{\text{tr-crt}} = 25$ are used in the present calculations. The value of β determines how sharp the transition is; it is set equal to 0.5 currently. Unfortunately this requires the calculation of integral length scale ℓ from the already uncertain calculations. This can be avoided by using, say, the turbulence intensity, i.e., $u_{\text{rms}}/U_{\text{inlet}}$, where $u_{\text{rms}} = \sqrt{2}k_{\text{res}}/3$, but it is more general to use a Reynolds number based on local turbulence quantities for transition criteria.

Equation (15) accounts for the laminar-turbulence transition; however there needs to be another safety factor at the high Reynolds number limit. Noting that LES gets more and more difficult as the Reynolds number increases, we suggest that the original LES_IQ should be restricted from above such that 100% or perfect LES (or DNS) is possible at high turbulence Reynolds numbers only if a grid resolution is achieved to fully resolve Kolmogorov scales. To this end a possible high Reynolds number empirical correction factor is

$$f_{\text{ret}} = \exp\left[-\gamma\left(\sqrt{\frac{h}{\eta} - h^*}\right)^{1/2} \text{Re}_t^{1/4}\right] \quad (16)$$

where $\gamma=0.02$ and $h^*=5$ (i.e., a grid resolution with $h/\eta=5$ is considered essentially a DNS; hence no correlation is necessary). The model constants in Eq. (16) are calibrated to achieve meaningful results for the plane jet simulations of Klein [6] thereafter they are kept unchanged. Equation (12) is multiplied by f_{lam} and f_{ret} to impose the corrections implied by Eqs. (15) and (16). The calibrated results as well as a discussion can be found in the application (Sec. 6).

4 Systematic Grid and Model Variation

Klein [6] and Freitag and Klein [7] proposed to assess the quality of LES by performing a systematic grid and model variation. The basic idea is, in addition to a grid variation, to change the model contribution. Intuitively it is clear that from such a model variation, the influence of the sgs parametrization can at least qualitatively be assessed. In order to quantify this concept, we assume in the following that the contribution from the numerical error (n) and the error contribution from the model term (m) are given by the right-hand side of the Taylor expansion, Eq. (17). Changing the model contribution by a certain factor α yields Eq. (18), and finally Eq. (19) represents the solution on a grid coarsened by a factor of β ,

$$u - u_1 = c_n h^n + c_m h^m \quad (17)$$

$$u - u_2 = c_n h^n + \alpha c_m h^m \quad (18)$$

$$u - u_3 = c_n (\beta h)^n + c_m (\beta h)^m \quad (19)$$

Combining Eqs. (17)–(19) yields the error contribution from the model term (Eq. (20)), together with an estimation of the total numerical error (Eq. (21)),

$$(u_2 - u_1)/(1 - \alpha) = c_m h^m \quad (20)$$

$$\frac{(u_3 - u_1) - (u_2 - u_1)(1 - \beta^n)/(1 - \alpha)}{(1 - \beta^n)} = c_n h^n \quad (21)$$

Rather than estimating the error contribution from the sum $c_n h^n + c_m h^m$, it is recommended to use the more conservative expression $|c_m h^m| + |c_n h^n|$ (see Eq. (22)),

$$\left| \frac{(u_2 - u_1)}{(1 - \alpha)} \right| + \left| \frac{(u_3 - u_1) - (u_2 - u_1)(1 - \beta^n)/(1 - \alpha)}{(1 - \beta^n)} \right| = |c_m h^m| + |c_n h^n| \quad (22)$$

The whole procedure is summarized below:

- Chose a grid refinement factor β and generate two grids.
- Chose a model variation factor α . If in the case of the Smagorinsky model C_s is modified, one has to keep in mind that the model parameter will appear squared in the equations.
- Perform three simulations: the standard LES with solution u_1 , one LES with a modified subgrid scale model with solution u_2 , and a standard LES on the coarse grid with solution u_3 .
- Set n equal to the theoretical order of the numerical scheme.
- The recommendation for the scaling exponent is $m=2/3$. For moderate Reynolds number flows, a higher value can be justified.
- Since a certain amount of conservatism is desirable, it is recommended to evaluate the uncertainty according to Eq. (22).
- If necessary, the individual error contributions can be estimated.

5 Estimation of Turbulence Scales and Scaling Exponents Relevant for Quality Assessment

The Kolmogorov scale can be estimated from

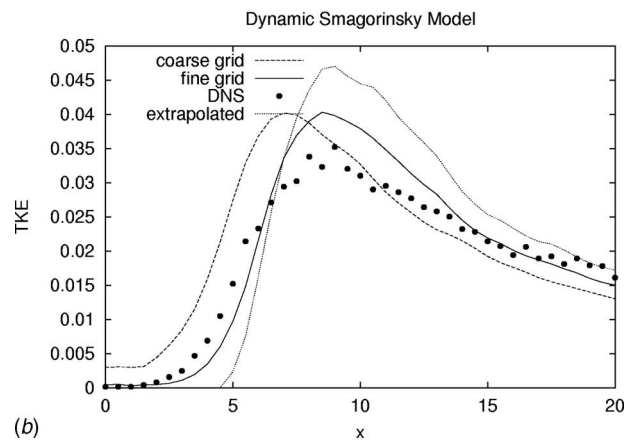
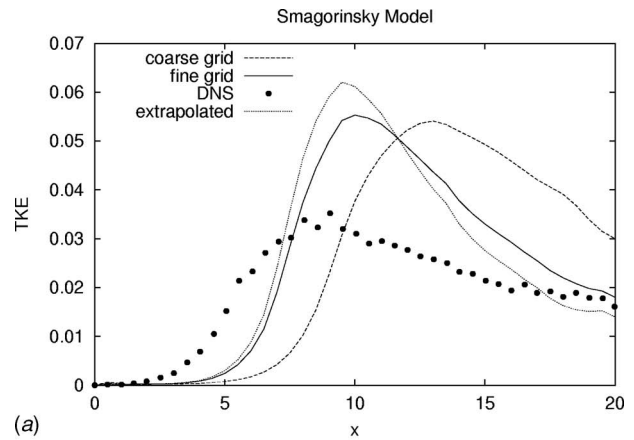


Fig. 2 Resolved turbulent kinetic energy profiles along the centerline of a jet; $\text{Re}=4000$ (based on inlet velocity=1.0 m/s and nozzle diameter=1.0 m): (a) SSM and (b) DSM

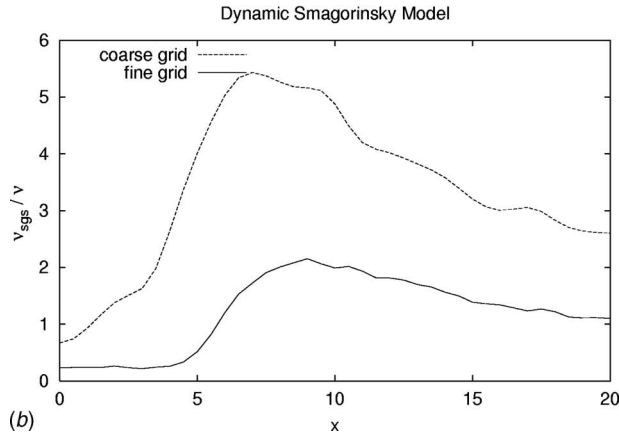
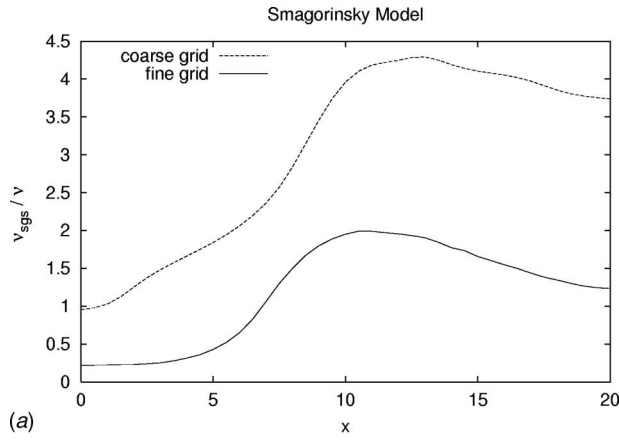


Fig. 3 Sgs-viscosity obtained from plane jet LES data

$$\eta = \left(\frac{v^3}{\varepsilon} \right)^{1/4} \quad (23)$$

with an estimate of ε from

$$\varepsilon = C \frac{u^3}{l} \quad (24)$$

When \bar{s} is given,

$$\bar{s} = \left(\frac{\varepsilon}{v_{\text{eff}}} \right)^{1/2} \quad (25)$$

If \bar{s} is not given, it can be calculated from the Smagorinsky model, i.e.,

$$\bar{s} = \frac{\langle v_{\text{sgs}} \rangle}{(C_s \Delta)^2} \quad (26)$$

In Eq. (24) $u = \sqrt{2k_{\text{tot}}/3}$ and $k_{\text{tot}} = k_{\text{res}} + k_{\text{sgs}} + k_{\text{num}}$. In common sub-grid scale models, k_{sgs} can be explicitly related to the model sub-grid viscosity v_{sgs} ; if only k_{sgs} is available, v_{sgs} can be estimated from

$$v_{\text{sgs}} = C_v \Delta \sqrt{k_{\text{sgs}}} \quad \text{or} \quad k_{\text{sgs}} = \left(\frac{v_{\text{sgs}}}{C_v \Delta} \right)^2 = C_k \Delta^2 \bar{s}^2 \quad (27)$$

where $C_k = (C_s^2 / C_v)^2$ and $C_v = 0.165$ (this follows from $\varepsilon_{\text{sgs}} = C_\varepsilon u_{\text{sgs}}^3 / \Delta$ and $u_{\text{sgs}} = \sqrt{2k_{\text{sgs}}/3}$; $v_{\text{sgs}} = C_\mu k_{\text{sgs}}^2 / \varepsilon_{\text{sgs}}$ and $C_\mu = 0.09$). This analysis yields a value for the constant $C_k = 0.0376$ if $C_s = 0.18$ (i.e., $C_s^2 = 0.032$; see Bogey and Bailly [17]). The mean value of C_k was obtained by Bogey and Bailly [17] for a round free jet as 0.01. If we take $C_s^2 = 0.032$, this yields $C_v = 0.32$ instead of 0.165. A value of 0.094 is suggested by Yoshizawa [18]. It

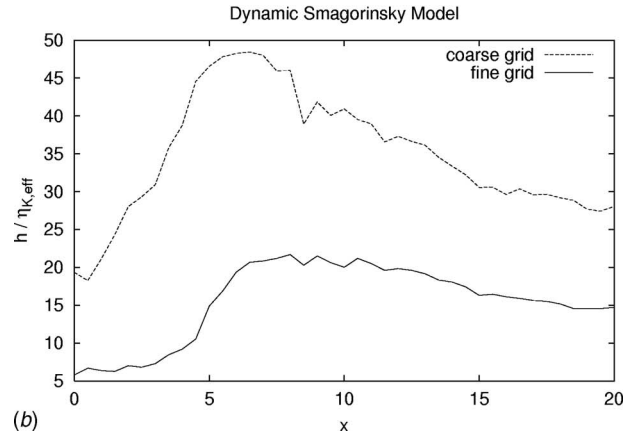
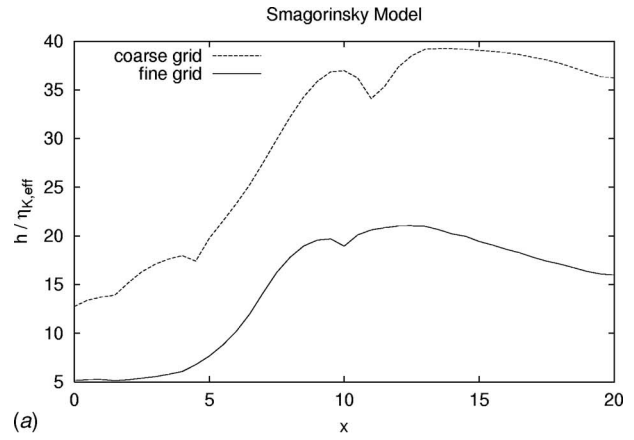


Fig. 4 Estimated Kolmogorov length scales for the plane jet data: (a) SSM and (b) DSM

seems that some calibrated value for C_v in the range of 0.05–0.30 can be used in the final analysis. Further work will determine what value is most appropriate for this constant. As suggested above, k_{num} can be estimated on a single grid from

$$k_{\text{num}} = C_n \left(\frac{h}{\Delta} \right)^2 k_{\text{sgs}} \quad (28)$$

where C_n is of order of magnitude 1.0, i.e., equal weightings of numerical and modeling errors when $h = \Delta$. We selected this relation based on the rationale that in most common applications of LES, $k_{\text{sgs}} \sim \Delta^p$, $k_{\text{num}} \sim h^q$, and $p = q \approx 2.0$, as argued above for Eq. (14).

On multigrid calculations, k_{num} can be estimated from

$$k_{\text{num}} = k_{\text{tot}} - k_{\text{res}} - k_{\text{sgs}} \quad (29)$$

after determining k_{tot} by extrapolation.

It should be noted that near a transition point from laminar to turbulent flow, all these constants should smoothly approach zero for consistency. This can be achieved by imposing a damping function in the form of Eq. (15) for any of these constants.

Using the relations from Celik et al. [16] in Eq. (9), one can relate h/η to other relevant parameters as follows:

$$\frac{h}{\eta} = \frac{1}{8} \frac{h}{\Delta} \text{Re}_t^{3/4} \quad (30)$$

The turbulence Reynolds number is given by

$$\text{Re}_t = \frac{u\ell}{\nu}, \quad u = \sqrt{2k/3} \quad (31)$$

$$\ell = \max(8h, 8\Delta, \ell_t, \ell_{\text{physical}}) \quad (32)$$

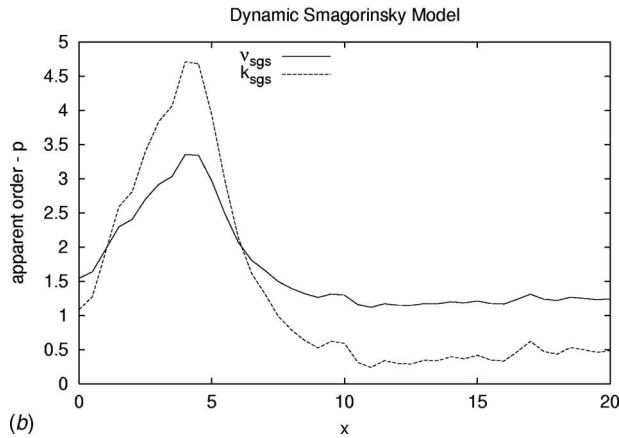
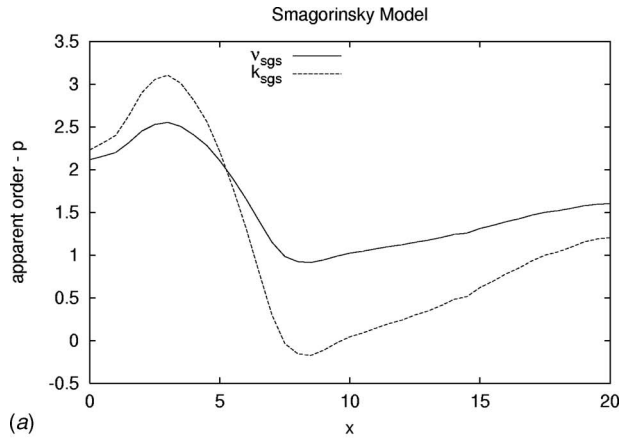


Fig. 5 Apparent order of modeled contributions for v_{sgs} and k_{sgs} : (a) SSM and (b) DSM

$$\ell_i = C_D \frac{k_{res}^{3/2}}{\langle \varepsilon \rangle} = \frac{k_{res}^{3/2}}{v_{eff} \bar{\varepsilon}^2} \quad (33)$$

where $C_D \approx 0.55$ and $\bar{\varepsilon}$ is given by Eq. (26); $\ell_{physical}$ is an upper bound that should be imposed by consideration of the flow problem; e.g., in a pipe flow it must be a fraction of the pipe radius, and so on. If the sgs model is not of a Smagorinsky type, then an approximate model for ν_{sgs} may be needed.

The relations cited above are used to estimate the local Kolmogorov scale for the plane jet case of Klein et al. [13], which contains resolved tke (Fig. 2) as well as sgs-viscosity (Fig. 3) from two models, namely, standard Smagorinsky model (SSM) and dynamic Smagorinsky model (DSM). As seen in Fig. 4, reasonable estimates are obtained as indicated by the DNS calculations of Klein [6] and Klein et al. [13]; in the fully turbulent jet regime, the coarse grid size is approximately 40, and the fine grid is approximately 20 times the Kolmogorov scale.

Single grid LES data usually contain k_{res} and ν_{sgs} . With this information, Eq. (26) can be used to calculate $\bar{\varepsilon}$, and then Eq. (25) can be used to calculate the dissipation rate, ε . One still needs an estimate for the numerical viscosity in order to calculate v_{eff} . This can be accomplished with the estimate of k_{num} from Eq. (28). Unfortunately, this equation will not reveal the sign of the numerical error, which can be negative or positive. If two grid data are available, Eq. (29) can be used instead of Eq. (28), with k_{tot} being estimated by extrapolation.

For the plane jet case of Klein et al. [13], k_{res} data (Fig. 2) and ν_{sgs} data (Fig. 3) were used to calculate v_{eff} , $\bar{\varepsilon}$, and ε , which in turn lead to the estimates given in Fig. 4 for the effective (or apparent) Kolmogorov length scale in their LES calculations. Note that both models seem to exhibit similar grid resolutions

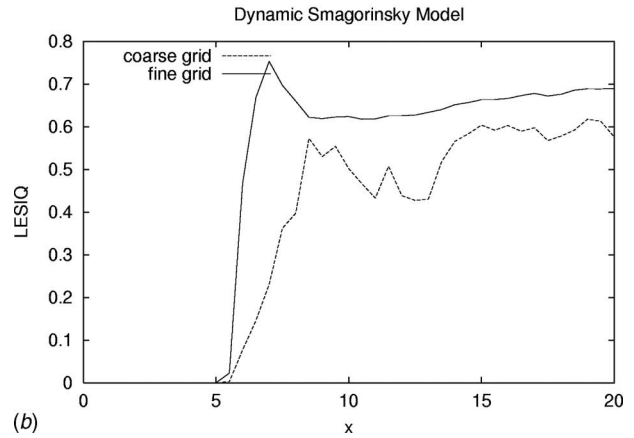
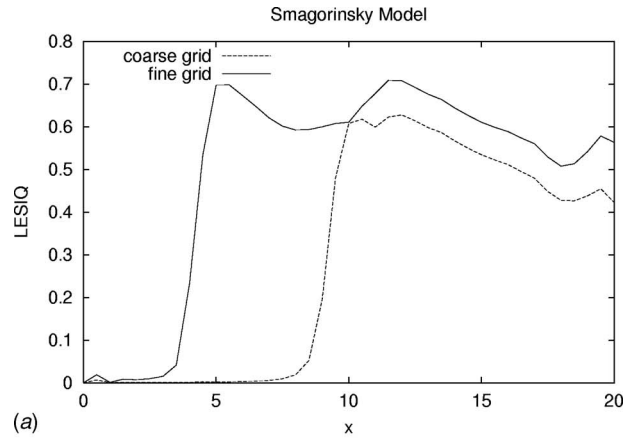


Fig. 6 Estimated LES_IQ for the plane jet LES data: (a) SSM and (b) DSM

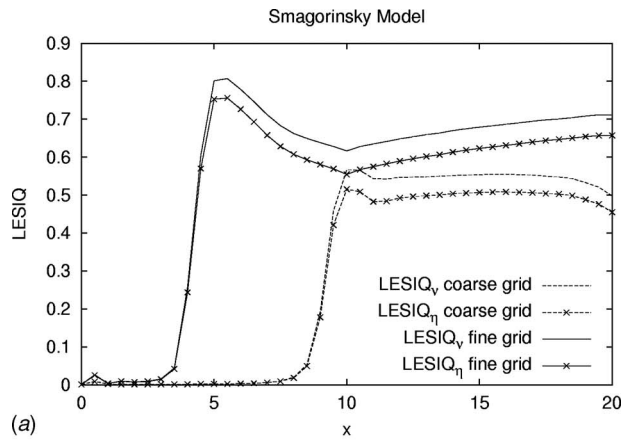
with respect to the Kolmogorov scale. This is probably because along the centerline the strain rate and, hence, the turbulent stresses are small. It should be mentioned that the extrapolated profiles do not necessarily tend toward DNS (Fig. 2); however, this trend is expected as the grid is refined and the location of transition is stabilized.

Another aspect of the present analysis is to study the convergence behavior of model contribution. This can be done by extrapolating ν_{sgs} or k_{sgs} to zero in the asymptotic range. Two grid calculations then can be used to calculate the apparent order from

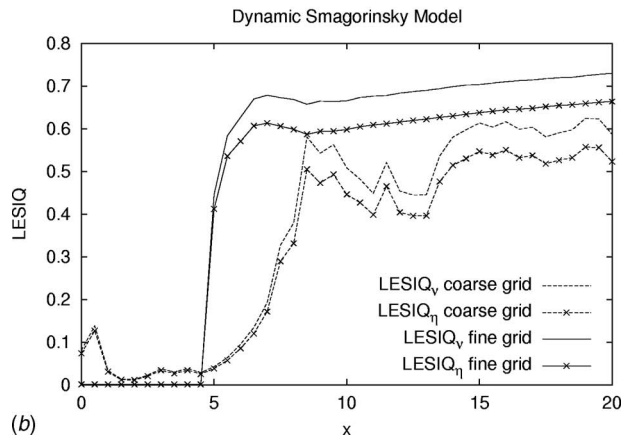
$$p_{\nu_{sgs}} = \frac{\ln \left[\frac{(\nu_{sgs})_{fg}}{(\nu_{sgs})_{cg}} \right]}{\ln \left[\frac{h_{fg}}{h_{cg}} \right]} \quad (34)$$

where the subscripts “fg” and “cg” denote the fine grid and coarse grid values, respectively. Similarly an apparent order $p_{k_{sgs}}$ for k_{sgs} can be calculated. The results of such a calculation are depicted in Fig. 5.

In the laminar flow region $0 < x/D < 4$, the results are not so meaningful, while in the rest of the domain the average convergence rates for ν_{sgs} is $4/3 = 1.33$, and for the normal stress k_{sgs} it is $2/3 = 0.67$. The average values over the whole domain are: $p_{sgs-vis-avr} = 1.57$; $p_{sgs-tke-avr} = 1.13$; when the laminar flow region is excluded, these values change to 1.1 and 0.6, respectively, which are in good agreement compared with the theoretical values of $4/3$ and $2/3$ for ν_{sgs} and k_{sgs} in the Smagorinsky model (Pope [19]).



(a)



(b)

Fig. 7 Estimated LES_IQ using v_{eff} and $\eta_{h,\text{eff}}$ for the plane jet LES data: (a) SSM and (b) DSM

6 Applications to Isothermal Flow

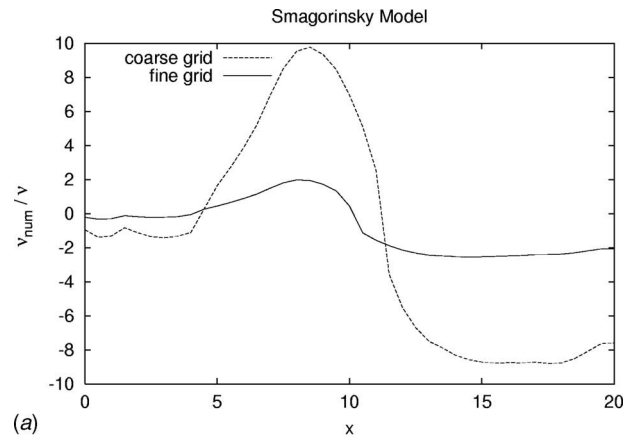
In this section the application of the proposed indices to the plane jet LES data at $\text{Re}=4000$ of Klein et al. [13] and Freitag and Klein [7] is discussed. The calculated LES_IQ values are shown in Figs. 6 and 7. These have been calibrated in a way using DNS data of Klein [6] and Klein et al. [13] to exhibit grid sensitivity while at the same time giving reasonable indices for grid resolution. This is indeed the case for both sgs models (i.e., SSM and DSM) also seen in Figs. 7(a) and 7(b). All of the measures described in Secs. 3 and 4 give reasonable values compared with DNS results (Fig. 2), which happened to be available in this case. The real test would be assessment of some independent cases to validate these suggested formulas. This is done in Sec. 7.

As mentioned in Sec. 1, one of the crucial issues in LES is to be able to quantify the numerical viscosity that is inherent in the discretization scheme. Once the total tke is estimated, k_{num} can be calculated from Eq. (29), and then using a similar relation to Eq. (27) numerical viscosity ν_{num} can be calculated, i.e.,

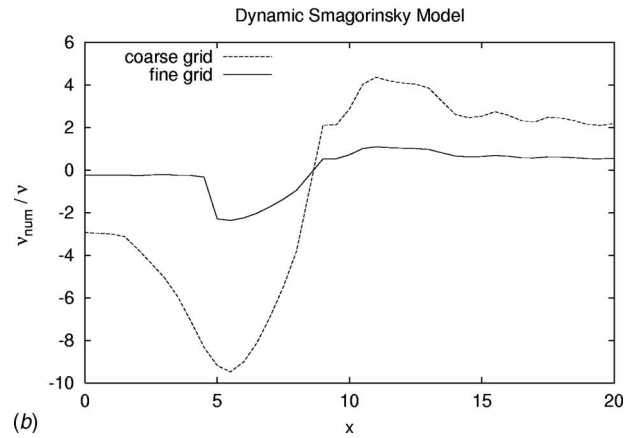
$$\nu_{\text{num}} = \text{sgn}(k_{\text{num}}) C_v \Delta \sqrt{\text{abs}(k_{\text{num}})} \quad (35)$$

Estimated dimensionless numerical viscosity levels are depicted in Fig. 8 for the data of Klein et al. [13]. It is interesting to see that the sign of ν_{num} in SSM is the opposite of that in DSM.

Moreover, there is roughly a fourfold decrease in numerical contribution when the grid size is decreased by half, indicating that the numerical scheme used is of second order. Comparing Fig. 8 to Fig. 3 we see that on the fine grid ν_{num} and ν_{sgs} are of the same order of magnitude approximately two times the laminar viscosity.



(a)



(b)

Fig. 8 Estimated numerical viscosity normalized by laminar viscosity for plane jet LES data: (a) SSM and (b) DSM

The information in Figs. 3 and 8 is used to calculate k_{sgs} and k_{num} via Eqs. (27) and (29), and the results are presented in Fig. 9 in terms of uncertainty U_k

$$U_k = k_{\text{sgs}} + \text{abs}(k_{\text{num}}) \quad (36)$$

Surprisingly, the estimated uncertainty in the tke from the present analysis closely resembles those (see Fig. 10) calculated using the method of Klein [6] using three calculations of the same case as explained above (see also Freitag and Klein [7] for more details). It seems that one calculation can be avoided with the help of a model equation such as Eq. (27) at the cost of perhaps losing some accuracy. It is also noteworthy to observe that even on a relatively coarse grid the estimated uncertainty is a good indicator being on the conservative side compared with DNS.

Finally, we present the results for the systematic grid and model variation approach. Axial profiles of uncertainty in the velocity and the turbulent kinetic energy for a plane jet LES with SSM are depicted in Fig. 10. The strong deviations after the jet breakup point ($x/D \approx 5$) are due to the fact that transition cannot be predicted properly using the Smagorinsky model. Besides the shape of the error profile, the error magnitude is predicted remarkably well, which holds true for the mean axial velocity as well as for the turbulent kinetic energy. The application of this approach to a channel flow simulation and a swirling recirculating flow is discussed in Klein [6] and Freitag and Klein [7].

7 Reacting Flow Applications

In this section we extend the previous investigations the first time to reacting flow. The analysis is done on LES data of Aluri et al. [20] for a 75 mm diameter, 320 mm long dump combustor with and without combustion. The inlet velocity and pressure are 45

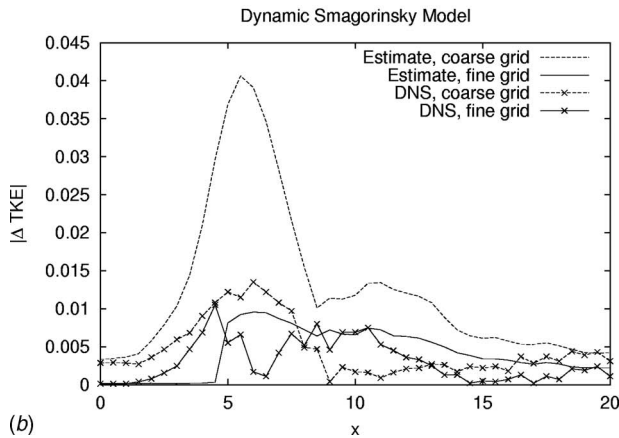
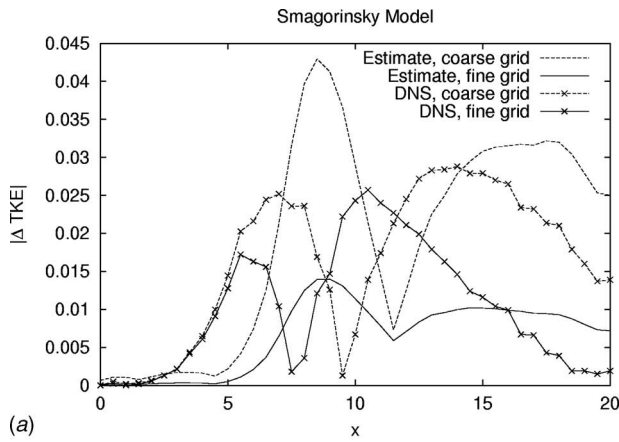


Fig. 9 Estimated uncertainty in tke for the plane jet data: (a) SSM and (b) DSM. The curves labeled as DNS are those obtained by subtracting k_{res} from k_{DNS} .

m/s and 1 bar, respectively, for both cases. The inlet temperatures are 300 K for the case without combustion (C-WO) and 673 K for combustion (C-WC). The adiabatic flame temperature and flue temperature for C-WC are 1750 K and 1512 K, respectively. The simulations were performed by Aluri et al. [20] using the commercial code FLUENT with the standard Smagorinsky model.

It is seen from the resolved tke profiles (Fig. 11) that transition to fully turbulent flow takes place much later ($x/d=6$) in the case of C-WC compared with that ($x/D=2$) in the case of C-WO. The Reynolds number at the inlet is 15,500 for C-WC versus 80,000 for C-WO. Since the vortex breakdown in the C-WC case will occur much later, these two cases cannot be compared fairly, although the LES were done in a similar manner on the same grid.

It is interesting to see that in C-WO the tke decreases as the grid is refined, while in C-WC it follows an opposite trend. This can be explained on the bases of effective Reynolds number

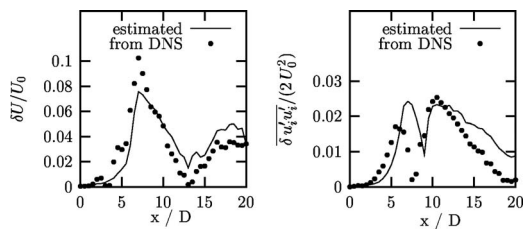


Fig. 10 Estimated uncertainty and error with respect to DNS for a plane jet. Velocity (left) and turbulent kinetic energy (right).

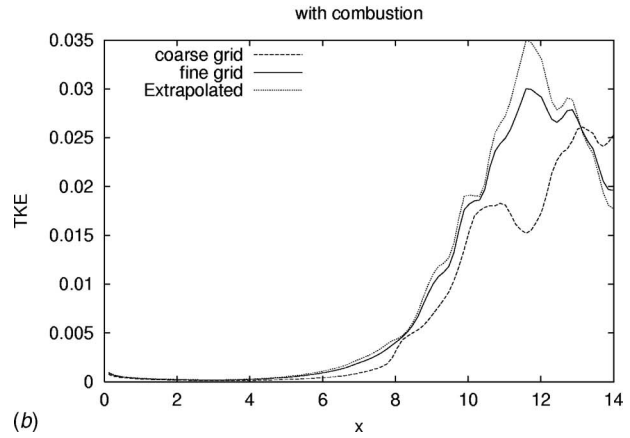
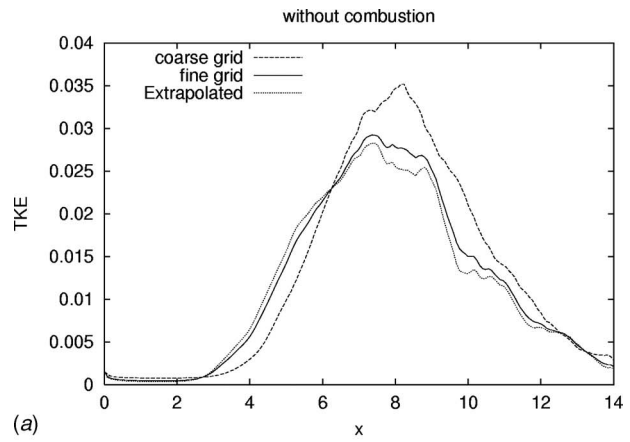


Fig. 11 Resolved tke profiles: (a) without combustion and (b) with combustion. Symbols in (a) denote the same as in (b).

where a lower Reynolds number will delay transition and cause an increase in the relative turbulence intensity; on the other hand, higher Reynolds numbers initiate earlier transition and yield lower turbulence intensities, as indicated (see Fig. 1(c)) by the DNS results of Klein et al. [13]. This means that in C-WO, as the grid is refined the effective Reynolds number should be higher for the fine grid case. This is indeed so (Fig. 12) while the relative sgs-viscosity decreases about four times from coarse grid to fine grid. On the other hand, in C-WC it increases slightly. Considering the convoluted influence of numerical dissipation, it is anticipated then that this opposite trend is possible in C-WC.

Figure 12 also shows that the sgs-viscosity relative to the laminar viscosity is in the C-WO case about five to ten times higher than the laminar viscosity, whereas in the C-WC case an opposite trend is observed; i.e., the sgs-viscosities are three to seven times lower than the local laminar viscosity. All these are indications that the case with combustion should exhibit a low Reynolds number (or pseudolaminar) flow behavior. It is also important to note that the laminar viscosity for C-WC is, depending on the reaction progress, at the order of five to ten times higher than the laminar viscosity for C-WO. The estimated turbulence Reynolds numbers for this case are in the range of 10–300 for the fine grid simulations (note that in the calculation of Re_τ , the uncertainty in length scale plays a significant role). The Smagorinsky model seems to be responding in the right way to this trend of low Reynolds number turbulent flow, while the sgs contribution to the energy dissipation is negligibly small, and hence all the dissipation is dictated by numerical viscosity, which is estimated (not shown here) to be of about the same magnitude as the local laminar viscosity, that is about five to ten times larger than the sgs-viscosity on the fine grid solution.

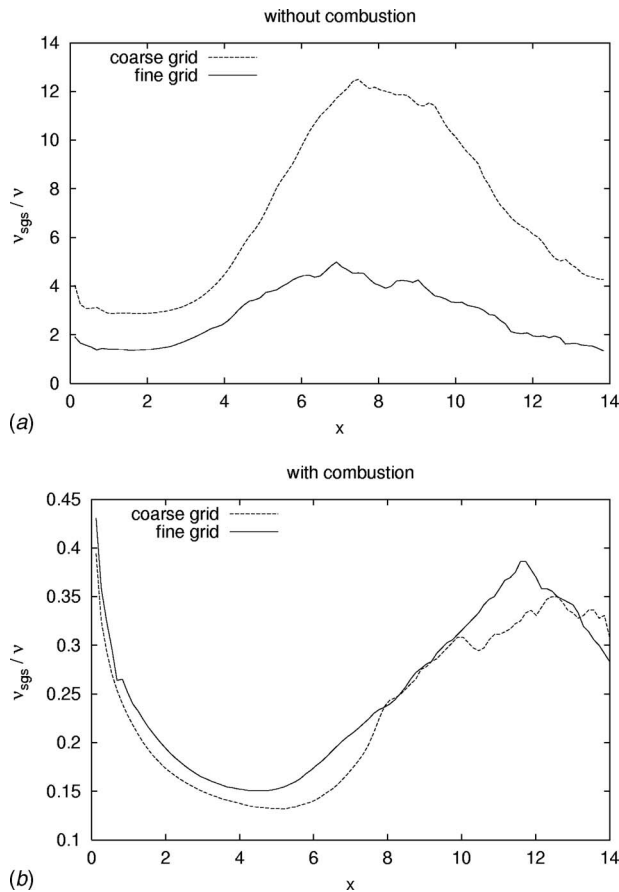


Fig. 12 Comparison of sgs-viscosity for cases (a) without and (b) with combustion

The estimated LES_IQ shown in Fig. 13 indicates that with the same grid resolution, the cold case without combustion (a high Reynolds number case) is more difficult to simulate than the case with combustion that is at relatively low Reynolds number. In the fully turbulent flow region the C-WO case indicates 50–60% resolution, where the C-WC case indicates 80–90% resolution. The index based on the effective eddy viscosity on a fine grid indicated a resolution of 60% and 85% for C-WO and C-WC cases, respectively.

These conclusions are also confirmed by the estimated Kolmogorov scales (see Fig. 14), which show that in C-WO the fine grid mesh size is about 20–40, and for C-WC it is four to eight times the local Kolmogorov scales. In the above example we considered only premixed turbulent combustion. For assessment of the resolution of nonpremixed combustion, Raman and Pitsch [21] suggested to use the subgrid scalar variance rather than subgrid tke. The criteria that they use for grid refinement can also be used for quality assessment. This needs to be studied further.

8 Conclusions and Recommendations

Although the methods proposed for the quantification of LES accuracy are still in their infancy stage, a limited number of applications presented here show encouraging results. To segregate modeling and discretization errors, it seems that a set of at least two to three grid calculations needs to be performed. This may be very expensive for applications of LES to complex industrial problems, and a tradeoff has to be made. To this end a hierarchy of methods, ranging from single grid calculations to three grid calculations, has been proposed, and several refinements compared with earlier work have been suggested. A new outcome of the present study is that the use of estimates of relevant flow

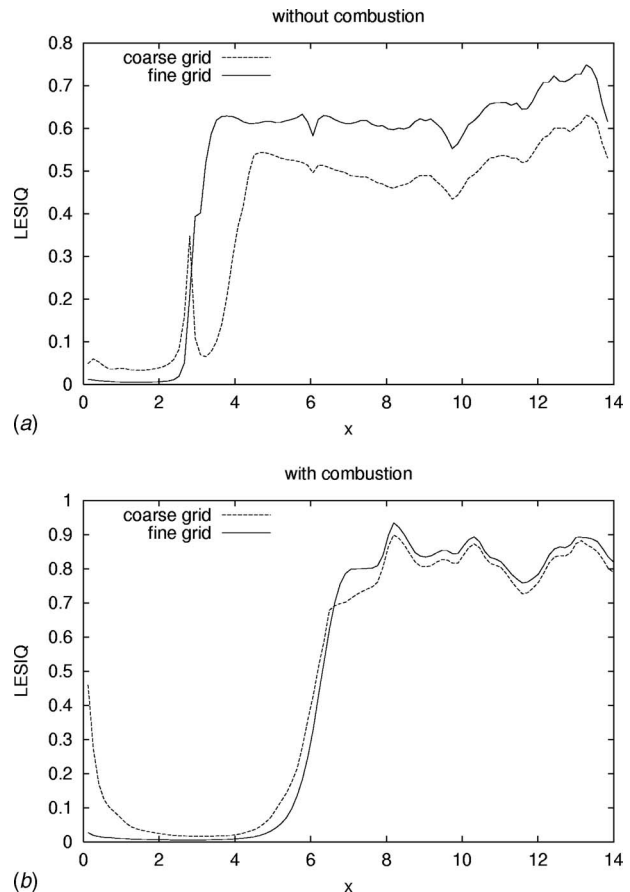


Fig. 13 Estimated LES_IQ based on turbulent kinetic energy: (a) without combustion and (b) with combustion

parameters has proven to be very useful. Even the more crude models (e.g., standard $k-\epsilon$ model) that may not be suitable for turbulent flow calculations may be useful in the estimation of uncertainties in LES.

The single grid estimators used in this work are based on either the relative grid size with respect to the Kolmogorov scale or the subgrid/numerical viscosity with respect to molecular viscosity. Hence it is expected that they are suitable for assessing the quality of LES in fully developed turbulent flow regions. However, close to viscous walls $\delta_v = \nu / u_\tau$ is the appropriate length scale rather than η , and it is anticipated that the accuracy of the single grid estimators deteriorates under such circumstances. Nevertheless they provide useful information in some regions of the computational domain, and they are easy and inexpensive to apply. The computationally more expensive multigrid studies such as the LES_IQ and the SGMV have a built-in grid sensitivity or even model sensitivity check. Hence, they are more robust, and it is expected that they yield reliable results under more general flow situations. Klein et al. [22] showed that the LESIQ as well as the SGMV are able to qualitatively predict an error landscape with an optimal refinement strategy, as defined in Meyers et al. [4], which supports the authors' point of view.

The authors hope that the error measures presented in this paper do not discourage the use of LES in engineering applications but rather encourage the LES community to either utilize more and more accurate numerical schemes to reduce the undesirable effects of numerical errors or at least to assess and control the errors using, e.g., one of the methods proposed in this work.

Finally it should be mentioned that the methods reviewed in this paper do not consider spectral aspects of the numerical errors nor that of the modeling contribution explicitly. There is a need for further study on both of these topics.

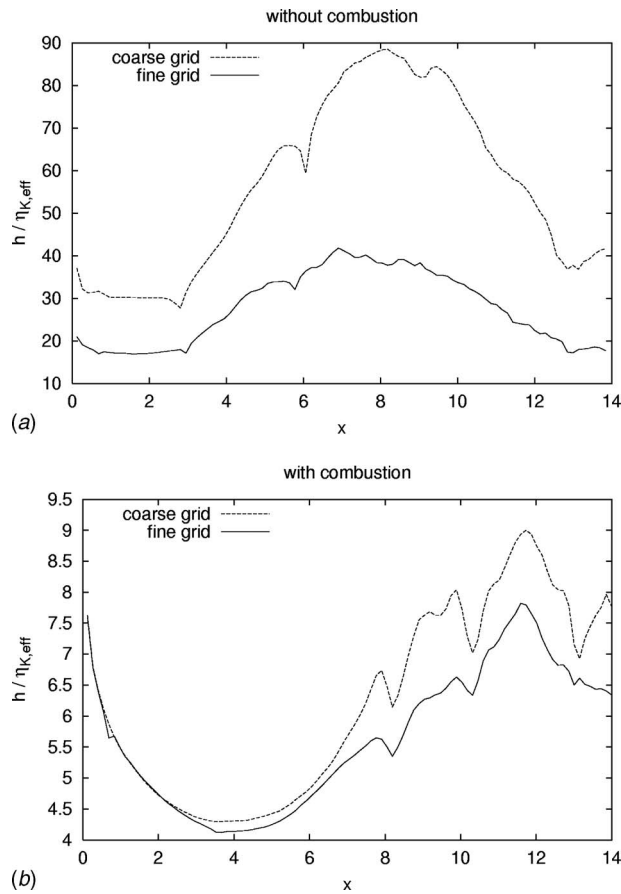


Fig. 14 Estimated Kolmogorov scales: (a) without combustion and (b) with combustion

Acknowledgment

Majority of the work presented in this paper was conducted while the lead author (I.C.) was on sabbatical leave at the Institute for Energy and Power-Plant Technology (EKT), Technical University of Darmstadt, Germany. I.C. wishes to express his gratitude to Professor Janicka and Professor Amsini Sadiki of EKT for facilitating his sabbatical leave. Many thanks are also due to Naresh K. Aluri of the University of Erlangen, Germany for his generous help in providing and interpreting his LES data on the dump combustor. Special recognition is due for discussions with J. Meyers of the University of Pierre Marie Curie, Paris, France on the for-

mulation of Eq. (28). Also many thanks to Ertan Karaismail for helping out in the preparation of the final manuscript.

Financial support by the German Research Foundation (DFG) Grant No. SFB 568 is gratefully acknowledged by the second author (M.K.).

References

- [1] Lund, T. S., 1997, "On the Use of Discrete Filters for Large Eddy Simulation," Center for Turbulence Research Annual Research Briefs.
- [2] Sagaut, P., 1998, *Large Eddy Simulation for Incompressible Flows*, Springer, New York.
- [3] Geurts, B. J., and Fröhlich, J., 2002, "A Framework for Predicting Accuracy Limitations in Large-Eddy Simulation," *Phys. Fluids*, **14**, pp. L41–L44.
- [4] Meyers, J., Geurts, B. J., and Baelmans, M., 2003, "Database Analysis of Errors in Large Eddy Simulation," *Phys. Fluids*, **15**(9), pp. 2740–2755.
- [5] Vreman, B., Geurts, B. J., and Kuerten, H., 1996, "Comparison of Numerical Schemes in Large Eddy Simulation of the Temporal Mixing Layer," *Int. J. Numer. Methods Fluids*, **22**, pp. 297–311.
- [6] Klein, M., 2005, "An Attempt to Assess the Quality of Large Eddy Simulations in the Context of Implicit Filtering," *Flow, Turbul. Combust.*, **75**, pp. 131–147.
- [7] Freitag, M., and Klein, M., 2006, "An Improved Method to Assess the Quality of LES in the Context of Implicit Filtering," *J. Turbul.*, **7**(40), pp. 1–11.
- [8] Celik, I., Klein, M., Freitag, M., and Janicka, J., 2006, "Assessment Measures for RANS/DES/LES: An Overview With Applications," *J. Turbul.*, **7**(48), pp. 1–27.
- [9] Ghosal, S., 1996, "An Analysis of Numerical Errors in Large-Eddy Simulations of Turbulence," *J. Comput. Phys.*, **125**, pp. 187–206.
- [10] Chow, F. K., and Moin, P., 2003, "A Further Study of Numerical Errors in Large Eddy Simulation," *J. Comput. Phys.*, **184**, pp. 366–380.
- [11] Vreman, B., Geurts, B., and Kuerten, H., 1997, "Large-Eddy Simulation of the Turbulent Mixing Layer," *J. Fluid Mech.*, **339**, pp. 357–390.
- [12] You, D., Mittal, R., Wang, M., and Moin, P., 2006, "Analysis of Stability and Accuracy of Finite-Difference Schemes on a Skewed Mesh," *J. Comput. Phys.*, **213**, pp. 184–204.
- [13] Klein, M., Sadiki, A., and Janicka, J., 2005, "Investigation of the Influence of the Reynolds Number on a Plane Jet Using Direct Numerical Simulation," *Int. J. Heat Fluid Flow*, **26**, pp. 722–731.
- [14] You, D., Mittal, R., Wang, M., and Moin, P., 2002, "Large Eddy-Simulation of a Rotor Tip-Clearance Flow," AIAA Paper No. 2002-0981.
- [15] Roache, P. J., 1998, *Verification and Validation in Computational Science and Engineering*, Hermosa, Albuquerque.
- [16] Celik, I., Cehreli, Z. N., and Yavuz, I., 2005, "Index of Resolution Quality for Large Eddy Simulations," *ASME J. Fluids Eng.*, **127**, pp. 949–958.
- [17] Bogey, C., and Bailly, C., 2005, "Large Eddy Simulation of Round Free Jets Using Explicit Filtering With/Without Dynamic Smagorinsky Model," *Proceedings of the Fourth International Symposium on Turbulence and Shear Flow Phenomena*, VA.
- [18] Yoshizawa, A., 1982, "A Statistically Derived Subgrid Model for the Large Eddy Simulation of Turbulence," *Phys. Fluids*, **25**(9), pp. 1532–1537.
- [19] Pope, S., 2000, *Turbulent Flows*, Cambridge University Press, Cambridge, UK.
- [20] Aluri, N. K., Muppala, S. P., Dinkelacker, F., Leipertz, A., and Celik, I. B., "LES of Premixed Turbulent High-Pressure Combustion at High Reynolds Number Flows," *Combust. Flame*, submitted.
- [21] Raman, V., and Pitsch, H., 2005, "Large-Eddy Simulation of a Bluff-Body-Stabilized Non-Premixed Flame Using a Recursive Filter-Refinement Procedure," *Combust. Flame*, **142**(4), pp. 329–347.
- [22] Klein, M., Meyers, J., and Geurts, B. J., 2007, "Assessment of LES Quality Measures Using the Error Landscape Approach," *Proceedings of the Workshop on Quality and Reliability of Large Eddy Simulation*, Leuven, Belgium.

Slip-Flow Pressure Drop in Microchannels of General Cross Section

M. Bahrami¹

Assistant Professor
e-mail: mbahrami@sfu.ca

A. Tamayol

Ph.D. Student
e-mail: ata42@sfu.ca

Mechatronic Systems Engineering,
School of Engineering Science,
Simon Fraser University,
BC, V3T 0A3, Canada

P. Taheri

Ph.D. Candidate
Department of Mechanical Engineering,
University of Victoria,
P.O. Box 3055,
Stn. CSC,
Victoria, BC, V8W 3P6, Canada

In the present study, a compact analytical model is developed to determine the pressure drop of fully-developed, incompressible, and constant properties slip-flow through arbitrary cross section microchannels. An averaged first-order Maxwell slip boundary condition is considered. Introducing a relative velocity, the difference between the bulk flow and the boundary velocities, the axial momentum reduces to Poisson's equation with homogeneous boundary condition. Square root of area is selected as the characteristic length scale. The model of Bahrami et al. (2006, "Pressure Drop of Laminar, Fully Developed Flow in Microchannels of Arbitrary Cross Section," ASME J. Fluids Eng., 128, pp. 1036–1044), which was developed for no-slip boundary condition, is extended to cover the slip-flow regime in this study. The proposed model for pressure drop is a function of geometrical parameters of the channel: cross sectional area, perimeter, polar moment of inertia, and the Knudsen number. The model is successfully validated against existing numerical and experimental data collected from different sources in literature for several shapes, including circular, rectangular, trapezoidal, and double-trapezoidal cross sections and a variety of gases such as nitrogen, argon, and helium.

[DOI: 10.1115/1.3059699]

Keywords: slip-flow, microchannels, general cross section, pressure distribution

1 Introduction

The fast-paced growth of microfluidic systems and their applications in electronics cooling, aerospace, micro electro mechanical systems (MEMS), medical, and biomedical devices has motivated many researchers to investigate microscale transport phenomena [1–3]. Microchannels are essential components of many microfluidic devices [4]. Several factors that differentiate microscale from conventional flows have been identified through a number of experimental, numerical, and analytical studies. These factors include noncontinuum regimes, surface roughness, and compressibility effects [5–7]. Due to the small size of these channels, the length scale is comparable to molecular mean free path; thus, deviation from the continuum theory should be considered. The nondimensional parameter used for analyzing this deviation is the Knudsen number defined as

$$\text{Kn} = \frac{\lambda}{\mathcal{L}} \quad (1)$$

where λ is the molecular mean free path and \mathcal{L} is an appropriate length scale of the channel. When the Knudsen number is in the range of $0.001 < \text{Kn} < 0.1$, a nonequilibrium state occurs very close to the wall, which is initiated from domination of molecular collisions with the walls over intermolecular collisions [8]. Hence, no-slip boundary condition is no longer valid on channel boundaries, where a slip-velocity exists. However, for the rest of the flow, the continuum assumption still holds. This is called *slip-flow regime*.

Pressure drop in microconduits with different cross sections including noncontinuum effects has been the subject of several

investigations. In rarefied gas flow, the friction factor reduces as the Knudsen number increases. This is demonstrated theoretically by Pfahler et al. [9], Ebert and Sparrow [10], Harley et al. [11], Morini and Spiga [12], and Beskok and Karniadakis [13]. Experimental studies conducted by Harley et al. [11], Choi et al. [14], Yu et al. [15], Arkilic et al. [16,17], Araki et al. [18], and Kim et al. [4] confirm that the continuum assumption with no-slip velocity on walls is unable to predict the flow behavior in microchannels in this range of Knudsen number.

Pfahler et al. [9] performed one of the first analytical and experimental investigations on rarefied flows. They reported the existence of slip-flow in microchannels through measuring an increase in mass flow rate when compared with the predicted values from the continuum (no-slip) theory.

Kim et al. [4] reported experimental data for rarefied flow through microtubes over the range of $0.0008 < \text{Kn} < 0.09$ and $0.03 < \text{Re} < 30$. They tested several gases such as nitrogen, helium, and argon. Araki et al. [18] reported results for pressure drop in trapezoidal and triangular channels in slip-flow regime where $0.011 < \text{Kn} < 0.035$ and $0.05 < \text{Re} < 4.2$ range. Arkilic et al. [16] included compressibility effects in their tests by conducting experiments in relatively higher Mach numbers. They also proposed an analytical model for analyzing compressible slip-flow in trapezoidal silicon microchannels; they did not report the range of Mach number in their tests. Arkilic et al. [17] conducted experiments to determine the effects of tangential momentum accommodation on the mass flow rate through trapezoidal microchannels in the slip-flow regime.

Ebert and Sparrow [9] formulated an analytical solution for slip-flow through rectangular channels. They realized that the effect of slip is to flatten the velocity distribution relative to that of a continuum flow. Assuming first-order slip boundary condition, Morini and co-workers [12,19] performed numerical studies for determination of pressure drop through microchannels of rectangular, circular, trapezoidal, and double-trapezoidal cross sections and reported their results in a tabular form for a range of cross section aspect ratio for the slip-flow regime. Using similar boundary conditions Khan and Yovanovich [20] developed a solution for

¹Corresponding author.

Contributed by the Fluids Engineering Division of ASME for publication in the JOURNAL OF FLUIDS ENGINEERING. Manuscript received April 9, 2008; final manuscript received October 2, 2008; published online February 5, 2009. Assoc. Editor: Ali Beskok. Paper presented at the Sixth International Conference on Nanochannels, Microchannels and Minichannels (ICNMM2008), Darmstadt, Germany, June 23–30, 2008.

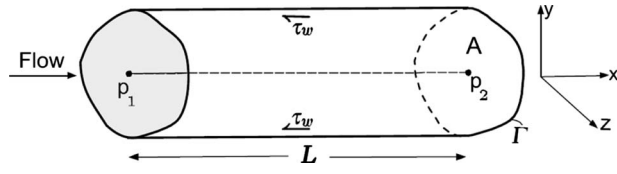


Fig. 1 Flow in arbitrary cross section microchannel

fluid flow and convective heat transfer in rectangular microchannels in slip-flow regime. Duan and Muzychka [21] proposed a model for the pressure drop of slip-flow through noncircular microchannels using the solution of the rectangular duct. They compared their model with the numerical data of Morini et al. [19] for common geometries. Their model is a function of the cross section aspect ratio defined for each geometry.

As a result of recent advances in microfabrication techniques, microchannels with different cross sectional geometries are fabricated for both commercial and scientific purposes. Bahrami et al. [22,23] developed a general model for prediction of pressure drop in microchannels of arbitrary cross section. Using the analytical solution of elliptical duct and the concept of Saint-Venant principle in torsion, they showed that the Poiseuille number, $f Re$ [24], is a function of the polar moment of inertia, area, and perimeter of the cross section of the channel. Their model showed good agreement with experimental and numerical data for a wide variety of cross sections such as rectangular, trapezoidal, triangular, circular, and moon shaped. The model of Bahrami et al., however, is restricted to no-slip velocity regime. The objective of this paper is to extend the model of Bahrami et al. [22,23] to the slip-flow regime.

In this study, a general model is developed for predicting the Poiseuille number of fully-developed flow in arbitrary cross section microchannels with slip regime. The proposed model is validated with numerical and experimental data from different sources for a variety of geometries, including circular, rectangular, trapezoidal, and double-trapezoidal cross sections and several gases such as nitrogen, argon, and helium.

2 Problem Statement

Fully-developed laminar, constant properties, and incompressible flow in microchannels of constant general cross section is considered (Fig. 1). The Mach number, $Ma = u/C$, where C is the sound velocity, can be used to determine the importance of the compressibility effects [24]. In general, the compressibility effects can be neglected for the Mach numbers lower than 0.3 [24]. Due to the small size of microchannels, the average velocity is typically higher than conventional pipes. Consequently, the pressure drop and the Mach number are high in microchannels even in low Reynolds numbers. Morini et al. [19] argued that the Mach number is proportional to multiplication of the Knudsen and the Reynolds numbers. It should be noted that in spite of the negligible compressibility effects in a wide range of Reynolds number in low Knudsen numbers, these effects can be neglected only for very low Reynolds numbers at higher Knudsen numbers [19].

Based on the Knudsen number, flow regimes can be categorized into four groups: continuum (no-slip), slip-flow, transition, and molecular flows [25]. For slip-flow regime where $0.001 < Kn < 0.1$, errors due to the use of Navier–Stokes (NS) equations are negligible. However, no-slip boundary condition is no longer valid on walls and a slip-velocity should be considered [8]. The first-order Maxwell boundary condition for slip-velocity is

$$u_s = \frac{\sigma - 2}{\sigma} \lambda \left. \frac{\partial u}{\partial n} \right|_{\text{wall}} \quad (2)$$

where the thermal creep effects on the solid-fluid interface are neglected [25]. Here, u_s is the local slip-velocity, σ is the tangential momentum accommodation factor, which is considered unity

for most of engineering applications [26], λ is the molecular mean free path, and n is the normal vector to the wall. Using above-mentioned assumptions, the momentum equation reduces to

$$\frac{dP}{dx} = \mu \left(\frac{\partial^2 u}{\partial y^2} + \frac{\partial^2 u}{\partial z^2} \right) \quad (3)$$

This equation should be solved along with the following boundary condition:

$$u_s = \frac{\sigma - 2}{\sigma} \lambda \frac{\tau_w}{\mu}, \quad \tau_w = \mu \left. \frac{\partial u}{\partial n} \right|_{\text{wall}} \quad (4)$$

where τ_w is the local wall shear stress. The set of governing equation and the boundary condition form a Poisson's equation with slip boundary condition. Because of the geometrical complexities, finding analytical solutions for the general cross section channels is highly unlikely. Therefore, we seek an approximate solution that can predict the pressure drop in arbitrary cross section with reasonable accuracy. This will provide a powerful tool that can be used in many practical instances such as basic design, parametric study, and optimization analyses, where often the trends and a reasonable estimate of the pressure drop are required.

3 Characteristic Length Scale

Selecting an appropriate and consistent characteristic length scale is an important part of developing a comprehensive general model. Selection of the characteristic length is an arbitrary choice and will not affect the final solution. However, a more appropriate length scale leads to more consistent results, especially when general cross section is considered. A circular duct is fully described with its diameter; thus the obvious length scale is the diameter (or radius). For noncircular cross sections, the selection is not as clear; many textbooks and researchers have conventionally chosen the hydraulic diameter, D_h , as the characteristic length. Yovanovich [27,28] introduced the square root of area (\sqrt{A}) as a characteristic length scale for heat conduction and convection problems. Later, Muzychka and Yovanovich [29] proposed the use of \sqrt{A} for the fully-developed flow in noncircular ducts. Bahrami et al. [22,23] showed through analysis that \sqrt{A} appears in the solution of fully-developed flow in noncircular ducts. They also compared both D_h and \sqrt{A} and observed that using \sqrt{A} as the characteristic length scale results in similar trends in Poiseuille number for microchannels with a wide variety of cross sections. Therefore, in this study, \sqrt{A} is selected consistently as the length scale throughout the analysis and in the definition of the Knudsen number. Using \sqrt{A} , Eq. (4) becomes

$$u_s = \frac{\sigma - 2}{\sigma} Kn \sqrt{A} \frac{\tau_w}{\mu} \quad (5)$$

4 Model Development

Equation (5) shows that slip-velocity is related to local wall shear stress, which depends on the topology of the boundary and the cross section. Averaging the wall shear stress over the perimeter of the channel, Eq. (5) becomes [24]

$$\bar{u}_s = \frac{\sigma - 2}{\sigma} Kn \sqrt{A} \frac{\bar{\tau}_w}{\mu} \quad (6)$$

where \bar{u}_s and $\bar{\tau}_w$ are the averaged slip-velocity and wall shear stress, respectively. Using an average (and constant) slip-velocity will simplify the solution to Eq. (3). This allows us to introduce a relative axial velocity, U , which is the difference between the bulk and the slip-velocities:

$$U = u - \bar{u}_s \quad (7)$$

After change in variable, Eq. (3) becomes

$$\frac{dP}{dx} = \mu \left(\frac{\partial^2 U}{\partial y^2} + \frac{\partial^2 U}{\partial z^2} \right) \quad (8)$$

Based on its definition, the relative velocity is zero on the channel walls. As a result, Eq. (8) becomes Poisson's equation with zero boundary condition. It is the same governing equation for fully-developed flow in the continuum regime. This equation has been solved for various geometries such as circular, rectangular, and elliptical ducts. The analytical solutions can be found in textbooks such as White [24] and Bejan [30]. A compact model for determination of Poiseuille number in general cross section channels has been presented by Bahrami et al. [22,23].

To determine the Poiseuille number, $f \text{ Re}$, Bahrami et al. [22,23] used the analytical solution of Eq. (8) for elliptical channel. They presented the final result in the following easy-to-use form:

$$f \text{ Re}_{\sqrt{A}} = 32\pi^2 I_p^* \frac{\sqrt{A}}{\Gamma}, \quad I_p^* = \frac{I_p}{A^2} \quad (9)$$

$$\text{Re}_{\sqrt{A}} = \frac{\rho \bar{u} \sqrt{A}}{\mu}, \quad f = \frac{2\bar{\tau}_w}{\rho \bar{u}^2}$$

where I_p^* is the nondimensional polar moment of inertia of the cross section and f and $\text{Re}_{\sqrt{A}}$ are the Fanning friction factor and Reynolds number based on \sqrt{A} , respectively. The elliptical channel was considered not because it is likely to occur in practice but rather to utilize the unique geometrical property of its velocity solution. The same approach is followed here. Starting from the elliptical cross section and using the axial relative velocity, one can find the average relative axial velocity \bar{U} for elliptical channels [24]:

$$\bar{U} = \frac{b^2 c^2}{4(b^2 + c^2)} \frac{\Delta P}{\mu L} \quad (10)$$

Applying a force balance in the channel leads to (see Fig. 1)

$$\bar{\tau}_w \Gamma L = \Delta P A \quad (11)$$

Cross sectional area and perimeter for elliptical channel are

$$A = \pi bc$$

$$\Gamma = 4bE(\sqrt{1 - \varepsilon^2}) \quad (12)$$

where $E(\varepsilon) = \int_0^{\pi/2} \sqrt{1 - \varepsilon^2 \sin^2 x} dx$ is the complete elliptic integral of the second kind. Using Eqs. (11) and (12) and defining an aspect ratio, ε , as the ratio of the channel major and minor axes, the average velocity can be presented as [22]

$$\bar{U} = \frac{\sqrt{\varepsilon} E(\sqrt{1 - \varepsilon^2}) \bar{\tau}_w \sqrt{A}}{\sqrt{\pi^3} (1 - \varepsilon^2) \mu} \quad (13)$$

This equation can be rewritten as

$$\bar{U} = \frac{\Gamma \bar{\tau}_w}{16\pi^2 \mu I_p^*} \quad (14)$$

Using Eqs. (14) and (7), the average channel velocity, \bar{u} , becomes

$$\bar{u} = \frac{\Gamma \bar{\tau}_w}{16\pi^2 \mu I_p^*} + \frac{\sigma - 2}{\sigma} \text{Kn} \frac{\bar{\tau}_w \sqrt{A}}{\mu} \quad (15)$$

Introducing Fanning friction factor and after some simplifications, one can write

$$f \text{ Re}_{\sqrt{A}} = \frac{2}{\frac{\Gamma}{16\pi^2 \sqrt{A} I_p^*} + \frac{\sigma - 2}{\sigma} \text{Kn}} \quad (16)$$

Note that Eq. (16) is a general equation; in the continuum limit, where $\text{Kn} \rightarrow 0$, Eq. (16) yields the model of Bahrami et al. [22],

i.e., Eq. (9). The relationship between $f \text{ Re}$ for slip-flow regime and the continuum flow is

$$f \text{ Re}_{\sqrt{A}} = \frac{1}{\frac{1}{f \text{ Re}_{\sqrt{A}}^{\text{no-slip}}} + \frac{\sigma - 2}{2\sigma} \text{Kn}} \quad (17)$$

Following Morini et al. [19], reduction in friction coefficient in slip condition, Φ , can be found as

$$\Phi = \frac{f \text{ Re}_{\sqrt{A}}}{f \text{ Re}_{\sqrt{A}}^{\text{no-slip}}} = \frac{1}{1 + \frac{\sigma - 2}{2\sigma} \alpha \text{Kn}} \quad (18)$$

where α was determined through numerical analysis for each geometry in Ref. [19]. Using the present model, Eq. (16), Φ can be found from

$$\Phi = \frac{f \text{ Re}_{\sqrt{A}}}{f \text{ Re}_{\sqrt{A}}^{\text{no-slip}}} = \frac{1}{1 + \frac{\sigma - 2}{\sigma} \frac{f \text{ Re}_{\sqrt{A}}^{\text{no-slip}}}{2} \text{Kn}} \quad (19)$$

Therefore, Φ can be determined once $f \text{ Re}_{\sqrt{A}}$ is known for the no-slip condition. Note that the value of Φ is always equal to or less than unity.

5 Model Verification

Although the presented approach is based on analytical solution for elliptical cross section, the final relationship is a function of general geometrical parameters that can be calculated for any cross sections. In this section, the present model is compared with the numerical and the experimental data available for several common cross sections. The proposed model is verified with numerical results of Morini et al. [19] for circular, rectangular, trapezoidal, and double-trapezoidal microchannels as well as experimental data published by Kim et al. [4] and Araki et al. [18] for circular and trapezoidal ducts, respectively. For convenience, the geometrical parameters needed for different cross sections are listed in Table 1. In Secs. 5.1–5.4 the value of tangential momentum accommodation factor, σ , is assumed to be 1. The available data in literature were reported based on the hydraulic diameter. The Knudsen and the Poiseuille numbers based on the hydraulic diameter can be converted to \sqrt{A} basis using the following relationships:

$$f \text{ Re}_{\sqrt{A}} = f \text{ Re}_{D_h} \frac{\Gamma}{4\sqrt{A}} \quad (20)$$

$$\text{Kn}_{\sqrt{A}} = \text{Kn}_{D_h} \frac{4\sqrt{A}}{\Gamma}$$

5.1 Circular Microchannels. Using the geometrical parameters of circular channels listed in Table 1, $f \text{ Re}_{\sqrt{A}}$ can be determined as

$$f \text{ Re}_{\sqrt{A}} = \frac{1}{\frac{1}{14.18} + \text{Kn}}, \quad \sigma = 1 \quad (21)$$

Morini et al. [19] proposed a similar correlation for $f \text{ Re}_{\sqrt{A}}$:

$$f \text{ Re}_{\sqrt{A}} = \frac{f \text{ Re}_{\sqrt{A}}^{\text{no-slip}}}{1 + 8 \text{Kn}} \quad (22)$$

In Table 2 the present model is compared with the analytical model proposed by Morini et al. [19], i.e., Eq. (22). As can be seen, the present model yields the exact same values reported in Ref. [19] over the slip-flow range of the Knudsen number.

Table 1 Geometrical characteristics of different cross sections

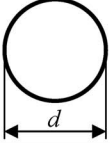

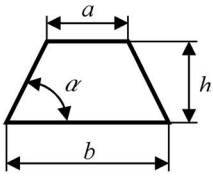
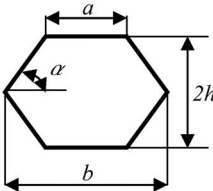
Cross-Section	Area (A)	Perimeter (Γ)	Non-Dimensional Polar Moment of Inertia (I_p^*)	Aspect Ratio (ε)
	$\frac{\pi d^2}{4}$	πd	$\frac{1}{2\pi}$	1
	$4ab$	$4(a+b)$	$\frac{1+\varepsilon^2}{12\varepsilon}$	$\frac{a}{b}$
	εh^2	$2h\left(\varepsilon + \sqrt{\varepsilon^2 - \beta\varepsilon^2 + 1}\right)$	$\frac{(6\varepsilon^2 + 2) + \beta(1 - 3\varepsilon^2)}{36\varepsilon}$	$\frac{a+b}{2h}$
	$2\varepsilon h^2$	$2h\left[\left(2\sqrt{\varepsilon^2 - \beta\varepsilon^2 + 1}\right) + \varepsilon + \frac{1}{\tan\alpha}\right]$	$\frac{(6\varepsilon^2 + 2) + \beta(1 - 3\varepsilon^2)}{18\varepsilon} - \frac{8}{9\varepsilon}\left(3 - \frac{1}{\varepsilon \tan\alpha}\right)^2$	$\frac{a+b}{2h}$

Figure 2 shows the comparison between the present model and experimental data published by Kim et al. [4]. They conducted tests with nitrogen, argon, and helium over a range of $0.0008 < Kn < 0.09$ and $0.03 < Re < 30$. The microtubes used in their experiments were made of quartz glass and had diameters ranging from $5 \mu\text{m}$ to $100 \mu\text{m}$. According to Morini et al. [31] the experimental uncertainty of pressure drop measurements is on the order of 8–14%.

As can be seen, the present model captures the trends of the experimental data over a range of geometrical and thermophysical parameters. Also note that most of the data fall within the $\pm 10\%$ bounds of the model.

5.2 Rectangular Microchannels. The geometrical characteristics and schematic of rectangular channels are presented in Table 1. Substituting required parameters in Eq. (16), $f Re_{\sqrt{A}}$ is determined as

Table 2 Comparison between present model and analytical model of Morini et al. [19]

Kn	$f Re_{\sqrt{A}}$ (model)	$f Re_{\sqrt{A}}$ [19]	Φ
0	14.180	14.180	1.000
0.001	14.080	14.080	0.993
0.005	13.695	13.695	0.966
0.01	13.241	13.241	0.934
0.03	11.693	11.693	0.825
0.06	9.948	9.948	0.702
0.09	8.656	8.656	0.610
0.1	8.297	8.297	0.585

$$f Re_{\sqrt{A}}^{\text{slip}} = \frac{1}{\frac{1}{\frac{4\pi^2(1+\varepsilon^2)}{3\sqrt{\varepsilon}(1+\varepsilon)}} - Kn}, \quad \sigma = 1 \quad (23)$$

Table 3 and Fig. 3 show the comparison of the proposed model, Eq. (16), with numerical results of Morini et al. [19] for a range of

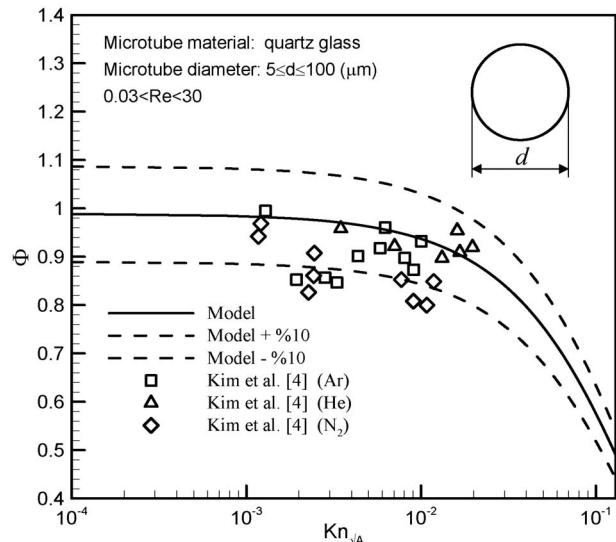


Fig. 2 Comparison of the model with experimental data of Kim et al. [4] for circular channels

Table 3 Comparison between model and numerical data [19]; rectangular cross section

$\varepsilon=0.01$				$\varepsilon=0.1$				$\varepsilon=0.3$			
Kn	$f Re_{\sqrt{A}}$ [19]	$f Re_{\sqrt{A}}$ (model)	Error (%)	Kn	$f Re_{\sqrt{A}}$ [19]	$f Re_{\sqrt{A}}$ (model)	Error (%)	Kn	$f Re_{\sqrt{A}}$ [19]	$f Re_{\sqrt{A}}$ (model)	Error (%)
0.0000	119.6	130.3	8.2	0.0000	36.8	38.2	3.6	0.0000	20.8	20.1	3.2
0.0002	118.2	128.6	8.2	0.0006	36.4	37.8	3.6	0.0008	20.6	20.0	3.1
0.0010	112.8	122.4	7.8	0.0029	34.9	36.2	3.7	0.0042	19.8	19.3	2.7
0.0015	109.8	118.8	7.6	0.0043	34.0	35.3	3.7	0.0063	19.4	18.9	2.4
0.0020	106.8	115.4	7.4	0.0057	33.2	34.4	3.7	0.0084	19.0	18.6	2.2
0.0050	92.1	98.5	6.5	0.0144	28.9	30.0	3.7	0.0211	16.8	16.6	1.0
0.0099	74.9	79.2	5.4	0.0287	23.7	24.7	3.7	0.0421	14.1	14.1	0.4
0.0149	63.1	66.2	4.7	0.0431	20.2	20.9	3.7	0.0632	12.1	12.3	1.5
0.0198	54.5	56.9	4.1	0.0575	17.5	18.2	3.8	0.0843	10.7	10.9	2.2

$\varepsilon=0.6$				$\varepsilon=0.8$				$\varepsilon=1$			
Kn	$f Re_{\sqrt{A}}$ [19]	$f Re_{\sqrt{A}}$ (model)	Error (%)	Kn	$f Re_{\sqrt{A}}$ [19]	$f Re_{\sqrt{A}}$ (model)	Error (%)	Kn	$f Re_{\sqrt{A}}$ [19]	$f Re_{\sqrt{A}}$ (model)	Error (%)
0.0000	15.5	14.4	7.1	0.0000	14.5	13.4	7.9	0.0000	14.2	13.2	8.1
0.0010	15.3	14.3	7.0	0.0010	14.4	13.3	7.8	0.0010	14.1	13.1	8.0
0.0048	14.9	14.0	6.5	0.0050	13.9	13.0	7.3	0.0050	13.7	12.7	7.4
0.0073	14.6	13.7	6.2	0.0075	13.7	12.8	7.0	0.0075	13.4	12.5	7.1
0.0097	14.3	13.5	5.9	0.0099	13.4	12.6	6.7	0.0100	13.2	12.3	6.8
0.0242	12.8	12.3	4.3	0.0248	12.1	11.5	5.1	0.0250	11.9	11.3	5.2
0.0484	10.9	10.7	2.3	0.0497	10.4	10.1	3.1	0.0500	10.2	9.9	3.1
0.0726	9.6	9.5	0.8	0.0745	9.1	8.9	1.6	0.0750	8.9	8.8	1.5
0.0968	8.5	8.5	0.3	0.0994	8.1	8.0	0.4	0.1000	8.0	7.9	0.3

$$\text{Error} = \frac{f Re_{\sqrt{A}} [19] - f Re_{\sqrt{A}} [\text{model}]}{f Re_{\sqrt{A}} [\text{model}]} \times 100$$

aspect ratio, $0.01 \leq \varepsilon \leq 1$. As can be seen, except for a few points, the agreement between the model and the numerical values is less than 8%.

5.3 Trapezoidal Microchannels. The cross section of an isosceles trapezoidal microchannel and its geometrical parameters are presented in Table 1. This is an important shape since this cross section is formed as a result of etching process in silicon wafers [19]. Furthermore, in the limit when the top side length, a , goes to zero, it yields an isosceles triangle and in another limit

when $a=b$, a rectangular channel will be formed. The geometrical characteristics of these limiting cases are listed in Table 4, where β in Tables 1 and 4 is a nondimensional parameter defined as

$$\beta = \frac{4ab}{(a+b)^2} \quad (24)$$

β is zero for triangular and 1 for rectangular conduits. The angle α (as shown in Table 1) is related to β and ε as [22]

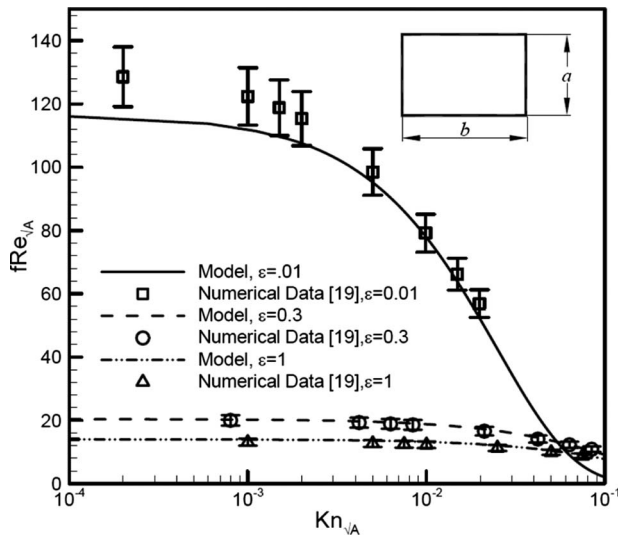


Fig. 3 Comparison of the model with numerical results of Morini et al. [19] for rectangular channels

Table 4 Limiting cases of isosceles trapezoid

Cross section	ε	β	f_p^*	\sqrt{A}/Γ
Isosceles triangular	$\frac{b}{2h}$	0	$\frac{3\varepsilon^2 + 1}{18\varepsilon}$	$\frac{\sqrt{\varepsilon}}{2(\sqrt{\varepsilon^2 + 1} + \varepsilon)}$
Equilateral triangular	$\frac{1}{\sqrt{3}}$	0	$\frac{\sqrt{3}}{9}$	$\frac{\sqrt{3}}{6\sqrt{3}}$
Rectangular	$\frac{b}{h}$	1	$\frac{\varepsilon^2 + 1}{12\varepsilon}$	$\frac{\sqrt{3}}{2(1 + \varepsilon)}$
Square	1	1	$\frac{1}{6}$	$\frac{1}{4}$

Table 5 Model versus data [19]; trapezoidal channels

$\varepsilon=20.07$				$\varepsilon=5.07$				$\varepsilon=2.7$			
Kn	$f Re_{\sqrt{A}}$ [19]	$f Re_{\sqrt{A}}$ (model)	Error (%)	Kn	$f Re_{\sqrt{A}}$ [19]	$f Re_{\sqrt{A}}$ (model)	Error (%)	Kn	$f Re_{\sqrt{A}}$ [19]	$f Re_{\sqrt{A}}$ (model)	Error (%)
0.0000	53.4	56.6	5.6	0.0000	27.1	27.1	0.0	0.0000	18.6	17.9	3.8
0.0004	52.8	56.0	5.6	0.0007	26.8	26.8	0.1	0.0008	18.4	17.8	3.7
0.0021	50.5	53.5	5.5	0.0034	25.7	25.9	0.4	0.0042	17.8	17.3	3.2
0.0031	49.2	52.0	5.4	0.0052	25.1	25.3	0.6	0.0063	17.4	17.0	2.9
0.0041	48.0	50.7	5.4	0.0069	24.6	24.8	0.8	0.0084	17.1	16.7	2.6
0.0104	41.6	43.8	5.0	0.0172	21.6	21.9	1.7	0.0209	15.2	15.1	1.0
0.0207	34.0	35.7	4.7	0.0345	17.9	18.5	2.9	0.0418	12.9	13.0	0.9
0.0311	28.8	30.1	4.4	0.0517	15.3	15.9	3.7	0.0628	11.2	11.5	2.3
0.0415	24.9	26.0	4.2	0.0689	13.4	14.0	4.3	0.0837	9.9	10.2	3.4

$\varepsilon=1.5$				$\varepsilon=0.9$				$\varepsilon=0.8$			
Kn	$f Re_{\sqrt{A}}$ [19]	$f Re_{\sqrt{A}}$ (model)	Error (%)	Kn	$f Re_{\sqrt{A}}$ [19]	$f Re_{\sqrt{A}}$ (model)	Error (%)	Kn	$f Re_{\sqrt{A}}$ [19]	$f Re_{\sqrt{A}}$ (model)	Error (%)
0.0000	15.4	14.5	6.1	0.0000	15.3	13.7	11.5	0.0000	15.4	13.7	12.7
0.0009	15.3	14.4	5.9	0.0009	15.2	13.7	11.3	0.0009	15.3	13.6	12.5
0.0045	14.8	14.0	5.4	0.0045	14.7	13.3	10.6	0.0044	14.8	13.3	11.7
0.0067	14.5	13.8	5.0	0.0067	14.5	13.1	10.1	0.0066	14.5	13.1	11.2
0.0090	14.3	13.6	4.7	0.0089	14.2	12.9	9.7	0.0088	14.3	12.9	10.7
0.0225	12.8	12.5	3.0	0.0223	12.8	11.9	7.4	0.0221	12.8	11.9	8.2
0.0449	11.0	10.9	0.8	0.0447	11.0	10.5	4.5	0.0442	11.0	10.5	4.9
0.0674	9.7	9.7	0.9	0.0670	9.6	9.4	2.2	0.0663	9.6	9.4	2.5
0.0899	8.6	8.8	2.2	0.0894	8.6	8.5	0.5	0.0884	8.6	8.5	0.6

$$\text{Error} = \frac{f Re_{\sqrt{A}} [19] - f Re_{\sqrt{A}} [\text{model}]}{f Re_{\sqrt{A}} [\text{model}]} \times 100$$

$$\sin \alpha = \frac{1}{\sqrt{\varepsilon^2 - \beta \varepsilon^2 + 1}} \quad (25)$$

Bahrami et al. [22] presented the Poiseuille number for the no-slip condition as

$$f Re_{\sqrt{A}}^{\text{no-slip}} = \frac{4\pi^2[(3\varepsilon^2 + 1) + \beta(-3\varepsilon^2 + 1)]\varepsilon\sqrt{\varepsilon}}{9(\varepsilon + \sqrt{\varepsilon^2 - \beta \varepsilon^2 + 1})} \quad (26)$$

Using Eqs. (16) and (26) one can calculate $f Re_{\sqrt{A}}$. In Table 5 the predicted results of the proposed model are compared with the numerical data of Morini et al. [19] with $\alpha=54.74$ deg. The agreement between the present model and the numerical data is within 8%; however, there are a few points, especially at relatively high or low aspect ratios, where differences up to 12% are observed.

Figure 4 shows the comparison between the proposed model and the experimental data of Araki et al. [18] for trapezoidal microchannels with $\alpha=54.74$ deg. They used two different channels with dimensions $b=41.5 \mu\text{m}$ and $41.2 \mu\text{m}$ and $h=5.56 \mu\text{m}$ and $2.09 \mu\text{m}$, respectively. These channels were made of silicon wafer with hydraulic diameters of $9.41 \mu\text{m}$ and $3.92 \mu\text{m}$. They conducted tests with nitrogen and helium over a range of $0.011 < Kn < 0.035$ and $0.05 < Re < 4.2$. The uncertainty of their measurements was reported to be 10.9%. As shown in Fig. 4, the values predicted by the model are within 10% accuracy of the data.

5.4 Double-Trapezoidal Microchannels. Double-trapezoidal cross section geometry is depicted in Table 1. Same as the trapezoidal cross section, the nondimensional parameter β is defined by Eq. (24).

Table 6 and Fig. 5 present the comparison between the proposed model with numerical data of Morini et al. [19] for α

$=54.74$ deg. As can be seen, except for a few points, the agreement between the model and the numerical values is less than 8%.

6 Summary and Conclusions

Pressure drop of the fully-developed, incompressible slip-flow through microchannels of general cross sections is investigated. An averaged first-order Maxwell boundary condition is assumed

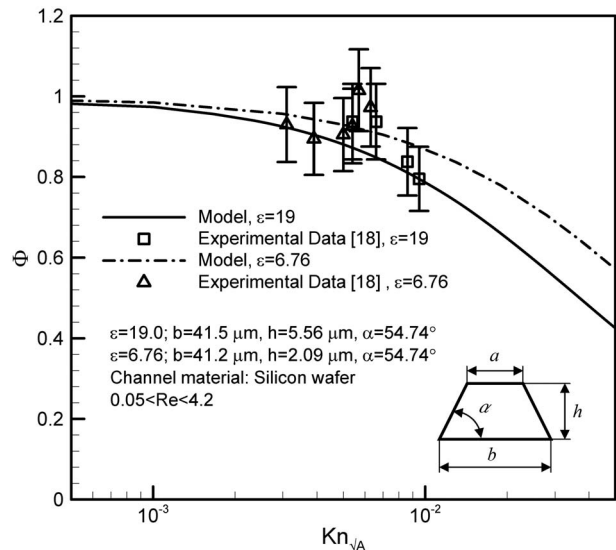


Fig. 4 Comparison of the model with experimental data of Araki et al. [18] for trapezoidal channels ($\alpha=54.74$ deg)

Table 6 Model versus data [19]; double-trapezoidal channels

$\varepsilon=0.83$				$\varepsilon=0.96$				$\varepsilon=1.29$			
Kn	$f Re_{\sqrt{A}}$ [19]	$f Re_{\sqrt{A}}$ (model)	Error (%)	Kn	$f Re_{\sqrt{A}}$ [19]	$f Re_{\sqrt{A}}$ (model)	Error (%)	Kn	$f Re_{\sqrt{A}}$ [19]	$f Re_{\sqrt{A}}$ (model)	Error (%)
0.0000	14.8	13.8	6.6	0.0000	14.7	13.9	6.0	0.0000	14.3	13.7	4.2
0.0010	14.6	13.7	6.5	0.0010	14.6	13.8	5.9	0.0011	14.1	13.6	4.1
0.0050	14.2	13.4	6.1	0.0051	14.1	13.4	5.5	0.0053	13.7	13.2	3.8
0.0075	13.9	13.2	5.8	0.0077	13.9	13.2	5.3	0.0079	13.5	13.0	3.7
0.0100	13.7	12.9	5.5	0.0103	13.6	13.0	5.1	0.0106	13.2	12.8	3.5
0.0251	12.3	11.8	4.2	0.0256	12.3	11.8	4.0	0.0265	11.9	11.6	2.8
0.0501	10.5	10.3	2.5	0.0513	10.5	10.2	2.6	0.0530	10.2	10.0	1.8
0.0752	9.2	9.1	1.2	0.0769	9.2	9.0	1.5	0.0795	9.0	8.9	1.0
0.1002	8.2	8.2	0.2	0.1025	8.2	8.1	0.7	0.1060	8.0	7.9	0.4

$\varepsilon=1.515$				$\varepsilon=1.79$				$\varepsilon=2.63$			
Kn	$f Re_{\sqrt{A}}$ [19]	$f Re_{\sqrt{A}}$ (model)	Error (%)	Kn	$f Re_{\sqrt{A}}$ [19]	$f Re_{\sqrt{A}}$ (model)	Error (%)	Kn	$f Re_{\sqrt{A}}$ [19]	$f Re_{\sqrt{A}}$ (model)	Error (%)
0.0000	14.1	13.6	3.5	0.0000	14.0	13.6	3.0	0.0000	14.7	14.3	2.9
0.0011	14.0	13.5	3.4	0.0011	13.9	13.5	3.0	0.0010	14.6	14.2	2.8
0.0053	13.5	13.1	3.2	0.0054	13.5	13.1	2.8	0.0052	14.1	13.8	2.6
0.0080	13.3	12.9	3.0	0.0080	13.2	12.9	2.6	0.0079	13.8	13.5	2.5
0.0107	13.1	12.7	2.9	0.0107	13.0	12.7	2.5	0.0105	13.6	13.3	2.4
0.0267	11.8	11.5	2.2	0.0268	11.7	11.5	1.9	0.0262	12.2	12.0	1.7
0.0534	10.1	10.0	1.3	0.0536	10.1	10.0	1.0	0.0525	10.5	10.4	0.9
0.0802	8.9	8.8	0.7	0.0803	8.8	8.8	0.4	0.0787	9.2	9.1	0.3
0.1069	7.9	7.9	0.2	0.1071	7.9	7.9	0.1	0.1049	8.1	8.2	0.2

$$\text{Error} = \frac{f Re_{\sqrt{A}} [19] - f Re_{\sqrt{A}} [\text{model}]}{f Re_{\sqrt{A}} [\text{model}]} \times 100$$

on the channel walls. Introducing a relative velocity, axial momentum equation reduces to Poisson's equation with no-slip boundary condition. Following Bahrami et al. [22,23] and using analytical solution for elliptical microchannels, a compact model is developed that predicts the Poiseuille number as a function of geometrical parameters of the duct. The presented model is more general than the model of Bahrami et al. and covers both slip-flow and no-slip regimes.

The model is successfully validated against existing numerical and experimental data in literature for a variety of shapes including circular, rectangular, trapezoidal, and double-trapezoidal cross sections, with a relative difference on the order of 8%.

Employing the proposed model, one only needs to compute the nondimensional parameter $I_p^* \sqrt{A} / \Gamma$ of the channel to determine the Poiseuille number. On the other hand, using the conventional method, Poisson's equation must be solved with slip boundary condition to find the velocity field and the mean velocity often numerically. Then the averaged wall shear stress should be calculated to find $f Re_{\sqrt{A}}$. This clearly shows the convenience of the proposed approximate model.

Acknowledgment

The authors gratefully acknowledge the financial support of the Natural Sciences and Engineering Research Council of Canada (NSERC).

Nomenclature

- A = cross sectional area, m^2
- C = sound velocity, m/s
- D_h = hydraulic diameter, m
- $E(\cdot)$ = complete elliptic integral of the second kind
- $f Re$ = Poiseuille number
- I_p = polar moment of inertia, m^4
- I_p^* = dimensionless polar moment of inertia, I_p / A^2
- Kn = Knudsen number
- \mathcal{L} = characteristic length, m
- Ma = Mach number, $Ma = u / C$
- P = pressure, N/m^2
- Re = Reynolds number
- \sqrt{A} = square root of area, m

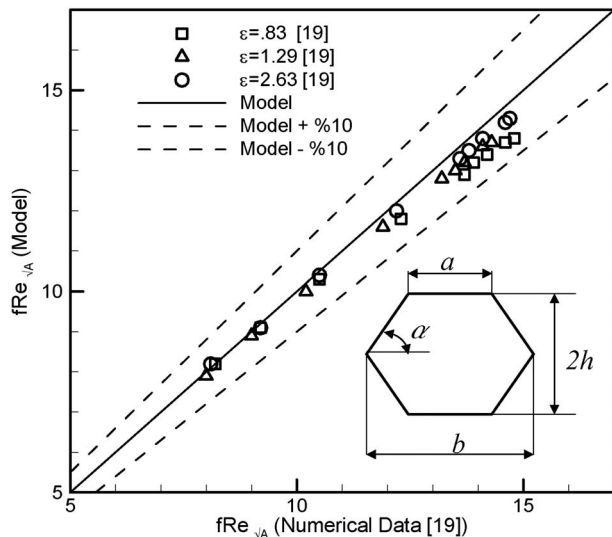


Fig. 5 Comparison of the model with numerical data of Morini et al. [19] for double-trapezoidal conduits

u = axial velocity, m/s
 u_s = local slip-velocity, m/s
 \bar{u}_s = average slip-velocity, m/s
 U = relative velocity, m/s

Greek Symbols

Γ = perimeter, m
 ε = aspect ratio
 λ = molecular mean free path, m
 μ = viscosity, N s/m²
 σ = tangential momentum accommodation factor
 $\bar{\tau}_w$ = averaged wall shear stress, N/m²
 τ_w = local shear stress, N/m²
 Φ = reduction in friction coefficient in slip condition, $f \text{ Re}_{\sqrt{A}}/f \text{ Re}_{\sqrt{A}}^{\text{no-slip}}$

References

- [1] Tuckerman, D. B., and Pease, R. F., 1981, "High-Performance Heat Sinking for VLSI," *IEEE Electron Device Lett.*, **2**, pp. 126–129.
- [2] Hsieh, S. S., Tsai, H. H., Lin, C. Y., Huang, C. F., and Chien, C. M., 2004, "Gas Flow in a Long Microchannel," *Int. J. Heat Mass Transfer*, **47**, pp. 3877–3887.
- [3] Zhu, X., Liao, Q., and Xin, M. D., 2006, "Gas Flow in Microchannel of Arbitrary Shape in Slip Flow Regime," *Microscale Thermophys. Eng.*, **10**(1), pp. 41–54.
- [4] Kim, M. S., Araki, T., Inaoka, K., and Suzuki, K., 2000, "Gas Flow Characteristics in Microtubes," *JSME Int. J., Ser. B*, **43**(4), pp. 634–639.
- [5] Bahrami, M., Yovanovich, M. M., and Culham, J. R., 2006, "Pressure Drop of Fully-Developed, Laminar Flow in Rough Microtubes," *ASME J. Fluids Eng.*, **128**, pp. 632–637.
- [6] Morini, G. L., 2004, "Laminar-to-Turbulent Flow Transition in Microchannels," *Microscale Thermophys. Eng.*, **8**, pp. 15–30.
- [7] Wu, H. Y., and Cheng, P., 2003, "Friction Factors in Smooth Trapezoidal Silicon Microchannels With Different Aspect Ratios," *Int. J. Heat Mass Transfer*, **46**, pp. 2519–2525.
- [8] Renksizbulut, M., Niazmand, H., and Tercan, G., 2006, "Slip Flow and Heat Transfer in Rectangular Microchannels With Constant Wall Temperature," *Int. J. Therm. Sci.*, **45**, pp. 870–881.
- [9] Pfahler, J., Harley, J., Bau, H., and Zemel, J. N., 1991, "Gas and Liquid Transport in Small Channels," *Micromechanical Sensors, and Actuators Systems*, ASME DSC 32, Winter Annual Meeting, Atlanta, GA, pp. 49–58.
- [10] Ebert, W. A., and Sparrow, E. M., 1965, "Slip Flow in Rectangular and Annular Ducts," *ASME J. Basic Eng.*, **87**, pp. 1018–1024.
- [11] Harley, J., Huang, Y., Bau, H., and Zemel, J. N., 1995, "Gas Flow in Microchannels," *J. Fluid Mech.*, **284**, pp. 257–274.
- [12] Morini, G. L., and Spiga, M., 1998, "Slip Flow in Rectangular Microtubes," *Microscale Thermophys. Eng.*, **2**(4), pp. 273–282.
- [13] Beskok, A., and Karniadakis, G. E., 1999, "A Model for Flows in Channels, Pipes, and Ducts at Micro and Nano Scales," *Microscale Thermophys. Eng.*, **3**, pp. 43–77.
- [14] Choi, S. B., Barron, R. F., and Warrington, R. O., 1991, "Fluid Flow and Heat Transfer in Microtubes," *Micromechanical Sensors, Actuators, and Systems*, ASME DSC 32, Winter Annual Meeting, Atlanta, GA, pp. 123–134.
- [15] Yu, D., Warrington, R., Barron, R., and Ameer, T., 1995, "An Experimental and Theoretical Investigation of Fluid Flow and Heat Transfer in Microtubes," *ASME/JSME Thermal Engineering Conference*, Vol. 1, pp. 523–530.
- [16] Arkilic, E. B., Schmidt, M. A., and Breuer, K. S., 1997, "Gaseous Slip Flow in Long Microchannels," *J. Microelectromech. Syst.*, **6**(2), pp. 167–178.
- [17] Arkilic, E. B., Breuer, K. S., and Schmidt, M. A., 2001, "Mass Flow and Tangential Momentum Accommodation in Silicon Micromachined Channels," *J. Fluid Mech.*, **437**, pp. 29–43.
- [18] Araki, T., Kim, M. S., Hiroshi, I., and Suzuki, K., 2000, "An Experimental Investigation of Gaseous Flow Characteristics in Microchannels," *Proceedings of International Conference on Heat Transfer and Transport Phenomena in Microscale*, Begell House, New York, pp. 155–161.
- [19] Morini, G. L., Spiga, M., and Tartarini, P., 2004, "The Rarefaction Effect on the Friction Factor of Gas Flow in Micro/Nano-Channels," *Superlattices Microstruct.*, **35**(3–6), pp. 587–599.
- [20] Khan, W. A., and Yovanovich, M. M., 2007, "Analytical Modeling of Fluid Flow and Heat Transfer in Micro/Nano-Channel Heat Sinks," *Proceedings of the IPACK2007*, Vancouver, BC, Canada.
- [21] Duan, Z., and Muzychka, Y. S., 2007, "Slip Flow in Non-Circular Microchannels," *Microfluid. Nanofluid.*, **3**, pp. 473–484.
- [22] Bahrami, M., Yovanovich, M. M., and Culham, J. R., 2006, "Pressure Drop of Laminar, Fully Developed Flow in Microchannels of Arbitrary Cross Section," *ASME J. Fluids Eng.*, **128**, pp. 1036–1044.
- [23] Bahrami, M., Yovanovich, M. M., and Culham, J. R., 2007, "A Novel Solution for Pressure Drop in Singly Connected Microchannels of Arbitrary Cross Section," *Int. J. Heat Mass Transfer*, **50**, pp. 2492–2502.
- [24] White, F. M., 1984, *Viscous Fluid Flow*, McGraw-Hill, New York.
- [25] Roy, S., Raju, R., Chuang, H. F., Cruden, B. A., and Meyyappan, M., 2003, "Modeling Gas Flow Through Microchannels and Nanopores," *J. Appl. Phys.*, **93**(8), pp. 4870–4879.
- [26] Karniadakis, G. E., and Beskok, A., 2002, *Micro Flows: Fundamentals and Simulation*, Springer, New York.
- [27] Yovanovich, M. M., 1974, "A General Expression for Predicting Conduction Shape Factors," *AIAA, Thermophysics and Space Craft Control*, Cambridge, Mass. London: MIT Press, 35, pp. 265–291.
- [28] Yovanovich, M. M., 1987, "New Nusselt and Sherwood Numbers for Arbitrary Isopotential Bodies at Near Zero Peclet and Rayleigh Numbers," *AIAA 22nd Thermophysics Conference*, Honolulu, HI.
- [29] Muzychka, Y. S., and Yovanovich, M. M., 2002, Laminar Flow Friction and Heat Transfer in Non-Circular Ducts and Channels Part, 1: *Hydrodynamic Problem*, *Compact Heat Exchangers: A Festschrift on the 60th Birthday of Ramesh K. Shah*, Grenoble, France, pp. 123–130.
- [30] Bejan, A., 1995, *Convection Heat Transfer*, Wiley, Englewood Cliffs, NJ.
- [31] Morini, G. L., Lorenzini, M., and Spiga, M., 2005, "A Criterion for Experimental Validation of Slip-Flow Models for Incompressible Rarefied Gases Through Microchannels," *Microfluid. Nanofluid.*, **1**, pp. 190–196.

Long-Wave Instabilities in a Non-Newtonian Film on a Nonuniformly Heated Inclined Plane

I. Mohammed Rizwan
Sadiq

e-mail: rizwan@smail.iitm.ac.in

R. Usha¹

e-mail: ushar@iitm.ac.in

Department of Mathematics,
Indian Institute of Technology Madras,
Chennai 600 036, India

A thin liquid layer of a non-Newtonian film falling down an inclined plane that is subjected to nonuniform heating has been considered. The temperature of the inclined plane is assumed to be linearly distributed and the case when the temperature gradient is positive or negative is investigated. The film flow is influenced by gravity, mean surface tension, and thermocapillary forces acting along the free surface. The coupling of thermocapillary instability and surface-wave instabilities is studied for two-dimensional disturbances. A nonlinear evolution equation is derived by applying the long-wave theory, and the equation governs the evolution of a power-law film flowing down a nonuniformly heated inclined plane. The linear stability analysis shows that the film flow system is stable when the plate temperature decreases in the downstream direction while it is less stable for increasing temperature along the plate. Weakly nonlinear stability analysis using the method of multiple scales has been investigated and this leads to a secular equation of the Ginzburg–Landau type. The analysis shows that both supercritical stability and subcritical instability are possible for the film flow system. The results indicate the existence of finite-amplitude waves, and the threshold amplitude and nonlinear speed of these waves are influenced by thermocapillarity. The nonlinear evolution equation for the film thickness is solved numerically in a periodic domain in the supercritical stable region, and the results show that the shape of the wave is influenced by the choice of wave number, non-Newtonian rheology, and nonuniform heating.

[DOI: 10.1115/1.3059702]

1 Introduction

An important class of problems in fluid mechanics involves viscous flows in the presence of free surfaces in fluid interfaces. The fluid motion and heat transport in thin free surface liquid films are of fundamental interest in basic industrial equipment such as steam condensers, wetted wall columns, liquid film evaporators, and other processes involving interfacial heat and mass transfer. In particular, the wavy free surface can enhance interfacial transfer. Thin film flows down inclined planes or vertical walls are of special interest and they belong to a class of convectively unstable open-flow system. They demonstrate a wide spectrum of wave dynamics transition. Interfacial waves propagating along the plane show fascinating nonlinear phenomena that include the development of waves at the surface of the fluid into large-amplitude strongly nonlinear localized structures such as solitary pulses, transverse secondary instabilities, and the development of spatiotemporal chaos. A vast body of literature exists on the thin-film instability and has been reviewed in Refs. [1,2]. The investigations based on linear stability analysis [3] show that the basic flat-film solution on an inclined plane is unstable to long-wavelength disturbances if the Reynolds number is greater than the critical value given by $Re_c = \frac{2}{3} \cot \beta$, where β is the angle of inclination with the horizontal. The investigations on the evolution of waves subsequent to wave inception have been made by developing approximate nonlinear stability theories. As the cut-off wave number is small for very thin layers, small wave number approximation and lubrication theory can be used to examine the

nonlinear extension of the stability analysis [4]. The investigations on weakly nonlinear stability analysis of the long-wave evolution equation up to various orders of accuracy performed in Refs. [5–7] show that the solution of the Benney-type equations predict supercritical or subcritical instabilities of the waves.

The flow and stability of thin, free surface, nonisothermal films are of importance in coating and heat transfer applications and they have been the source of both experimental and theoretical investigations for a number of years. In addition to surface wave instabilities, falling films on heated planes are susceptible to instabilities driven by shear stresses arising from the temperature dependence of the surface tension (Marangoni effect). A detailed review of interfacial thermocapillary phenomena is given by Nepomnyashchy et al. [8]. The effect of surface tension variation on the evolution of the free surface has been examined in several investigations [9–17]. When a temperature gradient is applied across a horizontal fluid layer, the layer being heated from below, two mechanisms related to the Marangoni (thermocapillary) effect can lead the liquid layer from a quiescent conducting state to convective motions [18]. Both of them originate from the interfacial stress generated at the interface by the surface tension gradient. This gradient can have two origins, either a modification of the temperature distribution in the bulk due to the advection by the velocity field, or a modulation of the free surface elevation, both of them generating a temperature gradient at the interface. The two mechanisms have been classified by Goussis and Kelly [16] as the *P*-mode and *S*-mode, respectively.

When the plate is tilted, the liquid drains downward due to gravity. Smith [19] concluded that gravity becomes important only at small wave numbers and for thin layers of very viscous fluids. If the layer thickness and the inclination angle are large enough to overcome hydrostatic stabilization, *H*-mode of instability is present and gives rise to the formation of surface waves

¹Corresponding author.

Contributed by the Fluids Engineering Division of ASME for publication in the JOURNAL OF FLUIDS ENGINEERING. Manuscript received May 9, 2007; final manuscript received April 23, 2008; published online February 5, 2009. Assoc. Editor: Malcolm J. Andrews.

propagating downstream. Again, for sufficiently thin layers, the instability occurs for long waves, because short waves are suppressed by capillary forces. For instability to occur owing to *H*-mode, a mean flow is necessary.

Falling film flows on a heated incline coupling the aforementioned instabilities have been studied often. An important observed phenomenon is flow instability in the form of gravity-driven surface waves whose wavelength is much larger than the mean film thickness. The waves enhance the heat transfer, but they also lead to the film breakdown and to the appearance of dry spots, thus decreasing the overall heat transfer rate. One way to prevent the film rupture is to impose a nonuniform heating along the inclined plane. Also, thermocapillary convection in a liquid film falling down a uniformly or locally heated substrate [8,13,14,20–24] have revealed the occurrence of novel instabilities. Recent experimental studies [21–27] have focused on thin films falling down inhomogeneously heated plates and the results show that nonuniform heating of falling liquid films may provide a promising solution to heat transfer enhancement, since it induces steady-state deformations of the liquid-gas interface that are beneficial to the heat transfer processes.

Frank and Kabov [28] investigated experimentally and numerically the three-dimensional regular structure formation in a locally heated falling film. A detailed review of the state of the art of nonuniformly heated films has been presented by Frank and Kabov [28]. It is worth mentioning here that the two-dimensional model of a steady laminar flow of a liquid film in a channel in the presence of a cocurrent gas flow examined by Gatapova et al. [29] showed the formation of a thermocapillary bump in the region where a thermal boundary layer emerges on the film surface.

Motivated by the need to understand the influence of nonuniform heating of a thin liquid film and to examine whether they help in improving the heat transfer from the film or hinder it by propelling the film to rupture, a number of studies on the dynamics and stability of nonuniformly heated Newtonian liquid films down an inclined film have been reported [30–34]. Liquid layers on a horizontal substrate with linear and spatially periodic temperature distributions have been studied by Tan et al. [31], Burelbach et al. [32], and VanHook et al. [33]. Scheid et al. [34] focused on the dynamics of a thin liquid film falling down a vertical plate with nonuniform sinusoidal temperature distribution.

Recently, long-wave instabilities in thin falling films on an inclined plate with linear distributions of the plate temperature have been studied in a series of papers [35–40]. Miladinova et al. [37] considered the effect of a constant temperature gradient imposed at the plate for an adiabatic liquid-gas interface and high Marangoni number. They examined the influence of thermocapillarity on the amplitudes and phase speeds of surface waves. Their linear stability analysis of transverse surface waves shows that a weak increase in heating downstream produces a decrease in the stability threshold, while a decrease in the temperature plays a stabilizing role. The numerical solution of the evolution equation shows the existence of permanent finite-amplitude waves, the shape of which depends mainly on the mean flow and mean surface tension, but their amplitudes and phase speeds are influenced by thermocapillarity.

Marangoni instability of a thin liquid film heated from below by a local heat source using the integral boundary layer approximation of the Navier–Stokes/energy equations and free surface boundary conditions was considered by Kalliadasis et al. [39]. Two-dimensional steady-state solutions show that the free surface profile develops a ridge upstream of the heater's center, where the wall temperature gradient is positive and a depression downstream of the heater's center where the wall temperature gradient is negative.

The linear stability of a liquid layer falling down an inclined wall heated by a downstream linearly increasing temperature distribution has been investigated by Demekhin et al. [40]. A detailed analysis of the Orr–Sommerfeld and linearized energy equations

via appropriate asymptotic and numerical methods has been performed. It is shown that hydrodynamic and Marangoni instabilities yield two types of transverse instabilities: long surface waves and convective rolls, and longitudinal convective rolls much like in the case of a uniformly heated wall.

The above investigations of coupled heat and fluid flow have been almost exclusively confined to Newtonian models. However, in many contexts in the industry, engineering and geology, the central problem surrounds how a heated non-Newtonian fluid flows under gravity. Applications include wire and fiber coating, polymer processing, food stuff processing, design of various heat exchangers, and chemical processing equipment. As the flow and heat transfer characteristics in such applications are affected not only by velocity and thermal conditions but also by the physical properties of the fluid film, the study of non-Newtonian film flow over a heated substrate gains importance.

The most important features of non-Newtonian fluids for heat transfer applications are the shear-rate dependence of the viscosity and the viscoelastic nature of these fluids. There have been a number of investigations examining the flow and stability of a viscoelastic fluid film on a vertical/inclined plane, which include the studies in Refs. [41–44]. In an earlier study, Sadiq and Usha [41] analyzed the linear instability in a thin viscoelastic liquid film on an inclined, nonuniformly heated wall. The results show that nonisothermal viscoelastic film on a cooled inclined substrate is more stable than the isothermal film and is less stable than the corresponding Newtonian film.

In order to characterize shear-rate dependence of viscosity, in the present study the constitutive equations for the power-law fluids are considered. The power-law viscosity model often fits rheological data well over certain stress ranges and has the benefit of analytical simplicity. This model has been used quite successfully in describing the rheological behavior of polymer solutions and gels. The primary goal of the present investigation is to assess the influence of shear-thinning or shear-thickening as delineated by the variable viscosity on both the flow and the heat transfer characteristics as compared with the Newtonian model. Since shear-thinning or shear-thickening is the most readily measurable non-Newtonian property, it is of practical interest to examine the flow properties that are associated with it and this in turn will help in an improved understanding of the physics involved in the hydrodynamically and thermally developed flow in heat exchangers, in electronic cooling, and in other applications, and also will assist in the design and manufacture of these products. This requires targeted local measurements and development of theoretical models for nonuniform heating of non-Newtonian liquid films down inclined or vertical substrates. The investigations on the flow and stability of a power-law fluid film on an inclined plane are restricted to either an isothermal film or a film that is uniformly heated from below [45–55].

In view of this, the dynamics and stability of a non-Newtonian liquid film (power-law model) on a nonuniformly heated or cooled inclined plane have been examined in this investigation. Such an investigation would help in understanding the influence of non-Newtonian rheology on the stability of inelastic films. The study is devoted to the problem of long-wave deformations, so that Marangoni effect would mean the thermocapillary long-wave instability or *S*-mode while *P*-mode is not considered.

In this paper, the long-wave instabilities of a power-law liquid film on an inclined plane with temperature field that increases or decreases linearly in the downstream direction has been examined. The constant temperature gradient imposed along the plane affects the basic flat-film state as well as the surface-wave instabilities induced by gravity. The finite-amplitude long-wave instabilities of two-dimensional power-law films have been considered. The method of multiple scales has been employed to solve the nonlinear generalized kinematic equation order by order. This leads to a secular equation of Ginzburg–Landau type from which expressions for threshold amplitude and nonlinear wave speed are

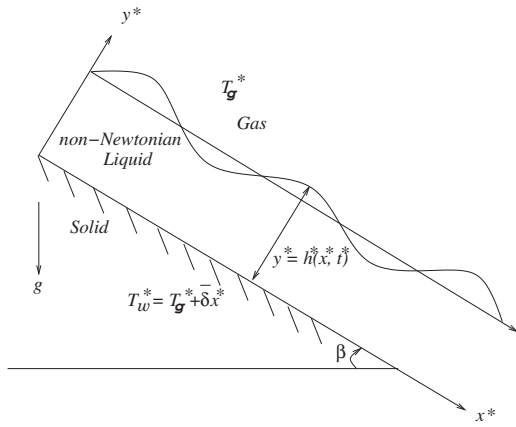


Fig. 1 Schematic representation of a thin power-law film flowing down a nonuniformly heated inclined plane

obtained. The analysis shows that supercritical stability and subcritical instability are both possible for the film flow system and that the power-law index n strongly influences the stability characteristics of the non-Newtonian inelastic fluids. A numerical method for solving the nonlinear evolution equation for the film thickness is discussed and numerical results describing the nonlinear effects are presented.

2 Mathematical Formulation

A thin power-law liquid film flowing down a plane inclined at an angle β with the horizontal has been considered (Fig. 1). A constant temperature gradient $\bar{\delta}$ has been imposed along the plane and $\bar{\delta}$ can take both positive or negative values. The film is bounded above by a motionless gas at ambient temperature T_g^* and pressure p_g^* . The free surface is assumed adiabatic. The origin is located on the plane surface where the temperature is T_g^* and a coordinate system is chosen with x^* as the streamwise coordinate along the plane and y^* as normal to the plane. The wall temperature is given by $T_w^* = T_g^* + \bar{\delta}x^*$, and it increases (decreases) in the streamwise direction with positive (negative) $\bar{\delta}$. The surface-tension σ^* depends linearly on temperature and is given by $\sigma^* = \sigma_0^* - \gamma(T^* - T_g^*)$, where σ_0^* is the mean surface tension at temperature T_g^* and $\gamma = -d\sigma^*/dT^*$ is a positive constant for most common liquids.

The governing equations are the two-dimensional continuity, momentum, and energy equations for the power-law fluid [7,45] given by

$$u_{x^*}^* + v_{y^*}^* = 0 \quad (1)$$

$$\rho(u_{t^*}^* + u^* u_{x^*}^* + v^* u_{y^*}^*) = -p_{x^*}^* + \rho g \sin \beta + (\tau_{xx}^*)_{x^*} + (\tau_{xy}^*)_{y^*} \quad (2)$$

$$\rho(v_{t^*}^* + u^* v_{x^*}^* + v^* v_{y^*}^*) = -p_{y^*}^* - \rho g \cos \beta + (\tau_{xy}^*)_{x^*} + (\tau_{yy}^*)_{y^*} \quad (3)$$

$$T_{t^*}^* + u^* T_{x^*}^* + v^* T_{y^*}^* = \chi(T_{xx}^* + T_{yy}^*) \quad (4)$$

where $\chi = \lambda/\rho c_p$ is the thermal diffusivity, c_p is the heat capacity, ρ is the density, and λ is the heat conductivity of the liquid. Here, u^* and v^* are the components of velocity in the x^* and y^* increasing directions (Fig. 1), p^* is the pressure, t^* is the time, g is the gravitational acceleration, T^* is the temperature of the film, and

$$\tau_{x^*x^*}^* = 2\mu_n^* \eta^* u_{x^*}^*, \quad \tau_{y^*y^*}^* = \tau_{x^*y^*}^* = \mu_n^* \eta^* (u_{y^*}^* + v_{x^*}^*)$$

$$\tau_{y^*y^*}^* = 2\mu_n^* \eta^* v_{y^*}^*, \quad \eta^* = [2(u_{x^*}^{*2} + v_{y^*}^{*2}) + (u_{y^*}^* + v_{x^*}^*)^2]^{(n-1)/2} \quad (5)$$

μ_n^* and n are constants for the particular liquid; μ_n^* is a measure of consistency of the liquid, the higher the μ_n^* , the more "viscous" is the liquid; and n is a measure of the degree of non-Newtonian behavior, the greater is the departure from unity, the more pronounced are the non-Newtonian properties of the liquid. When $n = 1$, the model corresponds to a Newtonian fluid. For $n < 1$, the model describes shear-thinning behavior and the fluid is called pseudoplastic. When $n > 1$, the fluid is called dilatant and exhibits shear-thickening behavior. The boundary conditions are the no-slip velocity and nonuniform heating along $y^* = 0$ and the balance of normal, tangential stresses and kinematic boundary condition at the interface $y^* = h^*(x^*, t^*)$. There is no transfer of heat from the liquid to the ambient gas across the interface.

Using the following scales for nondimensionalization:

$$x = \frac{x^*}{l}, \quad y = \frac{y^*}{h_0^*}, \quad h = \frac{h^*}{h_0^*}, \quad t = \frac{t^* \bar{u}_0}{l}, \quad p = \frac{p^* - p_g^*}{\rho \bar{u}_0^2}$$

$$T = \frac{T^* - T_g^*}{\bar{\delta} l}, \quad u = \frac{u^*}{\bar{u}_0}, \quad v = \frac{v^* l}{\bar{u}_0 h_0^*} \quad (6)$$

$$\bar{u}_0 = \left(\frac{\mu_n^*}{\rho h_0^{*n}} \right)^{1/(2-n)}, \quad (\tau_{xx}, \tau_{yy}) = \frac{(\tau_{x^*x^*}^*, \tau_{y^*y^*}^*)}{\mu_n^* \left(\frac{\bar{u}_0}{h_0^*} \right)^{n-1} \left(\frac{\bar{u}_0}{l} \right)}$$

$$\tau_{xy} = \frac{\tau_{x^*y^*}^*}{\mu_n^* \left(\frac{\bar{u}_0}{h_0^*} \right)^n}$$

the dimensionless form of the governing equations and boundary conditions are obtained as

$$u_x + v_y = 0 \quad (7)$$

$$\varepsilon(u_t + uu_x + vv_y) = -\varepsilon p_x + \text{Re}_n + \varepsilon^2(\tau_{xx})_x + (\tau_{xy})_y \quad (8)$$

$$\varepsilon^2(v_t + uv_x + vv_y) = -p_y - \text{Re}_n \cot \beta + \varepsilon(\tau_{xy})_x + \varepsilon(\tau_{yy})_y \quad (9)$$

$$\varepsilon \text{Pr}_n(T_t + uT_x + vT_y) = \varepsilon^2 T_{xx} + T_{yy} \quad (10)$$

$$u = 0, \quad v = 0, \quad T = x \quad (y = 0) \quad (11)$$

$$-p(1 + \varepsilon^2 h_x^2) + 2\varepsilon^3 h_x^2 \hat{\eta} u_x - 2\varepsilon h_x \hat{\eta} (u_y + \varepsilon^2 v_x) + 2\varepsilon \hat{\eta} v_y = \frac{Sh_{xx}(1 - \text{Ca}T)}{\sqrt{1 + \varepsilon^2 h_x^2}} \quad (y = h) \quad (12)$$

$$2\varepsilon^2 h_x \hat{\eta} (v_y - u_x) + (1 - \varepsilon^2 h_x^2) \hat{\eta} (u_y + \varepsilon^2 v_x) = -M_n(T_x + h_x T_y) \sqrt{1 + \varepsilon^2 h_x^2} \quad (y = h) \quad (13)$$

$$T_y - \varepsilon^2 h_x T_x = 0 \quad (y = h) \quad (14)$$

$$v = h_t + uh_x \quad (y = h) \quad (15)$$

where h_0^* is the mean film thickness, l is a length proportional to the disturbance wavelength, $\bar{\delta} l$ measures the temperature difference along the plate between two points separated by a wavelength, \bar{u}_0 is the characteristic velocity, $\varepsilon = h_0^*/l \ll 1$ is a small parameter, u and v are the nondimensional velocity components, p is the nondimensional pressure of the film, $h(x, t)$ denotes the nondimensional film thickness, and $\hat{\eta} = [2\varepsilon^2(u_x^2 + v_y^2) + (u_y + v_x)^2]^{(n-1)/2}$.

The dimensionless parameters that govern the film flow system are $\text{Re}_n = G \sin \beta$ (Reynolds number), $G = (\rho^2 l_0^{*n+2} / \mu_n^{*2})^{1/(2-n)} g$, $\text{Pr}_n = 1/\chi(\mu_n^* / \rho h_0^{*2n-2})^{1/(2-n)}$ (Prandtl number), $\text{Ca} = \gamma \bar{\delta} l / \sigma_0^*$ (capil-

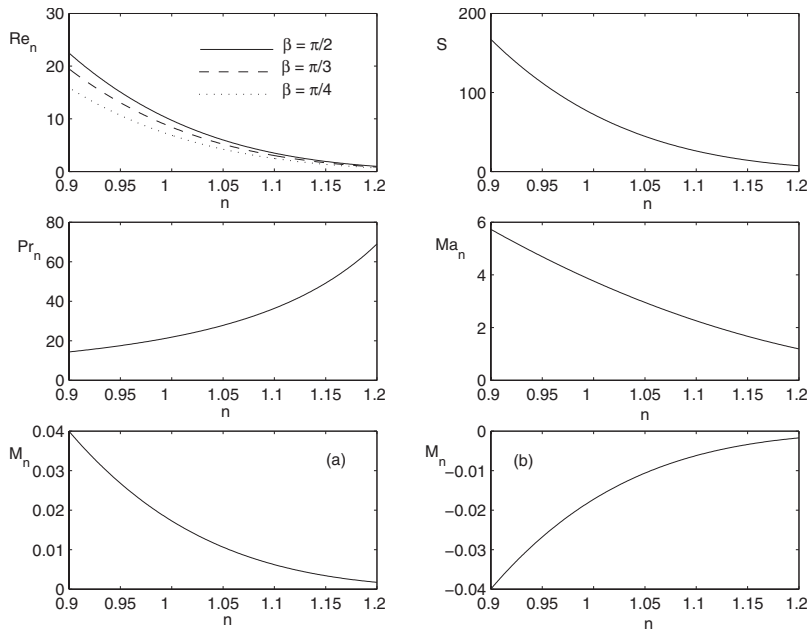


Fig. 2 Parameter plot as a function of power-law exponent n : (a) The temperature of the plate increases linearly in the downstream direction; (b) the temperature of the plate decreases linearly in the downstream direction

lary number), $S = \varepsilon^2 (\sigma_0^* / (\mu_n^{*2} / \rho^n h_0^{*3n-2})^{1/(2-n)})$ (surface tension parameter), $Ma_n = \gamma \bar{\delta} l / \chi (\rho^{n-1} h_0^{*n} / \mu_n^*)^{1/(2-n)}$ (Marangoni number), and $M_n = \varepsilon (Ma_n / Pr_n)$ (modified Marangoni number). It is to be noted that when $n=1$, Eqs. (7)–(15) reduce to the equations and boundary conditions describing the long-wave instabilities of non-uniformly heated Newtonian falling film analyzed by Miladinova et al. [37]. In practical applications, $S \approx O(1)$ and the analysis is performed by taking $Re_n \approx O(1)$, $Ca \approx O(\varepsilon^2)$, $Pr_n \approx O(1)$, and $M_n = \varepsilon (Ma_n / Pr_n) \approx O(1)$, and the estimates of the order of magnitudes of the dimensionless parameters are based on the values of the dimensional quantities $\rho = 998 \text{ kg/m}^3$, $\mu_n^* = 1.002 \times 10^{-3} \text{ mPa s}$, $h_0^* = 10^{-4} \text{ m}$, $\sigma_0^* = 0.0727 \text{ N/m}$, $\chi = 1.169 \times 10^{-7} \text{ m}^2/\text{s}$, $c_p = 4258.290735 \text{ W s/kg K}$, $\gamma = 0.1103 \times 10^{-3} \text{ N/mK}$, and $|\bar{\delta}| = 1 \text{ K/cm}$ [56,57]. With these values simi-

lar for all fluids, the differences in the results are solely due to the viscosity model. The parameters Re_n , Pr_n , S , Ma_n , and M_n are functions of the flow index n and are plotted in Fig. 2.

It is assumed that the velocity and temperature in the liquid film vary slowly along the plane, and the length of the surface waves is much larger than the mean film thickness. Since the long-wavelength modes are the most unstable ones for the film flow, the physical quantities u , v , p , and T are expanded in powers of the small parameter ε . Substituting these in Eqs. (7)–(15) and collecting the coefficients of like powers of ε , the zeroth and the first order equations are obtained and the solutions are determined. The evolution equation for film thickness is then obtained from Eq. (15) as

$$h_t + A(h)h_x + \varepsilon(B(h)h_x + C(h)h_{xxx})_x + O(\varepsilon^2) = 0$$

$$A(h) = (Re_n h - M_n)^{1/n} h$$

$$B(h) = \frac{\cot \beta}{n Re_n^2} \left[\frac{2n^3 ((-M_n)^{(2n+1)/n} - (Re_n h - M_n)^{(2n+1)/n})}{(n+1)(2n+1)} + \frac{2 Re_n n^2 h (Re_n h - M_n)^{(n+1)/n}}{(n+1)} - n Re_n^2 h^2 (Re_n h - M_n)^{1/n} \right] + \frac{M_n Pr_n}{2n Re_n^4} \left[\frac{2n^2 ((-M_n)^{(2n+1)/n} - (Re_n h - M_n)^{(2n+1)/n})}{(n+1)(2n+1)} + \frac{2 Re_n n h (Re_n h - M_n)^{(n+1)/n}}{(n+1)} + Re_n^2 h^2 (Re_n h - M_n)^{1/n} \right] \times \left[\frac{n^2 ((-M_n)^{(n+1)/n} - (Re_n h - M_n)^{(n+1)/n})}{(n+1)} + n Re_n h (Re_n h - M_n)^{1/n} \right] + \frac{n (Re_n h - M_n)^{2/n}}{Re_n^4 (n+1)} \left[-Re_n h + \frac{n}{n+1} (Re_n h - M_n) \right] \times \left[-\frac{2n (Re_n h - M_n)^{(2n+1)/n}}{2n+1} + Re_n h (Re_n h - M_n)^{(n+1)/n} - \frac{(-M_n)^{(2n+1)/n}}{(2n+1)} + (Re_n h - M_n) (-M_n)^{(n+1)/n} \right] + \frac{n^2 M_n (Re_n h - M_n)^{1/n}}{Re_n^4 (n+1)(2n+2)} \left[(Re_n h - M_n)^{(2n+2)/n} - \frac{(2n+2) Re_n h (Re_n h - M_n)^{(n+2)/n}}{n} - (-M_n)^{(2n+2)/n} \right] + \frac{n^2 (Re_n h - M_n)^{1/n}}{Re_n^4 (n+1)(2n+1)(2n+2)(3n+2)} \left[(Re_n h - M_n)^{(3n+2)/n} - \frac{(3n+2) Re_n h (Re_n h - M_n)^{(2n+2)/n}}{n} - (-M_n)^{(3n+2)/n} \right]$$

$$\begin{aligned}
& + \frac{n(\text{Re}_n h - M_n)^{1/n}}{\text{Re}_n^4(n+1)} \left[-\frac{2n^2(-M_n)^{(2n+1)/n}}{(n+1)(2n+1)} + \text{Re}_n^2 h^2 (\text{Re}_n h - M_n)^{1/n} - \frac{n \text{Re}_n h}{(n+1)} (\text{Re}_n h - M_n)^{(n+1)/n} \right] \left[(-M_n)^{(n+1)/n} \right. \\
& \left. + \frac{(n+1) \text{Re}_n h (\text{Re}_n h - M_n)^{1/n}}{n} - (\text{Re}_n h - M_n)^{(n+1)/n} \right] \\
C(h) = & \frac{S}{n \text{Re}_n^3} \left[\frac{2n^3(-M_n)^{(2n+1)/n} + (\text{Re}_n h - M_n)^{(2n+1)/n}}{(n+1)(2n+1)} + n \text{Re}_n^2 h^2 (\text{Re}_n h - M_n)^{1/n} - \frac{2 \text{Re}_n n^2 h (\text{Re}_n h - M_n)^{(n+1)/n}}{(n+1)} \right] \quad (16)
\end{aligned}$$

Equation (16) describes the evolution of a non-Newtonian falling film on a nonuniformly heated inclined plane and, when $n=1$, it reduces to that obtained by Miladinova et al. [37].

3 Stability Analysis

The base state is represented by

$$\begin{aligned}
u_0 &= \frac{n}{\text{Re}_n(n+1)} [(\text{Re}_n h - M_n)^{(n+1)/n} - [\text{Re}(h-y) - M_n]^{(n+1)/n}] \\
v_0 &= \frac{nh_x}{\text{Re}_n(n+1)} [(\text{Re}_n h - M_n)^{(n+1)/n} - [\text{Re}(h-y) - M_n]^{(n+1)/n}] \\
& - (\text{Re} h - M_n)^{1/n} y h_x \\
p_0 &= \text{Re}_n \cot \beta (h-y) - Sh_{xx}, \quad T_0 = x \quad (17)
\end{aligned}$$

with $h=1$. In order to use the normal mode analysis, it is assumed that

$$h(x,t) = 1 + H(x,t), \quad H(x,t) = \Gamma e^{i(kx-ct)+st} + \bar{\Gamma} e^{-i(kx-ct)+st} \quad (18)$$

where $H(x,t)$ is the unsteady part of the film thickness representing the disturbance component and Γ , k , c , and s are real and represent the amplitude, the wave number, the phase speed, and the growth rate of the disturbance, respectively. Inserting the normal mode representation, Eq. (18) into Eq. (16), and retaining terms up to the order of H^3 , the unsteady equation, which is locally valid, is obtained.

It describes the behavior of finite-amplitude disturbances on the film and it is used to predict the timewise behavior of an initially sinusoidal disturbance on the nonuniformly heated power-law fluid film.

4 Linear Stability Analysis

Inserting the normal mode representation (18) into the linearized part of the unsteady equation, the complex wave celerity is obtained and is given by

$$c + is = kA_1 + i\epsilon k^2(B_1 - k^2 C_1) \quad (19)$$

where c is the linear wave speed, s is the linear growth rate, and $A_1=A(1)$, $B_1=B(1)$, and $C_1=C(1)$. It is observed from Eqs. (16) and (19) that both the linear wave speed and the growth rate are influenced by thermocapillarity and non-Newtonian rheology. It is to be noted that for a uniformly heated Newtonian fluid layer, the thermocapillary force has no influence on the linearized phase speed [14]. For a nonuniformly heated Newtonian fluid, the results of the present study agree with Miladinova et al. [37]. The flow is linearly unstable for $s > 0$ and is in a linear stable condition for $s < 0$. For $s=0$, the flow is neutrally stable and the amplitude of the disturbance is neither amplified nor damped. The surface waves will grow for disturbance wave numbers smaller than the critical (cut-off) wave number given by $k_c=(B_1/C_1)^{1/2}$. This surface-wave instability is called primary instability and corresponds to a Hopf bifurcation from the flat-film solution. The emerging branch of solutions is called supercritical (subcritical) if

it bifurcates toward the region where $k < k_c$ ($k > k_c$).

The conditions obtained for linear stability of the nonuniformly heated power-law fluid film on an inclined plane have been numerically evaluated. The influence of the gravity and thermocapillarity on the film instability has been shown in Fig. 3, displaying the critical Reynolds number Re_c versus M_n for $S=0$ for different values of power-law index n . For each n , there is a value of Re_c below which the film flow system is stable, and as M_n increases, Re_c value decreases. The Marangoni number for which the critical Reynolds number is the smallest depends on n , which in turn depends on Pr_n . Further, Re_c is larger for a dilatant fluid in comparison to a pseudoplastic fluid when the temperature of the plane decreases linearly in the downstream direction. But Re_c is less for a dilatant fluid than for a pseudoplastic fluid when the temperature of the plane increases linearly in the downstream direction. In other words, the influence of Pr_n on two-dimensional stability threshold is related to the sign of the temperature gradient. As Pr_n increases with n , the above results imply that when M_n is negative, Re_c increases with Pr_n , while for positive values of M_n , it decreases with increasing Pr_n (except for small angles of inclination).

When the capillary force at the free surface is taken into consideration ($S \neq 0$), there exists a cut-off wave number k_c , for which the linear growth rate vanishes. The growth rate has a maximum for $k_m=k_c/\sqrt{2}$. The linear stability analysis yields the neutral stability curve, which separates the k_c-n plane into two regions. Figure 4 shows the neutral stability curves when the temperature of the plane increases or decreases in the downstream direction for different angles of inclination. In the region below each curve in Fig. 4, the film flow system is unstable. It is observed that, for each angle of inclination, the linearly unstable region is larger when the temperature of the plane increases than when the temperature of the plane decreases linearly downstream. In both the cases, the band of unstable wave numbers increases with the increase in angle of inclination for a power-law fluid film. Further, it is observed that, for each angle of inclination, a pseudoplastic fluid film is more unstable than a Newtonian/dilatant film, when the temperature of the plane either increases or decreases. However, when the temperature increases, it has a more destabilizing effect than when the temperature decreases. This behavior of the power-law film is to be expected since the effect of friction is to retard the flow and thus act as a stabilizing factor. A pseudoplastic fluid film has a tendency to decrease the laminar friction in the flow, which is caused by the viscous forces. As a result, a pseudoplastic fluid film becomes more unstable than a dilatant film. Further, increasing the shear-thinning aspect of the flow increases the destabilizing effect of a pseudoplastic film. On the other hand, increasing the shear-thickening aspect of the flow enhances the laminar friction in the dilatant film, with the result that the more the value of n for $n > 1$, the greater is the stabilizing effect. For small angle of inclination ($\beta=15$ deg), there is a critical value of n beyond which the power-law film is stable, when the temperature of the plate increases, while a temperature decrease stabilizes the film.

The linear stability analysis shows that a pseudoplastic fluid

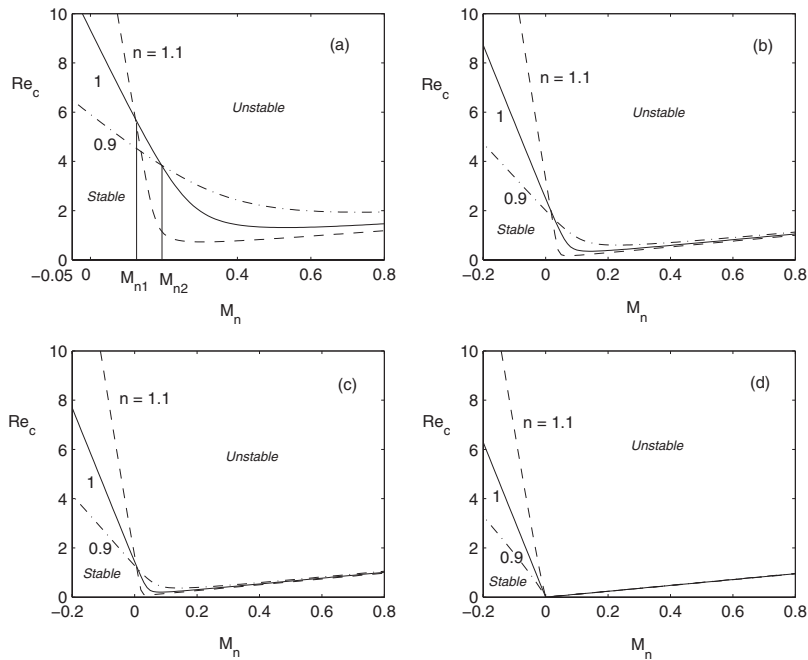


Fig. 3 Critical Reynolds number as a function of M_n for different values of n : (a) $\beta=15$ deg ($M_{n1}\approx 0.13, M_{n2}\approx 0.19$), (b) $\beta=45$ deg, (c) $\beta=60$ deg, and (d) $\beta=90$ deg

film is more unstable than a dilatant/Newtonian film when the temperature of the plane either increases or decreases. Further, the destabilizing effect is more when the temperature of the plane increases than when it decreases. This shows that a power-law fluid film down an inclined plane whose temperature decreases linearly downstream is more stable than a power-law film on an inclined plane, which is uniformly heated.

5 Weakly Nonlinear Stability Analysis

As the perturbed wave grows to a finite-amplitude, linear theory cannot be used to predict the flow behavior accurately. Therefore, in order to examine whether the finite-amplitude disturbances in the linearly stable region causes instability (subcritical instability) and to investigate whether the subsequent nonlinear evolution of

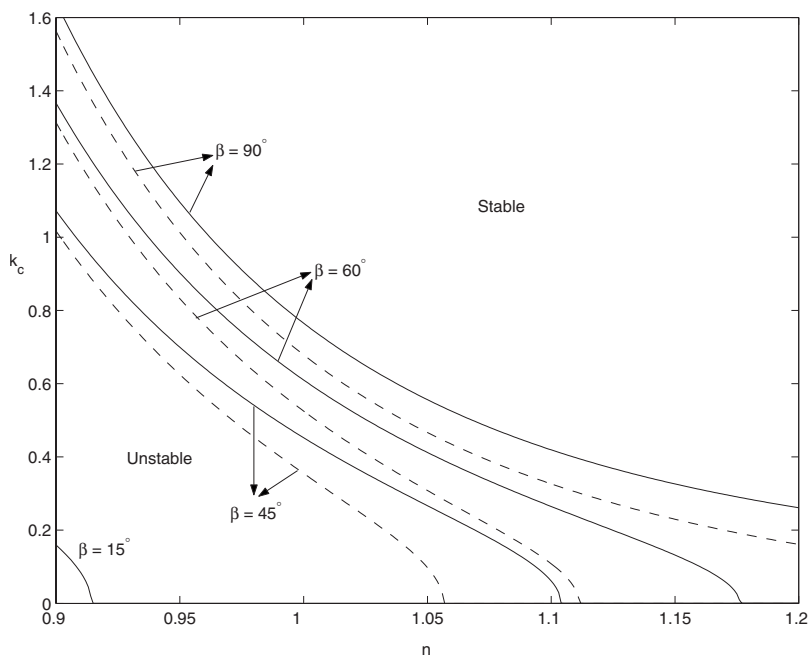


Fig. 4 Neutral stability curves for different angles of inclination: (—) temperature of the plane increasing linearly downstream and (- - -) temperature of the plane decreasing linearly downstream

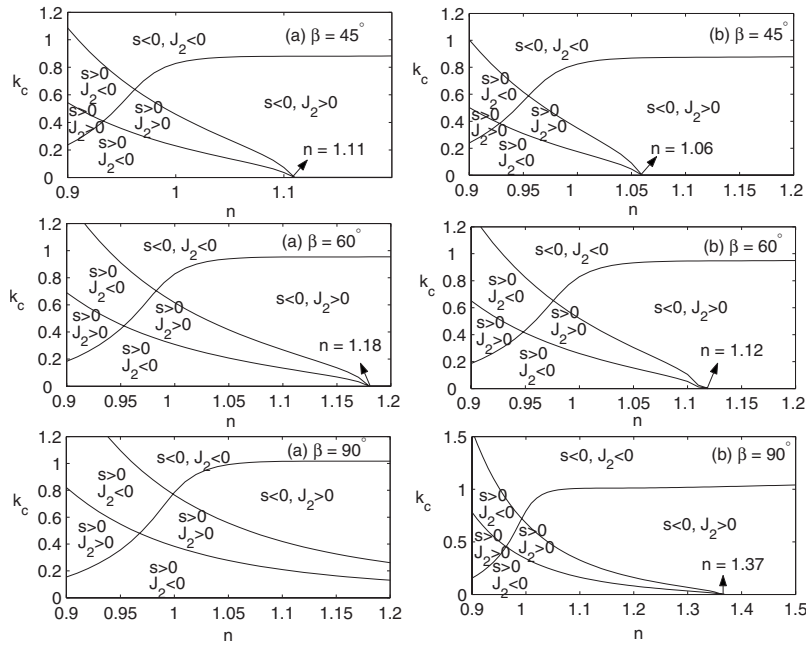


Fig. 5 Neutral stability curves for different angles of inclination: (a) temperature of the plane increasing linearly downstream and (b) temperature of the plane decreasing linearly downstream; $s > 0, J_2 < 0$ supercritical explosive state, $s > 0, J_2 > 0$ supercritical stable state, $s < 0, J_2 < 0$ subcritical unstable state, and $s < 0, J_2 > 0$ subcritical stable state

disturbances in the linearly unstable region develops into a new equilibrium state with a finite-amplitude (supercritical instability) or grows to be unstable, the weakly nonlinear stability analysis is employed.

The nonlinear stability analysis of the unsteady equation by the method of multiple scales [7] gives the threshold amplitude and nonlinear wave speed of the perturbation as

$$\alpha\Gamma_0 = \sqrt{\frac{s}{J_2}}, \quad N_c = c + s\frac{J_4}{J_2} \quad (20)$$

where α measures the distance from criticality, Γ_0 is the threshold amplitude of the perturbation, J_2 is the nonlinear amplification rate of the disturbance given by

$$J_2 = \varepsilon \left(7k^4 e_r C_1' - k^2 e_r B_1' - \frac{k^2}{2} B_1'' + \frac{k^4}{2} C_1'' \right) - k e_r A_1'$$

$$e_r = \frac{2(B_1' - k^2 C_1')}{(-4B_1 + 16k^2 C_1)}$$

$$J_4 = \varepsilon (7k^4 e_i C_1' - k^2 e_i B_1') + k e_i A_1' + k \frac{A_1''}{2}, \quad e_i = \frac{-A_1'}{\varepsilon(-4kB_1 + 16k^3 C_1)}$$

and $A_i^{(r)}$, $B_i^{(r)}$, and $C_i^{(r)}$ are the r th derivatives of A , B , and C (given by Eq. (16)) with respect to h and evaluated at $h=1$. It is observed from Eq. (20) that, in the linear unstable region ($s > 0$), the condition for existence of a supercritical stable region is $J_2 > 0$ and $\alpha\Gamma_0$ is the threshold amplitude. In the linear stable region ($s < 0$), if $J_2 < 0$, then the flow has the behavior of subcritical instability and $\alpha\Gamma_0$ is the threshold amplitude. The condition for the existence of a subcritical stable region is $s < 0, J_2 > 0$ and $J_2=0$ gives the condition of existence of a neutral stability curve. It is also observed from Eq. (20) that a negative value of J_2 can make the system unstable. In this case, if $s > 0$ then the amplitude of the disturbance may become larger than the threshold amplitude and cause the system to reach an explosive state. It is to be remarked here that the weakly nonlinear stability analysis of the first order

Benney-type equation (16) shows a possible subcritical bifurcation. However, such a possibility based on the weakly nonlinear analysis of Eq. (16) is not robust, as pointed out by Oron and Gottlieb [58]. In fact, they showed that the primary bifurcation of the second order Benney equation is supercritical for any Reynolds number.

Figure 5 shows the regions of subcritical instability ($s < 0, J_2 < 0$) in the linearly stable region and supercritical explosive state ($s > 0, J_2 < 0$) in the linearly unstable region. It is evident from Fig. 5 that both these states of the film flow system exist for a power-law film down an incline, where the temperature of the plane increases or decreases linearly downstream. The power-law film is supercritically stable in two regions. Further, the critical value of n below which the film flow system is unstable is larger when the temperature of the plane increases than when it decreases downstream for $\beta=45$ deg and $\beta=60$ deg.

It is observed from Fig. 6 that the threshold amplitude in the supercritical stable region is more for a power-law film when the temperature of the plate increases linearly downstream than when the temperature decreases. The same trend is exhibited by nonlinear wave speed.

6 Nonlinear Analysis

In order to understand the mechanism responsible for the transfer of energy from the basic state to the disturbance, the evolution of finite-amplitude perturbations is considered in this section. The non-Newtonian effect and the effect of nonuniform heating of the inclined plane are examined by solving the evolution equation (16) numerically in a periodic domain $[-\pi/k, \pi/k]$. It is to be noted that the length of the periodic domain has been chosen to be equal to one period of the surface temperature modulations. There may be instabilities whose wavelengths are larger than that of the period chosen. Therefore, if the computations are performed on a periodic domain, then it excludes the possibility of observing such instabilities. However, such computations have been made on a periodic domain to capture traveling-wave forms for isothermal/nonisothermal Newtonian and non-Newtonian films

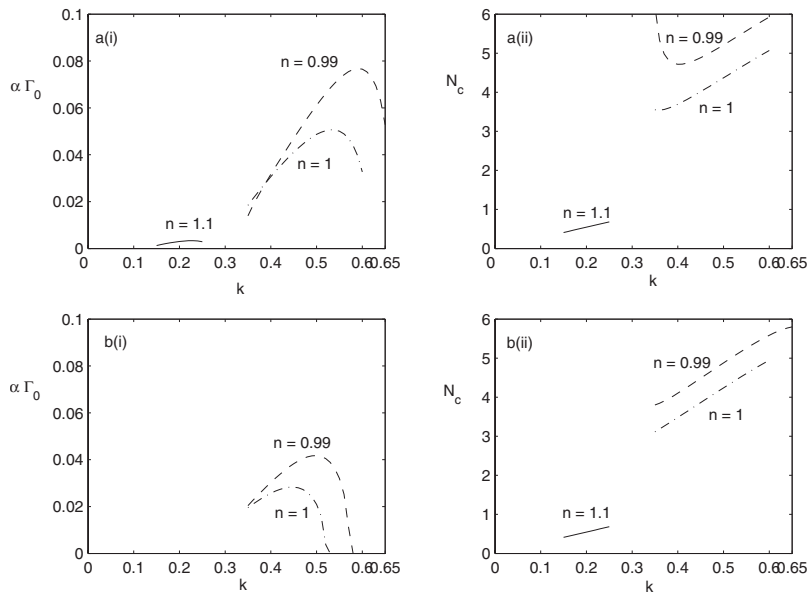


Fig. 6 Threshold amplitude and nonlinear wave speed in the supercritical stable region for $\beta=60$ deg when the plane temperature decreases linearly downstream: (a) plane temperature increases linearly downstream and (b) plane temperature decreases linearly downstream

[14,37,44,45]. It is therefore important to note that the results presented are consequences of the finite-size computational domain. The initial disturbance is assumed to be a sinusoidal wave with small amplitude given by

$$h(x,0) = 1 - 0.1 \cos(kx) \quad (21)$$

The final state of the disturbance is not sensitive to the choice of initial amplitude as demonstrated by Joo and Davis [59]. Lee's three-time level finite-difference method is used in solving the evolution equation (16). The finite-difference scheme achieves linearity in the unknown $h_{i,j+1}$ by evaluating all coefficients of $h_{i,j+1}$ at a time-level of known solution values, preserves stability by averaging $h_{i,j}$ over three-time levels, and maintains accuracy by using central difference approximations, where j denotes the number of time-step and i is a spatial grid point [60]. The discretization of the wave propagation term is given special attention so as to overcome the solution blowup for very small initial wave numbers. The scheme possesses both conservative and transportive properties and allows to follow the solution over larger periods of time. The resulting algebraic equations are solved using MATLAB and the iterations are continued until the local minimum layer thickness becomes smaller than the maximum error bound 10^{-6} . The computations are performed with $\Delta t=0.01$, and with number of nodes along the spatial direction as $N=100$ and $\Delta x = 2\pi/Nk$. It is to be noted that the solution obtained with decrease in Δt or increase in N does not show any deviation from the values presented in the results, for the desired degree of accuracy. In order to check the accuracy of the scheme, the computations are first performed for isothermal/nonisothermal Newtonian film on a rigid inclined plane for the set of parameters used by Miladinova et al. [37]. The results presented in Figs. 4, 5, 7, 8, 11, and 12 in Ref. [37] are reproduced. This gave the confidence in the applicability of the numerical scheme developed for the solution of the nonlinear equation governing the evolution of non-Newtonian film on a nonuniformly heated inclined plane and the solutions are obtained. Further, it is confirmed that the wave that emerges on the film surface does not change its shape for a relatively long period of time.

Typical results of the numerical solution immediately beyond an inception region for pseudoplastic liquid with $Re_n=9.224$ and dilatant liquid with $Re_n=7.671$ are presented in Figs. 7 and 8

when the temperature of the plate decreases/increases linearly downstream for $\beta=60$ deg. The permanent wave is nearly harmonic for initial wave numbers just below the cut-off wave number.

Free surface configurations are shown for k close to $k_s = (k_c/2)$ at different instants of time in Fig. 9 for a pseudoplastic fluid ($n=0.99$), when the temperature increases linearly downstream, for $Re_n=9.224$. The wave amplitude decays after reaching a maximum and the large-amplitude wave is followed by a small amplitude capillary wave.

For small times, the disturbance amplitudes grow and then decay due to the wave dispersion. The wave dispersion and coalescence continue for a longer period of time when the temperature decreases linearly (Fig. 10) than when the temperature increases linearly downstream. The comparison between the wave amplitudes indicates that the pseudoplastic fluid has a destabilizing effect on the film dynamics when the temperature of the plate increases linearly downstream. The evolution of h_{max} and h_{min} is presented in Fig. 11 for a pseudoplastic fluid, when temperature linearly increases downstream. At relatively small times, the amplitude of the initial harmonic disturbance grows with small initial disturbance wave numbers in accordance with linear theory. It exhibits a spatial maximum at least for some time in the cycle and is no longer strictly monotonically decreasing. The wave amplitude starts to evolve quickly with slight oscillations. The evolution of the free surface is time-dependent and oscillates slightly in amplitude. The corresponding figures for the spatiotemporal evolution of dilatant fluid are presented in Figs. 12 and 13. There are significant oscillations of both the maximum film thickness and the minimum one for the case of nonuniform heating of a dilatant fluid (Figs. 14 and 15). It appears that for the chosen values of the parameters of the non-Newtonian fluid, nonuniform heating promotes surface oscillations. Figure 16 shows the maximum and minimum amplitude of waves of a dilatant fluid ($n=1.1$) in the supercritical stable region when the temperature along the inclined plane increases linearly downstream. It is observed that oscillations in the wave structure are suppressed as Re_n is decreased. The long-time wave forms in this case are time-independent waves of permanent form that propagate.

Figures 17 and 18 display the permanent waves for $k=0.3$ and

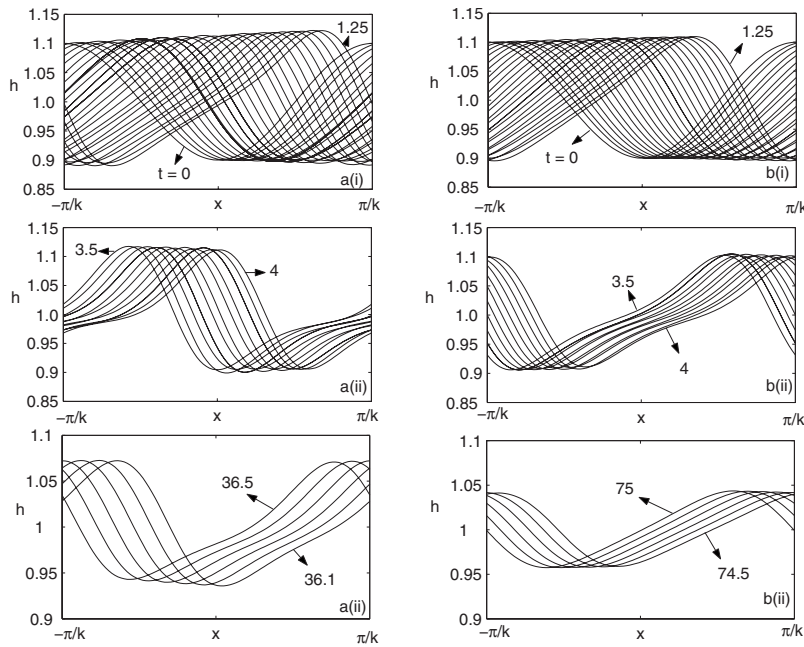


Fig. 7 Evolution of free surface of pseudoplastic and dilatant fluids in the supercritical stable region in an inclined wall ($\beta=60$ deg) when temperature decreases linearly downstream for $k=0.4$: (a) $n=0.99$, $Re_n=9.224$, and $M_n=-0.0189$; (b) $n=1.01$, $Re_n=7.671$, and $M_n=-0.0157$. (a) $k_c=0.5722$, $k_m=k_c/\sqrt{2}=0.4046$, and $k_s=k_c/2=0.2861$; (b) $k_c=0.4724$, $k_m=k_c/\sqrt{2}=0.33403$, and $k_s=k_c/2=0.2362$.

present a comparison of the film evolution between the Newtonian and non-Newtonian films on a nonuniformly heated plane. The wave grows initially in amplitude and travels downstream. For the

chosen wave number close to half the cut-off value, the surface-shape appears as a solitary wave. Pseudoplastic fluid has the largest amplitude for both cases of nonuniform heating of the plane.

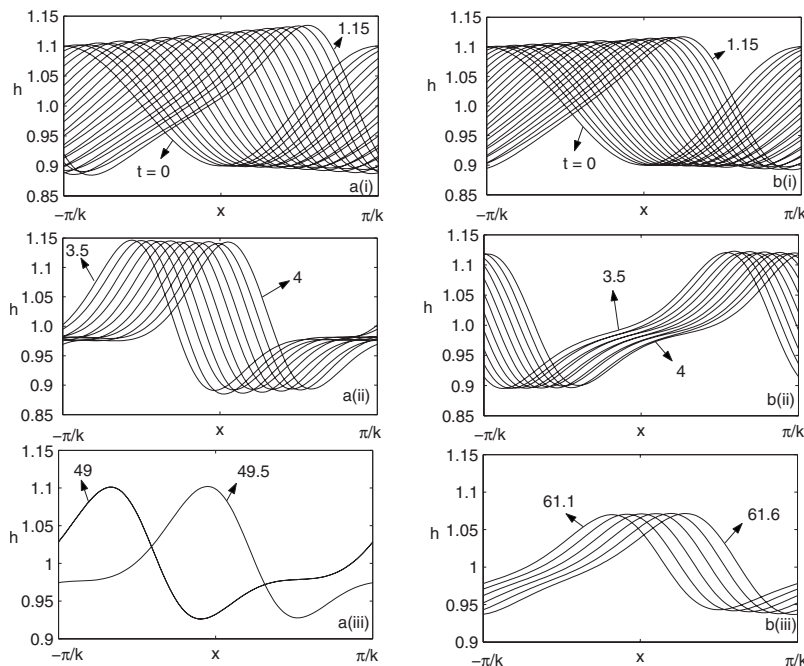


Fig. 8 Evolution of free surface of pseudoplastic and dilatant fluids in the supercritical stable region in an inclined wall ($\beta=60$ deg) when temperature increases linearly downstream for $k=0.4$: (a) $n=0.99$, $Re_n=9.224$, and $M_n=0.0189$; (b) $n=1.01$, $Re_n=7.671$, and $M_n=0.0157$. (a) $k_c=0.6652$, $k_m=k_c/\sqrt{2}=0.4704$, and $k_s=k_c/2=0.3326$; (b) $k_c=0.5698$, $k_m=k_c/\sqrt{2}=0.40291$, and $k_s=k_c/2=0.2849$.

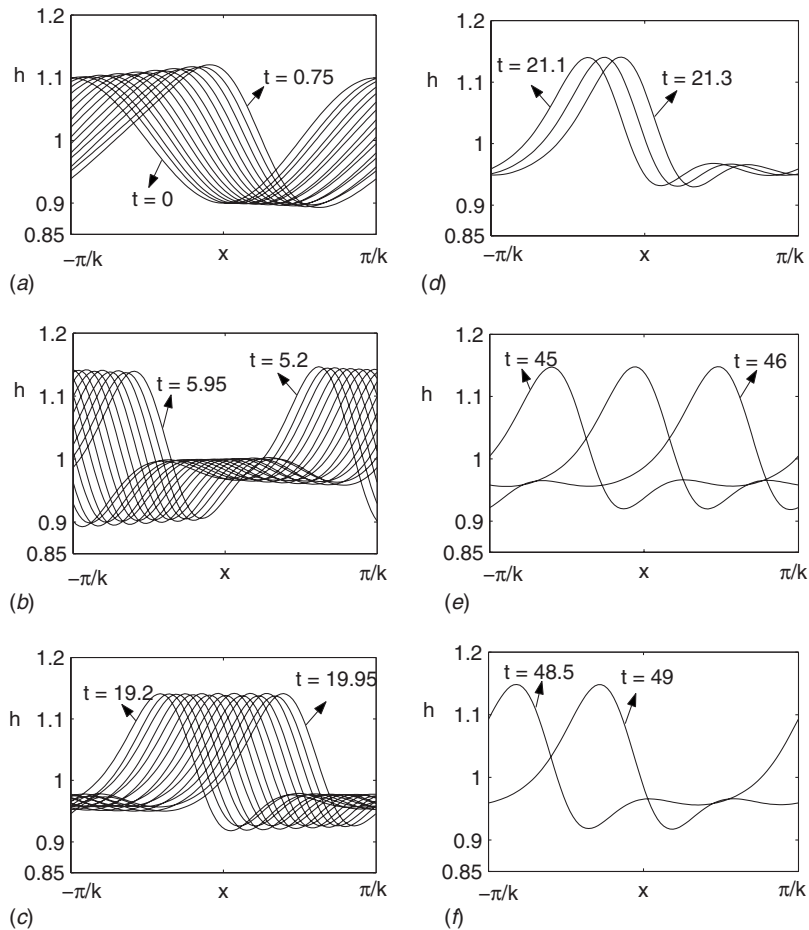


Fig. 9 Evolution of free surface ((a)–(f)) of a pseudoplastic fluid in the supercritical stable region in an inclined wall ($\beta=60$ deg) when temperature increases linearly downstream for $k=0.34$, $n=0.99$, $Re_n=9.224$, and $M_n=0.0189$; $k_c=0.6652$, $k_m=k_c/\sqrt{2}=0.4704$, and $k_s=k_c/2=0.3326$

Pseudoplastic fluids, in which viscosity decreases with increasing shear, transfer heat more rapidly but also more unevenly in convection than plain Newtonian fluids. However, decrease in the plate temperature decreases the wave amplitude, showing that the film flow system with decrease in temperature of the plate downstream has a stabilizing effect for a dilatant fluid.

When the plate is cooled in the downstream direction, the surface temperature at the trough ahead of the moving front is lower than that at the crest, and thermocapillary force acts in the same direction and it has a tendency to flatten the film and therefore has a stabilizing effect on the surface-wave evolution. On the other hand, when the temperature increases linearly downstream, then the surface temperature at the crest ahead of the moving front is higher than at the trough, and thermocapillary force acts in a direction opposite to that of gravity. In this case, the disturbance is amplified due to the increase in the tangential temperature-gradient ahead of the wave front. A pseudoplastic fluid film on a plate with temperature decreasing linearly downstream increases the disturbance amplitude further, thereby exhibiting the destabilizing effect on the film flow system. In fact, for the pseudoplastic fluid, viscosity is smallest along the rigid plate and increases in the regions close to the free surface. This results in the formation of surface waves with higher amplitudes. It is worth mentioning here that the long-wavelength disturbances originate at the free surface where vorticity is produced by the basic flow shear stress. On the other hand, the disturbances are damped for the dilatant fluids, since they are more viscous close to the rigid plate and viscosity is uniform along the plate. The general behavior of a

non-Newtonian, nonuniformly heated film is similar to that of a Newtonian, nonuniformly heated film, but the evolution of the non-Newtonian, nonuniformly heated film manifests itself in an oscillatory regime for certain values of the parameters governing the flow.

Figure 19 presents typical results of the numerical solution for the case of a linear decrease in plate temperature in the downstream direction and compares the free surface configuration with the corresponding Newtonian model presented by Miladinova et al. [37]. Figure 19(a) displays the free surface configurations for $k=1.3$ for two different values of the Marangoni number ($M_n=-0.01$ and $M_n=-0.02$), and it is observed that the code developed for the present model reproduces the solutions presented by Miladinova et al. [37] in Fig. 7 of their paper. For these values of the Marangoni number, the film flow is linearly unstable, and as has been pointed out by Miladinova et al. [37], the nonlinear wave evolution is similar to the isothermal case up to moderate times (as compared with Fig. 4(b) in Ref. [37]) but the wave amplitude changes from this case in the subsequent monotonic decay. It is observed that the amplitude growth stops due to thermocapillarity ($M_n=-0.01$), and the perturbation damps slowly and the free surface tends to the basic flat film ($M_n=-0.02$). Figures 19(b) and 19(c) show the free surface configurations for the long-wave instabilities of the nonuniformly heated non-Newtonian film considered in the present study. Free surface configurations for a linear decrease in plate temperature are given by solid curves for $M_n=-0.01$ and by dashed curves for $M_n=-0.02$ for $n=1$ (Newtonian

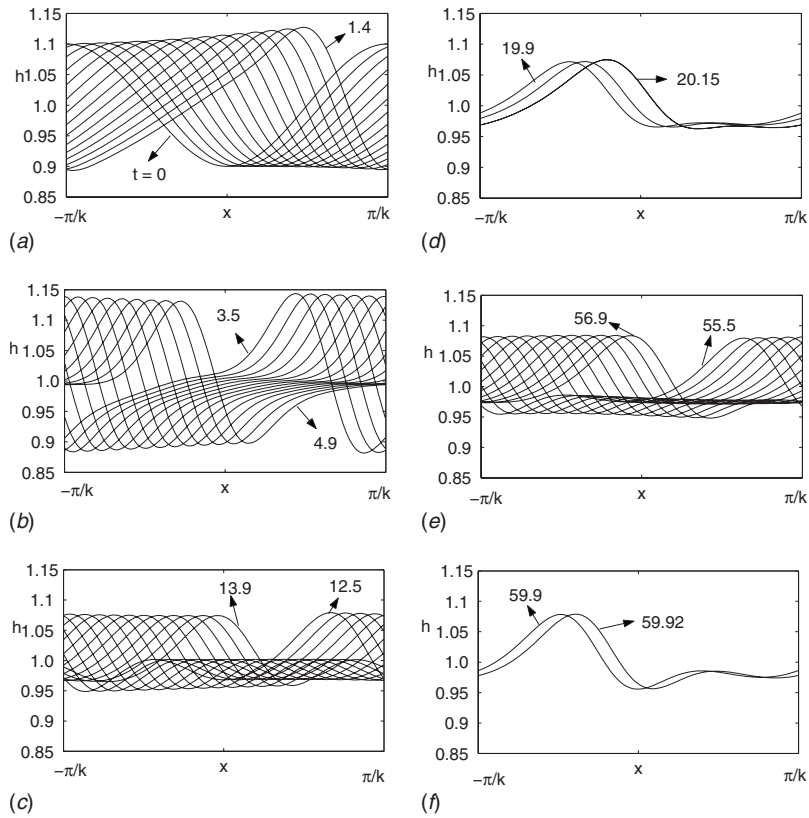


Fig. 10 Evolution of free surface (a)–(f) of a pseudoplastic fluid in the supercritical stable region in an inclined wall ($\beta=60$ deg) when temperature decreases linearly downstream for $k=0.3$, $n=0.99$, $Re_n=9.224$, and $M_n=-0.0189$; $k_c=0.5722$, $k_m=k_c/\sqrt{2}=0.4046$, and $k_s=k_c/2=0.2861$

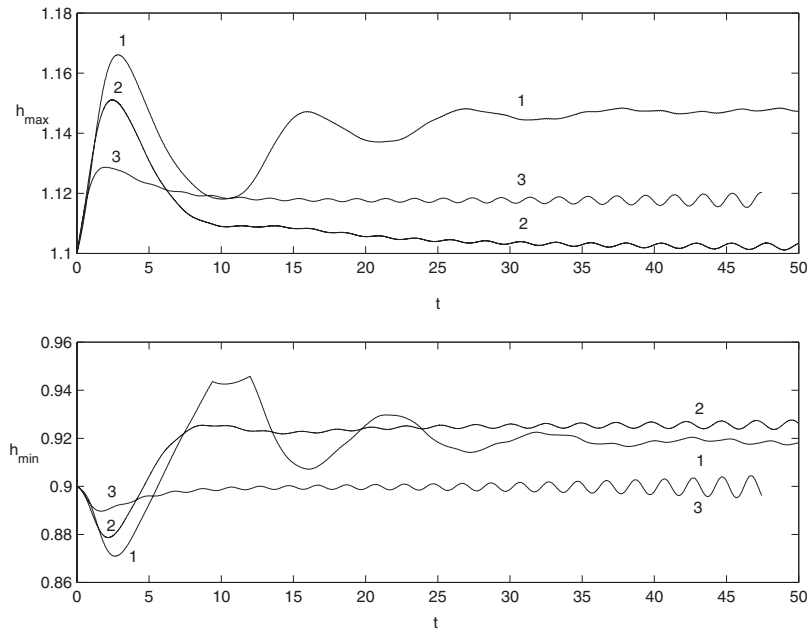


Fig. 11 Maximum and minimum amplitudes of waves of a pseudoplastic fluid in the supercritical stable region in an inclined wall ($\beta=60$ deg) when temperature increases linearly downstream for $n=0.99$, $Re_n=9.224$, and $M_n=0.0189$; (1) $k=0.34$, (2) $k=0.4$, and (3) $k=0.5$; $k_c=0.6652$, $k_m=k_c/\sqrt{2}=0.4704$, and $k_s=k_c/2=0.3326$

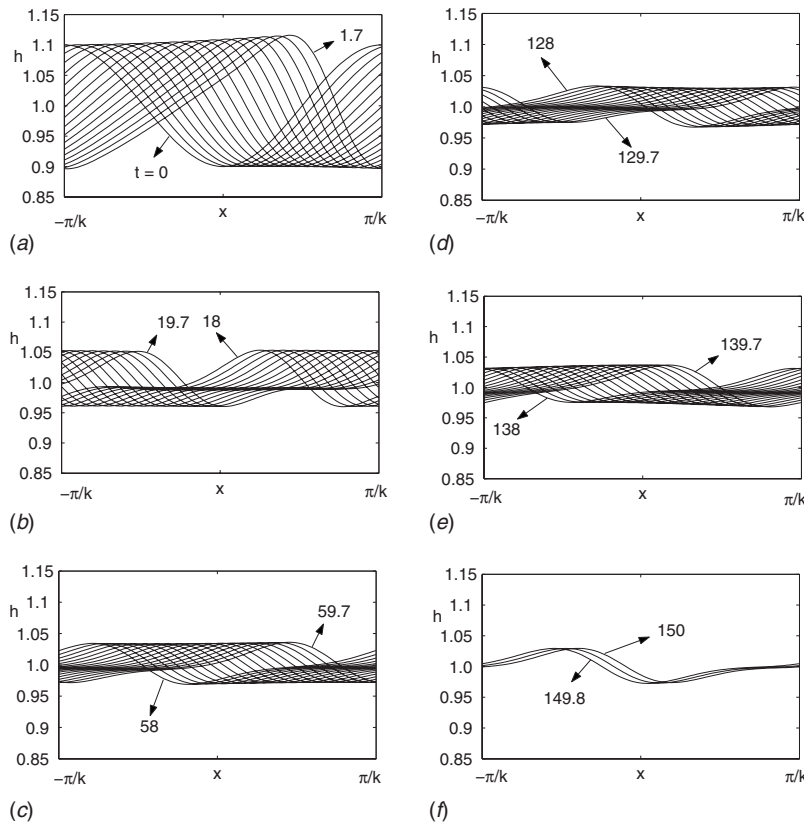


Fig. 12 Evolution of free surface ((a)–(f)) of a dilatant fluid in the supercritical stable region in an inclined wall ($\beta=60$ deg) when temperature decreases linearly downstream for $k=0.3$, $n=1.01$, $Re_n=7.671$, and $M_n=-0.0157$; $k_c=0.4724$, $k_m=k_c/\sqrt{2}=0.33403$, and $k_s=k_c/2=0.2362$

fluid), $n=1.1$ (dilatant fluid, Fig. 19(b)), and $n=0.95$ (pseudoplastic fluid, Fig. 19(c)). The figure shows that the behavior of the power-law dilatant fluid is analogous to the Newtonian model for these values of the Marangoni numbers. The free surface configuration damps slowly ($M_n=-0.01$) and is almost flat for $M_n=-0.02$ for the dilatant fluid (Fig. 19(b)). It is also observed that the wave amplitude for the dilatant fluid is smaller than that for the Newtonian fluid for these values of Marangoni number (Fig. 19(b)), indicating that the dilatant fluid tends to stabilize the film flow system for the case of a linear decrease in plate temperature. However, the behavior is different for the pseudoplastic fluid as is evident from Fig. 19(c). For both values of M_n , the wave amplitude increases for the pseudoplastic fluid in comparison to the Newtonian fluid, and the growth is more for $M_n=-0.01$ than for $M_n=-0.02$, indicating the destabilizing effects of the pseudoplastic fluid for the case of a linear decrease in the plate temperature in the downstream direction.

Figure 20(a)(i) and Fig. 20(a)(ii) show the free surface configurations presented by Miladinova et al. [37] for $Re_n=2.8$ and $k=0.9$ when $M_n=0.02$ (Fig. 12 in Ref. [37]) for the long-wave instabilities of a nonuniformly heated Newtonian film. The permanent wave forms when $M_n=0.02$ are presented in Fig. 20(b) for the pseudoplastic and dilatant fluids and are compared with that for a Newtonian fluid. The results show that the growth of the wave amplitude is smaller for a dilatant fluid than for a Newtonian fluid and that the trend is reversed for a pseudoplastic fluid.

The results presented by Miladinova et al. [45] for the nonlinear evolution of falling films of a power-law isothermal liquid films show that the free surface evolution of a power-law isothermal film is similar to that for a Newtonian isothermal film, but the shape and the amplitude of the permanent waves have been influenced strongly by the non-Newtonian fluid behavior. The present

study confirms the conclusions of Miladinova et al. [37] for a nonuniformly heated Newtonian film and Miladinova et al. [45] for a non-Newtonian film. The present study, in essence, reveals that the shape and amplitude of the permanent waves are influenced by both rheological properties of the fluid and the nonuniform heating of the fluid film down an inclined plane.

7 Conclusions

A thin liquid layer of a non-Newtonian film falling down an inclined plane that is subjected to nonuniform heating has been studied. The temperature of the inclined plane is assumed to be linearly distributed and the film flow is influenced by gravity, mean surface tension, and thermocapillary forces. The coupling of the thermocapillary instability and surface-wave instabilities is studied for two-dimensional disturbances through a nonlinear evolution equation derived by applying long-wave theory. Both the linear and weakly nonlinear stabilities have been investigated.

The free surface has been assumed adiabatic. The analysis has been performed under the assumption that the liquid film is very thin, the heat flux is weak, and the induced gravity-driven flow is relatively slow. That is, $|kh_x| \ll 1$ and this approximation gives qualitative results for the constant film thickness assumption at the zeroth order. It is important to note that this constant film thickness assumption with long-wave perturbations is a reasonable approximation only for certain segments of a power-law fluid film on an inclined plane with a temperature field decreasing or increasing linearly downstream along the surface.

The linear stability analysis of the evolution equation yields critical values of the Reynolds number and the dimensionless linearized phase speed for different values of the modified Marangoni number. The critical Reynolds number grows linearly

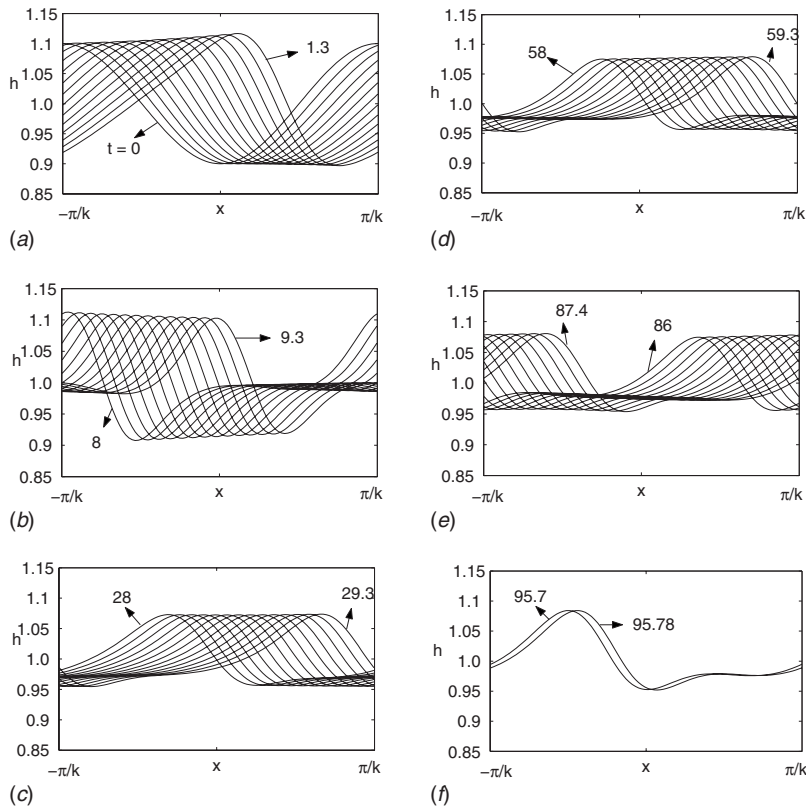


Fig. 13 Evolution of free surface ((a)–(f)) of a dilatant fluid in the supercritical stable region in an inclined wall ($\beta=60$ deg) when temperature increases linearly downstream for $k=0.3$, $n=1.01$, $Re_n=7.671$, and $M_n=0.0157$; $k_c=0.5698$, $k_m=k_c/\sqrt{2}=0.40291$, and $k_s=k_c/2=0.2849$

with the absolute value of the modified Marangoni number if the temperature of the plane is decreased in the downstream direction ($M_n < 0$). In this case, linear stability threshold increases with n .

There is a decrease in the critical Reynolds number as the temperature of the plane is increased linearly in the downstream direction. This reduction is important for dilatant fluids. Therefore,

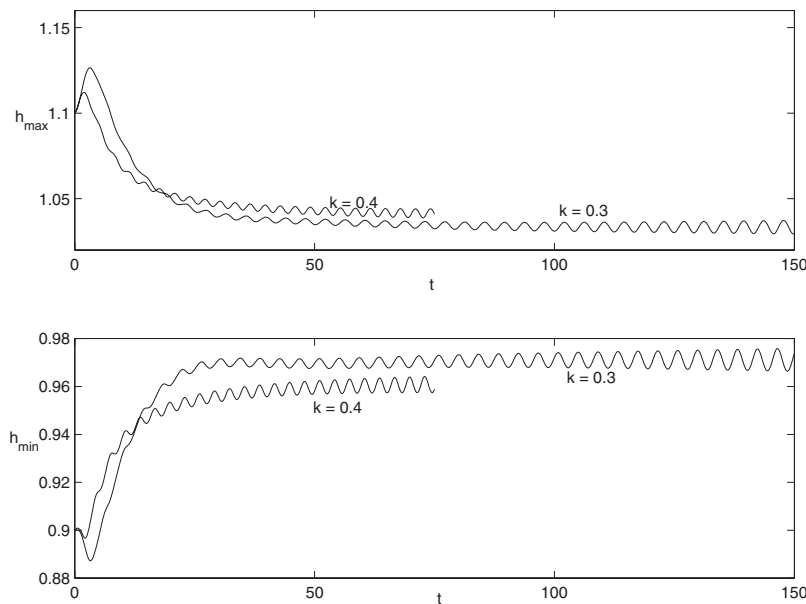


Fig. 14 Maximum and minimum amplitudes of waves of a dilatant fluid in the supercritical stable region in an inclined wall ($\beta=60$ deg) when temperature decreases linearly downstream for $n=1.01$, $Re_n=7.671$, and $M_n=-0.0157$; $k_c=0.4724$, $k_m=0.33403$, and $k_s=0.2362$

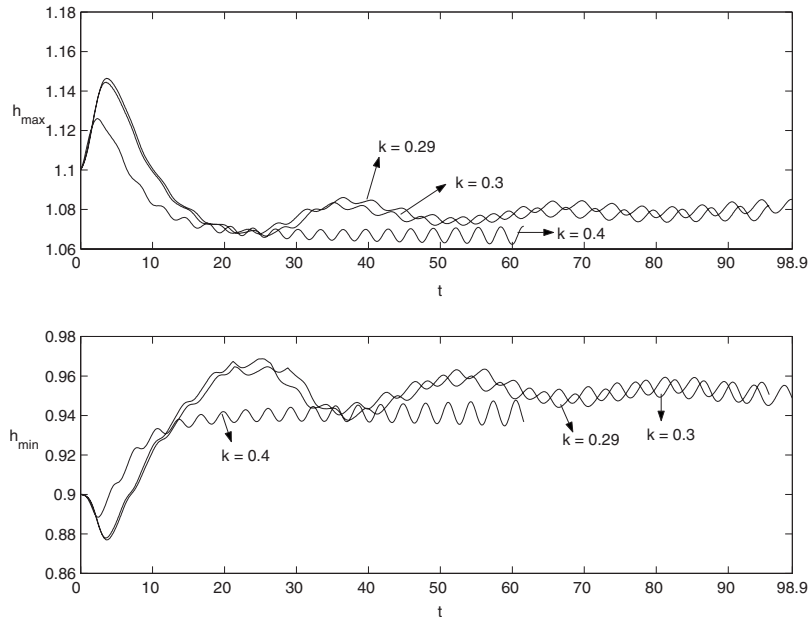


Fig. 15 Maximum and minimum amplitudes of waves of a dilatant fluid in the supercritical stable region in an inclined wall ($\beta=60$ deg) when temperature increases linearly downstream for $n=1.01$, $Re_n=7.671$, and $M_n=0.0157$; $k_c=0.5698$, $k_m=0.40291$, and $k_s=0.2849$

decreasing the temperature of the plane in the downstream direction has a considerable stabilizing effect on the Newtonian film, and this effect is enhanced for the dilatant fluid film but is less for the pseudoplastic fluid film. On the other hand, temperature increase plays a destabilizing role on the power-law film and the effect is more pronounced for pseudoplastic film than for a Newtonian film, so that the pseudoplastic film is more unstable than the Newtonian film; however, in this case, the dilatant fluid is less unstable than the Newtonian film.

The results of the weakly nonlinear stability analysis using the method of multiple scales show that both supercritical stability

and subcritical instability are possible for the film flow system. The analysis indicates the existence of finite-amplitude waves, and the threshold amplitude and nonlinear speed of these waves are influenced by thermocapillarity. Depending on the direction of the imposed temperature gradient, the thermocapillary effect can be either stabilizing or destabilizing. If the temperature of the inclined plane decreases in the downstream direction, then the surface temperature at the trough ahead of the moving front is lower than the temperature at the crest. The thermocapillary force acting in the same direction has a stabilizing effect on the surface-wave evolution. As a result, the disturbances converge to finite-

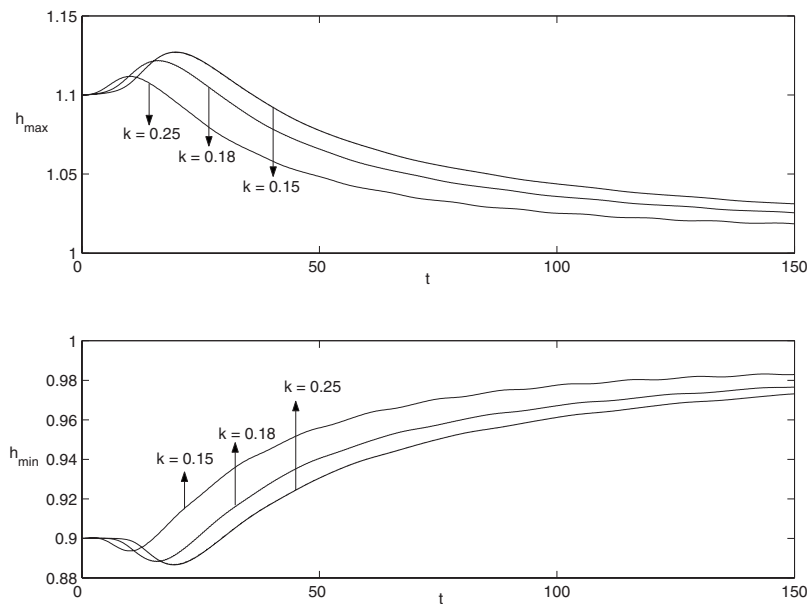


Fig. 16 Maximum and minimum amplitudes of waves of a dilatant fluid in the supercritical stable region in an inclined wall ($\beta=60$ deg) when temperature increases linearly downstream for $n=1.1$, $Re_n=3.0238$, and $M_n=0.00621$; $k_c=0.268$, $k_m=0.1895$, and $k_s=0.134$

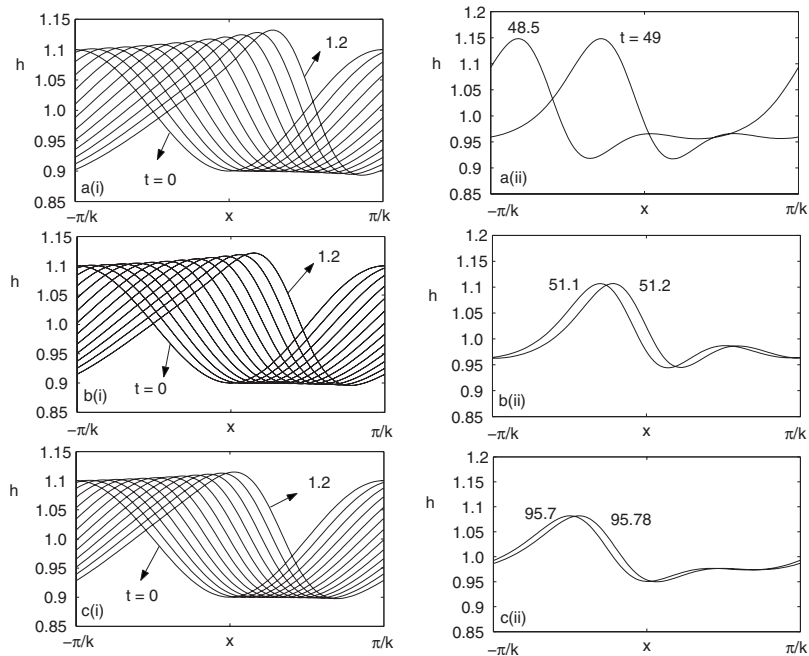


Fig. 17 Evolution of a free surface of (a) pseudoplastic, (b) Newtonian, and (c) dilatant fluids in the supercritical stable region in an inclined wall ($\beta = 60$ deg) when temperature increases linearly downstream for $k=0.3$: (a) $n=0.99$, $Re_n=9.224$, and $M_n=0.0189$; (b) $n=1$, $Re_n=8.42$, and $M_n=0.0173$; (c) $n=1.01$, $Re_n=7.671$, and $M_n=0.0157$

amplitude waves with small amplitudes. In the supercritical stable region, such waves in a dilatant fluid film have less threshold amplitude than in a Newtonian film, while the threshold amplitude in a pseudoplastic film is more than that in a Newtonian film.

When the temperature of the inclined plane increases in the downstream direction, the thermocapillary force acts in the opposite direction and therefore promotes the growth rate of the wave amplitude with respect to the isothermal film. In this case, the

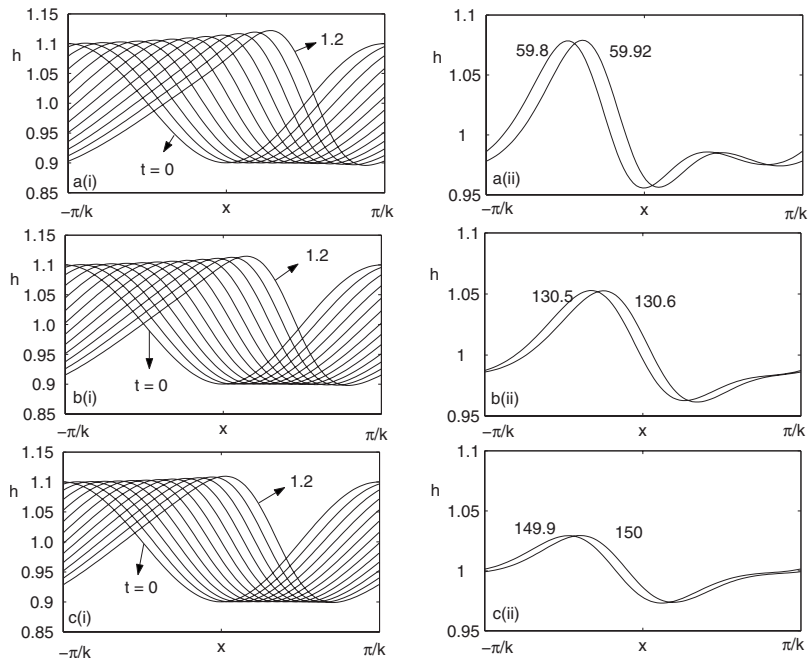


Fig. 18 Evolution of a free surface of (a) pseudoplastic, (b) Newtonian, and (c) dilatant fluids in the supercritical stable region in an inclined wall ($\beta = 60$ deg) when temperature decreases linearly downstream for $k=0.3$: (a) $n=0.99$, $Re_n=9.224$, and $M_n=-0.0189$; (b) $n=1$, $Re_n=8.42$, and $M_n=-0.0173$; (c) $n=1.01$, $Re_n=7.671$, and $M_n=-0.0157$

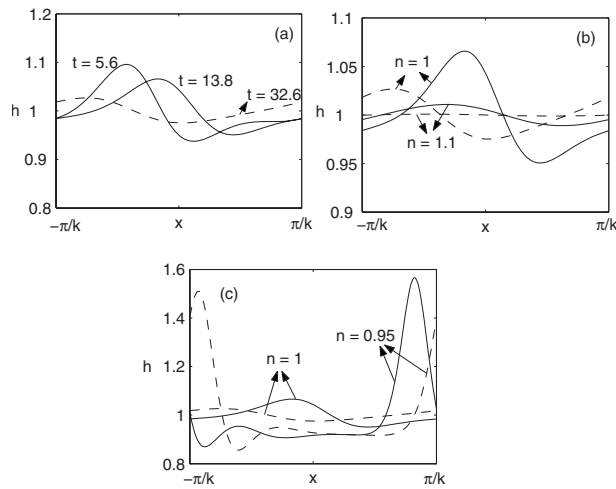


Fig. 19 Free surface configurations for a linear decrease in plate temperature for $Re_n=3.53$, when $\beta=45$ deg; (—) $M_n=-0.01$ and (- - -) $M_n=-0.02$

thermocapillary force draws the liquid from a hot trough to a cold crest in the direction opposite to gravity. As a result, the crest moves faster than the trough and increases the tangential temperature gradient ahead of the wave front. Therefore, the disturbance is amplified and thermocapillary force acting ahead of the wave front has a destabilizing effect. The threshold amplitude of finite-amplitude waves in the supercritical stable region is more for a pseudoplastic fluid film than for Newtonian and dilatant films. Thus, the nonuniform heating of the film influences the film instability through the thermocapillary force acting along the free surface, and the non-Newtonian rheology plays a vital role in either increasing or decreasing the threshold amplitude of waves with respect to Newtonian film.

Acknowledgment

The authors sincerely thank the referees for their very valuable suggestions and useful comments. Their comments have helped in improving the quality, content, and style of the paper. The authors

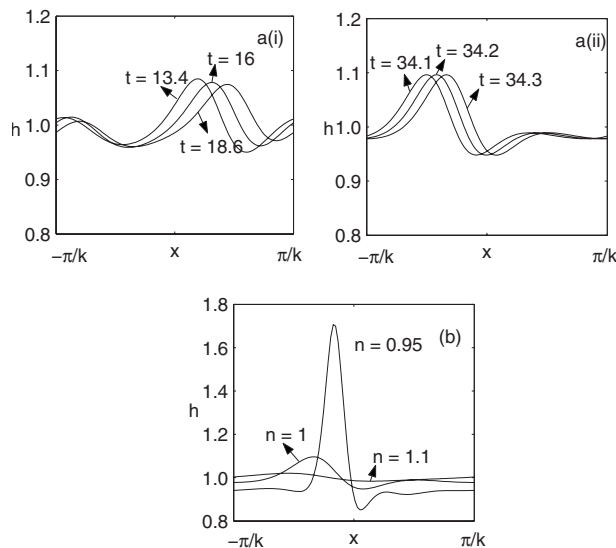


Fig. 20 Free surface configurations for a linear increase in plate temperature for $Re_n=2.8$ and $M_n=0.02$ when $\beta=45$ deg

also thank Professor Malcolm J. Andrews, Associate Editor, Journal of Fluids Engineering for his encouraging remarks and useful suggestions.

References

- [1] Chang, H.-C., 1994, "Wave Evolution on a Falling Film," *Annu. Rev. Fluid Mech.*, **26**, pp. 103–136.
- [2] Oron, A., Davis, S. H., and Bankoff, S. G., 1997, "Long-Scale Evolution of Thin Liquid Films," *Rev. Mod. Phys.*, **69**, pp. 931–980.
- [3] Yih, C.-S., 1963, "Stability of Liquid Flow Down an Inclined Plane," *Phys. Fluids*, **6**, pp. 321–334.
- [4] Benney, D. J., 1966, "Long Waves on Liquid Films," *J. Math. Phys.*, **45**, pp. 150–155.
- [5] Lin, S. P., 1969, "Finite-Amplitude Stability of a Parallel Flow With a Free Surface," *J. Fluid Mech.*, **36**, pp. 113–126.
- [6] Gjevik, B., 1970, "Occurrence of Finite Amplitude Surface Waves on Falling Liquid Films," *Phys. Fluids*, **13**, pp. 1918–1925.
- [7] Usha, R., and Uma, B., 2003, "Weakly Nonlinear Stability Analysis of Condensate/Evaporating Power-Law Liquid Film Down an Inclined Plane," *Trans. ASME, J. Appl. Mech.*, **70**, pp. 915–923.
- [8] Nepomnyashchy, A. A., Velarde, M. G., and Colinet, P., 2002, *Interfacial Phenomena and Convection*, Chapman and Hall, London/CRC, Boca Raton, FL.
- [9] Lin, S. P., 1975, "Stability of a Liquid Down a Heat Incline Plane," *Lett. Heat Mass Transfer*, **2**, pp. 361–370.
- [10] Sreenivasan, S., and Lin, S. P., 1978, "Surface Tension Driven Instabilities of a Liquid Film Flow Down a Heated Incline," *Int. J. Heat Mass Transfer*, **21**, pp. 1517–1526.
- [11] Smith, M. K., and Davis, S. H., 1983, "Instabilities of Dynamic Thermocapillary Liquid Layers. Part 1. Convective Instabilities," *J. Fluid Mech.*, **132**, pp. 119–144.
- [12] Smith, M. K., and Davis, S. H., 1983, "Instabilities of Dynamic Thermocapillary Liquid Layers. Part 2. Surface-Wave Instabilities," *J. Fluid Mech.*, **132**, pp. 145–162.
- [13] Kelly, R. E., Davis, S. H., and Goussis, D. A., 1986, "On the Instability of Heated Film Flow With Variable Surface Tension," *Proceedings of the Eighth International Heat Transfer Conference*, C. L. Tien, V. P. Carey, and J. K. Ferrell, eds., Hemisphere, New York, Vol. 4, pp. 1937–1942.
- [14] Joo, S. W., Davis, S. H., and Bankoff, S. G., 1991, "Long-Wave Instabilities of Heated Falling Films: Two-Dimensional Theory of Uniform Layers," *J. Fluid Mech.*, **230**, pp. 117–146.
- [15] Goussis, D. A., and Kelly, R. E., 1990, "On the Thermocapillary Instabilities in a Liquid Layer Heated From Below," *Int. J. Heat Mass Transfer*, **33**, pp. 2237–2245.
- [16] Goussis, D. A., and Kelly, R. E., 1991, "Surface Wave and Thermocapillary Instabilities in a Liquid Film Flow," *J. Fluid Mech.*, **223**, pp. 25–45.
- [17] Kalliadasis, S., Demekhin, E. A., Ruyer-Quil, C., and Velarde, M. G., 2003, "Thermocapillary Instability and Wave Formation on a Film Flowing Down a Uniformly Heated Plane," *J. Fluid Mech.*, **492**, pp. 303–338.
- [18] Colinet, P., Legros, J. C., and Velarde, M. G., 2001, *Nonlinear Dynamics of Surface-Tension-Driven Instabilities*, Wiley, New York.
- [19] Smith, K. A., 1966, "On Convective Instability Induced by Surface Gradients," *J. Fluid Mech.*, **24**, pp. 401–414.
- [20] Burelbach, J. P., Bankoff, S. G., and Davis, S. H., 1988, "Nonlinear Stability of Evaporating/Condensing Liquid Film," *J. Fluid Mech.*, **195**, pp. 463–494.
- [21] Kabov, O. A., 1996, "Heat Transfer From Small Heater to a Falling Liquid Film," *Heat Transfer Res.*, **27**, pp. 221–226.
- [22] Kabov, O. A., Marchuk, I. V., and Chupin, V. M., 1996, "Thermal Imaging Study of the Liquid Film Flowing on Vertical Surface With Local Heat Source," *Russ. J. Eng. Thermophys.*, **6**(2), pp. 105–138.
- [23] Kabov, O. A., and Chinnov, E. A., 1997, "Heat Transfer From a Local Heat Source to a Subcooled Falling Liquid Film Evaporating in a Vapor-Gas Medium," *Russ. J. Eng. Thermophys.*, **7**, pp. 1–34.
- [24] Kabov, O. A., 1998, "Formation of Regular Structures in a Falling Liquid Film Upon Local Heating," *Thermophys. Aeromechanics*, **5**, pp. 547–551.
- [25] Kabov, O. A., Legros, J. C., Marchuk, I. V., and Scheid, B., 2001, "Deformation of the Free Surface in a Moving Locally-Heated Thin Liquid Layer," *Fluid Dyn.*, **36**, pp. 521–528.
- [26] Zaitsev, D. V., Kabov, O. A., and Evseev, A. R., 2003, "Measurement of Locally Heated Liquid Film Thickness by a Double-Fibre Optical Probe," *Exp. Fluids*, **34**, pp. 748–754.
- [27] Kabov, O. A., Scheid, B., Sharina, I. A., and Legros, J. C., 2002, "Heat Transfer and Rivulet Structures Formation in a Falling Thin Liquid Film Locally Heated," *Int. J. Therm. Sci.*, **41**, pp. 664–672.
- [28] Frank, A. M., and Kabov, O. A., 2006, "Thermocapillary Structure Formation in a Falling Film: Experiment and Calculations," *Phys. Fluids*, **18**, p. 032107.
- [29] Gatapova, E. Ya., Kabov, O. A., and Marchuk, I. V., 2004, "Thermocapillary Deformation of a Locally Heated Liquid Film Moving Under the Action of a Gas Flow," *Tech. Phys. Lett.*, **30**, pp. 418–421.
- [30] Skotheim, J. M., Thiele, U., and Scheid, B., 2003, "On the Instability of a Falling Film Due to Localized Heating," *J. Fluid Mech.*, **475**, pp. 1–19.
- [31] Tan, M. J., Bankoff, S. G., and Davis, S. H., 1990, "Steady Thermocapillary Flows of Thin Liquid Layers," *Phys. Fluids A*, **2**, pp. 313–321.
- [32] Burelbach, J. P., Bankoff, S. G., and Davis, S. H., 1990, "Steady Thermocapillary Flows of Thin Liquid Layers, II. Experiment," *Phys. Fluids*, **2**, pp.

- [33] VanHook, S. J., Schatz, M. F., Swift, J. B., McCormick, W. D., and Swiney, H. L., 1997, “Long Wavelength Surface-Tension Driven Benard Convection: Experiment and Theory,” *J. Fluid Mech.*, **345**, pp. 45–78.
- [34] Scheid, B., Oron, A., Colinet, P., Thiele, U., and Legros, J. C., 2002, “Non-linear Evolution of Non-Uniformly Heated Falling Liquid Films,” *Phys. Fluids*, **14**(12), pp. 4130–4151.
- [35] Kalitzova-Kurteva, P., Slavtchev, S., and Kurtev, I., 2000, “Linear Instability in Liquid Layers on an Inclined, Non-Uniformly Heated Wall,” *J. Theor. Appl. Mech.*, **30**, pp. 12–23.
- [36] Slavtchev, S., Miladinova, S., Lebon, G., and Legros, J. C., 2001, “Marangoni Effect on the Instability of Non-Uniformly Heated Falling Films,” *Proceedings of the First International Symposium of Microgravity Research Applications in Physical Science and Biotechnology Energy Conservation Through Heat Transfer Enhancement of Heat*, Sorrento, Italy, Vol. 1, pp. 33–40, Eur. Space Agency, [Spec. Publ.] ESA SP-154.
- [37] Miladinova, S., Slavtchev, S., Lebon, G., and Legros, J. C., 2002, “Long-Wave Instabilities of Non-Uniformly Heated Falling Films,” *J. Fluid Mech.*, **453**, pp. 153–175.
- [38] Miladinova, S., Staykova, D., Lebon, G., and Scheid, B., 2002, “Effect of Non-Uniform Wall Heating on the Three-Dimensional Secondary Instability of Falling Films,” *Acta Mech.*, **156**, pp. 79–91.
- [39] Kalliadasis, S., Kiyashko, A., and Demekhin, E. A., 2003, “Marangoni Instability of a Thin Liquid Film Heated From Below by a Local Heatsource,” *J. Fluid Mech.*, **475**, pp. 377–408.
- [40] Demekhin, E. A., Kalliadasis, S., and Velarde, M. G., 2006, “Suppressing Falling Film Instabilities by Marangoni Forces,” *Phys. Fluids*, **18**(4), p. 042111.
- [41] Sadiq, I. M. R., and Usha, R., 2005, “Linear Instability in a Thin Viscoelastic Liquid Film on an Inclined, Non-Uniformly Heated Wall,” *Int. J. Eng. Sci.*, **43**, pp. 1435–1449.
- [42] Dandapat, B. S., and Gupta, A. S., 1997, “Long Waves on the Surface of a Viscoelastic Fluid Running Down an Inclined Plane,” *Rheol. Acta*, **36**, pp. 135–143.
- [43] Shaqfeh, E. S. G., Larson, R. G., and Fredrickson, G. H., 1989, “The Stability of Gravity Driven Viscoelastic Film Flow at Low to Moderate Reynolds Number,” *J. Non-Newtonian Fluid Mech.*, **31**, pp. 87–113.
- [44] Joo, S. W., 1994, “The Stability and Nonlinear Flow Development of a Viscoelastic Draining Film With Shear Thinning,” *J. Non-Newtonian Fluid Mech.*, **51**, pp. 125–140.
- [45] Miladinova, S., Lebon, G., and Toshev, E., 2004, “Thin-Film Flow of a Power-Law Liquid Falling Down an Inclined Plane,” *J. Non-Newtonian Fluid Mech.*, **122**, pp. 69–78.
- [46] Andersson, H. I., and Irgens, F., 1988, “Gravity-Driven Laminar Film Flow of Power-Law Fluids Along Vertical Walls,” *J. Non-Newtonian Fluid Mech.*, **27**, pp. 153–172.
- [47] Hwang, C. C., Chen, J. L., Wang, J. S., and Lin, J. S., 1994, “Linear Stability of Power-Law Liquid Film Flow Down an Inclined Plane,” *J. Phys. D*, **27**, pp. 2297–2301.
- [48] Gorla, R. R., 2001, “Rupture of Thin Power-Law Liquid Film on Cylinder,” *ASME J. Appl. Mech.*, **68**, pp. 294–297.
- [49] Pascal, J. P., and D’Alessio, S. J. D., 2007, “Instability of a Power-Law Fluid Down an Incline Subjected to Wind Stress,” *Appl. Math. Model.*, **31**, pp. 1229–1248.
- [50] Sathyagal, A. N., and Narasimhan, G., 1992, “On Rupture of a Thinning Film of Non-Newtonian Power-Law Fluid,” *Chem. Eng. Commun.*, **111**, pp. 161–166.
- [51] Hwang, C. C., and Chen, S. H., 1993, “Rupture Theory of Thin Power-Law Liquid Films,” *J. Appl. Phys.*, **74**, pp. 2965–2967.
- [52] Perazzo, C. A., and Gratton, J., 2003, “Thin Film of Non-Newtonian Fluid on an Incline,” *Phys. Rev. E*, **67**, p. 016307.
- [53] Ng, C. O., and Mei, C. C., 1994, “Roll Waves on a Shallow Layer of Mud Modelled as Power-Law Fluid,” *J. Fluid Mech.*, **263**, pp. 151–183.
- [54] Sisoiev, G. M., Dandapat, B. S., Matreyev, K. S., and Mukhopadhyay, A., 2007, “Bifurcation Analysis of the Travelling Waves on a Falling Power-Law Fluid Film,” *J. Non-Newtonian Fluid Mech.*, **141**, pp. 128–137.
- [55] Dandapat, B. S., and Mukhopadhyay, A., 2001, “Waves on a Film of Power-Law Fluid Flowing Down an Inclined Plate at Moderate Reynolds Number,” *Fluid Dyn. Res.*, **29**, pp. 199–220.
- [56] Lin, J. S., and Hwang, C. C., 2000, “Finite Amplitude Long-Wave Instability of Power-Law Liquid Films,” *Int. J. Non-Linear Mech.*, **35**, pp. 769–777.
- [57] Scheid, B., 2004, “Evolution and Stability of Falling Liquid Films With Thermocapillary Effects,” Ph.D. thesis, Université Libre de Bruxelles, Belgium.
- [58] Oron, A., and Gottlieb, O., 2004, “Subcritical and Supercritical Bifurcations of the First- and Second-Order Benney Equations,” *J. Eng. Math.*, **50**, pp. 121–140.
- [59] Joo, S. W., and Davis, S. H., 1992, “Instabilities of Three-Dimensional Viscous Falling Films,” *J. Fluid Mech.*, **242**, pp. 529–547.
- [60] Smith, G. D., 1986, *Numerical Solution of Partial Differential Equations: Finite Difference Methods*, 3rd ed., Oxford University Press, New York.

Effect of Geometrical Parameters on Vortex-Induced Vibration of a Splitter Plate

T. Pärssinen

Metso, Inc.,
P. O. Box 587,
FIN-40101 Jyväskylä, Finland
e-mail: tero.parsinen@metso.com

H. Eloranta

P. Saarenrinne

Institute of Energy and Process Engineering,
Tampere University of Technology,
P.O. Box 589,
FIN-33101 Tampere, Finland

An experimental study on the effects of various geometrical parameters to the characteristics of vortex-induced vibration (VIV) of a splitter plate is presented. The dynamic response of the fluid-structure system was measured using particle image velocimetry and laser telemetry simultaneously. Combined data of these techniques allow the assessment of the variation in the VIV response due to geometrical parameters, such as channel geometry, aspect ratio (AR), and trailing-edge thickness (d) as well as the imprint of the excited vibration mode on the flow. The effects of AR and d were both investigated with three different plate geometries and the effect of channel convergence was studied with a single plate geometry. Measurements were performed over a range of Reynolds numbers (Re). The results show that the vibrational response of the combined fluid-structure system is affected by the VIV instability in all cases. Within the measured Re range, a characteristic stepwise behavior of the frequency of the dominant vibration mode is observed. This behavior is explained by the synchronization between the vortex shedding frequency (f_0) and a natural frequency (f_N) of the fluid-structure system. The results further indicate that this response is modified by geometrical parameters. Channel convergence, i.e., flow acceleration, enhances the vortex shedding, which, in turn, increases the excitation level leading to stronger VIV. Channel convergence does not have a significant effect on f_0 or on the dimensionless vibration amplitude (A/d). An increase of both the number of excited f_N 's and the level of synchronization was observed with the lowest AR case. The results also suggest that d is the dominant geometrical parameter. It reduces both the A/d of the plate and the number of synchronization regions. This stronger effect on the response of the VIV system is due to the direct effect of d on the excitation mechanism. [DOI: 10.1115/1.2844584]

1 Introduction

Flow-induced vibrations are of common occurrence in several disciplines, e.g., in turbomachinery, aeronautics, and civil engineering. They can cause mechanical fatigue and eventually lead to structural damage. Often these forces are created by periodically shed vortices such as in this case, represented by a 2D plate in a parallel flow. These vortex-induced vibration (VIV) problems, even in the simplest case, are coupled and nonlinear in nature. Basically, this means that the response of a combined fluid-structure system is sensitive to surrounding flow environment and to the boundary conditions under which the system is exposed. Thus, minor changes in the excitation force, effective mass, or damping parameter can alter vibrational response of a system. As a consequence, the feedback process between the fluid and the structure remains obscure, leading to empirical, descriptive knowledge of VIV.

Majority of publications in the open literature are devoted to the forced vibration of circular cylinders, in which the structure is forced to vibrate in a surrounding fluid. Opposed to that, the present VIV case represented by a 2D plate in a parallel flow, however, falls under the category of free vibrations. The structural vibrations are induced by the shedding vortices and the structure is free to vibrate according to the excitation provided by the flow.

The literature concerning similar dynamics of free VIV of a splitter plate in moderate to high Re numbers is, to the best of the authors' knowledge, rather scarce. Some studies concerning rather similar phenomenon, though with a different structure, are New-

man and Karniadakis [1] and Evangelinos and Karniadakis [2]. Similar to the present setup, vortex shedding from the cable induces fluctuating forces, causing the cable to vibrate. Depending on the end conditions, structural properties, and Re, a standing wave vibration mode may build up along the cable. In the studies by Castro and Rogers [3] and Castro and Watson [4], the three dimensionality to the flow was introduced through changes of taper and aspect ratios, thus creating cellular vortex shedding in several cases. Hourigan et al. [5] studied vortex shedding from long blunt plates and observed vortex shedding lock-in and stepwise behavior in Strouhal number, based on the plate chord with increasing plate chord-to-thickness ratio.

The results presented in our earlier studies [6,7], hereafter referred to as EPS1 and EPS2, describing the spanwise variation of both vortex shedding and the energy of trailing-edge vibration show qualitative similarity with the literature concerning wakes of vibrating cables. The spanwise variation of the vortex shedding pattern was due to a standing wave vibration mode at the trailing edge of the splitter plate. Furthermore, EPS2 also showed that the vibration frequency is characterized by Re dependent stepwise behavior.

Also, So et al. [8] performed combined vibration and fluid velocity measurements to study fluid-structure interaction of circular cylinders in a cross-flow. They varied reduced velocity by using cylinders of different materials and by changing Re. Similar to this study, they observed that away from synchronization, several vibration frequencies and modes were excited, but at synchronization, a single mode dominates the vibratory response of the system. Furthermore, they observed only small effects of the vibration of the cylinder to the mean flow field. This is in contradiction to the present study where high amplitude vibratory re-

Contributed by the Fluids Engineering Division of ASME for publication in the JOURNAL OF FLUIDS ENGINEERING. Manuscript received April 18, 2007; final manuscript received October 8, 2007; published online February 9, 2009. Assoc. Editor: Juergen Kompenhans.

sponse of the plate dominates the mean flow pattern. These differences are to a large extent due to the different structural dynamics between the cylinder and the plate.

This paper continues the work of EPS1, EPS2, and Pärssinen et al. [9], hereafter referred to as PES by further exploring the details of the combined fluid-plate system. Now, detailed experiments are conducted to study the response of the plate by changing various geometrical parameters, such as channel convergence, aspect ratio (AR), and trailing-edge thickness (d).

Vandiver et al. [10] conducted a study on the lock-in behavior of flexible cylinders under sheared flow conditions. They observed several single-mode response natural frequencies of the cylinder with flows characterized by high shear. Their results also suggested that when such a single-mode response occurred, it prevented the excitation of weaker modes and had usually considerably stronger rms response than that of a multimode case. Lau et al. [11] studied the vibrational response of a flat plate and an airfoil. They observed a resonant behavior of a thin steel plate under the excitation provided by both the shear-layer vortices and the vortex shedding from the combined cylinder-plate system. Their conclusion is that the vibrations can alter the response of the entire fluid-structure system even though the system is at start assumed rigid. Also, Luk et al. [12] studied the structural resonance of an elastic airfoil. In their setup, the excitation was provided by oncoming vortices from two side-by-side circular cylinders. They used various cylinder diameters to provide a range of shedding frequencies that could lead to both aerodynamic and structural resonance of the airfoil. This method corresponds to the increasing excitation frequency from the trailing-edge vortices by increasing the flow velocity in this study. By using a laser vibrometer and hot wires, they deduced that the vortices could excite structural bending and torsional natural modes at a large Re range. The results in PES and in this present study agree with the observations by Luk et al. that when a structural resonance occurs, responses at other frequencies were attenuated.

This paper starts by presenting the experimental setup and measurement techniques in Sec. 2. Since the experimental procedures and analysis for particle image velocimetry (PIV) are explained in detail in the previous publications, see e.g., EPS1, they are repeated here only shortly. The measurements and analysis technique for laser telemetry (LT) data are similar to the procedure presented in PES and thus illustrated here only briefly. Section 3 starts by PIV data illustrating the differences between the flow properties with and without the freestream acceleration. Then, the effect of VIV to the response of the plate under the two different flow properties is highlighted with LT data. This is followed by a study on the effect of the variation of the aspect ratio of the splitter plate to the VIV phenomenon. Finally, the effect of trailing-edge thickness to the dynamics of the system is investigated. Conclusions are given in Sec. 4.

2 Experiments

2.1 Measurement Procedure. Experiments were conducted in two different flow channels. The channels were manufactured from Plexiglas to ensure optical access for the laser based measurement systems. They were installed into a recirculating water loop, equipped with a settling chamber for controlled low turbulence in-flow conditions. The channels were labeled as “Channel A” and “Channel B” corresponding to a straight channel and a convergent channel with rectangular cross sections, respectively. The cross-sectional flow area of Channel A is similar to Channel B’s outlet area, thus enabling the matching of flow rates and velocities. The sketches of Channels A and B with important dimensions and a coordinate system are presented in Figs. 1(a) and 1(b), respectively. The spanwise width of both channels is $120h$ ($h = 1$ mm).

The splitter plates used in these measurements were machined from polycarbonate due to its material characteristics. High elas-

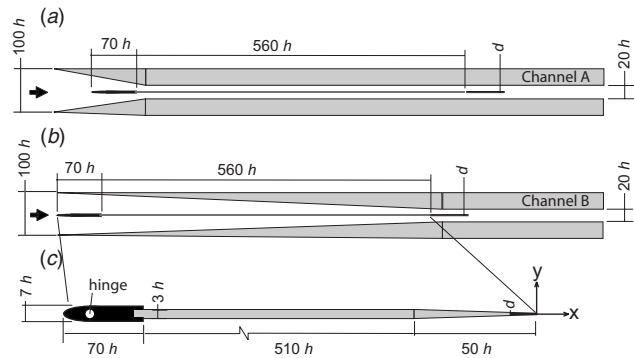


Fig. 1 Sketches of the (a) straight channel, (b) convergent channel, and (c) reference splitter plate

ticity enables high amplitude responses of the combined fluid-structure system. The length of the original plate used as a reference in all tests was $560h$. The body thickness of the plates is $3h$, which was then tapered from the last $50h$ to varying trailing-edge thicknesses (d). General information about the measurement setup and the used plate geometries is gathered in Table 1 and explained in more detail in Sec. 3

For all tests, the plates were hinged from the upstream end to the center of the channel inlet. The downstream end was free to move and interact with the flow. The plates were hinged to the sidewalls with a quasiwing attachment piece. The hinge had one pin on both sides between the channel wall and the wing piece, allowing the plate to move as it was attached with one axle through the channel. The body thickness of the wing piece was $7h$ and it had a rounded edge at the upstream side to minimize flow separation. With Channel A, the position of the hinge was chosen so that the flow area was similar to the cross-sectional flow area inside the channel, thus ensuring minimal effect of the tapered part to the flow. A sketch of the attachment piece is presented together with the reference splitter plate in Fig. 1(c).

The effect of the backward-facing step at the joint between the wing piece and the plate is assumed to be negligible due to the sufficiently long development length prior to trailing edge. We have studied the effect of various inlet conditions previously (EPS1) using screens, honeycombs, and even a direct connection to the pipeline. The response of the system was dominated by the excitation provided by the vortex shedding at the trailing edge, and the inlet conditions had a negligible role. Turbulence intensity

Table 1 General measurement information

Flow channels			
Nozzle exit/channel area	120 mm × 20 mm		
Test Re	$2 \times 10^3 - 20 \times 10^3$		
U_E at the trailing edge	2–10 m/s		
Freestream TI	1–5%		
Plates for test			
Material	Polycarbonate		
	E (GPa)	ρ (kg/m ³)	
	2.2	1200	
Original size (L/H)	560 mm × 117 mm		
Position	Horizontal midplane		
	d (mm)	L (mm)	AR (L/H)
$d_{1.2}/AR_{1.1}$; reference plate	1.2	560	4.8
$d_{0.6}$	0.6	560	4.8
$d_{1.8}$	1.8	560	4.8
$AR_{1/2}$	1.2	280	2.4
$AR_{1/4}$	1.2	140	1.2

was measured to be in the vicinity of 5% in the freestream at the trailing edge. Thus, it is not expected to influence the behavior of the VIV system [13].

EPS1 and EPS2 provided some basic characteristics of the combined fluid-structure system, such as the formation mechanism and the nature of the Re dependency. In PES, we studied the effect of various material parameters on the response of the system using plates of different material. Now, the response of the VIV system was studied by varying geometrical parameters, such as the trailing-edge thickness (d) and aspect ratio (AR). Also, the differences in the vibrational response of the plate, in a convergent channel and in a straight channel, were investigated.

To this end, LT and PIV were used to measure the vibrational response of the plate and the resulting effects on the flow, respectively. First, the effect of the transverse vibration to vortex shedding was measured simultaneously by LT measurements at the x - y plane. Next, the mean flow pattern was measured at the x - z plane by reproducing similar flow conditions. At this plane, the streamwise streaks resulting from the cellular shedding, due to the standing wave vibration mode of the plate, are easily observed. It will be seen later that the response of the system has a good repeatability between two consecutive measurements as the results from x - y and x - z planes correspond.

With both techniques, 39 flow rates were measured. The flow rate was increased in small increments, and a similar set of experiments was conducted for each step. The flow rate was characterized by Re, based on the freestream velocity at the plate trailing edge (U_E) and the tip thickness (d). The Re for each case is given in Sec. 3. Both measurement systems were fixed onto a 3D-traversing system to enable the measurement of the same spanwise (z) position. Using the traversing system, the LT and x - y plane measurements were conducted simultaneously at the spanwise position related to the highest amplitude response at each Re. In the case of a random low amplitude vibration, the measurements were conducted at the midspan of the plate.

The quantities used in this study are as follows: plate trailing-edge thickness (d), length of the plate (L), spanwise width of the plate (H), aspect ratio ($AR=L/H$), freestream velocity (U_E), plate vibration frequency (f_0), estimated vortex shedding frequency (f_s), Reynolds number ($Re=U_E d/\nu$), kinematic viscosity (ν), y displacement (A), nondimensional vibration amplitude (A/d), nondimensional vibration frequency ($St_0=f_0 d/U_E$), Strouhal number ($St_s=f_s d/U_E$), reduced velocity ($U_r=1/St_0$), and turbulence intensity ($TI=U_{RMS}/U$). The velocity decomposition follows the conventional Reynolds decomposition ($u'=u-U$), where u' is the velocity fluctuation, u is the instantaneous velocity, and U is the mean velocity.

2.2 Particle Image Velocimetry. Standard 2D-2C PIV measurements were performed both in the x - y and x - z planes. In all measurement cases, the position of the x - z plane was fixed. x - y plane was moved with the 3D-traversing system, together with the LT, within the spanwise width of the x - z plane, to the point of the highest amplitude response at each Re. The upstream edge of all measurement windows was located right at the trailing edge.

In the x - y plane, the PIV data were acquired simultaneously with the LT experiments and naturally from the same spanwise position. Thus, the estimation of the vortex shedding frequency (f_s) and the effect of the transverse vibration could be assessed. A measurement area of size $30 \times 11h^2$ (x - y) was used, yielding a spatial resolution of $0.4h$. The streamwise centerline of the x - y plane coincided with the wake symmetry plane.

The flow field in the x - z plane was measured next to complement the x - y plane data. A sufficiently large measurement window was used to ensure that the area covers at least one wavelength of the standing vibration mode of the plate. Also, as the assessment of mean flow patterns does not involve high requirements for measurement, the use of large window was justified. An area of

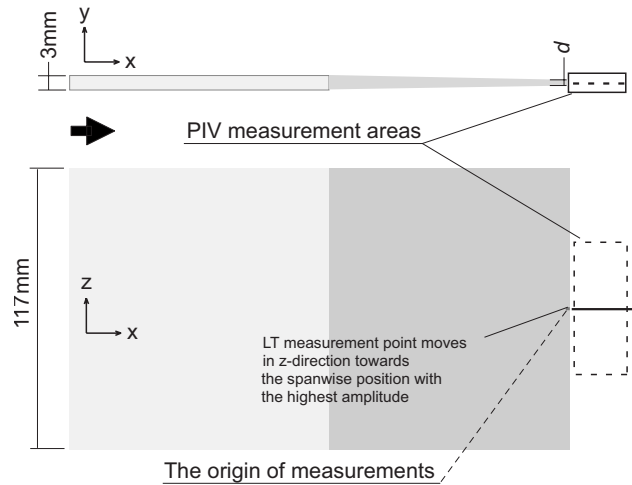


Fig. 2 PIV and LT measurement positions

$75 \times 30h^2$ (z - x) was used, resulting in a resolution of $0.9h$. Figure 2 presents sketches of the PIV and LT measurement positions with some important dimensions and the flow direction (black arrow).

The spanwise periodic mean flow pattern often seen in the x - z plane in, e.g., EPS1 is a result of cellular vortex shedding due to the standing vibration mode of the plate. Thus, the mode shape of the plate at a certain frequency can be deduced from the PIV measurements.

For each measurement, a set of 500 velocity fields was acquired for statistical analysis at both measurement planes. A standard two-pass fast Fourier transform (FFT) algorithm utilizing decreasing interrogation area size ($64 \times 64 \text{pix}^2 / 32 \times 32 \text{pix}^2$) and 50% overlapping between adjacent interrogation areas was used to calculate the vector fields. Generally, less than 2% of the data was removed in the validation process. Validation was based both on the absolute and local median velocity compared to the 3×3 neighborhood for both velocity components separately. Most of the spurious vectors were found in the very near wake where the gradients were large. A conventional estimate of accuracy for a standard PIV system with an adequate seeding is approximately 0.1 pixel, which is seen sufficient for our purposes.

The standard PIV data are not time resolved and hence the vortex shedding frequency (f_s) cannot be estimated directly from the data. However, the vortex convection velocity at the shear layer of the wake can be estimated from the x - y plane images and then used to estimate f_s . From the set of the 500 measured instantaneous velocity fields, we first calculate the mean and rms velocity fields. Then, with image analysis techniques, we find the points of the highest shear from both upstream and downstream parts of the wake. It is assumed that the convection velocity of the vortices is the mean velocity along the streamline connecting these points. As the flow accelerates, we take the average of these two values and use it as an approximation for the convection velocity of the vortices in the shear layer. This velocity value divided by the spatial wavelength of the vortices, from the standard PIV data, gives us the estimate of f_s . This approximation was also used in PES where it was found sufficiently accurate and reliable. A similar but reversed technique as f_s was known was used by Luk et al. [12] when they calculated the separation distances between the starting vortices in their study.

2.3 Laser Telemetry. LT is a single beam laser displacement sensor. It uses a high accuracy charge coupled device (CCD) cell sensor to measure surface position. The position of the reflected light on the CCD cell moves as the distance between the cell and the measurement target changes. The system uses a triangulation procedure to improve the accuracy of the light detection. For op-

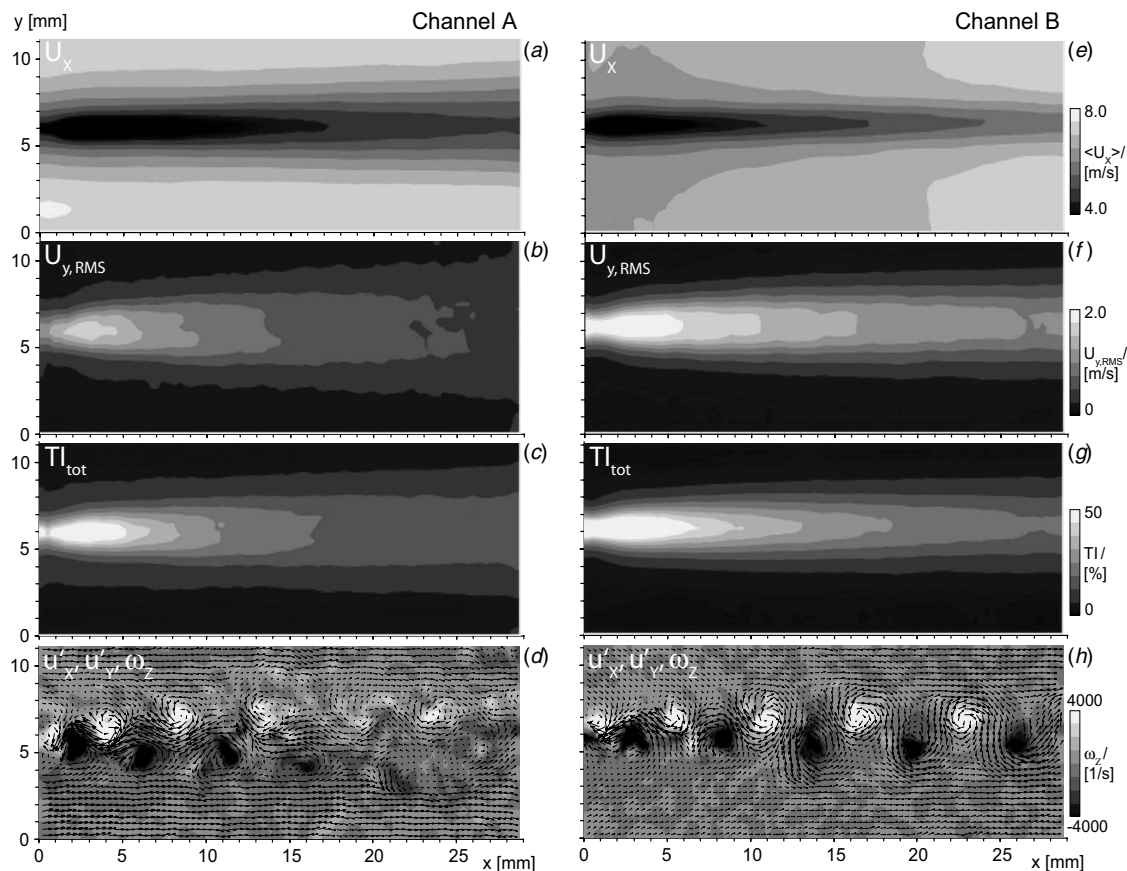


Fig. 3 Contours of (a) U_x , (b) $U_{y,rms}$, (c) total TI, and (d) an instantaneous velocity field in Channel A and (e) U_x , (f) $U_{y,rms}$, (g) total TI, and (h) an instantaneous velocity field in Channel B with the reference plate

timel signal quality, the measured surface should be opaque. To this end, approximately a 5 mm wide thin stripe of silver paint was sprayed on the trailing edge of each polycarbonate plate. The system used in these experiments was a Keyence LK-G157. It can measure with a sampling frequency up to 50 kHz and with a measurement resolution up to $0.5 \mu\text{m}$. With optimal measurement conditions, the assigned measurement error is in the order of 0.1%.

The used sampling rate was 20 kHz and the number of samples was 100,000 in each measurement. The system was calibrated to correct the refractive errors due to the interfaces between different materials in the optical path. The position data were analyzed by a FFT algorithm. The length of the FFT was 8092 units, the signal was divided into sections, and 50% overlapping was used in the spectral estimation, based on the Welch method [14]. The midspan measurement position of the LT system at the trailing edge is also indicated in Fig. 2.

As the LT is a single beam system, the data were influenced by the vibration of the entire flow facility. These low frequency vibratory motions were excited by the rotary motions of the motor and the pump impeller. The effect of this frequency modulation on the response of the system has been studied previously in PES and found negligible.

3 Results and Discussion

A series of earlier publications (EPS1, EPS2, and PES) has introduced a VIV phenomenon at the trailing edge of a splitter plate in a convergent channel. The combined fluid-structure system is controlled by a VIV instability, resulting in a standing sinusoidal vibration mode at the trailing edge of the splitter plate. The vortex shedding is confined to well defined and spatially fixed

cells separated by narrow regions of less organized shedding. This is a consequence of high amplitude vibration in the antinode area and low amplitude vibration in the spanwise fixed node area. The mean flow field at the x - z plane is characterized by higher velocity streamwise streaks at the nodes. Antinode areas possess a considerably lower streamwise velocity with secondary flows as the freestream penetrates inside the wake. In the following section, new results provide more information on the response of the VIV system in respect to the effects of various geometrical parameters.

3.1 Effect of Channel Geometry on Flow Properties. We start Sec. 3 by investigating how the channel geometry affects the wake flow properties. We demonstrate these differences with example data selected at the middle of the measured Re range. The measurement points are marked in the frequency plots in Figs. 4(a) ($f_0 = 1007 \text{ Hz}$) and 4(b) ($f_0 = 1001 \text{ Hz}$). At the selected points, the vibration data show quasi-identical synchronization behavior with both channel geometries regardless of the different wake properties, as will be shown. The measurements were conducted right after the trailing edge in the x - y plane with the reference plate.

First, the contours of the streamwise mean velocity (U_x) in both channels are presented in Figs. 3(a) and 3(e), respectively. It can be observed that the thinner boundary layer, due to the accelerating mean flow in Channel B, leads to a thinner and more intensive wake. In Channel A, the wake spreads and decays as the mean velocity slowly decreases with increasing downstream distance. This is portrayed more illustratively in the following. Figures 3(b) and 3(f) present the contours of the wall-normal rms velocity ($U_{y,rms}$) for both cases. The results show that velocity fluctuations of the wall-normal velocity component, which are related to the

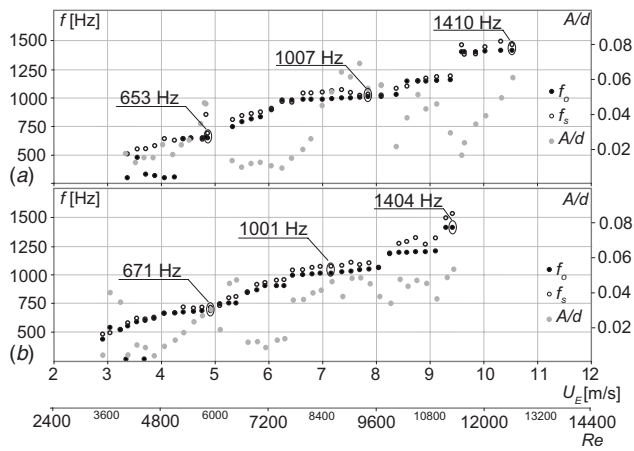


Fig. 4 The vibrational response of the reference plate in (a) Channel A and (b) Channel B

vortex shedding, possess clearly higher energy and extend further downstream in Channel B. Similar observation can be made with turbulence intensity (TI_{tot}), presented in Figs. 3(c) and 3(g). In addition, the TI_{tot} results suggest that also the relative magnitude of $U_{y,rms}$ is higher in the Channel B case. Thus, in Channel A, the velocity fluctuations attenuate more rapidly without the continuous energy input from the accelerating mean flow.

The last part of the figure, Figs. 3(d) and 3(h), presents typical examples of instantaneous velocity fields. Contours in the background represent the spanwise vorticity (ω_z) and the vectors the instantaneous velocity components u'_x and u'_y . The same features can also be observed in these fields. The vorticity is considerably higher and the vortices, as they gain energy from the accelerating shear layer, are preserved over the entire measurement window. In Channel A, the shedding process is less intense and random due to the lower energy transfer from the mean flow. Thus, vortices die out quickly and the wake starts to decay.

3.2 Effect of Channel Geometry on VIV. Until now, all our previous studies concerning the VIV of a splitter plate have been conducted in a convergent channel due to its relevance in a related practical application. The hypothesis has been that the flow acceleration has mainly a modifying effect and would not be a necessary condition for VIV to form. Now, the effect of the channel convergence to the dynamics of VIV was studied in more detail.

First, the vibration frequency (f_0) and the estimated vortex shedding frequency (f_s) for the reference plate measured in Channels A and B are presented in Figs. 4(a) and 4(b), respectively. The values of f_0 in the plot refer to the dominating peak in the spectrum, i.e., the peak corresponding to the frequency of the vibration mode with the highest amplitude (energy) response at a given Re. The estimation of f_s was done using the spatial wavelength and the convection velocity of vortices calculated from the PIV velocity fields as described above. All the measurements in this section were done using the reference plate.

The results show the characteristic stepwise behavior of f_0 and f_s with increasing flow rate. The entire measured Re range, excluding the very beginning, was occupied by almost a continuous chain of excited natural frequencies (f_N) of the combined fluid-structure system. f_N 's manifest themselves as the synchronized frequency areas, i.e., ranges of rather constant f_0 and f_s in the plot, and are referred to as frequency branches, following the notations of our earlier publications. Within the frequency branch, the vortex shedding is tuned to a value amplified by the fluid-structure system. Typically, there is a discontinuous jump between two branches as the flow rate exceeds a threshold value for the higher branch. At that point, the VIV system drifts out of balance, as f_s and f_0 slowly creep within the frequency branch, and then syn-

chronize to a higher state sustained by the instability. This drifting of frequency is assumed to be a low mass ratio effect explained by the added mass [15]. The added mass was also studied by Willden and Graham [16]. They deduced that the fluid is dominant over structural dynamics in low mass ratio and can shift the frequency of oscillation. As the measured range was almost fully characterized by VIV, f_s was not the shedding frequency of a fixed body, but a frequency induced by VIV. Furthermore, at the lower Re region, f_s displayed a tendency toward linear increase between branches. At these points, f_s was not sufficiently close to an excitable f_N of the system and the structure did not respond. With other geometrical parameters, the situation was somewhat different, as will be seen in the following.

For Channel B (Fig. 4(b)), a similar vibrational response was observed despite the differences in the freestream and wake properties. In this case, the freestream velocity was approximately 0.5 m/s lower due to difficulties in flow rate when changing between Channels A and B. The results confirm that this was not a significant variation.

Now, f_s was more closely synchronized to f_0 , even at the beginning of the measured Re range with lower velocity and excitation energy. This indicates that the acceleration of the wake flow enhances the synchronization process of VIV by increasing the level of vorticity in the wake, as will be seen later. Also, the thinner boundary layers on both sides of the plate could enhance the shedding process. It can also be observed that despite the different flow conditions, the frequency branches extended over a similar range of Re. The abovementioned creeping of the frequency inside a branch can also be detected here and perhaps slightly more pronounced. This suggests that the flow acceleration enhances the effect of the added mass on the response of the VIV system.

Corresponding dimensionless vibration amplitudes (A/d) are also presented in Figs. 4(a) and 4(b). The amplitude (A) was chosen to be the standard deviation of the y -displacement signal. The use of the full rms value was justified as in a great majority of measurement points there existed only one dominating peak in the spectrum at the expected f_0 . A was normalized with the trailing-edge thickness (d) of the plate.

A distinct correlation between the synchronization regions and high A/d was observed for both cases. However, few interesting observations can still be deduced from the data. Firstly, in Channel A the highest A/d values are more confined into single peaks within a synchronization region. It must be pointed out though, that these peaks actually have a higher maxima value compared to Channel B. This was somewhat surprising since the more intense excitation and the larger cross-section of Channel B at the trailing-edge suggests that higher A/d would occur. This indicates that the response amplitude is restricted by the mechanical properties of the plate. Secondly, the more intensive synchronization of the two frequencies in Channel B inflicts only a minor effect on A/d . The main effect is the formation of a somewhat higher mean A/d level. Finally, the results show that with identical mechanical properties of the plate, the dynamic response of the combined fluid-structure system is mainly governed by excitation, while freestream properties have only a minor effect.

Note that Fig. 4(a) and the appropriate conclusions thereafter are used as a reference in the sections studying aspect ratio and trailing-edge thickness effects.

Previous results indicated that despite the different flow properties, the response of the fluid-structure system has a quite similar nature in both channels. To further illustrate the vibrational response of both cases, the power spectra of the vibration together with the resulting vibration mode are investigated next.

In EPS1 and EPS2, we showed the forming mechanism of the synchronized VIV where a cellular vortex shedding was induced by the spanwise standing wave vibration mode. This resulted to a spanwise periodic mean flow pattern in the x - z plane, with spanwise wavelength matching to the fixed nodes of the standing vi-

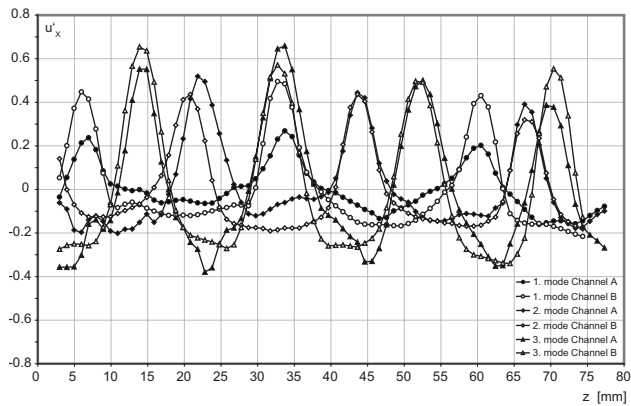


Fig. 5 Spanwise profiles of U_x velocity with the reference plate both in Channels A and B

bration mode of the plate. Thus, the vibration mode can qualitatively and even to some degree quantitatively be evaluated using only flow measurement data.

To this end, Figs. 5 and 6 present the spanwise profiles of the streamwise mean velocity (U_x) and the corresponding vibration data from both channels, respectively. The used data points from the three synchronization regions are marked in Figs. 4(a) and 4(b). Data from the same measurement points was used both in Figs. 5 and 6.

Firstly, from Fig. 5, it can be observed that the wavelengths of the spanwise periodic flow patterns are similar at corresponding f_0 in both channels. This indicates that the same f_N of the combined fluid-structure system were excited regardless of the differences in flow properties. Secondly, the spanwise spacing has a decreasing tendency with increasing Re, as has also been observed in earlier

studies.

Next, Fig. 6 presents the examples of the plate trailing-edge y -displacement signal and the corresponding estimated power spectra from the same data points. Note that the time in the x axis has an arbitrary value. Despite the fact that vorticity and thus the excitation level were higher in Channel B, the vibration amplitudes and the energy in the spectra do not display considerable differences. This indicates that there exists an amplitude maximum controlled by the structure, independent of the level of excitation. Generally, both f_0 and A/d increase as the flow rate increases, as is expected.

As a conclusion, it can be deduced that the acceleration of the mean flow is not a cause or even a necessary condition for the initiation of the VIV.

3.3 Effect of aspect ratio on VIV. In this section, we show results from the measurements with varying aspect ratio (AR). There are several definitions in the literature for AR depending on the field of application. Due to our application, we have chosen to present AR as the ratio between the streamwise and spanwise dimensions of the plate with the streamwise length being the variable while spanwise width remains constant. Three different AR, namely, AR_1 , $AR_{1/2}$, and $AR_{1/4}$, were measured. AR_1 refers to the reference plate, for which the results were already presented in Fig. 4(a). $AR_{1/2}$ and $AR_{1/4}$ plates correspond to a half and to a quarterlength plate, respectively (see Table 1). A similar set of measurements, as previously was carried out for the different AR in Channel A.

Due to the various lengths of the plates, the boundary layers have a different thickness at the trailing edge. It is known that the thinner boundary layer at separation can lead to enhanced vortex shedding. However, it is assumed that the boundary layers have a sufficient development length even with $AR_{1/4}$ to have only a minor effect on the dynamic response of the plate. This was con-

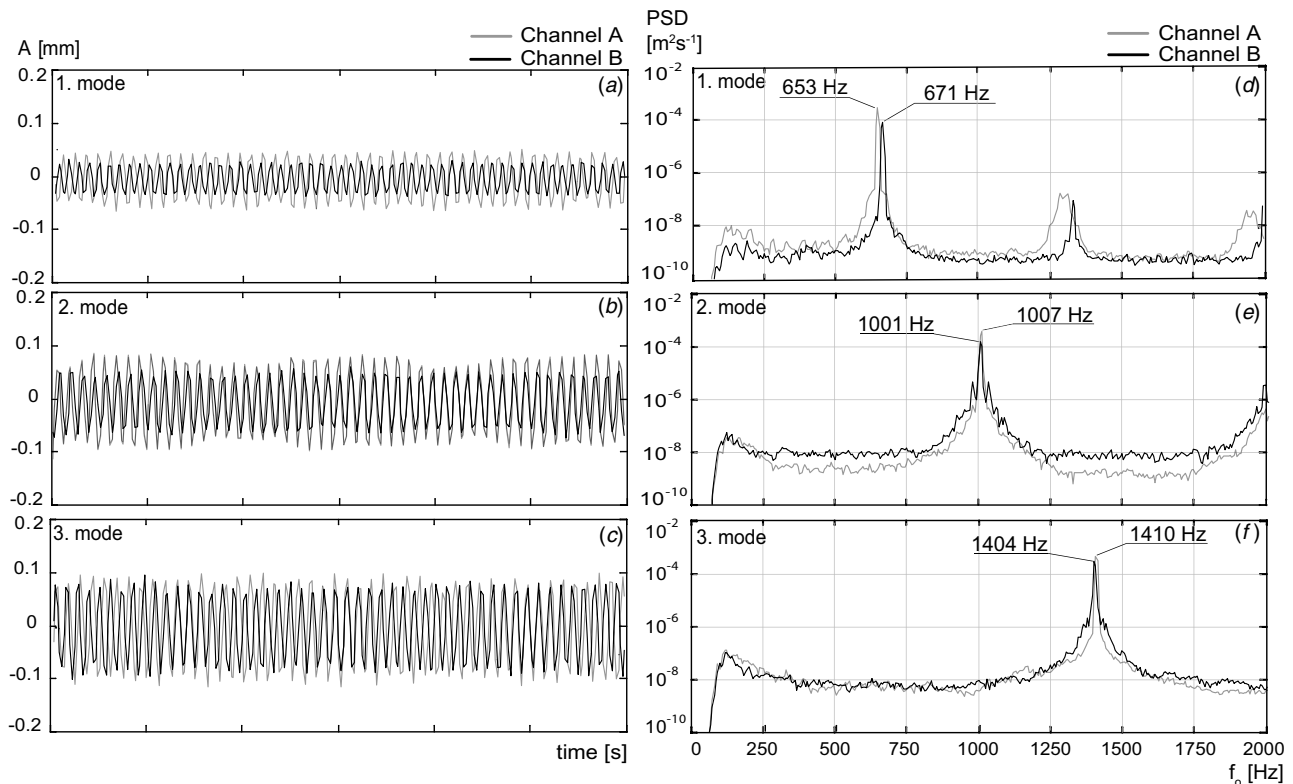


Fig. 6 Time trace of trailing-edge y displacement of the reference plate at (a) 1., (b) 2., and (c) 3. mode and the corresponding estimated power spectrum at (d) 1., (e) 2., and (f) 3. mode both in Channels A and B

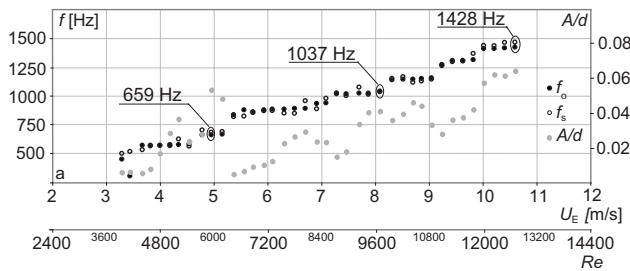


Fig. 7 The response of $AR_{1/4}$ plate in Channel A

firmed with the results in the previous section, where the considerably lower boundary layer thickness at separation in Channel B did not significantly change the response of the reference plate.

The results of $AR_{1/2}$ plate show that the first halving of the plate had no considerable effect on the response of the VIV system and thus will not be presented here separately. The frequency branches occurred practically in identical positions in the Re range and at similar frequencies. This indicates that AR_1 and $AR_{1/2}$ plates possess the same excitable f_N despite the rather large change in the AR value. From the point of view of this study, this result is rather considerable, though it remains unclear whether this behavior is just typical solid mechanical characteristics of the plate.

The study is continued with results for the $AR_{1/4}$ plate in Fig. 7. Now, the length of the plate was only $\frac{1}{4}$ of the original length. The basic nature of the VIV is similar including the stepwise increase of f_0 and f_s together with the highest vibration amplitudes correlating with the synchronization regions. Even with this quarter length plate, f_0 and f_s and thus St had a quite similar nature compared to the AR_1 plate, due to the constant d and U values.

However, the results for $AR_{1/4}$ plate also displayed some noticeable changes. Perhaps, as the most important, the measurements indicate that the lower AR value narrows the width of the frequency branches. To put it in another way, the number of excited f_N of the combined fluid-structure system increases within the measured Re range. It is assumed to be an effect of the change in the material parameters of the plate, such as stiffness. Another important observation with $AR_{1/4}$ plate was the increase in the synchronization level between f_0 and f_s . Thus, the fluid-structure system was in a synchronization state throughout the measured Re range. This could also be attributed as an effect of the increased stiffness of the plate. As the material damping generally diminishes with increasing stiffness, the system can actually be more susceptible to excitation at least if the mass of the system remains constant. Wang et al. [17] studied the VIV of elastic side-by-side cylinders. They found that the behavior of system f_N 's is a combined effect of mass, stiffness, and damping ratios with varying cylinder spacings. In PES, plates with various materials were studied and it was found that a combined effect of increased mass and stiffness was required to considerably affect the dynamic response of the fluid-structure system.

A/d is also presented in Fig. 7. The formation of the new excited f_N can also be observed here as the measurement points with higher A/d correlate with the new frequency branches.

Previous results have shown the differences in the vibrational behavior of the VIV system with various AR values. Now, the effect of AR will be further illustrated with similar data as in Figs. 5 and 6. Three profiles of U_X have been selected from all AR cases at corresponding measurement points. For AR_1 , the same data were used as in Figs. 5 and 6. As the data for the $AR_{1/2}$ plate are essentially identical to AR_1 , the same measurement points were used. For the $AR_{1/4}$ plate, the used data points are marked in Fig. 7. The vibration modes were again indirectly studied through the spanwise profiles of U_X , as depicted in the previous section. Figure 8 presents the examples of spanwise profiles of U_X measured

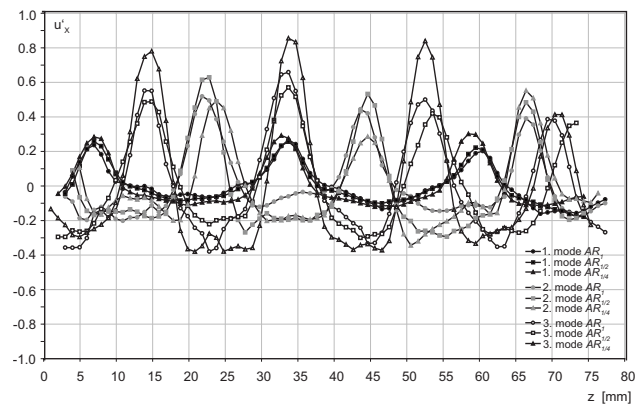


Fig. 8 Spanwise profiles of U_X velocity in Channel A for AR_1 , $AR_{1/2}$, and $AR_{1/4}$ plates at selected Re

in the x - z plane. The plot illustrates how the f_N were changed with varying AR. In addition to the similar f_N in all cases, it can be seen from Fig. 7 that several other f_N emerged with $AR_{1/4}$ case. This indicates that the changed material parameters of the plate, such as stiffness and damping, can change the response of the plate by inducing additional modes. Accordingly, the system's increased susceptibility to excitation leads to a higher level of synchronization and to a change in the dynamic response, e.g., to the increased number of excited f_N .

The selected power spectra of the plate y displacement with different AR cases are presented in Fig. 9. These examples clearly illustrate that regardless of the considerable change in AR, the vibrational response remains similar. There exist only minor differences between the frequency and energy of the peaks and the noise level.

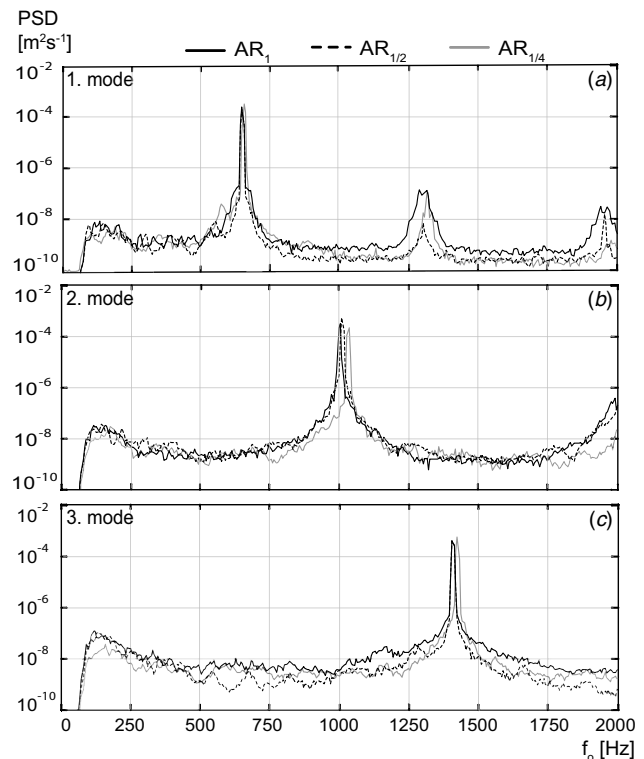


Fig. 9 The estimated power spectra of trailing-edge y displacement at (a) 1., (b) 2., and (c) 3. mode with varying AR at selected Re

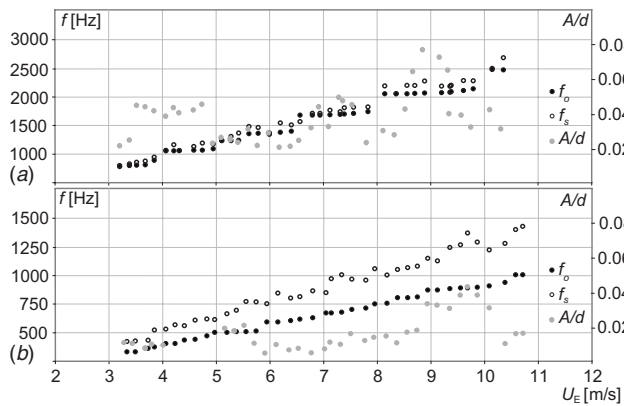


Fig. 10 The dynamic response of (a) $d_{0.6}$ and (b) $d_{1.8}$ plates in Channel A as a function of U_E

3.4 Effect of Trailing-Edge Thickness on VIV. Finally, the effect of trailing-edge thickness (d) to the response of the fluid-structure system was studied. The same measurement procedure as in the previous sections was now conducted with three different d . The plates were labeled as $d_{0.6}$, $d_{1.2}$, and $d_{1.8}$ corresponding to d values of $0.6h$, $1.2h$, and $1.8h$, respectively. All measurements were carried out in Channel A and again $d_{1.2}$ refers to the reference plate, for which the results were presented in Fig. 4(a). The authors recognize that Re range is different for all three cases due to the different d . Here, the purpose was to study the cases with equal flow rates, which stems from the requirements placed by the relevant practical applications.

Figure 10(a) shows the dynamic response of the $d_{0.6}$ plate. Note that the vertical axis values have changed as thinner d produces higher f_0 and f_s with the same flow rate. A typical behavior of the VIV system can be observed. Compared to the $d_{1.2}$ plate, presented in Fig. 4(a), the results indicate that $d_{0.6}$ was more receptive to excitation. The measured range consisted of more distinct chain of continuously excited f_N . Also, the jumps from one frequency branch to the next were more distinct. This higher susceptibility to excitation was assumed to be an effect of the increased elasticity of the thinner trailing edge.

The consequences of the more elastic structure of the $d_{0.6}$ plate can also be observed from the A/d plot, presented also in Fig. 10(a). Now, both the maximum and the mean value of A/d were higher than with the reference case ($d_{1.2}$). The system responded with significant amplitude even at the lowest flow rates and at the edges of the frequency branches. The transition ranges between branches are usually associated with lower level of synchronization and thus A/d .

Corresponding results for the $d_{1.8}$ plate are presented in Fig. 10(b). As can be seen, a very different picture emerges. Now, the off-synchronization state between f_0 and f_s was apparent at most measurement points. As a result, more of a linear increase of f_0 and f_s was observed instead of the more commonly seen stepwise behavior. Thus, only two rather weak f_N were excited within the measured range. These were at $U_E=5.1$ m/s and $U_E=8.9$ m/s. The weak natural modes can also be observed from the A/d plot in Fig. 10(b). Despite the prominent difference between f_0 and f_s at these quasysynchronized frequency branches, A/d displayed surprisingly high values. This indicates that with the $d_{1.8}$ plate, the fluid-structure system does not possess continuously distributed f_N , as the excitation frequency differs considerably from the excited f_N .

Next, the dynamics of the system is illustrated further by presenting the nondimensional vibration frequency (St_0) of all three cases in Fig. 11. The plot consists of the same data as in the frequency plots (Figs. 4(a), 10(a), and 10(b)), but now, the dynamics of the system can be more easily observed. A resonance

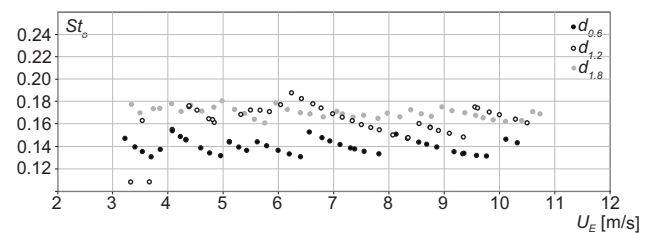


Fig. 11 Dimensionless vibration frequency (St_0) of (a) $d_{0.6}$, (b) $d_{1.2}$, and (c) $d_{1.8}$ plates as a function of U_E

occurs when f_0 is amplified in the vicinity of a f_N of the combined fluid-structure system. Due to the coupled nature of VIV, the synchronized f_s will also be amplified. As soon as the St_0 drifts far away from the value of a fixed body, the VIV instability finds a new balanced state from the next synchronization region, i.e., the f_N . This process is repeated over the entire measured range and as a result, a distinct sawtooth profile emerges for $d_{0.6}$ and $d_{1.2}$ plates. The results indicate that St_0 values increase with d as the mean St_0 increases from 0.14 for the $d_{0.6}$ plate to 0.175 for the $d_{1.8}$ plate. To put it in another way, a more intensive fluid-structure interaction leads to lower St_0 . For the $d_{1.8}$ plate, a tendency toward a linear, instead of a sawtooth profile, is clear, indicating that the behavior of the system approached that of a fixed plate. Generally, it is assumed that due to the increased stiffness of the $d_{1.8}$ plate, the structure was less susceptible to excitation.

4 Conclusions

The effect of various geometrical parameters on the dynamic response of VIVs of a splitter plate in water flow was experimentally investigated using PIV and LT. The studied cases included the effect of the channel convergence, aspect ratio (AR), and the trailing-edge thickness (d). The measured Reynolds number range varied approximately from 2000 to 20,000, i.e., 3–11 m/s at the trailing edge.

Within the measured Re range, majority of the cases were characterized with a VIV behavior. This was manifested as a distinct stepwise increase of both the vibration frequency (f_0) and the vortex shedding frequency (f_s). Results also indicated that the vibratory response of the system was dependent on geometrical parameters in some cases.

Firstly, in the convergent channel, the vortex shedding process was more stable. This is due to the continuous energy transfer from the accelerating mean flow. Thus, the level of synchronization increased as the excitation energy increased. However, flow acceleration was not assumed to change f_0 or A/d of the plate. Secondly, the results suggest that a modification of aspect ratio from AR to $1/4AR$ has a considerable effect on the dynamics of the system by increasing the number of excited f_N . This is assumed to be an effect of a change in the material parameters of the plate, such as stiffness and damping, whose change is known to be able to shift the f_N of a system.

Finally, the results showed that the trailing-edge thickness (d) is the dominating geometrical parameter in this study. This can be related to two facts. Firstly, d controls the scales of the wake and the vortices. This, in turn, determines f_s and affects considerably the amount of energy in the exciting vortices. d also contributes directly on the systems material parameters, such as stiffness and damping values. Plates with lower d were characterized with a continuous chain of f_N through the entire measured Re range. Opposed to that, in the highest d case, the number of excited f_N diminished considerably. With higher d cases, f_0 and A/d were lower and the fluid-structure system was less susceptible to excitation.

Generally, the behavior of f_N of a fluid-structure system is dependent on the combined effect of the system mass, stiffness, and

damping. Thus, regardless of several illustrating results, due to the complex nature of the feedback process between the fluid and the structure, exact effects of the various geometrical parameters remain somewhat veiled.

Acknowledgment

Financing from the Academy of Finland (Grant No. 104835) is gratefully acknowledged.

References

- [1] Newman, D., and Karniadakis, G. E., 1996, "Simulations of Flow Over a Flexible Cable: A Comparison of Forced and Flow-Induced Vibration," *J. Fluids Struct.*, **10**, pp. 439–453.
- [2] Evangelinos, C., and Karniadakis, G., 1999, "Dynamics and Flow Structures in the Turbulent Wake of Rigid and Flexible Cylinders Subject to Vortex-Induced Vibrations," *J. Fluid Mech.*, **400**, pp. 91–124.
- [3] Castro, I. P., and Rogers, P., 2002, "Vortex Shedding From Tapered Plates," *Exp. Fluids*, **33**, pp. 66–74.
- [4] Castro, I. P., and Watson, L., 2004, "Vortex Shedding From Tapered, Triangular Plates: Taper and Aspect Ratio Effects," *Exp. Fluids*, **37**, pp. 159–167.
- [5] Hourigan, K., Thompson, M. C., and Tan, B. T., 2001 "Self-Sustained Oscillations in Flows Around Long Blunt Bodies," *J. Fluids Struct.*, **15**, pp. 387–398.
- [6] Eloranta, H., Pärssinen, T., and Saarenrinne, P., 2005 "Fluid-Structure Interaction of a Splitter Plate in a Convergent Channel," *Exp. Fluids*, **39**, pp. 841–855.
- [7] Eloranta, H., Pärssinen, T., Saarenrinne, P., Poranen, J., and Sekki, H., 2006, "On the Fluid-Structure Interaction of a Splitter Plate: Vibration Modes and Reynolds Number Effects," *Exp. Fluids*, **41**, pp. 66–76.
- [8] So, R. M. C., Zhou, Y., and Liu, M. H., 2000, "Free Vibrations of an Elastic Cylinder in a Cross Flow and Their Effects on the Near Wake," *Exp. Fluids*, **29**, pp. 130–144.
- [9] Pärssinen, T., Eloranta, H., and Saarenrinne, P., 2007 "Experimental Investigation of Material Effects on Free Vibration of a Splitter Plate," *Exp. Fluids*, **42**, pp. 349–362.
- [10] Vandiver, J. K., Allen, D., and Li, L., 1996, "The Occurrence of Lock-in Under Highly Sheared Conditions," *J. Fluids Struct.*, **10**, pp. 555–561.
- [11] Lau, L. Y., So, R. M. C., and Leung, R. C. K., 2004, "Flow-Induced Vibration of Elastic Slender Structures in a Cylinder Wake," *J. Fluids Struct.*, **19**, pp. 1061–1083.
- [12] Luk, K. F., So, R. M. C., Leung, R. C. K., Lau, Y. L., and Kot, S. C., 2004, "Aerodynamic and Structural Resonance of an Elastic Airfoil Due to Oncoming Vortices," *AIAA J.*, **42**(5), pp. 899–907.
- [13] Blevins, R. D., 1990, *Flow-Induced Vibration*, 2nd ed., Van Nostrand Reinhold, New York.
- [14] Welch, P. D., 1967, "The Use of Fast Fourier Transform for the Estimation of Power Spectra: A Method Based on Time Averaging Over Short, Modified Periodograms," *IEEE Trans. Audio Electroacoust.*, **AU-15**, pp. 70–73.
- [15] Vikestad, K., Vandiver, J. K., and Larsen, C. M., 2000, "Added Mass and Oscillation Frequency for a Circular Cylinder Subjected to Vortex-Induced Vibrations and External Disturbance," *J. Fluids Struct.*, **14**, pp. 1071–1088.
- [16] Willden, R. H. J., and Graham, J. M. R., 2001, "Numerical Prediction of VIV on Long Flexible Circular Cylinders," *J. Fluids Struct.*, **15**, pp. 659–669.
- [17] Wang, Z. J., Zhou, Y., and So, R. M. C., 2003, "Vortex-Induced Vibration Characteristics of Two Fixed-Supported Elastic Cylinders," *ASME J. Fluids Eng.*, **125**(3), pp. 551–560.

Modeling of Cavitation Bubble Dynamics in Multicomponent Mixtures

Si Huang

College of Industrial Equipment and Control
Engineering,
South China University of Technology,
Guangzhou 510641, China

A. A. Mohamad

Department of Mechanical Engineering,
University of Calgary,
Calgary, AB, T2N 1N4, Canada

Investigation on cavitation in multicomponent (solid-liquid and liquid-liquid) mixtures has many applications in the industries and engineering. In this paper, for simulation of multicomponent mixtures, a set of equations with first-order bubble-wall Mach number is derived for a single spherical bubble in quasihomogeneous mixtures. Cavitation bubble behaviors in several kinds of liquid-liquid and solid-liquid mixtures are numerically calculated based on the current model, including the temporal variations in the bubble radius, pressure, and temperature inside the bubble. Specifically, the analysis is focused on the impact of pressure and temperature, while the bubble collapses in the mixtures. The computed results are compared with the previously reported experimental ones to demonstrate the validity of the current model and the numerical procedures.
[DOI: 10.1115/1.3077138]

Keywords: modeling, cavitation bubble dynamics, multicomponent mixtures

1 Introduction

Cavitation bubbles in multiphase and multicomponent flows are encountered in many fields of engineering, such as chemical processes, petroleum industries, geothermal power plants, pumping system in sediment-laden rivers, and hydraulic transports of sewage and slurries. Furthermore, some researchers [1–5] have, in the recent decade, worked on sonochemistry using synthetic acoustic cavitation for chemical reactions. The media that induce cavitation bubbles in these cases are mixtures of either solid-liquid or liquid-liquid. So far a number of theoretical and experimental works have been performed [6–10] on bubble behaviors and cavitation erosion with additives in Newtonian and non-Newtonian liquids. However, there were comparatively limited publications on the modeling of cavitation bubble dynamics in liquids with the additives of different materials. Shima and Tsujino [11,12] used the power law and Powell–Eyring models, respectively, to study a single bubble behavior in polymer solutions and to show the influences of the initial bubble radius and the polymer concentration on the bubble collapse pressure. Brujan et al. [13] investigated the behavior of laser-induced cavitation bubbles in polymer solutions with different rheological properties by means of high-speed photography and compared it with the behavior of bubbles in water. Furthermore, Brujan [14] developed a bubble dynamics model in a compressible viscoelastic liquid by means of a simplified singular-perturbation method to first order in the bubble-wall Mach number. It was concluded that rheology of the liquid strongly influences the behavior of bubble including sound emission. Wojs et al. [15] presented a mathematical model for a single bubble dynamics in a viscoelastic liquid and found out that the polymer additive weakens the phenomenon of cavitation.

Unlike in a pure liquid, in which the sonic velocity is constant, the sonic velocity in multicomponent mixtures varies with the material properties and concentrations of the constituents. The analysis of a bubble in multicomponent mixtures is more complex than in a single-phase liquid. The physical properties of pure liquid are considerably different from those after adding either an

other kind of liquid or solid particles. Furthermore, the complexity of analysis increases if the individual components have phase slip velocities.

In this work, a new set of equations with first-order bubble-wall Mach number are derived for a single spherical bubble in a mixture. It is intended to clarify the bubble behavior and the impulse pressure occurring from the bubble collapse in multicomponent mixtures. The time variations in the bubble radius, pressure, and temperature inside bubble are obtained numerically by solving the bubble equations.

2 Theoretical Model

2.1 Acoustic Speed in Multicomponent Mixtures. Acoustic waves travel through a single-phase fluid with a velocity that depends on the fluid density and compressibility. In multiphase and multicomponent mixtures, the wave speed is dependent on the material properties of the multiconstituents as well as their relative concentrations. A simple phenomenological model [16], shown in Eq. (1), describes the homogeneous mixture in terms of its average density and compressibility. This model fits the available experimental data of sound speed in suspensions very well for most cases

$$c_m = \sqrt{dp/d\rho_m} = \left(\sum_{k=1}^K \rho_k \alpha_k \sum_{k=1}^K \frac{\alpha_k}{\rho_k c_k^2} \right)^{-1/2} \quad (1)$$

where c , α , and ρ are wave speed, volume fraction, and density, respectively. Subscripts k and m represent component (or phase) and mixture, respectively. K is the total number of components.

2.2 Defining Composition-Dependent Properties for Multicomponent Mixtures. Physical properties of a mixture are dependent on those in each composition. Surface tension effects can be neglected for most cases that cavitation occurs (usually $Re \gg 1$ $We \gg 1$). In current modeling, the term of surface tension is still reserved in the equation by simply using the surface tension value of the primary phase because the influence of surface tension becomes important as the bubble volume becomes very small. Viscosity of a mixture can be defined as a function of composition. For the liquid-liquid cases, the viscosity of the mixture could be determined by mass-weighted-mixing law

Contributed by the Fluids Engineering Division of ASME for publication in the JOURNAL OF FLUIDS ENGINEERING. Manuscript received September 25, 2007; final manuscript received November 16, 2008; published online February 4, 2009. Review conducted by Joseph Katz.

$$\mu_m = \sum_{k=1}^K \rho_k \mu_k \quad (2)$$

For the solid-liquid mixtures, the concentration and the size distribution of particles are important factors in the calculation of the effective viscosity. Usually granular viscosity is introduced to determine the viscosity of the suspension. The averaged viscosity would contain shear viscosity arising from particle momentum exchange due to translation and collision. The collisional and kinetic parts are added to give the solids shear viscosity

$$\mu_m = \mu_{\text{col}} + \mu_{\text{kin}} \quad (3)$$

The collisional part of the shear viscosity is modeled as [17,18]

$$\mu_{\text{col}} = \frac{4}{5} \alpha_s \rho_s d_s g_{0,ss} (1 + e_{ss}) \left(\frac{\theta_s}{\pi} \right)^{1/2} \quad (4)$$

For the kinetic viscosity, the expression introduced by Syamlal et al. [18] is commonly used

$$\mu_{\text{kin}} = \frac{\alpha_s \rho_s \sqrt{\theta_s \pi}}{6(3 - e_{ss})} \left[1 + \frac{2}{5} (1 + e_{ss}) (3e_{ss} - 1) \alpha_s g_{0,ss} \right] \quad (5)$$

where d_s is the equivalent diameter of solid particles, e_{ss} is the coefficient of restitution for particle collisions, $g_{0,ss}$ is the radial distribution function, and θ_s is the granular temperature.

2.3 Governing Equations for Multicomponent Mixtures.

The Euler–Euler approach is adopted in this study for a big volume fraction range of the dispersed phase in a multicomponent system. Among the models of the Euler–Euler approach, the mixture model is simplified for the full Eulerian multiphase model, especially when the interphase laws are unknown. The mixture model is applicable for particle-laden flows with low loading, bubbly flows, and sedimentation. In addition, the mixture model can be used to calculate non-Newtonian viscosity. The continuity equation for the mixture is

$$\frac{\partial \rho_m}{\partial t} + \nabla \cdot (\rho_m \mathbf{v}_m) = 0 \quad (6)$$

where ρ_m is the mixture density:

$$\rho_m = \sum_{k=1}^K \rho_k \alpha_k \quad (7)$$

\mathbf{v}_m is the mass-averaged velocity

$$\mathbf{v}_m = \frac{1}{\rho_m} \sum_{k=1}^K \rho_k \alpha_k \mathbf{v}_k \quad (8)$$

\mathbf{v}_k is the velocity of phase k . The momentum equation for the mixture can be obtained by summing the individual momentum equations for all phases. It can be expressed as

$$\frac{\partial}{\partial t} (\rho_m \mathbf{v}_m) + \nabla \cdot (\rho_m \mathbf{v}_m \mathbf{v}_m) = -\nabla p + \mu_m \nabla^2 \mathbf{v}_m + \nabla \cdot \left(\sum_{k=1}^K \alpha_k \rho_k \mathbf{v}_{dr,k} \mathbf{v}_{dr,k} \right) \quad (9)$$

where $\mathbf{v}_{dr,k}$ is the drift velocity for phase k

$$\mathbf{v}_{dr,k} = \mathbf{v}_k - \mathbf{v}_m \quad (10)$$

Assuming that the mixture is in quasihomogeneous conditions, the drift velocity for each phase is approximated to be zero. Such an assumption is reasonable for the cases of suspensions with low particle concentration and finely distributed particles, and for most cases of miscible liquid-liquid mixtures. Equation (9) becomes

$$\frac{\partial}{\partial t} (\rho_m \mathbf{v}_m) + \nabla \cdot (\rho_m \mathbf{v}_m \mathbf{v}_m) = -\nabla p + \mu_m \nabla^2 \mathbf{v}_m \quad (11)$$

Therefore, the equations of continuity and momentum, for multicomponent mixtures, are exhibited in Eqs. (6) and (11), respectively.

2.4 Bubble Equations in Mixtures. Some simplification is essential to derive bubble equations in mixtures. The current model focuses on single bubble dynamics, where the bubble should be much larger than the particles in the fluid medium, and the influence of gravity, bubble-bubble interaction, and bubble-particle interaction is neglected. Similar to most bubble models previously developed [19,14], viscous effect of fluids is only taken into account at the normal stress on bubble wall. With the further assumption of spherical symmetry and irrotational radial flow, Eqs. (6) and (11) can be written as

$$\frac{\partial \rho_m}{\partial t} + \frac{1}{r^2} \frac{\partial}{\partial r} (\rho_m r^2 v_m) = 0 \quad (12)$$

$$\frac{\partial v_m}{\partial t} + v_m \frac{\partial v_m}{\partial r} + \frac{1}{\rho_m} \frac{\partial p}{\partial r} = 0 \quad (13)$$

Using the definition of sound speed (Eq. (1)) and enthalpy

$$h = \int_{p_\infty}^p dp / \rho_m \quad (14)$$

and introducing a velocity potential φ so that $v_m = \partial \varphi / \partial r$, Eqs. (12) and (13) can be rewritten as

$$\frac{1}{c_m^2} \left(\frac{\partial h}{\partial t} + v_m \frac{\partial h}{\partial r} \right) + \nabla^2 \varphi = 0 \quad (15)$$

$$\frac{\partial \varphi}{\partial t} + \frac{1}{2} v_m^2 + h = 0 \quad (16)$$

The mixture at infinity is assumed to be undisturbed, and the time derivative of φ is taken to have vanished. The kinematic boundary condition at bubble wall $r=R(t)$ is

$$u|_{r=R} = U = \frac{dR}{dt} \quad (17)$$

where U is the velocity of bubble wall. And the condition on the normal stress is

$$p_B = p_g + p_v - \frac{1}{R} (2\sigma_m + 4\mu_m U) \quad (18)$$

where p_B , p_g , and p_v are the pressure at the bubble wall, the pressure inside the bubble, and the vapor pressure, respectively. For the purpose of simplification, p_g and temperature T_g can be assumed as uniform inside the bubble and determined by assuming as adiabatic, hence

$$p_g = p_0 (R_0/R)^{3\gamma} \quad (19)$$

$$T_g = T_0 (R_0/R)^{3(\gamma-1)} \quad (20)$$

where γ is the adiabatic index, and subscript 0 denotes the initial value. The values of p_0 and T_0 are obtained according to the equilibrium relationship

$$p_0 = p_\infty - p_v + \frac{2\sigma_m}{R_0} \quad (21)$$

$$T_0 = T_\infty \quad (22)$$

Equations (14)–(16) can be further manipulated; by applying the singular-perturbation methods [14,19], one can obtain the equation of bubble-wall motion in a multicomponent mixture with the first order in Mach number

$$\left(1 - \frac{U}{c_m}\right)R \frac{dU}{dt} + \frac{3}{2}\left(1 - \frac{U}{3c_m}\right)U^2 = \left(1 + \frac{U}{c_m} + \frac{R}{c_m} \frac{d}{dt}\right) \frac{p_B - p_A}{\rho} \quad (23)$$

where p_A is the ambient pressure. Specifically for the driving sound field, p_A is taken as

$$p_A = p_\infty(1 - \varepsilon \sin \omega t) \quad (24)$$

ε , f , and $\omega=2\pi f$ are the amplitude, conventional frequency, and angular frequency of the driving sound field, respectively. The initial conditions are given as

$$R|_{t=0} = R_0, \quad U|_{t=0} = 0 \quad (25)$$

Thus, Eqs. (17)–(25) are proposed as the general bubble equations for a multicomponent mixture. Apparently, the forms of bubble equations in mixtures are identical with those in water, except c_m , μ_m , ρ_m , and σ_m are replaced by c , μ , ρ , and σ , respectively.

3 Numerical Method

It is more appropriate to transform the bubble equation into dimensionless form. We can set dimensionless quantities as

$$R = R_0 R^*, \quad t = t^*/\omega, \quad U = \omega R_0 U^*, \quad p = p_0 p^* \quad (26)$$

$$p_\infty = p_0 p_\infty^*, \quad c_m = \omega R_0 c_m^*, \quad p_v = p_0 p_v^*, \quad T = T_\infty T^* \quad (26)$$

Furthermore, the following dimensionless parameters have been introduced:

$$Z = p_0/\rho_m \omega^2 R_0^2, \quad W = 2\sigma/R_0 p_0, \quad M = 4\mu_m \omega/p_0 \quad (27)$$

Then the governing equations can be written as

$$\frac{dR^*}{dt^*} = U^* \quad (28)$$

$$\frac{dU^*}{dt^*} = \frac{X_2 + (X_3 + X_4 + X_5)Z}{X_1} \quad (29)$$

$$p^* = (1/R^*)^{3\gamma}, \quad T^* = (1/R^*)^{3(\gamma-1)} \quad (30)$$

$$R^*|_{t^*=0} = 1, \quad U^*|_{t^*=0} = 0 \quad (31)$$

where

$$X_1 = 1 + \frac{ZM}{R^*(c_m^* - U^*)}, \quad X_2 = -\frac{3U^{*2}(1 - U^*/3c_m^*)}{2R^*(1 - U^*/c_m^*)}$$

$$X_3 = \frac{\varepsilon p_\infty^* \cos t^*}{c_m^* - U^*} \quad (32)$$

$$X_4 = \frac{1 + U^*/c_m^*}{R^*(1 - U^*/c_m^*)} \left(p^* - \frac{W - MU^*}{R^*} + p_v^* - p_\infty^* + \varepsilon p_\infty^* \sin t^* \right)$$

$$X_5 = \frac{dp^*/dt^* + WU^*/R^{*2} + MU^{*2}/R^{*2}}{c_m^* - U^*}$$

Fourth-order Runge–Kutta integration scheme is used to solve the set of equations (28)–(32). Usually, it needs small time step for higher amplitudes. To insure the validity of the numerical scheme and code, the predicted results are compared with Cramer and Lauterborn's results [20] in which the medium is water. The comparison indicated that both the results are in good agreement.

4 Calculation Results and Discussion

Several kinds of multicomponent mixtures including solid-liquid and liquid-liquid were calculated. The operational and initial conditions used in current computations are shown in Table 1, while the constituents and their physical properties are shown in Table 2.

Table 1 Operational and initial conditions used in computation

f (kHz)	p_∞ (N/m)	p_v (N/m)	T_∞ (K)	γ	ε	R_0 (μm)
20	9.8067	2.481	293	4/3	1.0	50, 60, 80, 100

Quartz particle ($d_s=10 \mu\text{m}$) was chosen for the solid-liquid case in calculation. The range of particle mass fraction is $x=0-20\%$. For the cases of the liquid-liquid mixtures, three kinds of nonaqueous liquids, water-acetone, water-ethanol and water-glycerol, were calculated for the range of volume fraction $\alpha=0-1$. The values, such as ε and R_0 , were chosen, the same as those by other researchers [11,12,19,20]. The calculations included the variations in the bubble radius, pressure, and temperature against time. The most interesting parameters among these results are the impact pressures and temperatures developed by the bubble while collapsing in the mixtures.

Figure 1 gives a typical example of bubble experiences ($R_0=50 \mu\text{m}$) in three different surrounding media: water, quartz-water mixture ($x=0.2$), and water-glycerol mixture ($\alpha=0.7$). The time history of the ambient pressure, bubble radius, pressure, and temperature inside the bubble are displayed in Fig. 1. It is found that the cycles of bubble oscillation in both mixtures of quartz-water and water-glycerol become longer compared with that in water. Damping effect on $R(t)$ curve in the case of water-glycerol is especially considerable due to the influence of its high viscosity.

Table 2 Physical properties for components (293 K)

Constituent	c (m/s)	ρ (g/cm^3)	$\sigma \times 10^3$ (N/m)	$\mu \times 10^3$ (Pa s)
Water	1450	0.9982	72.75	1.002
Acetone	1170	0.791	23.7	0.316
Ethanol	1207	0.786	22.75	1.20
Glycerol	1986	1.264	63.4	1491
Quartz	5400	2.73		

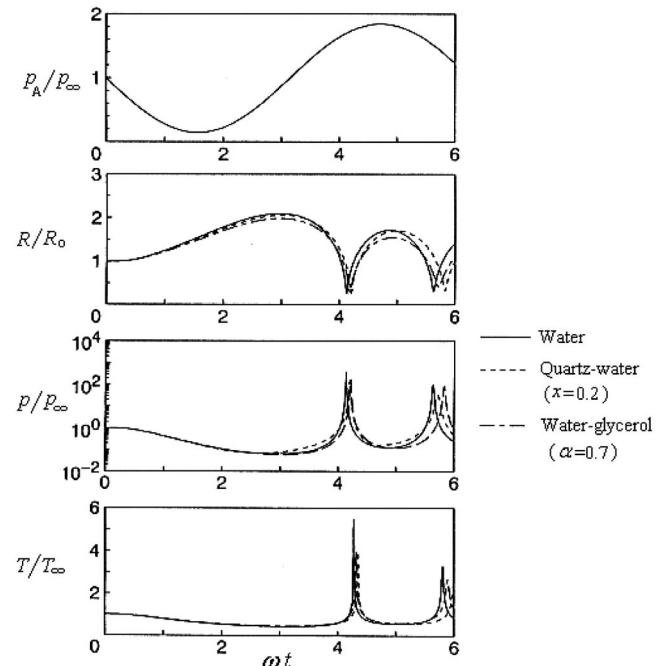


Fig. 1 Variation in bubble radius, pressure, and temperature

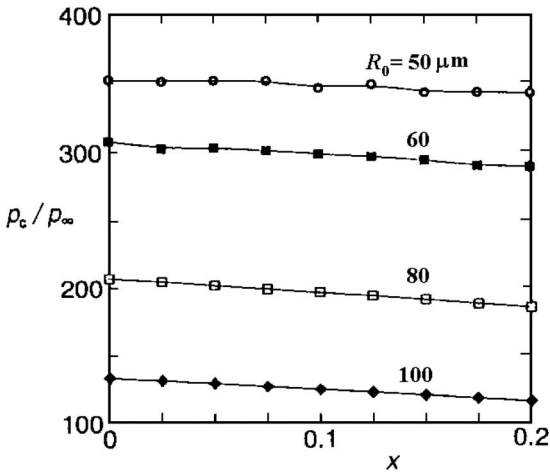


Fig. 2 Bubble collapse pressure p_c in quartz-water mixtures

On the other hand, the impact pressure and temperature, while the bubble collapses in the quartz-water mixture, have been reduced to the same order as those in the water-glycerol mixture. This result implies that the collapse in pressure and temperature may also be restrained remarkably in a liquid with an additive of solid particles.

Figure 2 shows the effect of particle mass fraction on the bubble collapse pressure p_c in quartz-water mixtures with different initial bubble radii ($R_0=50, 60, 80, 100 \mu\text{m}$). It can be seen that the bubble collapse pressure approximately undergoes a linear decrease as the particle concentration increases. The effect of glycerol content on the bubble collapse pressure in water-glycerol mixtures is shown in Fig. 3. The bubble collapse pressure also declines with the increase in glycerol volume fraction. Because the most remarkable difference in physical properties between water and glycerol is that of viscosity, the result in Fig. 3 could be regarded as the influence of liquid viscosity.

If a nondimensional pressure variable

$$\bar{p}_c = (p_c - p_{2c}) / (p_{1c} - p_{2c}) \quad (33)$$

is introduced, where p_{1c} and p_{2c} are the bubble collapse pressure in components 1 and 2, respectively; the curves of p_c in Figs. 2 and 3 are basically identical for different values of R_0 . Therefore, we can just use one of the values of R_0 in the following calculation for simplicity.

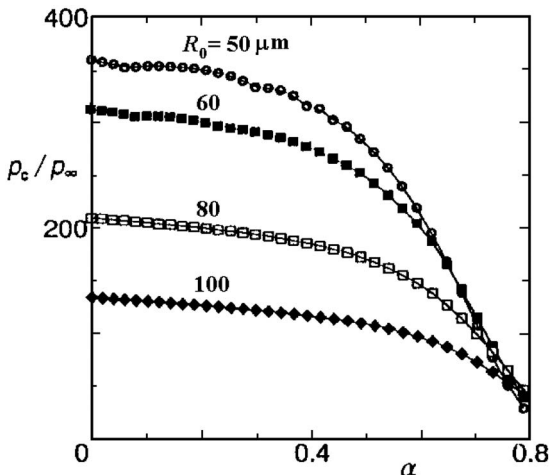


Fig. 3 Bubble collapse pressure p_c in water-glycerol mixtures

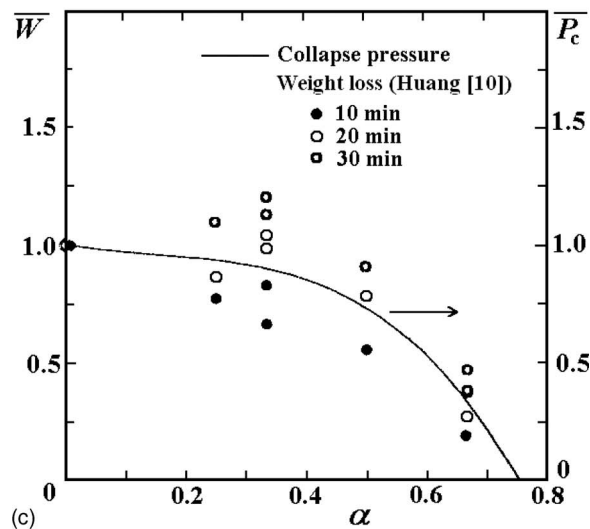
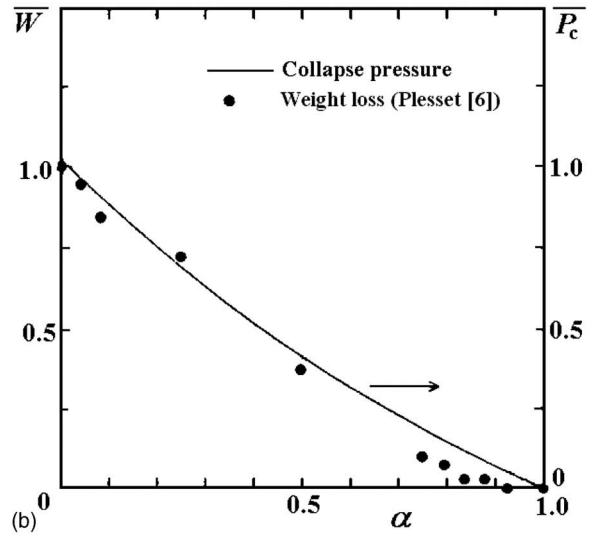
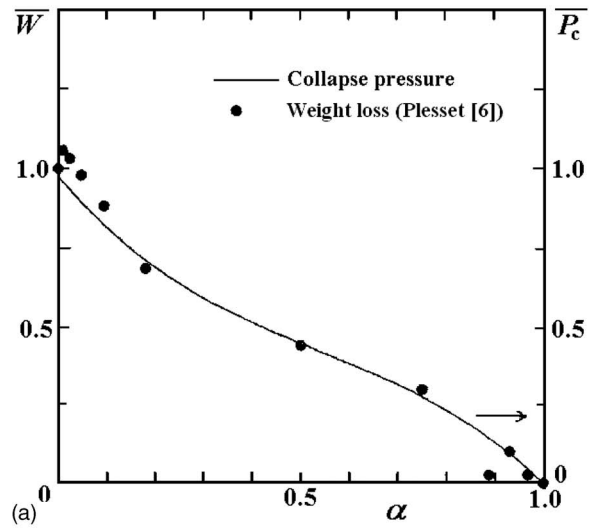


Fig. 4 Comparison of computed \bar{p}_c and measured \bar{W} in liquid-liquid mixtures: (a) water-acetone, (b) water-ethanol, and (c) water-glycerol

5 Comparison of Calculation and Measurement

It is necessary to compare the calculated results with measurement to verify the validity of the developed model. However, it is

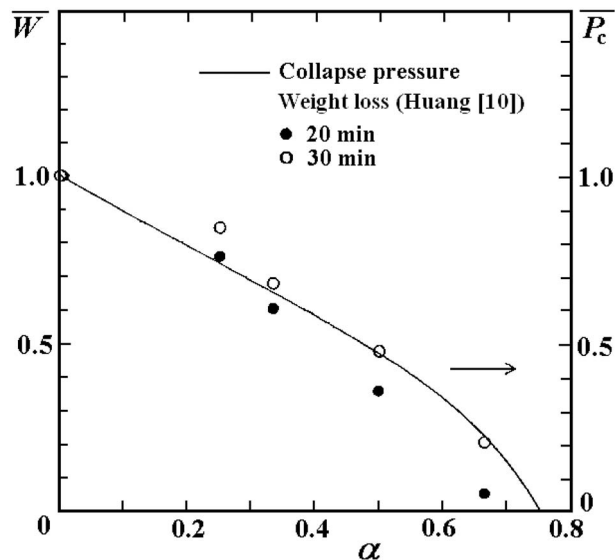


Fig. 5 Comparison of computed \bar{p}_c and measured \bar{W} in quartz-water-glycerol ($x=0.2$, $d_s=10 \mu\text{m}$)

almost impossible to find the corresponding measurement data on bubble collapse pressure and temperature in multicomponent mixtures. A simple way, as an approximation, is to consider the measurement of cavitation erosion in multicomponent mixtures, since the erosion quantity is proportional to the intensity of impact pressure while the cavitation bubble collapses.

5.1 Cavitation Damage in Liquid-Liquid Mixtures. Figure 4 shows the comparison of computed dimensionless bubble collapse pressure \bar{p}_c and dimensionless weight loss of the specimens

$$\bar{W} = (W - W_2)/(W_1 - W_2) \quad (34)$$

due to the cavitation erosion in the measurement by Plesset [6] and Huang et al. [10] for the mixtures of water-acetone, water-ethanol, and water-glycerol, where W_1 and W_2 represent the weight loss in components 1 and 2, respectively. For these measurements of cavitation erosion, copper was chosen as the test specimen. Piezoelectric drive units with a frequency of 20 kHz were employed. Test apparatus were instrumented to control the temperature of the fluid medium and the amplitude of the vibrating horn. As demonstrated in these figures, the calculated results quite agree with experimental data, although there is somewhat a scattering of measured data in Fig. 4(c).

5.2 Cavitation Damage in Solid-Liquid Mixtures. The test result in Ref. [10] indicated that the abrasion of particle in solid-liquid mixtures is greatly weakened as the viscosity of carrying liquid is increased. It is reasonable to suppose that cavitation damage is predominant in viscous mixtures. Figure 5 displays the comparison of computed dimensionless bubble collapse pressure \bar{p}_c and dimensionless weight loss \bar{W} of copper specimens in quartz-water-glycerol mixtures ($x=0.2$, $\alpha=0-0.75$, $d_s=10 \mu\text{m}$). Theoretical values show again a good agreement with the measurement qualitatively.

6 Conclusion

With the assumption that multicomponent mixtures (solid-liquid and liquid-liquid) are quasihomogeneous, a set of equations with first-order bubble-wall Mach number is suggested for a single bubble in the mixtures. A number of circumstances, arising in multicomponent fluids such as sonic speed, density, viscosity, and surface tension, could cause notable variation in bubble behaviors. The following conclusions can be summarized as follows

1. With the additives of solid particles and the increase in liquid viscosity, the time history of bubble radius tends to delay, and the impact pressure is reduced by a respective degree when the bubble collapses.
2. The computed results of bubble collapse pressures qualitatively agree well with the experimental weight loss by the vibratory cavitation erosion to demonstrate the validity of the theoretical model and computational schemes of the present study.

References

- [1] Birkin, P. R., Offin, D. G., Joseph, P. F., and Leighton, T. G., 2005, "Cavitation, Shock Waves and the Invasive Nature of Sonochemistry," *J. Phys. Chem. B*, **109**(35), pp. 16997-17005.
- [2] Gogate, P. R., and Pandit, A. B., 2005, "A Review and Assessment of Hydrodynamic Cavitation as a Technology for the Future," *Ultrason. Sonochem.*, **12**(1-2), pp. 21-27.
- [3] Suslick, K. S., and Price, G. J., 1999, "Applications of Ultrasound to Materials Chemistry," *Annu. Rev. Mater. Sci.*, **29**, pp. 295-326.
- [4] Suslick, K. S., Mdleleni, M. M., and Ries, J. T., 1997, "Chemistry Induced by Hydrodynamic Cavitation," *J. Am. Chem. Soc.*, **119**(39), pp. 9303-9304.
- [5] Thompson, L. H., and Doraiswamy, L. K., 1999, "Sonochemistry: Science and Engineering," *Ind. Eng. Chem. Res.*, **38**(4), pp. 1215-1249.
- [6] Plesset, M. S., 1970, "Cavitation Erosion in Nonaqueous Liquids," *J. Basic Eng.*, **92**(4), pp. 807-814.
- [7] Ashworth, V., and Procter, R. P. M., 1975, "Cavitation Damage in Dilute Polymer-Solutions," *Nature (London)*, **258**(5530), pp. 64-66.
- [8] Hoyt, J. W., 1976, "Effect of Polymer Additives on Jet Cavitation," *ASME J. Fluids Eng.*, **98**(1), pp. 106-112.
- [9] Shima, A., Tsujino, T., Nanjo, H., and Miura, N., 1985, "Cavitation Damage in Polymer Aqueous Solutions," *ASME J. Fluids Eng.*, **107**(1), pp. 134-138.
- [10] Huang, S., Ihara, A., Watanabe, H., and Hashimoto, H., 1996, "Effects of Solid Particle Properties on Cavitation Erosion in Solid-Water Mixtures," *ASME J. Fluids Eng.*, **118**(4), pp. 749-755.
- [11] Shima, A., and Tsujino, T., 1976, "Behavior of Bubbles in Polymer Solutions," *Chem. Eng. Sci.*, **31**(10), pp. 863-869.
- [12] Shima, A., and Tsujino, T., 1981, "Effect of Polymer Concentration on the Bubble Behavior and Impulse Pressure," *Chem. Eng. Sci.*, **36**(5), pp. 931-935.
- [13] Brujan, E. A., Ohl, C. D., Lauterborn, W., and Philipp, A., 1996, "Dynamics of Laser-Induced Cavitation Bubbles in Polymer Solutions," *Acust. Acta Acust.*, **82**(3), pp. 423-430.
- [14] Brujan, E. A., 1999, "A First-Order Model for Bubble Dynamics in a Compressible Viscoelastic Liquid," *J. Non-Newtonian Fluid Mech.*, **84**(1), pp. 83-103.
- [15] Wojs, K., Steller, R., and Redzicki, R., 2004, "Studies of the Cavitation Bubble Oscillation in a Viscoelastic Liquid," *Inzynieria Chemiczna i Procesowa*, **25**(2), pp. 455-471.
- [16] Wallis, G. B., 1969, *One-Dimensional Two-Phase Flow*, McGraw-Hill, New York.
- [17] Gidaspow, D., Bezbaruah, R., and Ding, J., 1992, "Hydrodynamics of Circulating Fluidized Beds: Kinetic Theory Approach," *Proceedings of the Seventh Engineering Foundation Conference on Fluidization*, pp. 75-82.
- [18] Syamlal, M., Rogers, W., and O'Brien, T. J., 1993, "MFIX Documentation: Theory Guide," Technical Report Nos. DOE/METC-9411004 and NTIS/DE9400087.
- [19] Prosperetti, A., and Lezzi, A., 1986, "Bubble Dynamics in a Compressible Liquid. Part 1. First-Order Theory," *J. Fluid Mech.*, **168**, pp. 457-478.
- [20] Cramer, E., and Lauterborn, W., 1981, "Dynamics and Acoustic Emission of Spherical Cavitation Bubbles in a Sound Field," *Acustica*, **49**(3), pp. 226-238.

Parameters for Assessing Oil Reservoir Water Flooding Additives

Nico Reuvers

Michael Golombok¹

e-mail: m.golombok@tue.nl

Department of Mechanical Engineering,
Technische Universiteit Eindhoven,
P.O. Box 513,
5600 MB Eindhoven, The Netherlands

This paper is concerned with deriving parameters for assessing the effectiveness of fluid additives to improve water flooding during enhanced oil recovery. We focus particularly on the use of rheological modifiers, which do not show monotonic behavior with the shear rate within the rock pores. We derive figures of merit based on (1) relative retardation in high and low permeability rock, (2) profile flattening, and (3) injectivity index. Only the last of these provides a measure of water flood profile improvement while maintaining sufficient fluid flow and production levels. [DOI: 10.1115/1.3077142]

1 Introduction

Displacement of oil by water is the major method for enhancing oil recovery beyond that obtained by natural pressure drive [1,2]. Following oil reservoir driven primary production (the “gusher”), injection wells are drilled in the vicinity of the production well and water is pumped down. The pressure difference between injector and producer wells displaces water through the permeable regions of the reservoir and forces oil toward the producer (Fig. 1). This secondary water flood is by far the most effective method for recovering oil [3]. Ideally a uniform water front steadily displaces the oil, and the reservoir would be swept of oil ahead of the front (A in Fig. 1). In a real situation it is not possible to generate such uniform flat fronts because we have point sources (the injection wells) and point sinks (the producer wells). As a result the areal sweep efficiency is never 100% [4]. A major part of the effort in secondary oil recovery is physically to design injector and producer well layouts (5 spot, 7 spot, etc.), which will maximize areal sweep efficiency.

Even were it possible to have a so-called line drive, a flat frontal advance is still impossible. The following two factors inhibit the achievement of maximum areal sweep efficiency [5]:

- Nonuniform permeability of the reservoir: this leads to “channeling” and ultimately water breakthrough.
- The different viscosities of the injected and swept fluid: this leads to viscous fingering which occurs even in a medium of uniform porosity.

Both these effects—which are not always clearly differentiated—can be represented as a distortion of the idealized flat front (A) to a distorted frontal advance (B) in Fig. 1. The water cut at the producer well increases. At this point any further injected water will flow straight to the producer well. The result is that large areas of the reservoir remain “unswept” and the oil is not recovered [6]. Thus the oil recovered from a reservoir is usually in the range 15–50% with an average around 35%, i.e., most of the oil remains in situ.

A major effort over the past 25 years has been to find additives that will change the water front profile and prevent breakthrough in the permeable regions. This involves modifying the viscosity of the injection fluid. (Frequently applied are chemical surface modifiers designed to detach residual oil from the rock surfaces it is

wetting, but these so-called tertiary enhanced oil recovery methods are not discussed here [7].) These viscosity additives typically fall into two categories: time dependent setting gels and rheological materials. Time dependent setting gels consist of chemically activated systems such as polyacrylamides, which are pumped down the producer well and preferably penetrate the permeable region close to the producer [8]. The materials are then chemically activated and gelled into a highly viscous form effectively reducing the permeability of the more open regions, which they have preferentially penetrated prior to activation.

In this work we are concerned with the use of materials whose flow is modified in regions of varying permeabilities due to the variation in shear rate experienced by fluid subjected to a pressure difference. We consider the phenomenon of rheological flow improvers in permeable media. These materials show viscosity variations dependent on the flow, i.e., so-called shear thinners and shear thickeners. For water breakthrough inhibition the desired form is the latter-so-called shear thickeners. We may semiquantitatively identify regions of high permeability with high shear rate so that a shear thickener would be an ideal solution for making the water front more spatially uniform during flooding [9,10]. It is more than 25 years since the first studies of the effect of shear thickeners during enhanced oil recovery (EOR) were published [11]. These all proceeded from the assumption of monotonic shear thinners or thickeners typified by a power law response

$$\mu = K\dot{\gamma}^{n-1} \quad (1)$$

($n=1$ describes a classic Newtonian fluid of constant viscosity, if $n < 1$ then the fluid is shear thinning and for $n > 1$ it is shear thickening). However there are two major reasons why classical shear thickeners do not work, as follows:

- The region where the shear rate is highest will be in the producer bore where it is desirable that the viscosity should NOT be thickened. A classical power law shear thickener will result in flow reduction in the producer well bore
- Classical shear thickeners (in the sense of “dilatants”) are expensive to apply. They have to be used in relatively high concentrations (e.g., 25% m/m) and the cost would make use during oil recovery economically prohibitive.

The major problem thus remains the monotonically increasing behavior of viscosity with shear rate in classical shear thickeners. A typical example is shown in Fig. 2(a). Figure 2(b) by contrast shows the typical viscosity response of a new class of materials—shear induced structure (SIS) viscosity modifiers [12–14]. These are characterized by nonmonotonic behavior. Classic viscosity meter tests show that the viscosity increases to a maximum with shear rate and then decreases again. The position of the maximum

¹Also at Shell Exploration and Production, Kessler Park 1, 2288 GS Rijswijk, The Netherlands.

Contributed by the Fluids Engineering Division of ASME for publication in the JOURNAL OF FLUIDS ENGINEERING. Manuscript received May 26, 2008; final manuscript received December 22, 2008; published online February 4, 2009. Assoc. Editor: Theodore Heindel.

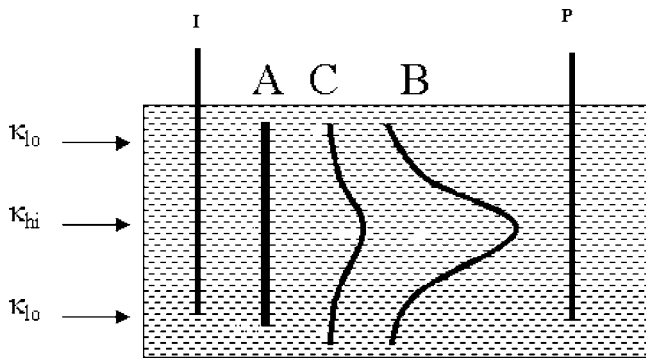
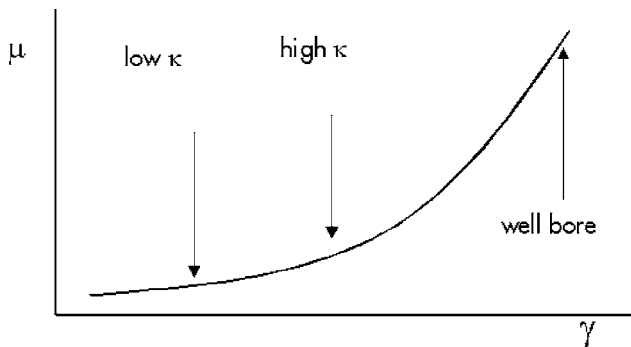


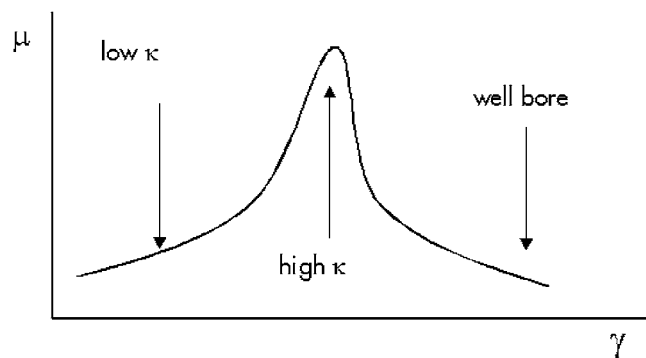
Fig. 1 Water profile between an injector (I) and producer (P) in a section of reservoir rock with schematically indicated regions of low permeability (κ_{lo}) and high permeability (κ_{hi}). Line A indicates the idealized water front advance and curve B indicates the varying profile fronts, which arise due to varying permeability. Curve C shows profile obtained after the use of additives described in the text.

as well as the width and strength of the response are defined by the absolute and relative concentrations of two components. These are typically a surfactant and a cosolute.

We have recently shown that these shear induced structure materials can selectively lead to slowing down in regions of high rock permeability while maintaining flow in the other lower per-



(a)



(b)

Fig. 2 Two responses for viscosity as a function of shear rate: (a) classic monotonic power law response for a shear thickener, and (b) response associated with shear induced structure materials

Table 1 Rocks used as experimental studies to represent extremes of permeability in an oil reservoir

	Rock type	κ (mD)	ϕ
High perm	Berea sandstone	300	20
Low perm	Fontainebleau	30	6

meability regions [9]. In Sec. 2 we summarize typical experimental results from previous studies, which demonstrate the empirical background to this study. Section 3 then compares and contrasts three parameters for applying observed results to volume recovery with an extended analysis of the physical meaning in terms of volume oil recovery from a reservoir rock during secondary flooding operations.

2 Novel Flooding Additives

The essential effect, which we wish to achieve is to retard the flow in the “nose” of profile B in Fig. 1, i.e., to slow down the flow in regions of channeling and breakthrough. Ideally then we wish to return the profile B back to something approaching A, as shown in the profile C in Fig. 1. In recent experimental studies [9] we have shown that this is achieved by applying shear induced structure materials in the form of surfactant/solute combinations previously reported in the classic Couette cell or other flow tube configurations. Our laboratory experiments use the standard method of core flow experiments where a pressure drop is applied across rock samples representing the extreme permeability ranges of the reservoir. For example, a typical oil reservoir will have a whole distribution of permeabilities from low mD ($1D = 10^{-12} \text{ m}^2$) to the order of 1D. The “range” can be represented by carrying out flow measurements on cores representative of the lower and upper range permeabilities. In this work we used (Table 1) rock cores of 30 mD and 300 mD. The reader is referred to a previously reported work [9] for the full experimental details.

Figure 3 summarizes a typical set of experimental results in two rock samples: a highly permeable Berea sandstone and a lower permeability Fontainebleau sandstone. The graph displays the pressure drop as a function of the velocity of fluid through the rock sample. For each rock sample, we show a core flow result for flow with water and with an aqueous solution containing SIS additives. The lower slope water line refers to the higher permeabil-

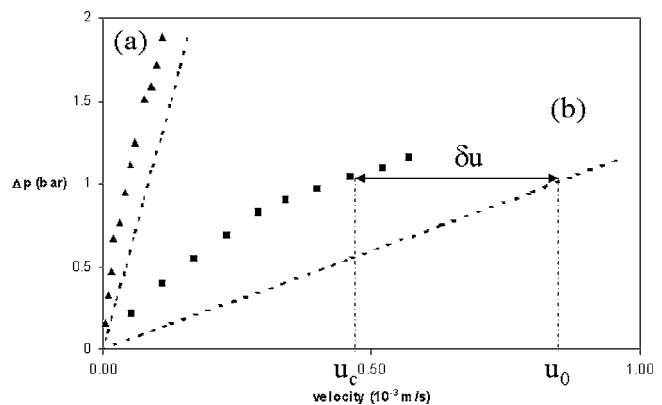


Fig. 3 Pressure drop as a function of superficial velocity for water (straight line) and a solution containing shear induced structure additives (positively deviating curve). (a) refers to a low permeability Fontainebleau sandstone and (b) to a high permeability Berea sandstone. The parameters defined in the text are indicated.

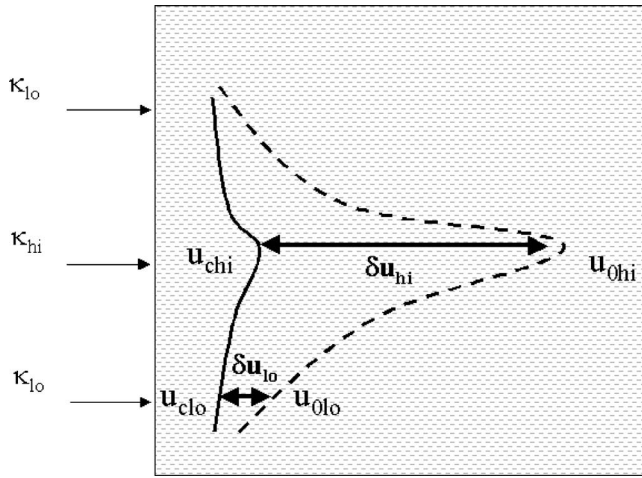


Fig. 4 Effect of shear induced structure materials on flow in regions of high and low reservoir permeabilities. Parameters defined in the text are indicated. The dotted line refers to water flow and the solid line refers to flow after addition of chemicals.

ity Berea sandstone, and the higher slope water line refers to the lower permeability Fontainebleau sample. These both follow the classical Darcy response given by

$$u = \frac{\kappa \Delta p}{\mu \Delta x} \quad (2)$$

The curved lines in Fig. 3, which positively deviate from the linear Darcy response refer to the observed pressure drop and fluid velocities when small quantities of the surfactant/cosolute combinations mentioned above were added to water at 0.1–1 mM concentrations. In our studies these have been principally cetyl trimethyl ammonium bromide (CTAB) and sodium salicylate (NaSal). These materials potentially overcome both the objections raised above in that they require only small concentrations, and the viscosity does not monotonically increase with shear rates. They can be tuned (by varying concentrations) to give a particular viscosity response at a particular range of shear rate. The observable result is that at a reference pressure drop, the SIS solution flow is retarded with respect to pure water. Most importantly, we have shown that, at a reference pressure difference, the flow is selectively retarded more in a high permeability rock than in a low permeability rock. Moreover the effect is not simply due to surface absorption because it manifests itself only at certain concentrations in the indicated range, and normal water flow is restored when pure water is again fed through the system.

The relative retardation δu is indicated in Fig. 3 at a reference pressure difference as this is relevant when considering how this effect will manifest itself in real oil field operations. In real oil fields the pressure difference between the injector and producer wells is constant. The resulting flows need to be equalized across the varying permeability rock sections by use of the novel additives. What this effectively means is that the flow in highly permeable regions is more retarded so that the profile C is obtained as shown in Fig. 1. This means that breakthrough at the production bore will also be delayed, and accordingly more oil will be swept from the reservoir during flooding. This is shown in more details in Fig. 4 where a number of parameters (defined below) are also stipulated in order to quantitatively characterize the improvement to reservoir sweep.

The problem is that there is no easy way to assess the efficiency of these additive materials based on these simple lab tests. In this study we postulate a number of different quantitative parameters or figures of merit to assess how effectively the flow improvers work. The unusual rheological response of these novel materials

means that one must be careful in how one quantifies performance and accordingly we develop new parameters as a basis for future flow improvement assessment.

3 Figures of Merit

3.1 Relative Retardation. As outlined above, the challenge is how to translate small scale experimental measurements on core samples in order to estimate how uniform the profile can be made in a real situation. We start by evaluating the relative retardation for each of the rock core samples representing the range of a typical reservoir, i.e., the high permeability Berea sandstone ($\kappa_{hi} = 300$ mD) and lower permeability Fontainebleau sandstone ($\kappa_{lo} = 30$ mD). Under the applied pressure drop we observed different relative retardations which we now quantify. Note that we do not attempt to address the microscopic issues of defining shear in a porous medium—this is the subject of other work [15]—but confine ourselves to the observables of the system, which define the profile across regions of varying flow, namely, the pressure drop and the resulting fluid velocity. If the velocity of our base fluid (water or brine) is u_0 (at a reference pressure of say 1 bar) then, when a chemical is added, this is retarded to u_c (Fig. 3). We then have a change in the velocity defined by

$$\delta u = u_0 - u_c \quad (3)$$

Of course this is not sufficient in itself to compare the flows in low and high permeability rocks because these are of different orders of magnitude. We can define such an absolute retardation for both the high and the low permeability regions in the flow (Fig. 4). The relative retardation is defined by

$$\alpha = \frac{\delta u}{u_0} \quad (4)$$

With each core sample, we obtain the corresponding velocity reduction δu_{hi} and δu_{lo} with corresponding values α_{hi} and α_{lo} . The sweep velocity for aqueous solutions containing the shear induced structure materials is greatly reduced compared with the base fluid water. Moreover this reduction is much higher in high permeability rocks than in lower permeability ones, i.e., the profile in Fig. 1 is flattened as we show in Fig. 4.

We start by showing that having more retardation in the high permeability region is not identical to flattening the profile. α should be greater for higher permeability rock rather than for lower permeability i.e., the condition $\alpha_{hi} > \alpha_{lo}$ (Fig. 4). We can define the relative change as the ratio of α in the high to the lower permeability regions, as follows:

$$\beta = \frac{\alpha_{hi}}{\alpha_{lo}} \quad (5)$$

in which case, the desired regime is that where $\beta > 1$. We have previously assumed relative retardations $\alpha > 0$ because we have been observing viscosity enhancement due to shear thickening [9]. However, in fact, negative values are possible and we have observed these. Figure 5 shows a plot of α_{hi} versus α_{lo} for various concentrations of the surfactant and cosolute. The explanation is related to the nonmonotonic behavior of the viscosity with the permeability, which we have identified. Thus the levels of shear thinning portion of the curve shown in Fig. 2(b). The reason that one of δu_{hi} or δu_{lo} may be negative is because of a viscosity reducing effect, which effectively increases the velocity under a given applied pressure compared with that of the base fluid.

We may enumerate the different effects possible and represent them as modifications to the breaking through profile represented in Fig. 1. The possible modifications (either shear thinning or thickening) in the low and high permeability zones are shown in Fig. 6. The direction of the arrows thus refers to the change in velocity δu of Eq. (3). An arrow to the left indicates retardation of

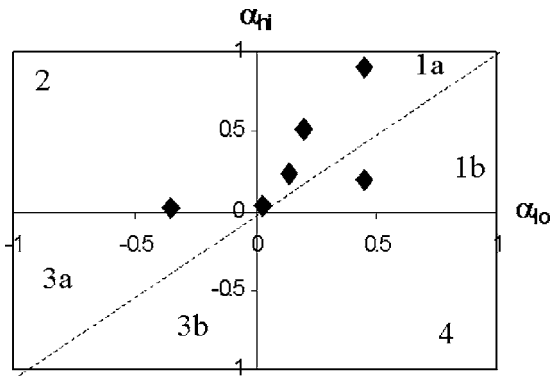


Fig. 5 Relative retardation ratios for a high permeability rock as a function of relative retardation in low permeability rock for different concentrations of shear induced structure additives in water. The four regions defined in the text for flow behavior are also indicated.

velocity due to viscosity increase, i.e., $u_c < u_0$ and thus $\delta u > 0$. An arrow to the right indicates that $u_c > u_0$, i.e., $\delta u < 0$ corresponding to viscosity decrease.

How do these viscosity changes relate to the processes of shear thinning and shear thickening? The action that occurs has its physical origin related to where the profile in Fig. 2(b) falls with respect to the base fluid viscosity and at which positions related to the rock permeability. Figure 6 shows the changes through the varying permeability profiles. When reduced to a comparison of a representative low and high permeability core experiments under identical pressure drops, we may show the changes to the high and low permeability rock velocities u_{0hi} and u_{0lo} as in Fig. 7. We can identify four cases in terms of shear thinning and shear thickening:

Case 1: $\delta u_{lo} > 0$, $\delta u_{hi} > 0$ is determined by increased viscosity compared with the base fluid (water) in both low and high permeability regions.

Case 2: $\delta u_{lo} < 0$, $\delta u_{hi} > 0$ is determined by reduced viscosity in the low permeability region and increased viscosity in the high permeability regions.

Case 3: $\delta u_{lo} < 0$, $\delta u_{hi} < 0$ is determined by reduced viscosity in both low and high permeability regions

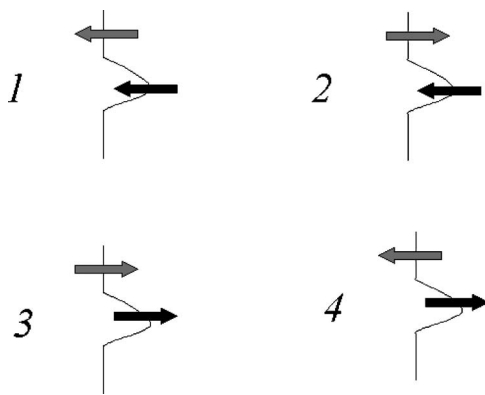


Fig. 6 Different possible effects on high and low permeability sections of flow profiles as a result of shear induced structure chemical solution. The dark and gray arrows refer to regions of high and low permeabilities, respectively. The arrow to the right indicates acceleration and the arrows to the left indicate retardation.

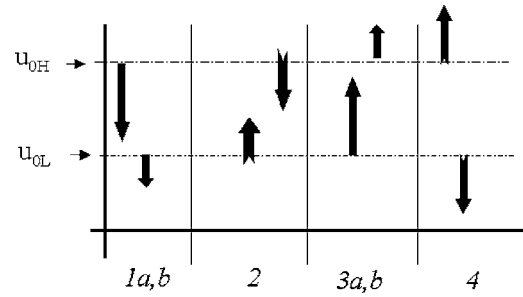


Fig. 7 The velocity decrease or increase with respect to the water velocity (u_{0H} , u_{0L}). An upwards directed arrow indicates a velocity increase with respect to the base fluid. A velocity decrease is indicated by a downward arrow.

Case 4: $\delta u_{lo} > 0$, $\delta u_{hi} < 0$ is determined by increased viscosity in the low permeability region and reduced viscosity in the high permeability region.

These cases can be classified by plotting α_{hi} versus α_{lo} as in Fig. 5. The β factor is defined in Eq. (5) and represents the slope of the line to the origin. Whereas we originally considered only cases where $\alpha_{hi} > \alpha_{lo} > 0$, it is now clear that other nonpositive values of β need to be considered. For example it can be seen that Case 4 never leads to frontal profile flattening. Similarly Case 2 always leads to some improvement. However for Cases 1 and 3, the relative magnitudes of the changes (as determined by the relative retardations) determine whether there is an improvement. Thus we can divide Case 1 into two subcases, where the relative retardation in the high permeability zone is higher than that in the low permeability zone, i.e., $\alpha_{hi} > \alpha_{lo}$ so that the profile is flattened as opposed to the converse in which case the nonuniformity is increased. The same applies to Case 3 where the desirable result is that $|\alpha_{lo}| > |\alpha_{hi}|$, i.e., the low permeability front catches up with the high permeability one. However bearing in mind that α_{hi} , $\alpha_{lo} < 0$ this results in $0 < \beta < 1$. The use of β is thus somewhat confusing as shown in Table 2 where we show that β of itself does not really correlate with profile uniformity.

The desirable cases are all above the axis $\alpha_{hi} = \alpha_{lo}$, i.e., $\beta = 1$. The physical origins of the different behaviors are a consequence of the nonmonotonic rheological behavior shown in Fig. 2(b), and we may relate each of the six cases we have identified to either shear thickening or shear thinning behavior with respect to the base fluid. An improved profile flattening quantitative criterion is now considered.

3.2 Profile Flattening. It is clear from Sec. 3.1 that our relative retardation ratio β is not a very good measurement of the effectiveness of profile flattening. This arises primarily because not only shear thickening can improve performance during a water flood, but also shear thinning, depending on the match between the rock permeability and the viscosity curve maximum in Fig. 2(b). Moreover, β does not give a quantitative measurement of the improvement to the profile flatness. For example, consider the cases identified in Table 2. There we see that, depending on whether it is shear thickening in the more permeable region or

Table 2 Identification of favorable profile changes in terms of relative retardation ratio

Case	δu_{lo} (α_{lo})	δu_{hi} (α_{hi})	β	More uniform	Less uniform
1	> 0	> 0	+	$\beta > 1$ (1a)	$\beta < 1$ (1b)
2	< 0	> 0	-	$\nabla \beta$	-
3	< 0	< 0	+	$\beta < 1$ (3a)	$\beta > 1$ (3b)
4	> 0	< 0	-	-	$\nabla \beta$

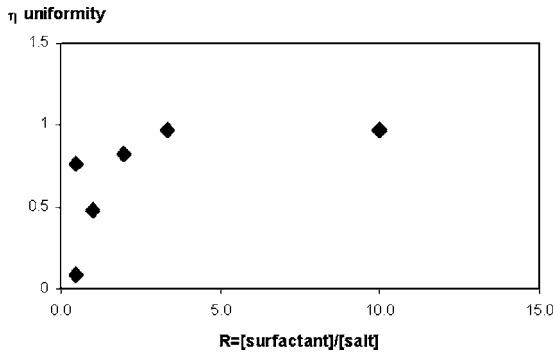


Fig. 8 Uniformity index η as a function of the ratio of the surfactant to salt concentration

shear thinning in the less permeable region, $\beta > 1$ is not necessarily the right criterion to use. Profile uniformity can be indicated by all sorts of values of β other than the positive ones first indicated. Indeed, the value of β says nothing about whether we have made the advancing front uniformly flat for the different lateral regional variations of permeability.

The actual defining condition for improved profile uniformity would be that the front velocities with additives in the high and low permeability regions are equivalent irrespective of the mechanism, i.e., $u_{\text{chi}} = u_{\text{clo}}$. We then define the difference between the two as

$$\delta u_c = u_{\text{chi}} - u_{\text{clo}} \quad (6)$$

We can influence only the velocity profile of the chemical solution. The ideal result would be a uniform profile ($u_{\text{chi}} = u_{\text{clo}}$), but by adding the chemicals we hope to make the velocity difference within the profile smaller. By comparing the velocity difference in the profile *after* the chemicals are added with the situation *before*, we obtain the following quantitative measurement for the improvement of profile “flatness:”

$$\eta = \frac{\delta u_c}{\delta u_0} = \frac{u_{\text{chi}} - u_{\text{clo}}}{u_{0\text{hi}} - u_{0\text{lo}}} \quad (7)$$

In case of a uniform profile ($u_{\text{chi}} = u_{\text{clo}}$) $\eta = 0$. When $0 < \eta < 1$, the velocity difference in the chemical profile is smaller than in the initial water profile ($\delta u_c < \delta u_0$). The shape of the velocity profile is exactly the same (unaltered) as for water, when $\eta = 1$. A smaller velocity difference has a more uniform profile. If, for example, $\eta = 0.5$, the velocity difference is only half as big as it was for water. A η larger than 1 indicates a larger velocity difference ($\delta u_c > \delta u_0$) in the chemical profile, i.e., the nonuniformity has increased.

The velocity for water in the high permeable layer ($u_{0\text{hi}}$) is, according to definition, larger than the velocity in the low permeable layer ($u_{0\text{lo}}$). Negative values of η are caused by $u_{\text{clo}} > u_{\text{chi}}$. The chemical solution then has the largest velocity in the low permeable layer. The velocity difference between the high permeable and the low permeable layer is a measure for the shape of the profile. By comparing this velocity difference before and after the chemicals are added, a measure for flattening effectiveness is found. In contrast to the β ratio, the η ratio gives a direct measure for the profile flatness and the improvement with respect to water.

Using the β factor defined above, we have previously been unable to find any correlation in permeable flow with concentration based on the relative retardation [9]. Other studies in Couette cells had indicated that the ratio of dilatant to salt concentration $R = [\text{dilatant}]/[\text{salt}]$ was an important factor [12–14]. Figure 8 shows a plot of η as a function of this ratio R . The best performance is obtained when this ratio is kept small as this appears to give the most uniform profile, and this is best achieved by using a

low dilatant concentration and a higher salt concentration. However clearly η is not a good measure for similar reasons as explained for β and demonstrated in Table 2, i.e., one obtains enhanced uniformity for $0 < \eta < 1$ but reduced uniformity if $\eta > 1$ or $\eta < 0$. This leads us to another parameter, which we now discuss.

3.3 Injectivity Index. Neither β nor η provide information about the velocity of the chemical solution through the reservoir, i.e., the sweep velocity. They merely indicate how uniform the profile is. The problem with this is that a (more) uniform velocity profile can be created by a very high retardation, which would lead to very low production rates. This leads to the conclusion that two separate parameters for shape and sweep velocity are needed. So far we used only the (Darcy) apparent fluid velocity. The real velocity inside the pores of a rock is determined by the part of the rock that is accessible to flow. The porosity (ϕ) should be taken into account, as follows:

$$v = \frac{u}{\phi} \quad (8)$$

In Eq. (8), u is the superficial fluid (Darcy) velocity, and v is the real (sweep) velocity.

To find separate figures of merit for both sweep velocity and uniformity we use the injectivity defined by the ratio of flow (or equivalently velocity) to pressure drop $u/\Delta p$. When the ratio is computed against a reference value, we obtain an injectivity index:

$$I = \frac{u_2/\Delta p_2}{u_1/\Delta p_1} \quad (9)$$

All our experiments are conducted at the same constant pressure drop, so Eq. (9) reduces to

$$I = \frac{u_2}{u_1} \quad (10)$$

For our purposes (ranking performance with respect to shape or velocity), the subscripts 1 and 2 refer to different solutions or different permeability zones. For evaluation of performance we assume again that the profile is uniform when the velocity in the high permeability zone is equal to the velocity in the low permeability zone. Expressed in real velocities, this equality would be $v_{\text{chi}} = v_{\text{clo}}$. The base fluid nonuniformity between low and high permeabilities is not now measured by a difference as in Sec. 3.2 but by a ratio $v_{0\text{lo}}/v_{0\text{hi}}$. With the addition of the rheology modifying chemicals, it changes to

$$I_1 = \frac{v_{\text{clo}}}{v_{\text{chi}}} \quad (11)$$

When the profile is uniform, according to our definition, this index is equal to 1. A value between 0 and 1 describes how much the velocities differ from each other.

If ϕ_H and ϕ_L are the porosity in the high and in the low permeable layers, respectively, then we obtain

$$I_1 = \frac{u_{\text{clo}} \phi_{\text{hi}}}{u_{\text{chi}} \phi_{\text{lo}}} \quad (12)$$

The chemicals have the biggest impact on the velocity in the high permeable layer because of the higher shear rates. Especially the high permeable layer needs to be included into the performance index for sweep velocity. The superficial velocity difference with water in the high permeable layer can be put into a second performance index, as follows:

$$I_2 = \frac{u_{\text{chi}}}{u_{0\text{hi}}} \quad (13)$$

This second index ensures that the sweep rates are not reduced too much with respect to the base fluids. (It does not really make any difference here whether Darcy or pore velocity is used because the

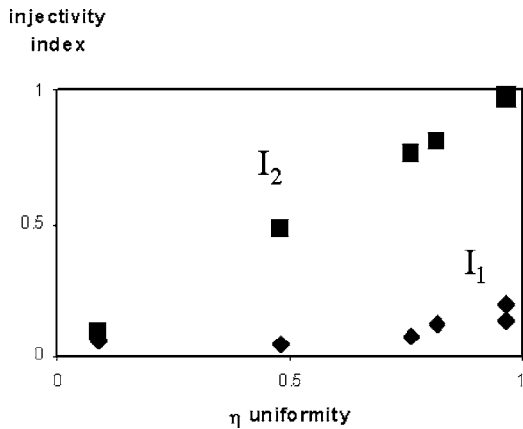


Fig. 9 Relationship between relative injectivity indices (defined in text) and the profile uniformity parameter

ratio of both are the same in Eq. (13).) It is ideally equal to 1 and the reservoir is swept at economic rates. When this index for sweep velocity is approximately equal to zero, then the velocity for the chemical solution is also approximately zero, which would lead to a stop of the oil production. There will be an optimum profile flattening while maintaining flow and there should be a balance between the shape of the profile and the sweep velocity, or between I_1 and I_2 . Since both indices should be as close to unity as possible, then by combining the two we obtain

$$\frac{u_{clo}}{u_{0hi}} = \frac{\phi_{lo}}{\phi_{hi}} \quad (14)$$

Thus optimal performance is obtained when the superficial velocity of the SIS solution in the low permeability region, divided by base fluid velocity in the high permeability region, is matched to the relative porosities in these two regions.

Figure 9 shows that there is a good correlation between our correlated uniformity index η and the two injectivity indices. Naturally I_2 correlates very strongly because it contains the same terms and, in general, $u_{clo} \ll u_{chi}$ so that $\eta \approx I_2$. As indicated this refers to the residence time and ensures that flow is not now slowed so much that production is lost. The correlation with I_1 is somewhat weaker but clearly is better at higher values of η . This last point illustrates the superiority of the described injectivity indices over the uniformity factor η . Whereas the desired value of η should be close to zero, our ratioing method based on injectivity indices monotonically increases with performance. Figure 9 shows that we can maximize the best available pore velocity while not increasing residence time (i.e., reduced flow). The reason I_1 does not approach 1 is because it is a measure of pore rather than Darcy sweep superficial velocity. The best value of I_1 obtained was about 0.2; however this corresponds in our system to a Darcy velocity ratio of 0.67, which is an improvement over the base fluid (i.e., pure water) case.

4 Conclusion

This study was motivated by the wish to derive a parameter for laboratory core flow experiments, which can be used to estimate the efficacy of novel rheological additives to flatten the profile of a water flood during secondary oil recovery. Our original Darcy based experimental retardation is rather ambiguous and this also applies to a successive parameter directly based on profile flattening. These two parameters were both arithmetic. Consideration of normalized flow comparisons based on injectivity indices seem better suited as figures of merit. They also have a relationship to the chemical concentrations in the solutions, something which has eluded correlation in studies of permeable flow until now. Our

current studies are aimed at applying shear induced structure mixtures based on previous Couette cell studies to flow in permeable reservoir rock. The effect on performance in the higher temperature and more saline conditions of real reservoirs also needs attention plus, of course, the actual performance during two phase flow where oil is actually displaced rather than the single phase experiments described here. The parameters we have derived for profile control can then be compared with the actual volumetric sweep efficiency for recovering oil in secondary flooding conditions.

Acknowledgment

We would like to thank colleagues Dr. Ben van den Brule and Dick Ligthelm of Shell Exploration and Production for useful and illuminating discussions.

Nomenclature

- I = injectivity index ratio
- K = constant in non-Newtonian power law
- N = non-Newtonian index
- P = pressure (Pa)
- U = Darcy velocity (m/s)
- V = real (pore) velocity (m/s)
- x = axial distance (m)
- α = relative retardation
- β = relative retardation ratio
- γ = shear rate (s^{-1})
- κ = permeability (m^2)
- μ = viscosity (Pa s)
- η = profile flatness ratio
- ϕ = porosity

Subscripts

- 0 = base fluid
- c = chemicals
- hi = high permeability
- lo = low permeability

References

- [1] Dowd, W. T., 1974, *Secondary and Tertiary Oil Recovery Processes*, Interstate Oil, Oklahoma City, OK.
- [2] Schumacher, M. M., 1978, *Enhanced Oil Recovery: Secondary and Tertiary Methods*, NoyesData Corporation, Park Ridge, NJ.
- [3] Schulte, W., 2005, "Challenges and Strategy for Increased Oil Recovery," Society of Petroleum Engineers, Paper No. 2005-5351.
- [4] Craig, F., Jr., 1971, *The Reservoir Aspects of Water Flooding*, Society of Petroleum Engineers, Richardson, TX.
- [5] Ahmed, T., 2000, *Reservoir Engineering Handbook*, Gulf, Houston, TX.
- [6] Poettmann, F. H., 1974, *Secondary and Tertiary Oil Recovery Processes*, The Interstate Oil Compact Commission, Oklahoma City, OK.
- [7] Sorbie, K. D., and Phil, D., 1991, *Polymer-Improved Oil Recovery*, CRC, Boca Raton, FL.
- [8] Gulick, K. E., Holditch, S. A., and McCain, W. D., 1988, "Water-Flooding Heterogeneous Reservoirs: An Overview of Industry Experiences and Practices" Society of Petroleum Engineers, Paper No. 40044-13.
- [9] Golombok, M., Crane, C., Ineke, E., Harris, J., and Welling, M., 2008, "Novel Additives to Retard Permeable Flow," *Exp. Therm. Fluid Sci.*, **32**(8), pp. 1499–1503.
- [10] Scheidegger, A. E., 1958, *The Physics and Flow Through Porous Media*, University of Toronto Press, Toronto, Canada.
- [11] Jones, W. M., 1980, "Polymer Additives in Reservoir Flooding for Oil Recovery: Shear Thinning or Shear Thickening?" *J. Phys. D: Appl. Phys.*, **13**, pp. L87–L88.
- [12] Wang, S.-Q., Hu, Y., and Jamieson, A. M., 1994, "Formation of Nonequilibrium Micelles in Shear and Elongational Flow," *ACS Symposium Series 578 Structure and Flow in Surfactant Solutions*, ACS, Washington, DC.
- [13] Cressely, R., and Hartmann, V., 1998, "Rheological Behaviour and Shear Thickening Exhibited by Aqueous CTAB Micellar Solutions," *Eur. Phys. J. B*, **6**, pp. 57–62.
- [14] Kim, W.-J., and Yang, S.-M., 2000, "Effects of Sodium Salicylate on the Microstructure of an Aqueous Micellar Solution and Its Rheological Responses," *J. Colloid Interface Sci.*, **232**, pp. 225–234.
- [15] Reuvers, N., and Golombok, M., 2008, "Shear and Permeability in Water Flooding," *Transp. Porous Media*, doi:10.1007/s11242-008-9313-x, pp. 1–5.

Improvements of Particle Near-Wall Velocity and Erosion Predictions Using a Commercial CFD Code

Yongli Zhang¹

e-mail: yongli-zhang@utulsa.edu

Brenton S. McLaury

Siamack A. Shirazi

Department of Mechanical Engineering,
University of Tulsa,
800 South Trucker Drive,
Tulsa, OK 74104

The determination of a representative particle impacting velocity is an important component in calculating solid particle erosion inside pipe geometry. Currently, most commercial computational fluid dynamics (CFD) codes allow the user to calculate particle trajectories using a Lagrangian approach. Additionally, the CFD codes calculate particle impact velocities with the pipe walls. However, these commercial CFD codes normally use a wall function to simulate the turbulent velocity field in the near-wall region. This wall-function velocity field near the wall can affect the small particle motion in the near-wall region. Furthermore, the CFD codes assume that particles have zero volume when particle impact information is being calculated. In this investigation, particle motions that are simulated using a commercially available CFD code are examined in the near-wall region. Calculated solid particle erosion patterns are compared with experimental data to investigate the accuracy of the models that are being used to calculate particle impacting velocities. While not considered in particle tracking routines in most CFD codes, the turbulent velocity profile in the near-wall region is taken into account in this investigation, and the effect on particle impact velocity is investigated. The simulation results show that the particle impact velocity is affected significantly when near-wall velocity profile is implemented. In addition, the effects of particle size are investigated in the near-wall region of a turbulent flow in a 90 deg sharp bend. A CFD code is modified to account for particle size effects in the near-wall region before and after the particle impact. It is found from the simulations that accounting for the rebound at the particle radius helps avoid nonphysical impacts and reduces the number of impacts by more than one order-of-magnitude for small particles (25 μm) due to turbulent velocity fluctuations. For large particles (256 μm), however, nonphysical impacts are not observed in the simulations. Solid particle erosion is predicted before and after introducing these modifications, and the results are compared with experimental data. It is shown that the near-wall modification and turbulent particle interactions significantly affect the simulation results. Modifications can significantly improve the current CFD-based solid particle erosion modeling. [DOI: 10.1115/1.3077139]

Keywords: CFD, particle tracking, particle-wall interaction, erosion modeling

1 Introduction

In the oil and gas industry, erosion of production equipment caused by the impact of solid particles such as sand extracted from the well along with the produced fluid is a common occurrence. When sand particles impinge on the inner walls of piping, they can remove wall material. The process by which wall material is removed due to particle impacts is referred to as solid particle erosion. Solid particle erosion can be extremely expensive and can require components to be frequently repaired or replaced. In addition, component failure can result in expensive system shutdowns, causing loss of valuable production revenue.

The erosion process is complex and many factors, such as production flow rate, sand flow rate, fluid properties, sand properties, sand shape, sand size, equipment wall material, and geometry of the equipment can affect the severity of erosion. In order to keep

the piping system operating safely and to minimize the loss caused by solid particle erosion, an erosion prediction method accounting for these main factors is needed. With the ability of predicting solid particle erosion, one can estimate service life and predict erosion patterns and the locations in the geometry where severe erosion is likely to occur. A wide variety of erosion prediction methods has been proposed by many investigators. Since the early 1990s, CFD has been widely used for solid particle erosion prediction. McLaury [1] implemented a CFD-based generalized erosion prediction model to account for erosion resulting from both direct and random impingements and demonstrated its applicability to some two-dimensional geometries. Forder et al. [2] numerically calculated the erosion in oilfield control valves using a CFD-based method. Edwards [3] implemented a comprehensive erosion prediction procedure into a commercial CFD code called CFX. This procedure took into account general 3D geometries and applied erosion equations developed in the Erosion-Corrosion Research Center (E/CRC) at the University of Tulsa [4,5]. Applying this CFD-based erosion prediction procedure, investigators at the E/CRC predicted erosion in elbows, plug tees, sudden contractions, and sudden expansions and compared results with experimental data. Chen et al. [6] added a stochastic rebound model [7] and investigated the relative erosion severity in elbows and plug

¹Corresponding author.

Contributed by the Fluids Engineering Division of ASME for publication in the JOURNAL OF FLUIDS ENGINEERING. Manuscript received November 16, 2007; final manuscript received December 19, 2008; published online February 5, 2009. Assoc. Editor: Malcolm J. Andrews. Paper presented at the 2006 ASME Fluids Engineering Division Summer Meeting and Exhibition (FEDSM2006), Miami, FL, July 17–20, 2006.

tees. In another study, Keating and Nestic [8] applied the CFD approach to investigate the erosion-corrosion problems in U-bends. Recently, Zhang et al. [9] conducted a series of CFD-based erosion modeling. The particle tracking, erosion equation, and the entire CFD-based erosion modeling procedure are validated by comparing with extensive experimental data.

2 Description of Computation Model

Currently, most commercial CFD codes allow the user to calculate particle trajectories using a Lagrangian approach. In this work, FLUENT 6 is employed and several modifications have been made to it. Three primary steps are involved in the CFD-based erosion prediction model: flow modeling, particle tracking, and applying erosion equations. At low solid particle concentrations, the presence of the solid particles does not have a significant effect on the continuous phase so that particle tracking can be performed after flow modeling. However, for high solid particle concentration flows, the influence of phase coupling has to be considered so the flow modeling and particle tracking have to be performed simultaneously. In order to obtain a reasonable statistical distribution and to reduce scatter in erosion predictions, a large number of particles are normally required to perform the particle tracking. Each particle is tracked through the flow domain separately, and the particle-wall interaction information is then recorded and used to calculate the erosion.

The particle trajectory is determined by integrating the force balance on the particle. This force balance equates the particle inertia with the forces acting on the particle (Newton's second law). This equation can be written as

$$m_p \frac{d\mathbf{V}_p}{dt} = \Sigma \mathbf{F} \quad (1)$$

where m_p is the particle mass, and \mathbf{V}_p is the particle velocity.

The right hand side of Eq. (1) represents the total force exerted on the particle. In this work, the total force consists of the drag force, the pressure gradient force, the buoyancy force, and the added mass force. In addition, to account for the effect of the turbulence on the particle motion, a discrete random walk (DRW) model, or "eddy lifetime" model, is applied in this work, which is available in FLUENT 6 [10], to determine the fluid velocity fluctuation at the particle location.

During particle trajectory calculation, the particle-wall interaction information such as impact speed, impact angle, and impact location as well as impact intensity is stored. This information is then applied to the appropriate erosion equations, which relate the particle impact information to the corresponding erosion, to compute the erosion.

The severity of erosion highly depends on the speed and angle of the impacting particles. Many erosion equations have been proposed by investigators. In this work, the one proposed by Zhang et al. [9] is applied and takes the following form:

$$ER = C(BH)^{-0.59} F_s^n V_p^n F(\theta)$$

$$F(\theta) = 5.40\theta - 10.11\theta^2 + 10.93\theta^3 - 6.33\theta^4 + 1.42\theta^5 \quad (2)$$

where ER is the erosion ratio, defined as the amount of mass lost by the wall material due to particle impacts divided by the mass of particles impacting; BH is the Brinell hardness of the wall material; F_s is the particle shape coefficient; $F_s = 1.0$ for sharp (angular), 0.53 for semirounded, or 0.2 for fully rounded sand particles; V_p is the particle impact speed in m/s; θ is the impact angle in radians; and $n = 2.41$ and $C = 2.17 \times 10^{-7}$ are empirical constants.

Unlike particle tracking, which is built in the CFD code, the erosion equation has to be specified by the user. During the particle tracking, the erosion equation is applied for each particle impingement on the wall to calculate the corresponding erosion ratio. The erosion ratio is then stored in the computational cell where the impingement occurs.

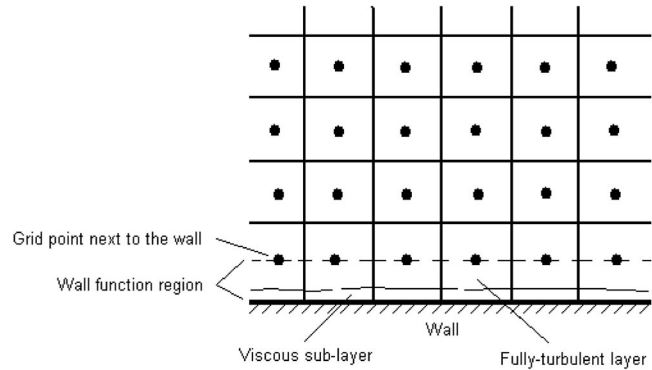


Fig. 1 Wall function region in FLUENT

Once the erosion ratio is obtained, the wall material mass loss rate can be calculated by multiplying the erosion ratio by the sand mass flow rate. Then the wall thickness loss rate (or penetration rate) can be calculated for each computational cell, provided the cell surface area and the wall material density, by assuming the mass loss is uniformly distributed over the cell surface. The penetration rate can be obtained from erosion ratio using

$$PR = ER \times \dot{m}_{sand} / \rho_{wall} / A_{cell} \quad (3)$$

where PR is penetration rate in m/s, ER is the erosion ratio defined in Eq. (2), \dot{m}_{sand} is sand mass flow rate, ρ_{wall} is density of the wall material, and A_{cell} is the area of the computational cell.

In pipe or other wall-bounded turbulent flows, the presence of walls has a significant effect on both the mean velocity field and the velocity fluctuations. In order to successfully predict solid particle erosion, an accurate representation of the flow and solid particle trajectories in the near-wall region is significant. Since flow variables have large gradients near the wall, momentum exchange occurs vigorously in this region and can have a strong effect on the impact velocities.

In order to improve the current CFD-based erosion prediction procedure, two main modifications have been implemented into FLUENT 6 in this work. The first modification is to include the standard wall-function effect when a particle is traveling in the near-wall region. The second modification is to rebound the particle at a particle radius from the wall. These two modifications are described as follows.

2.1 Including Standard Wall Function in Particle Near-Wall Tracking. In order to avoid resolving the viscosity-affected region so as to reduce the computational resource requirements, wall functions, or other near-wall models are applied in FLUENT 6 to bridge the wall and the grid points right next to the wall (Fig. 1).

Usually a particle takes several steps to move through a computational cell. At the beginning of each step, some flow variables at the particle location have to be obtained from the information stored at the involved cell center. For inner cells, this can be carried out by making use of the transport quantities and their gradients that are calculated by FLUENT and stored at each cell center (cell-center-gradient approach), as shown in Fig. 2. However, the cell-center-gradient approach cannot properly resolve the flow field in the near-wall region. In FLUENT 6, the near-wall effect is not taken into account in the particle tracking, and the particles are handled the same way as in regions far away from the wall.

Figure 3 shows the calculated u^+ values in a near-wall region of a 90 deg sharp bend with 1 in. ID. This geometry is selected because erosion data exist for this bend. The flow field is simulated using the second order Reynolds stress model (RSM) in FLUENT 6. The u^+ values are plotted along the Z direction line 1 in. upstream from the inner corner. The crosses represent the u^+ values calculated using the cell-center-gradient approach, while the

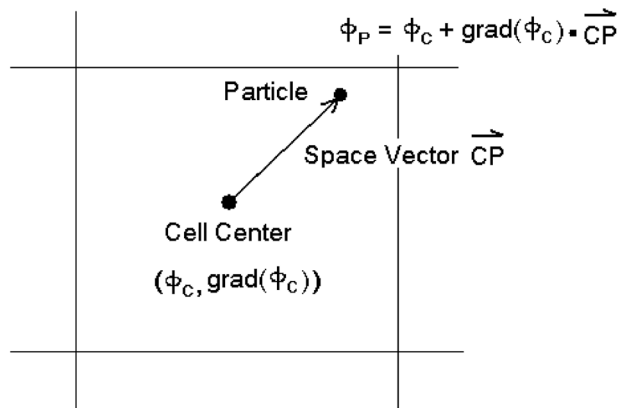


Fig. 2 Determining variables at particle location (for inner cells)

lines are obtained from the so called linear-law and log-law wall functions, respectively. In the wall-function region (namely, between the wall and the first numerical point), the cell-center-gradient approach overpredicts the flow velocity and therefore has a significant impact on the particle-wall interaction.

In order to improve the current particle trajectory calculation in this work, the standard wall functions, namely, the log-law for $y^+ > 11$ (for turbulent core) and the linear law for $y^+ \leq 11$ (for sublayer and buffer), are considered in the particle tracking in the wall-function region. The effect of this modification on particle motion and erosion prediction will be discussed.

2.2 Rebound at Particle Radius. FLUENT 6 and some other CFD codes assume particles have zero volume when deciding whether a particle hits the wall (Fig. 4, left hand). However, simulations show that rebounding the particle at a particle radius (Fig. 4, right hand) has a significant impact on particle trajectory calculation, especially for small particles ($25 \mu\text{m}$ sand in this work).

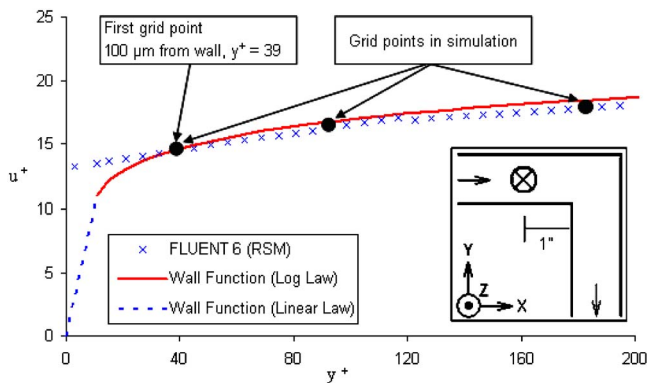


Fig. 3 u^+ comparison between calculated (CFD) and standard wall-function (linear law and log law) velocity profiles

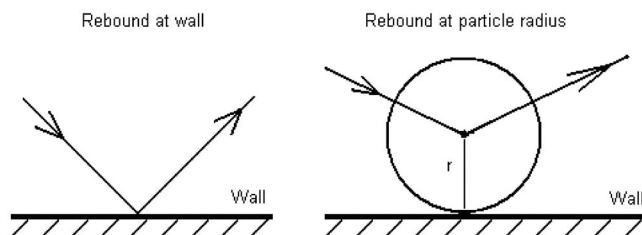


Fig. 4 Schematics of rebound at wall and rebound at particle radius

Table 1 Sharp bend erosion test conditions (from Ref. [11])

Test	Conditions
Test 1	256 μm sand, 50 ft/s, 10 flow hours
Test 2	25 μm sand, 50 ft/s, 10 flow hours
Test 3	25 μm sand, 85.8 ft/s, 2 flow hours
Test 4	256 μm sand, 85.8 ft/s, 2 flow hours

Therefore, rebound at the particle radius has also been implemented into FLUENT 6 in this work. The effect of this modification on particle trajectory calculations and erosion predictions will be discussed and the result will be compared with experimental data.

3 Experiments and Data Used for Evaluation

Erosion tests on the geometry of interest are conducted by Baker Oil Tools for four different flow conditions as listed in Table 1 [11]. These tests examined sand erosion with water as the carrier fluid. In each of the four test conditions, five 1 in. ID 90 deg sharp bends with different materials, namely, Inconel 718, nickel alloy 825, 25% Cr, nickel alloy 925, and 13% Cr L-80 are placed in a series, respectively, from upstream to downstream in the test section. Flow velocities of 50 ft/s and 85.8 ft/s are achieved based on downhole flow velocities of interest and maximum pump flow capacity. The sands chosen for testing are 256 μm rounded quartz and 25 μm sharp silica sand, to simulate production and injection flow conditions, respectively. For all four tests, the sand concentration is approximately 1% of the weight of the liquid. The running time of these tests is also listed in Table 1. In Sec. 4, the data of tests 3 and 4 are scaled to 10 flow hours.

Figure 5 shows a schematic of the test setup. Each test section consists of two identical specimens, one upstream and one downstream, joined together at the ends, which are cut 45 deg by high axial compressive force, forming a sharp 90 deg pipe elbow. The specimen diagram with wall thickness measurement locations indicated is shown in Fig. 6. The thickness of the wall at these locations is measured (before and after the test) using an ultrasonic thickness gauge with an accuracy of about 0.001 mm.

4 Results and Discussion

In order to evaluate the effect of the modifications described previously, a series of simulations are performed for a 90 deg sharp bend under conditions listed in Table 1. Figure 7 shows a schematic of the geometry and its dimensions used in the simulations. The geometry consists of overall hexahedral computational cells as illustrated in Fig. 8. FLUENT 6 and the RSM turbulence model with standard wall functions and other default parameters

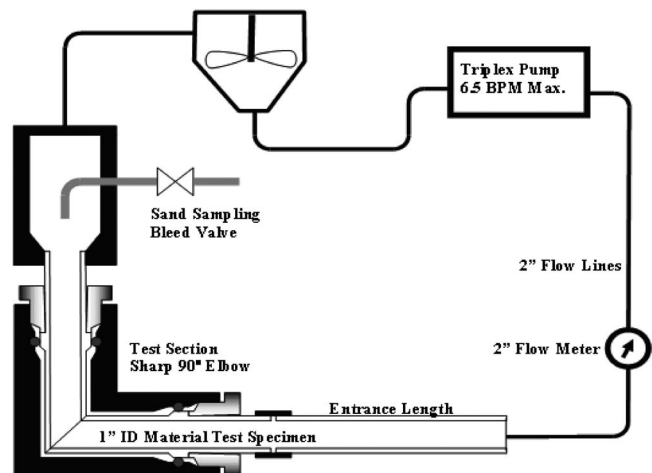


Fig. 5 Schematic of flow loop (from Ref. [11])

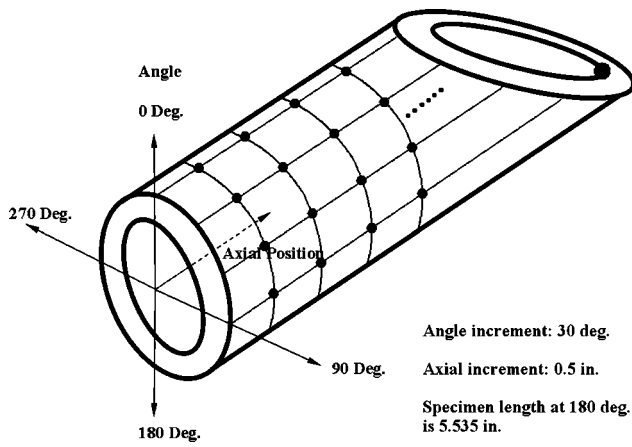


Fig. 6 Material specimen wall thickness measurement (from Ref. [11])

are applied in these simulations. A velocity inlet with 8% turbulent intensity and 1 in. turbulent length scale is specified at the inlet of the geometry. The outlet is just an “outflow” boundary. The second order upwind scheme is applied to momentum, turbulent kinetic energy, turbulent dissipation rate, and Reynolds stresses equations. The differencing scheme for pressure is also second order. Everything else uses the default in FLUENT 6. The scaled residual for continuity converges to the order of 10^{-5} and all other variables converge to about 10^{-6} or 10^{-7} . Since the standard wall functions are applied, values of y^+ of the near-wall cells are checked, and they are between 30 and 200 for most regions,

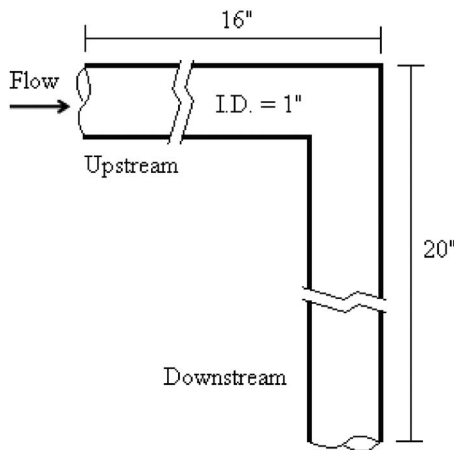


Fig. 7 90 deg sharp bend used in simulations

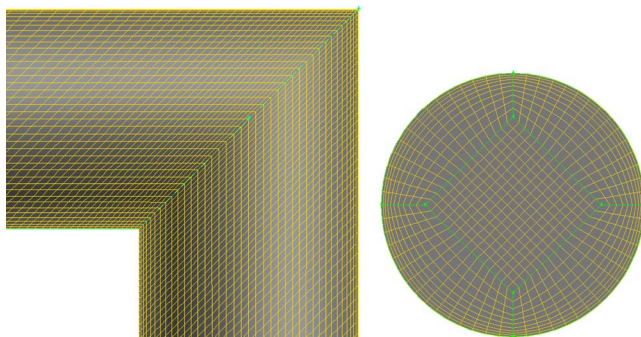


Fig. 8 Mesh around the corner and on the inlet of the 90 deg sharp bend

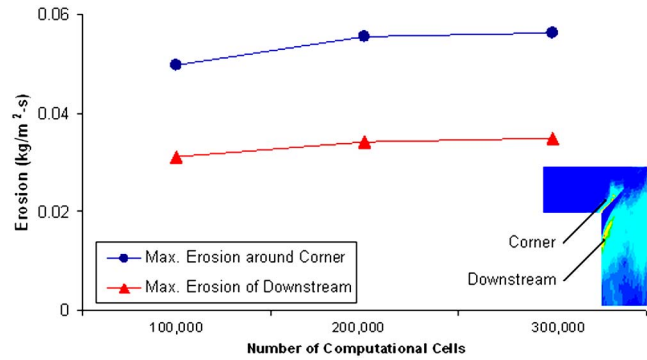


Fig. 9 Predicted erosion using different types of mesh

especially the region with the maximum erosion rate. For some regions right around the corner, y^+ is quite small, sometimes less than 10. Grid sensitivity analysis is carried out and Fig. 9 shows the results. Figure 10 shows results of the sensitivity analysis of the number of particles being simulated. It is deemed appropriate to apply 300,000 computational cells and 100,000 particles to provide erosion results independent of grids and the number of particles. For each condition listed in Table 1, simulations are run with or without applying the two modifications described previously, and the simulation results are compared with the experimental data as discussed below.

4.1 Simulation Results. Table 2 lists the ratio of maximum predicted erosion to maximum measured erosion for both upstream and downstream sections for all four cases. Ratio 1 is the ratio without applying either modification to the FLUENT 6 built-in erosion prediction procedure. Ratio 2 is the ratio after applying the rebound at particle radius. Ratio 3 is the ratio applying standard wall functions in the particle near-wall trajectory calculation. Ratio 4 is obtained after applying both modifications mentioned above.

From values of Ratio 1 in Table 2, it is seen that the FLUENT 6 built-in particle tracking and the erosion equation (Eq. (2)) predicted the erosion caused by large sand (in tests 1 and 4) very well. For small sand (in tests 2 and 3), however, the unmodified procedure overpredicts the erosion by a factor of around 17–78.

The comparison of values of ratios 1 and 4 in Table 2 indicates that applying these two modifications slightly influences the predicted erosion for tests 1 and 4 in which large sand is used. But for tests 2 and 3 where small sand is involved, these two modifications reduce the predicted erosion dramatically and bring the ratio much closer to 1.0. In addition, the predicted erosion patterns for the upstream sections of tests 2 and 3 with small sand ($25 \mu\text{m}$) agree better with the experimental data after applying these two

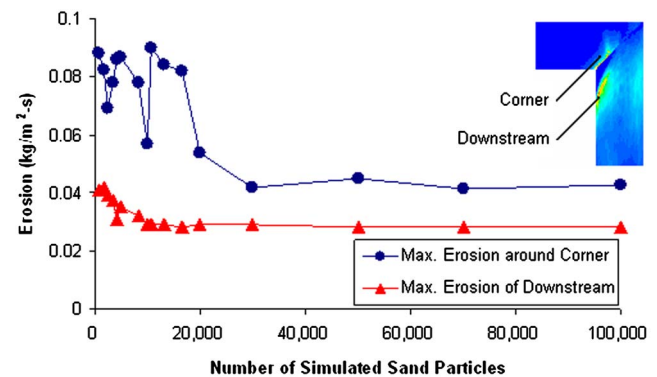


Fig. 10 Effect of the number of particles being simulated

Table 2 Ratio of maximum predicted erosion to maximum measured erosion

	Test 1 (50 ft/s, 256 μm)		Test 2 (50 ft/s, 25 μm)		Test 3 (85.8 ft/s, 25 μm)		Test 4 (85.8 ft/s, 256 μm)	
	Up	Down	Up	Down	Up	Down	Up	Down
Ratio 1	0.44	0.77	16.7	23.6	75.1	77.6	0.69	1.89
Ratio 2	0.36	0.60	1.10	1.32	4.19	6.19	0.62	1.03
Ratio 3	0.34	0.73	8.07	11.1	37.1	35.7	0.65	1.33
Ratio 4	0.33	0.63	0.59	0.94	2.48	3.67	0.63	1.05

Note: "Up" represents "Upstream" and "Down," "Downstream."
 $F_w=0.2$ for tests 1 and 4, 1.0 for tests 2 and 3 (see Eq. (2)).
 Ratio 1: No modification to the FLUENT particle tracking procedure..
 Ratio 2: Rebound at particle radius only..
 Ratio 3: Standard wall-function velocity profile only..
 Ratio 4: Both modifications.

modifications, which will be discussed in Sec. 4.2.

In order to study the detailed effect of the two modifications, the predicted erosion value is extracted for each point on the ge-

ometry surface corresponding to the measurement locations indicated in Fig. 6. Then these extracted erosion values are compared with the experimental data. In the following figures, the erosion

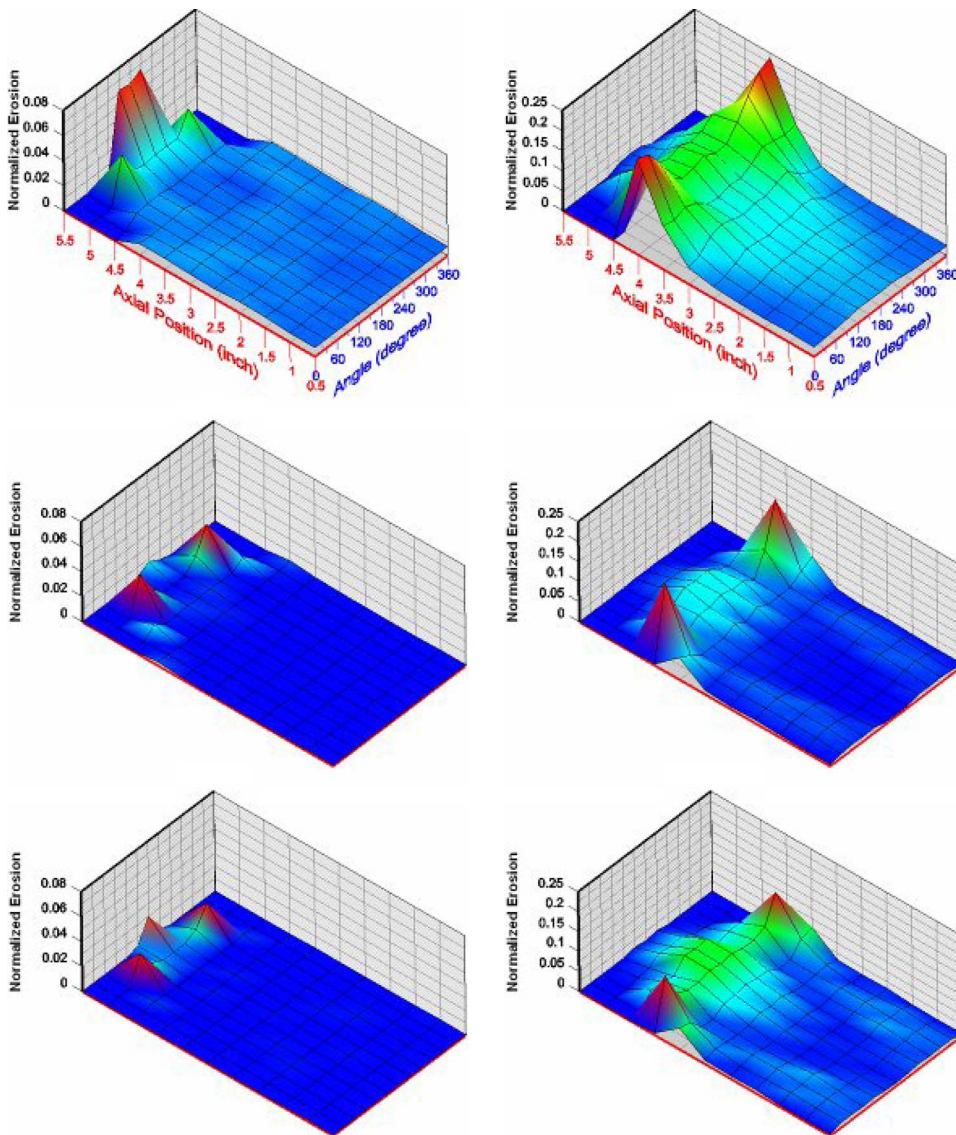


Fig. 11 Effects of the modifications on erosion pattern (test 1, 50 ft/s, 256 μm): left column: upstream; right column: downstream; first row: experimental data; second row: prediction without modifications; and third row: prediction with both modifications

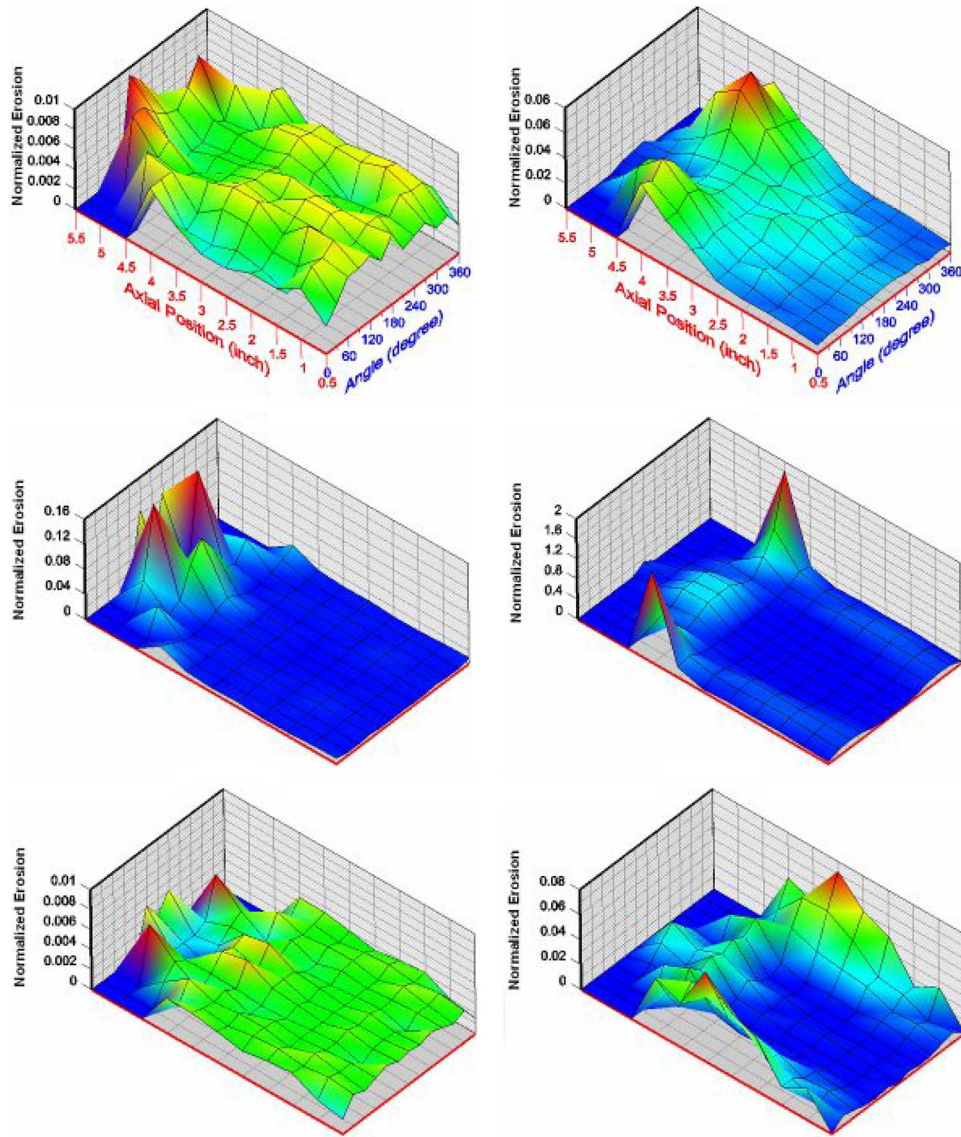


Fig. 12 Effects of the modifications on erosion pattern (test 2, 50 ft/s, 25 μm): left column: upstream; right column: downstream; first row: experimental data; second row: prediction without modifications (note the change in scale); and third row: prediction with both modifications

values are normalized with respect to the maximal measured erosion of all tests. The 3D surface plots of the normalized experimental results, erosion prediction without and with applying the modifications are displayed in Figs. 11–14 for all four cases.

4.2 Erosion Pattern. The experimental results (in Figs. 11–14) show that the maximum wall thickness loss occurs on the inner wall (between 0 and 30 deg or symmetrically opposite at 330–360 deg as indicated in Fig. 6) of the downstream specimen for all four cases. For the upstream section, the erosion patterns are slightly different for large sand (256 μm) and small sand (25 μm). Small sand causes a more uniformly distributed wall thickness loss.

Solid particle erosion has two primary mechanisms. First, if the flow is significantly redirected by the geometry, the mean component of fluid velocity toward the wall will provide momentum to the sand in the same direction so that the sand can cross streamlines and impinge on the wall. This is called direct impingement. Second, the velocity fluctuations can also impart momentum to

the sand in the direction to the wall. Therefore, impingements can happen in regions of high turbulence. Impingements caused by turbulent fluctuations are referred to as random impingements.

For this sharp bend geometry, a very strong secondary flow exists in the downstream section after the corner. Many particles are driven toward the inner wall of downstream by the secondary flow and cause heavy erosion by direct impingements. Therefore, both small (25 μm) and large (256 μm) particles cause similar erosion patterns on the downstream surface. In the upstream section, however, the erosion is mainly caused by random impingements, since there is no significant flow redirection. Smaller particles are more easily influenced by the fluid velocity fluctuations and result in a more spread-out erosion pattern on the upstream surface.

From the simulation results it is seen that the CFD model predicts the erosion pattern for the large sand very well, both with and without applying the two modifications in the particle tracking. For the small sand, however, these modifications produce

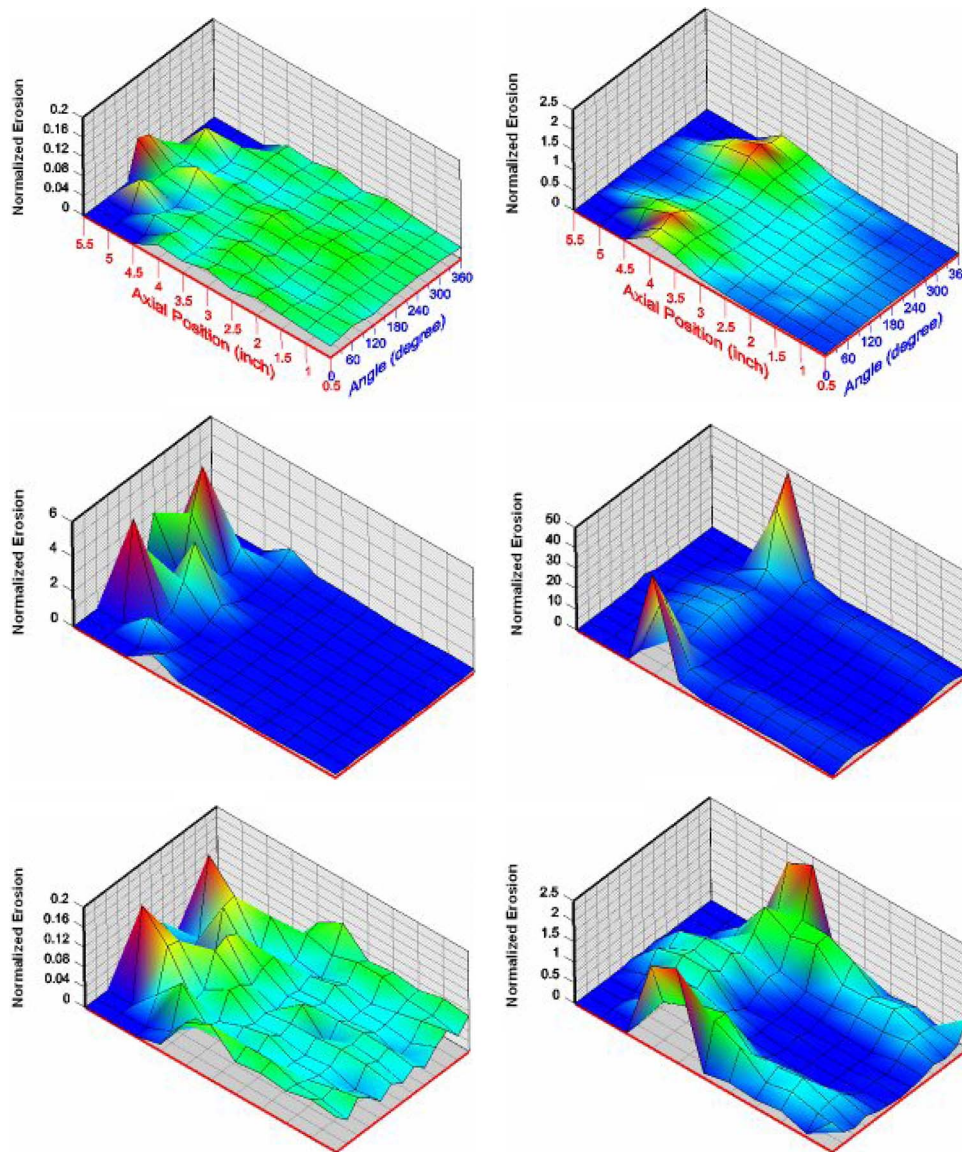


Fig. 13 Effects of the modifications on erosion pattern (test 3, 85.8 ft/s, 25 μm): left column: upstream; right column: downstream; first row: experimental data; second row: prediction without modifications (note the change in scale); and third row: prediction with both modifications

much better results than the FLUENT built-in procedure.

4.3 Effect of Velocity. It is believed that higher particle impact velocities cause more erosion. This is reflected in Eq. (2) and proved by both experimental and simulation results.

It is also found from previous figures that the erosion patterns are similar for cases with only different inlet velocities. However, it is not safe to say that velocity does not have impact on the erosion pattern since only two different velocities are examined.

4.4 Effect of Standard Wall Functions on Near-Wall Particle Tracking. The comparison between ratios 1 and 3 in Table 2 indicates that applying standard wall functions in the near-wall particle tracking reduces the erosion prediction slightly for 256 μm sand, and by a factor of about 2 for 25 μm small sand. Further analysis of particle-wall interaction information shows that the effect of applying standard wall functions in the near-wall particle tracking is to reduce the particle impact velocity therefore the erosion. This effect is stronger for small sand than for large

sand, as reflected by the reduction factors mentioned above.

The comparison between ratios 2 and 4 in Table 2 shows that, after applying rebound at a particle radius, applying standard wall functions in the near-wall particle tracking has almost no influence on the erosion prediction for 256 μm large sand. This is because in these simulations the computational cells next to the walls have a thickness of about 100 μm , which is less than the sand radius. Therefore, the 256 μm sand has not traveled into the wall-function region (between the wall and the first numerical point) before rebounded from the wall.

4.5 Effect of Rebound at Particle Radius. More detailed investigation of near-wall particle trajectories and particle-wall interaction information (impact speed, impact angle, and impact number) reveals that nonphysical trajectories and therefore non-physical impacts occur in the near-wall region for small particles. Figure 15 shows the schematic of a nonphysical trajectory and impact. V_w and V_r are the particle velocity when particle rebounds from the wall and a radius distance from the wall, respectively.

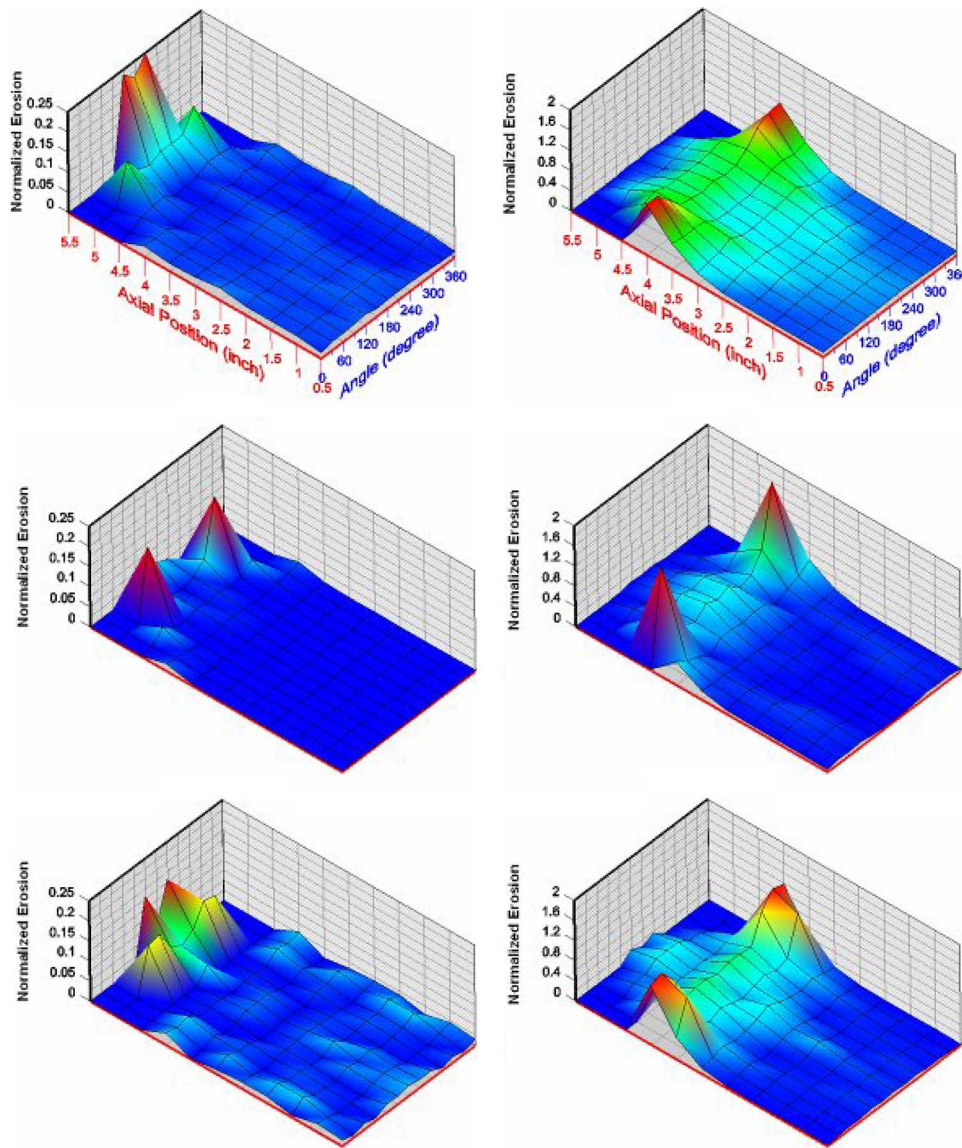


Fig. 14 Effects of the modifications on erosion pattern (test 4, 85.8 ft/s, 256 μm): left column: upstream; right column: downstream; first row: experimental data; second row: prediction without modifications; and third row: prediction with both modifications

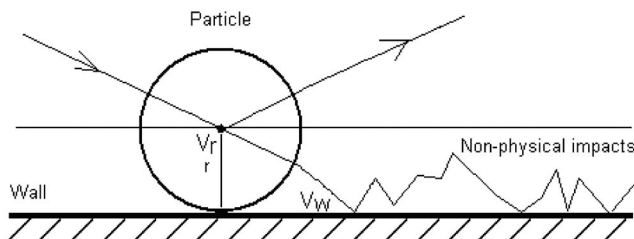


Fig. 15 Nonphysical particle trajectory near the wall

When the particle is approaching the wall, the fluid and particle velocity components normal to the wall will decrease. Therefore, it is easy for the fluid velocity fluctuation to drive particles to the wall and cause more impacts. From the simulation results, it is found that rebounding at a particle radius from the wall significantly reduces the (nonphysical) impact number and therefore the predicted erosion for small sand. However, for large sand, the

nonphysical trajectories are not observed. This is why rebounding at a particle radius does not have an important impact on erosion prediction for large sand.

5 Conclusions

Two modifications, applying standard wall functions in the near-wall particle tracking and rebounding the particle at a radius from the wall, are made to the current FLUENT 6 built-in particle trajectory calculation model. Simulations with or without applying these modifications are conducted and the results are compared with the data. The conclusions are as follows.

- (1) In this work, the initial velocity does not have significant impact on the erosion pattern.
- (2) Fine sand may cause more uniformly distributed erosion in random impingement regions than large sand does.
- (3) For 256 μm rounded sand, the FLUENT 6 built-in model predicts the erosion very well. But for 25 μm sharp sand, it overpredicts the erosion by a factor about 17–78.
- (4) Applying standard wall functions in the near-wall particle

tracking reduces the predicted erosion slightly for the large particles and by a factor about 2 for the small particles.

- (5) For 25 μm sand in the simulations, nonphysical trajectories and impingements are observed in the near-wall region. Rebound at the particle radius helps to avoid the nonphysical impingements and the corresponding erosion. For 256 μm sand, the nonphysical impingements are not observed.

References

- [1] McLaury, B. S., 1996, "Predicting Solid Particle Erosion Resulting From Turbulent Fluctuations in Oilfield Geometries," Ph.D. thesis, The University of Tulsa, Tulsa.
- [2] Forder, A., Thew, M., and Harrison, D., 1998, "Numerical Investigation of Solid Particle Erosion Experienced Within Oilfield Control Valves," *Wear*, **216**, pp. 184–193.
- [3] Edwards, J., 2000, "Development, Validation, and Application of a Three-Dimensional, CFD-Based Erosion Prediction Procedure," Ph.D. thesis, The University of Tulsa, Tulsa.
- [4] McLaury, B. S., 1993, "A Model to Predict Solid Particle Erosion in Oilfield Geometries," MS thesis, The University of Tulsa, Tulsa.
- [5] Ahlert, K., 1994, "Effects of Particle Impingement Angle and Surface Wetting on Solid Particle Erosion of AISI 1018 Steel," MS thesis, The University of Tulsa, Tulsa.
- [6] Chen, X., McLaury, B., and Shirazi, S. A., 2002, "Effect of Applying a Stochastic Rebound Model in Erosion Prediction of Elbow and Plugged Tee," *ASME FED*, **257**, pp. 247–254.
- [7] Grant, G., and Tabakoff, W., 1975, "Erosion Prediction in Turbomachinery Resulting from Environmental Solid Particles," *J. Aircr.*, **12**(5), pp. 471–478.
- [8] Keating, A., and Nestic, S., 2001, "Numerical Prediction of Erosion-Corrosion in Bends," *Corrosion (Houston)*, **57**, pp. 621–633.
- [9] Zhang, Y., Reuterfors, E. P., McLaury, B. S., Shirazi, S. A., and Rybicki, E. F., 2007, "Comparison of Computed and Measured Particle Velocities and Erosion in Water and Air Flows," *Wear*, **263**, pp. 330–338.
- [10] FLUENT, 2003, *FLUENT 6.1 User's Guide*, Fluent Inc.
- [11] Russell, R. D., Shirazi, S. A., and Macrae, J., 2004, "A New Computational Fluid Dynamics Model To Predict Flow Profiles and Erosion Rates in Downhole Completion Equipment," SPE Paper No. SPE90734.

Modeling the Onset of Gas Entrainment in a Single Downward Discharge From a Stratified Gas-Liquid Region With Liquid Crossflow

R. C. Bowden

I. G. Hassan¹

e-mail: ibrahimh@alcor.concordia.ca

Department of Mechanical and Industrial
Engineering,
Concordia University,
Montreal, QC, H3G 2W1, Canada

The critical height at the onset of gas entrainment, in a single downward oriented discharge from a stratified gas-liquid region with liquid crossflow, was modeled. The assumptions made in the development of the model reduced the problem to that of a potential flow. The discharge was modeled as a point-sink while the crossflow was said to be uniform at the main pipe inlet. The potential function was determined from a superposition of known solutions for a point-sink and uniform flow. The resulting system of three equations demonstrated that the flow field was dominated by the discharge and crossflow Froude numbers. The system was solved numerically and provided a relationship between the geometry, flow conditions, dip location, and critical height. The model predicted that the critical height increased with the discharge Froude number and decreased with the crossflow Froude number. With no imposed crossflow, the model prediction demonstrated agreement with transient and quasisteady experimental data to within $\pm 30\%$. Existing experimental correlations showed inconsistent crossflow effects on the critical height and disagreed with the model predictions at high discharge Froude numbers. [DOI: 10.1115/1.3059586]

Keywords: onset of gas entrainment, crossflow, critical height, point-sink

1 Introduction

The cooling system incorporated in a Canada Deuterium and Uranium (CANDU) nuclear reactor stores coolant in a reservoir known as a header. Coolant flows from the header to the fuel channels through a network of interconnecting pipes known as feeders. A break in the system, or a pump failure, may cause a stratified two-phase environment within the header and could result in a two-phase mixture to flow into the fuel channels. Two-phase flow may have detrimental effects on the designed cooling effectiveness and could potentially lead to a rise in reactor core temperature beyond safety limits.

Over the past three decades, loss-of-coolant accident (LOCA) research has been motivated, in part, by pressurized water reactor (PWR) safety and accident analysis codes. Codes, such as RELAP5-3D, use experimentally or analytically derived thermohydraulic models in their predictions. The horizontal stratification entrainment model is used to simulate, for example, a pressurized reservoir under stratified two-phase conditions with a bottom or side oriented discharge [1].

In 1980, Zuber [2] presented a technical report to the U.S. Nuclear Regulatory Commission regarding small break LOCA's relevant to PWR's. The report described the phenomena that resulted during a small break on the side of a large pipe containing stratified layers of gas and liquid fluid phases. With single-phase liquid initially flowing into the discharge, the onset of gas entrainment (OGE) was described by mechanisms that included either vortex induced or vortex-free gas entrainment. The critical liquid

height (H_{OGE}) at which vortex-free OGE occurred was found to be a function of the discharge flow Froude (Fr_d) number as

$$\frac{H_{\text{OGE}}}{d} = C_1(\text{Fr}_d)^{C_2} \quad (1)$$

where

$$\text{Fr}_d = \frac{4\dot{m}_L}{\pi(gd^5\rho_L(\rho_L - \rho_G))^{1/2}} \quad (2)$$

The break size of diameter (d) with the single-phase liquid discharge mass flow rate (\dot{m}_L), liquid density (ρ_L), gas density (ρ_G), and gravitational acceleration (g) was included in the definition of the Froude number. The coefficients (C_1 and C_2) were found to be $C_1=0.574$ and $C_2=0.667$ for $H_{\text{OGE}}/d < 1$ and $C_1=0.624$ and $C_2=0.4$ for $H_{\text{OGE}}/d > 1$ from transient experiments of a liquid draining through a single orifice located at the bottom of a large reservoir [3]. Similar transient experiments were also performed using a range of reservoir and discharge sizes with two stratified fluids of varying densities, viscosities, and surface tension coefficients [4,5]. The fluid combinations included air-water, kerosene-water, corn oil-water, turpentine-water, and silicone oil-water [4], as well as air and liquid ethanol [5]. Both studies confirmed the flow field as being vortex-free at the onset of two-phase flow. Notably, Lubin and Springer [4] derived their own analytical model whose final form was similar to that of Eq. (1) with coefficients $C_1=0.624$ and $C_2=0.4$.

A variety of quasisteady stratified two-phase experiments were also conducted, where the liquid height in the reservoir was controlled, with one or two discharges on a flat vertical wall [6–10] or with up to three discharges on a curved surface [11–13]. These studies reported the critical height at the onset of vortex-free gas entrainment for the various geometries and flow configurations

¹Corresponding author.

Contributed by the Fluids Engineering Division of ASME for publication in the JOURNAL OF FLUIDS ENGINEERING. Manuscript received August 1, 2007; final manuscript received November 19, 2008; published online February 5, 2009. Assoc. Editor: Malcolm J. Andrews.

(single or multiple discharges) and corroborated the functional relationship between the critical height and the discharge Froude number. Of these, the onset of gas entrainment in a single downward discharge was investigated by Hassan et al. [12] and later by Ahmad and Hassan [13] for a wide range of discharge Froude numbers. The test section in these two studies was modeled from a typical header-feeder bank in a CANDU cooling system. A similar curved-wall scaled test section was also used, in conjunction with particle image velocimetry (PIV), to investigate the liquid side flow field at the onset of gas entrainment in a single downward discharge [14]. The PIV results demonstrated a highly radial liquid velocity field, directed toward the branch center, and a very weak liquid tangential velocity, which helped to corroborate the vortex-free flow field.

Ahmed et al. [15] theoretically modeled the onset of gas entrainment in a single discharging side branch, installed on a flat vertical wall, from a smooth-stratified gas-liquid region. Each fluid phase was assumed to be incompressible, inviscid, irrotational, and quasisteady with negligible surface tension. The authors asserted that a vortex-free dip formed in the gas-liquid interface, above the discharge inlet, at the onset of gas entrainment. They applied Bernoulli's equation at a point on the undisturbed interface and at the lowest point of the dip for each fluid phase. With the assertion that the gas phase was stagnant, the difference in liquid level between the undisturbed interface and the lowest point of the dip was found to be a function of the liquid phase velocity. The liquid velocity was determined by treating the discharge as either a point-sink or a finite sized branch. The authors also used an OGE criterion, based on the work of Taylor [16], which stated that a liquid surface would become unstable if accelerated at a rate greater than that of gravity. A simplification of the point-sink approach reduced their model to the form found in Eq. (1) with $C_1=0.625$ and $C_2=0.4$, which is consistent with Lubin and Hurwitz [3]. The finite-branch model was carried out by solving Laplace's three-dimensional equation, resulting from a potential function being applied to the continuity equation, with the appropriate boundary conditions. The finite-branch model demonstrated a better ability to predict the physical limits at low discharge Froude numbers than the point-sink model. Andaleeb et al. [17] used a similar point-sink approach to model a single side or bottom oriented discharge on a curved wall. The wall effects were considered through the inclusion of the wall geometry in the determination of the total flow area surrounding the point-sink. The predicted critical height demonstrated very good agreement with Ahmad and Hassan's [13] experimental results for a single side or bottom oriented discharge on a curved wall.

The onset of vortex-free gas entrainment in a single discharge on the side or bottom of a large enclosed reservoir has been extensively investigated [3–15,17]. These configurations have demonstrated experimentally that the flow of liquid into the discharge is, to some extent, symmetrical about the discharge centerline axis. The theoretical studies also used this observation as a basis for the point-sink and finite-branch modeling approaches—both of which produce an axisymmetric flow field. In practice, however, the configuration of the system may cause the flow of liquid into the discharge to be asymmetrical. For example, if the discharge is installed at the bottom of a horizontal stratified pipe, with concurrent gas-liquid flow from one end of the pipe to the other (crossflow), the flow field could no longer be considered as symmetric about the discharge centerline axis. Experimental studies have shown that crossflow can dramatically affect the critical height at the onset of vortex-free gas entrainment [18–23].

1.1 Single and Multiple Discharges With Crossflow. Reimann and Khan [18] investigated the critical height at the onset of vortex-free gas entrainment (H_{OGE}) for a range of discharge Froude (Fr_d) numbers and correlated their results in the form of Eq. (1) yielding $C_1=0.9625$ and $C_2=0.4$. Their air-water experiments were conducted at pressures up to 0.5 MPa in a 206 mm

internal diameter horizontal pipe with a single downward discharge whose diameter ranged between 6 mm, 12 mm, and 20 mm. The crossflow mass flow rate ranged between 0.2 kg/s and 11 kg/s with liquid heights varying between 14.01 mm and 94.76 mm. It was discussed that the imposed crossflow in the pipe had negligible influence on the critical height since the single-phase liquid discharge velocity (up to 60 m/s) was much larger than the liquid inlet crossflow velocity (0.2–0.8 m/s). Their reported value of C_1 (0.9625), however, implies that an influence does exist when compared with that obtained by Lubin and Hurwitz [3] ($C_1=0.624$). Images showed that the conically shaped vortex-free gas entrainment flow structure was also shifted downstream in the crossflow direction.

Smoglie and Reimann [19] supported the vortex-free observations and further indicated that this flow structure was always present at superficial exit crossflow velocities (V_{L2}) above 0.36 m/s. They correlated their results using the K parameter, represented here as

$$K = 1.10 \left(\frac{H_{OGE}}{d} \right) Fr_d^{-0.4} \quad (3)$$

which was described as a function of exit ($\rho_L V_{L2}^2$) and discharge ($\rho_L V_{L3}^2$) momentum fluxes through the ratio R as

$$R = \frac{\rho_L V_{L2}^2}{\rho_L V_{L3}^2} \quad (4)$$

The authors reported a constant value of $K=1.17$ fitted to their experimental data, in the vortex-free flow domain, for $0.1 \times 10^{-4} \leq R \leq 40 \times 10^{-4}$. Using $K=1.17$, their correlation can be represented in the form of Eq. (1) with $C_1=1.06$ and $C_2=0.4$.

Maciaszek and Micaelli [20] later found that a value of $K=0.4$ fit their experimental data for substantially higher exit liquid velocities ($V_{L2}=3$ m/s) with a ratio of exit to discharge momentum fluxes (R) of approximately 0.1. Their test section geometry was comparable in size to that of Reimann and Khan [18] and Smoglie and Reimann [19], with main pipe diameters of 80 mm and 135 mm and discharge diameters of 12 mm and 20 mm, respectively. Their operating pressure, however, was substantially higher and ranged between 2 MPa and 7 MPa. This allowed them to achieve the higher exit liquid velocities (V_{L2}). They provided a correlation that compensated the effects of the momentum flux as

$$\frac{H_{OGE}}{d} = \left(\frac{\pi}{4} \right)^{0.4} [1 - R^{0.2}] Fr_d^{0.4} \quad (5)$$

The correlation in Eq. (5) can be represented in the form of Eq. (1), using $R=0.1$, with $C_1=0.335$ and $C_2=0.4$.

Schrock et al. [21] reported the critical height at the onset of gas entrainment in a bottom branch using both steam-water and air-water as operating fluids. The facility consisted of a 102 mm internal diameter horizontal pipe with circular branches having diameters of 4 mm, 6 mm, and 10 mm, with operating pressures up to 1.07 MPa. Their gas entrainment results did not correlate well in the form of Eq. (1) and instead were found to be best fitted by

$$Fr_d Bo^2 N_\mu^{-1/2} = 19.4 \left(\frac{H_{OGE}}{\left(\frac{\sigma}{g \Delta \rho} \right)^{1/2}} \right)^{2.2} \quad (6)$$

which shows that critical height (H_{OGE}) is related to surface tension (σ) and viscosity (μ) through the Bond (Bo) and viscosity (N_μ) numbers as

$$Bo = \frac{d(g \Delta \rho)^{1/2}}{\sigma^{1/2}} \quad (7)$$

and

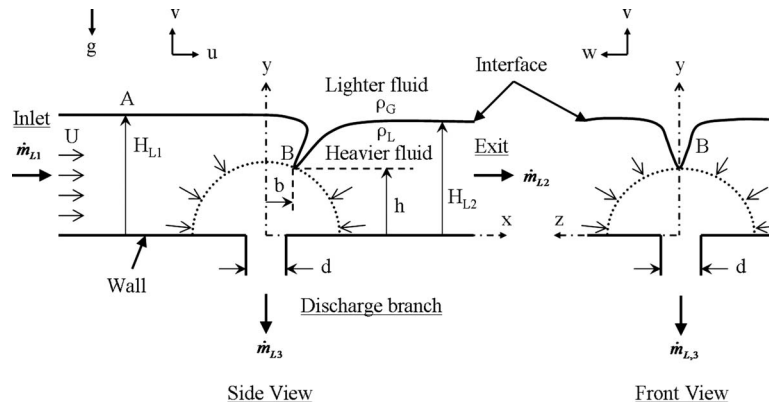


Fig. 1 Geometry and coordinate system

$$N_{\mu} = \mu \left(\frac{g \Delta \rho}{\rho_L^2 \sigma^3} \right) \quad (8)$$

Yonomoto and Tasaka [22] reported the critical height at the onset of vortex-free gas entrainment using air and water. Their test facility consisted of a 190 mm² horizontal duct with a single downward discharge whose diameter varied between 10 mm, 15 mm, and 20 mm at an operating pressure of between 0.4 MPa and 0.7 MPa. The authors provided a simplified theoretical model in the same form as Eq. (1) with $C_1=0.555$ and $C_2=0.4$. The simplified model considered the discharge to be a point-sink, and neglected the effects of viscosity, compressibility, and phase change. By comparing their analytical and experimental results, the authors were able to provide a correction factor, C , to compensate for crossflow effects as

$$C = 1.7 \exp \left[-1.0 \left(\frac{\dot{m}_{L2}}{\dot{m}_{L1}} - 1.2 \right)^8 \right] + 0.4 \frac{\dot{m}_{L2}}{\dot{m}_{L1}} + 1.4 \quad (9)$$

This correction factor is a function of the exit (\dot{m}_{L2}) and inlet (\dot{m}_{L1}) liquid mass flow rates and was used to find the corrected Froude number ($Fr_{d,corrected}$) as

$$Fr_{d,corrected} = \frac{4.35}{C} \left(\frac{H_{OGE}}{d} \right)^{2.5} \quad (10)$$

Kowalski and Krishnan [23] performed full scale experiments in a test facility that is typical of a CANDU primary cooling loop. Two horizontal headers were connected to each other by 30 feeder branches. The experiments consisted of single and two turret injection tests with two-phase mass flows ranging between 30 kg/s and 60 kg/s of water and 0.05 kg/s and 2.4 kg/s of steam. The authors observed that even a small amount of injected steam caused flow stratification within the header. Under these conditions, the injected two-phase flow impinged on the steam-water interface causing an imposed axial velocity (crossflow) within the header. Correlations for the critical height in a single discharge were presented as a function of the branch location, and for a downward discharge it was represented as

$$\frac{H_{OGE}}{d} = 0.463 (Fr_d^{0.32}) \left(\frac{\rho_L}{\Delta \rho} \right)^{0.16} \quad (11)$$

1.2 Summary and Contributions of This Study. The onset of vortex-free gas entrainment has been studied for a variety of geometries and flow conditions and these can be separated into those with and without an imposed crossflow. The correlations that compensate for crossflow effects, or include crossflow implicitly, were found to have poor agreement and even contradictory results [18–23]. The theoretical works, which did not include crossflow, showed a promising ability to predict the critical height [15,17]. The point-sink and finite-branch approaches were in

agreement at higher discharge Froude numbers ($Fr_d > 10$). At the lower Froude numbers, the point-sink approach was unable to appropriately predict the physical limits but can be considered a viable option with $Fr_d > 10$. The present study theoretically investigates crossflow effects using a point-sink approach for a single downward oriented discharge.

2 Theoretical Analysis

The geometry considered in this study is presented in Fig. 1. A single downward discharge, with a diameter d , is installed on a flat horizontal wall. The origin of the coordinate system ($x=0, y=0, z=0$) is located at the center of the discharge inlet. A semi-infinite stratified two-phase flow of heavier and lighter fluids exists above the discharge. Here the heavier fluid is considered as the liquid (L) phase, with density ρ_L , and the lighter fluid as the gas (G) phase, with density ρ_G . The heavier fluid initially flows through the discharge with a mass flow rate of \dot{m}_{L3} . The bulk flow, which passes parallel to the flat wall, called here the crossflow, enters with a mass flow rate of \dot{m}_{L1} and exits downstream at \dot{m}_{L2} . The two phases extend toward infinity in the x and z directions and are bounded at $y=0$ by the solid wall. The heavier fluid flows with a uniform velocity U from $x=-\infty$ in the *positive-x* direction. The lighter fluid phase is considered stagnant.

The flow field is considered quasisteady, incompressible, inviscid, and irrotational, with negligible surface tension. These assumptions reduce the problem to a potential flow, which is governed by forces of inertia and gravity. The 3D continuity equation in Cartesian coordinates (x, y, z) with velocity, $\mathbf{V} = u\mathbf{i} + v\mathbf{j} + w\mathbf{k}$ is

$$\frac{\partial u}{\partial x} + \frac{\partial v}{\partial y} + \frac{\partial w}{\partial z} = 0 \quad (12)$$

The irrotationality condition can be satisfied through definition of a potential function (Φ), which is related to the velocity through $\mathbf{V} = \nabla \Phi$, and produces Laplace's differential equation as

$$\frac{\partial^2 \Phi}{\partial x^2} + \frac{\partial^2 \Phi}{\partial y^2} + \frac{\partial^2 \Phi}{\partial z^2} = 0 \quad (13)$$

which is an elliptic-type linear homogeneous partial differential equation. A linear combination of two solutions, say, Φ_1 and Φ_2 , is also a solution, which means

$$\Phi = \Phi_1 + \Phi_2 \quad (14)$$

By treating the discharge as a point-sink and the crossflow as a uniform velocity, with known potential functions, the linearity theorem presented in Eq. (14) can be used directly. The superposition of known potential functions for a point-sink in uniform flow, following Schetz and Fuhs [24], results in the three-dimensional flow field being represented by

$$\Phi = Ux + \frac{M}{\sqrt{x^2 + y^2 + z^2}} \quad (15)$$

where the uniform velocity is U and the sink strength, M , is defined for a half-sink due to the intersection with the flat wall as

$$M = \frac{\dot{m}_{L3}}{2\pi\rho_L} \quad (16)$$

2.1 Onset of Gas Entrainment. With single-phase liquid flow through the discharge, and the inlet liquid height (H_{L1}) well above the discharge inlet, the two-phase interface is flat. As H_{L1} is reduced, a vortex-free dip begins to form in the interface, as shown in Fig. 1. The dip is located at point B with coordinates $(b, h, 0)$. A small reduction in H_{L1} causes the dip to suddenly extend into the discharge inlet resulting in both fluid phases flowing into the branch. This sudden collapse of the interface is termed the onset of gas entrainment and it occurs at a critical value of H_{L1} called H_{OGE} . The sudden collapse of the interface is a result of the liquid acceleration at point B exceeding that of gravity [15]. The liquid momentum ($1 > \dot{m}_{L2}/\dot{m}_{L1} > 0$) causes the dip to shift downstream a distance $x=b$. The basis of the dip shift is found in experimental images of the phenomena that clearly indicate its existence, although not explicitly discussed in their studies [18,19]. The dip shift will be considered in the development of the present model.

2.1.1 Equilibrium at the Interface. The potential flow field allows Bernoulli's equation to be applied along the gas-liquid interface between two convenient points, A and B . On the liquid side, it can be written using the difference in pressure (P) between points A and B , ($P_A - P_B$), as

$$P_A - P_B = \frac{\rho_L(V_B^2 - V_A^2)}{2} + \rho_L g(y_B - y_A) \quad (17)$$

Similarly, on the lighter fluid phase side, which is stagnant, the pressure difference can be expressed as

$$P_A - P_B = \rho_G g(y_B - y_A) \quad (18)$$

Combining the right-hand sides of Eqs. (17) and (18) results in

$$V_A^2 - V_B^2 = \frac{2\Delta\rho}{\rho_L} g(y_B - y_A) \quad (19)$$

where $\Delta\rho = \rho_L - \rho_G$. The liquid velocity at point B is defined as

$$V_B^2 = u_B^2 + v_B^2 + w_B^2 \quad (20)$$

and is found using the potential function definition ($\mathbf{V} = \nabla\Phi$) as

$$u_B = \left. \frac{\partial\Phi}{\partial x} \right|_{x=b, y=h, z=0} = U - \frac{Mb}{(b^2 + h^2)^{3/2}} \quad (21)$$

$$v_B = \left. \frac{\partial\Phi}{\partial y} \right|_{x=b, y=h, z=0} = -\frac{Mh}{(b^2 + h^2)^{3/2}} \quad (22)$$

$$w_B = \left. \frac{\partial\Phi}{\partial z} \right|_{x=b, y=h, z=0} = 0 \quad (23)$$

Considering that $V_A = U$, $y_A = H_{OGE}$, and $y_B = h$, substituting Eqs. (20)–(23) into Eq. (19), using the discharge strength definition in Eq. (16), and nondimensionalizing using the discharge branch diameter d , results in

$$\frac{H_{OGE}}{d} = \frac{h}{d} + \frac{\text{Fr}_d^2}{128} \left(\frac{d^4}{(b^2 + h^2)^2} \right) - \frac{\text{Fr}_d \text{Fr}_U}{8} \left(\frac{bd^2}{(b^2 + h^2)^{3/2}} \right) \quad (24)$$

Using the same definition as in Eq. (2) to define the discharge Froude number Fr_d , with $\dot{m}_L = \dot{m}_{L3}$, and introducing the crossflow Froude number (Fr_U) defined as

$$\text{Fr}_U = \frac{U}{\sqrt{gd}} \left(\frac{\rho_L}{\Delta\rho} \right)^{1/2} \quad (25)$$

The resulting Eq. (24) demonstrates that the critical liquid height is governed by the Froude number, which is a ratio of inertial and gravitational forces. There are three unknowns in Eq. (24), namely, H_{OGE} , h , and b , which require two additional equations to close the system.

2.1.2 Onset Criterion. The second equation is found by considering the vertical acceleration at point B , as outlined by Ahmed et al. [15], such that

$$[a_y]_{B(x=b, y=h, z=0)} = -g \quad (26)$$

which states that the onset criterion is due to the instability caused by the acceleration of point B equaling that of gravity. The vertical acceleration of point B is

$$[a_y]_{B(x=b, y=h, z=0)} = \left(\frac{\partial v}{\partial t} + u \frac{\partial v}{\partial x} + v \frac{\partial v}{\partial y} + w \frac{\partial v}{\partial z} \right)_{B(x=b, y=h, z=0)} \quad (27)$$

For steady state and no variation in the x or z directions, substitution of the potential function definition ($\mathbf{V} = \nabla\Phi$) into Eq. (27) results in

$$[a_y]_{B(x=b, y=h, z=0)} = \left(\frac{\partial\Phi}{\partial y} \cdot \frac{\partial^2\Phi}{\partial y^2} \right)_{B(x=b, y=h, z=0)} \quad (28)$$

Finding the second derivative of Φ with respect to y yields

$$\frac{\partial^2\Phi}{\partial y^2} = \frac{M}{(x^2 + y^2 + z^2)^{3/2}} \left[\frac{3y^2}{(x^2 + y^2 + z^2)} - 1 \right] \quad (29)$$

Substituting Eqs. (22) and (29) into Eq. (28) at point B and then equalizing it with $-g$, as in Eq. (26), and using the definition of discharge strength in Eq. (16) and nondimensionalizing, results in

$$\text{Fr}_d^2 \left(\frac{hd^5}{(b^2 + h^2)^3} - \frac{3h^3 d^5}{(b^2 + h^2)^4} \right) + 64 \left(\frac{\rho_L}{\Delta\rho} \right) = 0 \quad (30)$$

2.1.3 Offset Distance Criterion. The third equation is developed by considering a stationary dip in the streamwise direction (x -coordinate). This occurs as a result of the point-sink and uniform flow velocities having equal magnitudes, and opposite directions, at point B . The criterion may be expressed as

$$\left. \frac{Mx}{(x^2 + y^2 + z^2)^{3/2}} \right|_{B(x=b, y=h, z=0)} = U \quad (31)$$

By substituting the definition of discharge strength in Eq. (16), as well as the coordinates of point B , into Eq. (31) and nondimensionalizing produces

$$\text{Fr}_U - \frac{\text{Fr}_d}{8} \left(\frac{d^2 b}{(b^2 + h^2)^{3/2}} \right) = 0 \quad (32)$$

2.2 Special Case ($\text{Fr}_U = 0$). When the crossflow Froude number is zero ($\text{Fr}_U = 0$), which occurs when there is no imposed liquid flow in the main pipe, that is, $\dot{m}_{L1} = -\dot{m}_{L2}$, the outcome is a special case. This implies that the offset distance, b , is uniquely zero. The number of unknowns is reduced to 2, requiring only two equations to close the system. A quick check of Eq. (32) verifies that with $\text{Fr}_U = 0$ and $\text{Fr}_d > 0$, the offset distance must be $b = 0$. With $b = 0$, Eq. (30) reduces to

$$\frac{h}{d} = \frac{\text{Fr}_d^{0.4}}{2} \left(\frac{\Delta\rho}{\rho_L} \right)^{0.2} \quad (33)$$

and substituting this into Eq. (24) results in

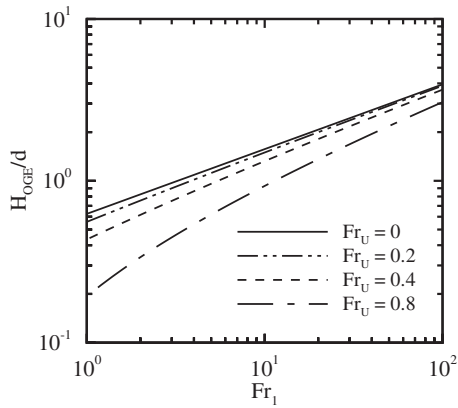


Fig. 2 Effect of Fr_U on the critical height H/d

$$\frac{H_{OGE}}{d} = Fr_d^{0.4} \left[\frac{1}{2} \left(\frac{\Delta\rho}{\rho_L} \right)^{0.2} + \frac{1}{8} \left(\frac{\rho_L}{\Delta\rho} \right)^{0.8} \right] \quad (34)$$

If the lighter fluid density is negligible, that is, $\Delta\rho \approx \rho_L$ then Eq. (34) is reduced to

$$\frac{H_{OGE}}{d} = 0.625 Fr_d^{0.4} \quad (35)$$

3 Results and Discussion

3.1 Solution. The model consists of three nonlinear equations, Eqs. (24), (30), and (32), with three unknowns, these being the critical height, H_{OGE} , and the location of the dip at $x=b$ and $y=h$. These unknowns are governed by the applied flow conditions defined by the discharge and crossflow Froude numbers, Fr_d and Fr_U , respectively. The system of equations was evaluated numerically through use of MATLAB 7.0 *fsolve* function. The discharge Froude number, Fr_d , was tested between 0.1 and 100, while the crossflow Froude number, Fr_U , ranged between 0 and 1. With these parameters, residuals in each of the three equations were 1×10^{-11} or less.

3.2 Effect of Fr_U on H_{OGE}/d . The special case, where $Fr_U = 0$, along with cases of $Fr_U = 0.2, 0.4,$ and 0.8 are presented in Fig. 2. The $Fr_U = 0$ case shows the highest critical height for any combination of Fr_d or Fr_U . This implies that any imposed crossflow will decrease the critical height. For a constant crossflow Froude number (Fr_U), as the discharge strength, Fr_d , increases, the curve approaches the $Fr_U = 0$ line. Physically, this means that the discharge becomes increasingly dominant in the flow field. At lower discharge Froude numbers ($Fr_d < 10$), the influence of the crossflow Froude number is more pronounced.

3.3 The Dip Location. The variation in the dip height, h/d , is presented in Fig. 3. The trend is similar to that of H_{OGE}/d shown in Fig. 2, as might be expected. The ratio of the critical height to dip height, H_{OGE}/h , is presented in Fig. 4, demonstrating the effects of crossflow and discharge strengths, Fr_U and Fr_d , respectively. The $Fr_U = 0$ line shows a constant value where $H_{OGE}/h = 1.25$, and is consistent with an earlier point-sink analysis for a side discharge on a flat vertical wall with no imposed crossflow [15]. For cases with crossflow, the effect of Fr_U is a decrease in H_{OGE}/h for all Fr_d . At low values of Fr_d , H_{OGE}/h decreases dramatically with $Fr_U = 0.8$ and indicates that values of $H_{OGE}/h < 1$ were found. Values of H_{OGE}/h lower than 1 violate the physics of the problem because it implies that the dip is located above the gas-liquid interface. A value of $H_{OGE}/h = 1$, as Fr_d approaches zero, would be physically more appropriate since it implies that the dip disappears from the two-phase interface—substitution of

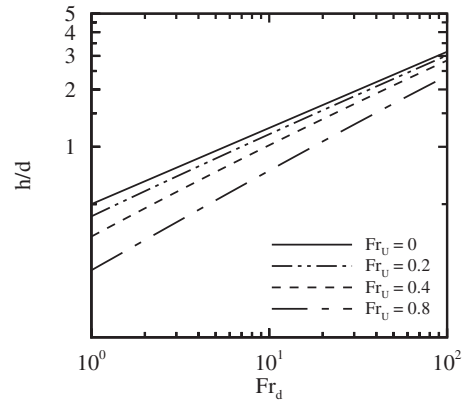


Fig. 3 Variation in dip height, h/d

$Fr_d = 0$ into Eq. (24) yields the same conclusion.

The shift in the dip location downstream of the discharge centerline was defined at $x=b$. The effects of Fr_d and Fr_U on b/d (b was nondimensionalized with the discharge diameter d) are shown in Fig. 5. An increase in crossflow strength, Fr_U , results in an increase in b/d , as might be expected, and is due to the increase in x -momentum. On the other hand, the results indicate that an increase in discharge strength, Fr_d , also results in an increase in the dip offset distance, b/d . While an increase in b/d with Fr_d might not be implicit, this trend can be explained with the aid of Fig. 6. This figure highlights the behavior of the dip location using a ratio of dip offset distance and dip height, b/h . As the discharge strength, Fr_d , increases, the result is a decrease in b/h . As Fr_d increases, it becomes the dominant player in the flow field and, as

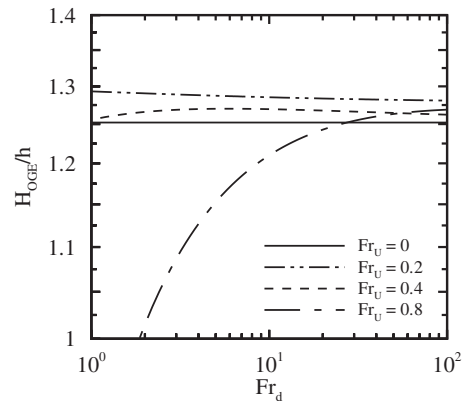


Fig. 4 Variation in H_{OGE}/h

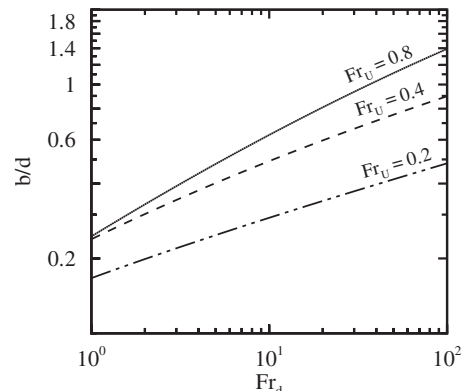


Fig. 5 Variation in dip offset distance, b/d

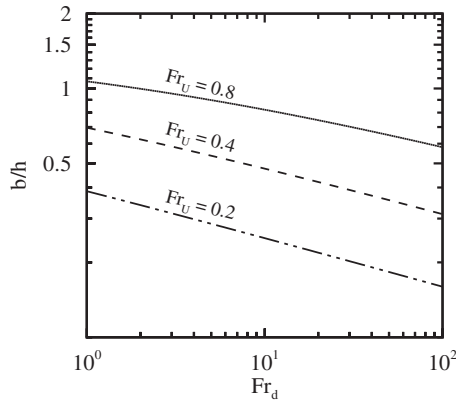


Fig. 6 Variation in the offset distance, b , with the dip height, h

a result, forces the dip to move closer to the y -axis (passing vertically through the discharge center) resulting in a decrease in b/h .

3.4 Conservation of Mass by Control Volume. A control volume approach is used in order to evaluate the crossflow mass flow rate at the inlet and exit of the domain. This step is necessary in order to compare with published experimental data, which typically cite crossflow as a mass flow rate rather than velocity. The analysis is presented for cases with an imposed liquid flow, i.e., $Fr_U > 0$. The bottom wall is assigned a finite size in the z -direction, called the plate width (W), so the liquid cross-sectional areas at the inlet ($x \rightarrow -\infty$) and exit ($x \rightarrow \infty$) can be defined. This follows from considering the inlet mass flow rate (\dot{m}_{L1}) as

$$\dot{m}_{L1} = \rho_L(H_{L1}W)V_{L1} \quad (36)$$

the exit mass flow rate (\dot{m}_{L2}) as

$$\dot{m}_{L2} = \rho_L(H_{L2}W)V_{L2} \quad (37)$$

and the discharge mass flow rate (\dot{m}_{L3}) as

$$\dot{m}_{L3} = \rho_L \left(\frac{\pi d^2}{4} \right) V_{L3} \quad (38)$$

The liquid velocity is defined as V_L , while subscripts 1, 2, and 3 denote the inlet, the exit, and the discharge, respectively. The liquid height at the inlet and exit are defined as H_{L1} and H_{L2} , respectively. The cross-sectional areas of the liquid phase at the inlet and exit are therefore $H_{L1}W$ and $H_{L2}W$, respectively. Considering the conservation of mass from the definitions in Fig. 1, the resulting liquid mass flow rates at the inlet (\dot{m}_{L1}) and exit (\dot{m}_{L2}) and discharge (\dot{m}_{L3}) are conserved, requiring that $\dot{m}_{L1} = \dot{m}_{L2} + \dot{m}_{L3}$. The definition of \dot{m}_{L3} could be found in terms of the discharge Froude number by rearranging Eq. (2) as $\dot{m}_{L3} = (Fr_d/4)(\pi\sqrt{gd^5\rho_L\Delta\rho})$.

From the boundary conditions at the inlet ($x = -\infty$), at the onset of gas entrainment $H_{L1} = H_{OGE}$, and $V_{L1} = U$. To find the exit liquid velocity, V_{L2} , consider the definition of the potential function as $x \rightarrow \infty$, resulting in $V_{L2} \rightarrow U$. The inlet and exit mass flow rates can be rewritten as a function of the crossflow Froude number using Eq. (25) as $\dot{m}_{L1} = \rho_L(H_{OGE}W)Fr_U\sqrt{gd}$ and $\dot{m}_{L2} = \rho_L(H_{L2}W)Fr_U\sqrt{gd}$, respectively. Inserting these definitions into the conservation of mass ($\dot{m}_{L1} = \dot{m}_{L2} + \dot{m}_{L3}$) and rearranging in terms of the exit liquid height, H_{L2} , results in

$$\frac{H_{L2}}{d} = \frac{H_{OGE}}{d} - \frac{\pi}{4} \left(\frac{d}{W} \right) \left(\frac{\Delta\rho}{\rho_L} \right)^{1/2} \left(\frac{Fr_d}{Fr_U} \right) \quad (39)$$

The equation states that the exit liquid height, H_{L2} , will be less than the critical liquid height, H_{OGE} , if the plate width, W , has a finite size. As the plate width approaches infinity, the exit liquid

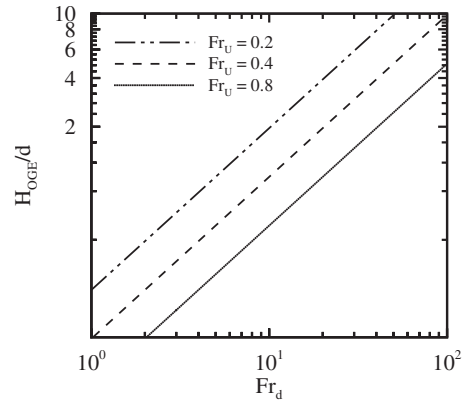


Fig. 7 Example of critical values causing flow reversal ($d/W = 0.05$)

height, H_{L2} , approaches the value of H_{OGE} .

If a positive real value of the exit liquid height, H_{L2} , is found from Eq. (39)—given that the crossflow and discharge Froude numbers are positive and nonzero, and the plate has a finite size, W —then the exit mass flow rate, \dot{m}_{L2} , will have a positive value. If an exit height of $H_{L2} = 0$ is found, it implies that there is no flow ($\dot{m}_{L2} = 0$) at the exit. Furthermore, negative values of H_{L2} imply that the exit mass flow rate, \dot{m}_{L2} , is negative and is called flow reversal. In this case, the liquid is flowing into the control volume at the exit control surface rather than flowing out. By inserting $H_{L2} = 0$ into Eq. (39) and rearranging the equation, the limit where flow reversal occurs can be defined as

$$\frac{H_{OGE}}{d} \Big|_{H_{L2}=0} = \frac{\pi}{4} \left(\frac{d}{W} \right) \left(\frac{\Delta\rho}{\rho_L} \right)^{1/2} \left(\frac{Fr_d}{Fr_U} \right) \quad (40)$$

A sample of flow conditions causing flow reversal at the exit are shown in Fig. 7 with $d/W = 0.05$ and $\Delta\rho = \rho_L$.

3.5 Comparison With Previous Studies

3.5.1 Benchmark Case ($Fr_U = 0$). Experiments conducted without any imposed crossflow, $Fr_U = 0$, are representative of the special case derived in Eq. (35). Both quasisteady [12–14] and unsteady [4,5] experimental results have been reported and are presented in Fig. 8. The present model ($Fr_U = 0$) agrees well with the experiments and demonstrates a $\pm 30\%$ range of maximum error. It is interesting to note, however, that the maximum devia-

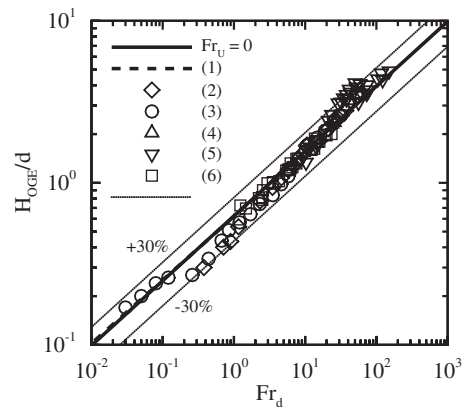


Fig. 8 Comparison of the special case model ($Fr_U = 0$) with theoretical work of (1) Andaleeb et al. [17], and experimental works of (2) Bowden and Hassan [14], (3) Ahmad and Hassan [13], (4) Hassan et al. [12], (5) Abdalla and Berenyi [5], and (6) Lubin and Springer [4]

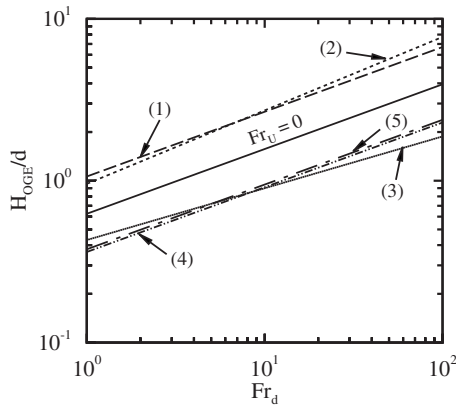


Fig. 9 Effect of crossflow with comparison to experimentally obtained correlations by (1) Smogle and Reimann [19], (2) Schrock et al. [21], (3) Kowalski and Krishnan [23], (4) Maciaszek and Micaelli [20], and (5) Yonomoto and Tasaka [22]

tion occurs at either low ($Fr_d < 1$) or high ($Fr_d > 100$) discharge Froude numbers. It is possible to speculate that in these ranges the critical height is influenced by additional forces not considered by the Froude number, and could be an interesting future direction to consider. Aside from the methodologies used by these experimental studies to record the critical height (quasisteady versus unsteady), there are also significant differences in the two fluids used (gas-liquid and liquid-liquid), as well as the geometry of the test sections (discharge diameter, pipe diameter, and pipe orientation). All things considered, the agreement helps to validate the point-sink approach, which includes the inviscid, incompressible, irrotational, quasisteady, and negligible surface tension assumptions used in the development of the present model. The model developed by Andaleeb et al. [17] is also presented in Fig. 8. Their prediction lies on the same line as the present study with less than 1% deviation for $Fr_d > 0.1$.

3.5.2 Including Crossflow. The effects of crossflow on the critical height are presented in Fig. 9 by comparing correlations developed from selected quasisteady experimental studies. These correlations are compared with the benchmark case with no imposed crossflow, $Fr_U = 0$, and as described by Eq. (35). There is poor agreement between these correlations and the present model, and is particularly true at high discharge Froude numbers. The results presented in Fig. 2 demonstrated that as Fr_d increased the model predictions converged to the $Fr_U = 0$ case. The convergence at $Fr_U = 0$ is physically appropriate since the discharge flow becomes increasingly dominant over the crossflow. The experimentally derived correlations presented in Fig. 9, however, do not converge to the $Fr_U = 0$ prediction as Fr_d increases, but rather run parallel or even diverge.

There is also a large discrepancy between the correlations regarding the effects of crossflow on the critical height. Comparing with the benchmark case, $Fr_U = 0$, two of the correlations indicate that crossflow causes the critical height to increase [19,21] while the remaining three correlations indicate a decrease in H_{OGE} [20,22,23]. Maciaszek and Micaelli [20] explained that liquid crossflow caused the vortex-free gas core formation to be suppressed and resulted in a substantial decrease in critical height. The authors tested exit liquid velocities, V_{L2} , up to 3 m/s, which was substantially higher than the approximately 0.36 m/s exit liquid velocity reported by Smogle and Reimann [19], and attributed this difference to the sharp decrease in critical height. The present model corroborates Maciaszek and Micaelli's [20] findings that an imposed liquid crossflow, $Fr_U > 0$, decreases the critical height for a given discharge Froude number, Fr_d , as was verified in Fig. 2. The critical height predicted by this correlation is presented in Fig. 10 for a range of momentum fluxes, R , using a selected cross-

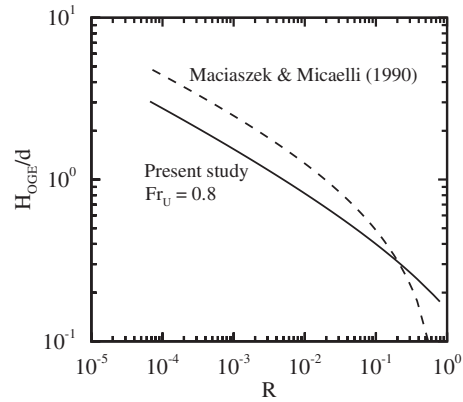


Fig. 10 Comparison of point-sink model with experimentally derived correlation compensating for crossflow effects [20] using ratio of exit to discharge momentum fluxes in Eq. (5)

flow value of $Fr_U = 0.8$. The critical height predicted by the present model is also presented in this figure. There is good trend agreement, and it is interesting to note that their experiments were performed at approximately $R = 0.1$, which is close to the point where the two curves intersect.

The correlation developed by Yonomoto and Tasaka [22] includes a ratio of exit to inlet mass flow rates as a compensating factor for crossflow effects. This correlation is presented in Fig. 11 for a range of mass flow rate ratios using a selected value of $Fr_U = 0.6$. Their experiments were conducted using a square ($190 \times 190 \text{ mm}^2$) channel with a single downward discharge ($d/W = 0.052, 0.079, \text{ and } 0.105$). Using the conservation of mass analysis outlined in Sec. 3.4, it is possible to compare the present model with their correlation for a range of mass flow rate ratios. There is a good trend agreement, and although the present model underpredicts the correlation, it is within the data fit error used to find the compensating factor in Eq. (9).

4 Conclusions

The study presented a theoretical model to predict the critical height at the onset of gas entrainment in a single downward discharge installed on a flat plate with liquid crossflow. The model used a potential flow approach and represented the discharge by a three-dimensional sink superimposed in a uniform flow. The resulting equations demonstrated that the flow field was dominated by the discharge and crossflow Froude numbers, Fr_d and Fr_U , respectively. Generally, crossflow caused a decrease in the critical height for vortex-free gas entrainment. Through conservation of

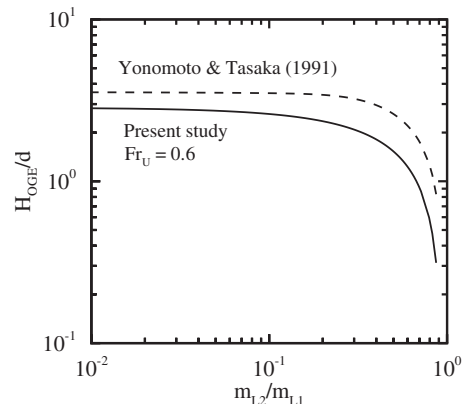


Fig. 11 Comparison with correlation compensating for crossflow effects [22] using ratio of exit to inlet mass flow rates in Eq. (10)

mass, there were some limiting cases causing flow reversal; these were dependant on flow conditions (Fr_d and Fr_U) and geometry (d/W). Comparison of the benchmark case ($Fr_U=0$) with both quasisteady and unsteady experimental data showed good agreement with a maximum deviation of 30%. Several experimentally obtained correlations were compared with the benchmark case and these demonstrated significant discrepancies with regard to the effects of crossflow; they showed either an increase or a decrease in critical height.

Acknowledgment

Financial support of the Natural Sciences and Engineering Research Council of Canada (NSERC) and the Canada Foundation for Innovation (CFI) is gratefully acknowledged.

Nomenclature

- a = acceleration (m/s^2)
 b = dip offset distance (m)
 Bo = Bond number, $Bo=d(g\Delta\rho)^{1/2}/\sigma^{1/2}$
 C = crossflow correction factor, Eq. (9)
 C_1, C_2 = constants, Eq. (1)
 d = discharge diameter (m)
 Fr_d = discharge Froude number,
 $Fr_d=4\cdot\dot{m}_{L3}/\pi\sqrt{g\cdot d^5\cdot\rho_L\cdot\Delta\rho}$
 $Fr_{d, corrected}$ = corrected theoretical Froude number
 Fr_U = crossflow Froude number, $Fr_U=\frac{U}{\sqrt{gd}}$
 g = acceleration due to gravity (m/s^2)
 h = dip height (m)
 i, j, k = unit vector directions
 H = liquid height (m)
 H_{OGE} = critical height at onset of gas entrainment (m)
 K = constant in Eq. (3)
 \dot{m} = mass flow rate (kg/s)
 \dot{m}_d = discharge mass flow rate, general for gas or liquid flows in Eq. (1) (kg/s)
 M = point-sink strength, $M=\dot{m}_L/2\pi\rho_L$ (m^3/s)
 N_μ = viscosity number, $N_\mu=\mu(g\Delta\rho/\rho_L^2\sigma^3)$
 P = pressure (N/m^2)
 R = ratio of momentum fluxes, $R=\rho_L V_{2L}^2/\rho_L V_{3L}^2$
 t = time (s)
 u, v, w = velocity components in Cartesian coordinates (m/s)
 U = imposed crossflow velocity (m/s)
 \mathbf{V} = velocity, $\mathbf{V}=u\mathbf{i}+v\mathbf{j}+w\mathbf{k}$ (m/s)
 W = total width of wall in z -direction (m)
 x, y, z = Cartesian coordinate system

Greek

- μ = fluid viscosity ($N\ s/m^2$)
 ∇ = differential operator,
 $\nabla=(\partial/\partial x)\mathbf{i}+(\partial/\partial y)\mathbf{j}+(\partial/\partial z)\mathbf{k}$
 σ = gas-liquid interface surface tension (N/m)
 Φ = potential function (m^3/s)
 ρ = fluid density (kg/m^3)
 $\Delta\rho$ = difference in density between fluid phases (kg/m^3)

Subscripts

- A = point upstream of the discharge
 B = lowest point of the dip
 d = discharge
 G = gas phase

- L = liquid phase
 1, 2, 3 = subscripts for the inlet (1), exit (2), and discharge (3) flows

References

- [1] Ardron, K. H., and Bryce, W. M., 1990, "Assessment of Horizontal Stratification Entrainment Model in RELAP5/MOD2 by Comparison With Separate Effects Experiments," Nucl. Eng. Des., **122**, pp. 263–271.
- [2] Zuber, N., 1980, "Problems in Modeling of Small Break LOCA," Nuclear Regulatory Commission, Report No. NUREG-0724.
- [3] Lubin, B. T., and Hurwitz, M., 1966, "Vapor Pull-Through at a Tank Drain—With and Without Dielectrophoretic Baffling," *Conference on Long Term Cryo-Propellant Storage in Space*, NASA Marshall Space Center, Huntsville, AL, p. 173.
- [4] Lubin, B. T., and Springer, G. S., 1967, "The Formation of a Dip on the Surface of a Liquid Draining From a Tank," J. Fluid Mech., **29**, pp. 385–390.
- [5] Abdalla, K. L., and Berenyi, S. G., 1969, "Vapor Ingestion Phenomenon in Weightlessness," Lewis Research Center, National Aeronautics and Space Administration, Report No. NASA TN D-5210.
- [6] Parrott, S. D., Soliman, H. M., Sims, G. E., and Krishnan, V. S., 1991, "Experiments on the Onset of Gas Pull-Through During Dual Discharge From a Reservoir," Int. J. Multiphase Flow, **17**, pp. 119–129.
- [7] Hassan, I. G., Soliman, H. M., Sims, G. E., and Kowalski, J. E., 1996, "Discharge From a Smooth Stratified Two-Phase Region Through Two Horizontal Side Branches Located in the Same Vertical Plane," Int. J. Multiphase Flow, **22**, pp. 1123–1142.
- [8] Hassan, I. G., Soliman, H. M., Sims, G. E., and Kowalski, J. E., 1996, "Experimental Investigation of the Two-Phase Discharge From a Stratified Region Through Two Side Branches Oriented Horizontally," Exp. Therm. Fluid Sci., **13**, pp. 117–128.
- [9] Hassan, I. G., Soliman, H. M., Sims, G. E., and Kowalski, J. E., 1998, "Two-Phase Flow From a Stratified Region Through a Small Side Branch," ASME J. Fluids Eng., **120**, pp. 605–612.
- [10] Maier, M. R., Soliman, H. M., and Sims, G. E., 2001, "Onsets of Entrainment During Dual Discharge From a Stratified Two-Phase Region Through Horizontal Branches With Centerlines Falling in an Inclined Plane: Part 2—Experiments on Gas and Liquid Entrainment," Int. J. Multiphase Flow, **27**, pp. 1029–1049.
- [11] Crowley, C. J., and Rothe, P. H., 1981, "Flow Visualization and Break Mass Flow Measurements in Small Break Separate Effects Experiments," *Proceedings of Small Break Loss-of-Coolant Accident Analysis in LWRs*, Monterey, CA, Vol. 4, pp. 89–103.
- [12] Hassan, I. G., Soliman, H. M., Sims, G. E., and Kowalski, J. E., 1997, "Single and Multiple Discharge From a Stratified Two-Phase Region Through Small Branches," Nucl. Eng. Des., **176**, pp. 233–245.
- [13] Ahmad, T., and Hassan, I., 2006, "Experimental Investigation on the Onset of Gas Entrainment From a Stratified Two-Phase Region Through Multiple Branches Mounted on a Curved Surface," ASME J. Fluids Eng., **128**, pp. 726–733.
- [14] Bowden, R. C., and Hassan, I. G., 2007, "Flow Field Characterization at the Onset of Gas Entrainment in a Single Downward Discharge Using Particle Image Velocimetry," ASME J. Fluids Eng., **129**, pp. 1565–1576.
- [15] Ahmed, M., Hassan, I., and Esmail, N., 2003, "Modeling the Onset of Gas Entrainment Through a Finite-Side Branch," ASME J. Fluids Eng., **125**, pp. 902–909.
- [16] Taylor, G. I., 1950, "The Instability of Liquid Surfaces When Accelerated in a Direction Perpendicular to the Planes," Proc. R. Soc. London, Ser. A, **201**, pp. 192–196.
- [17] Andaleeb, A., Hassan, I., Saleh, W., and Ahmad, I., 2006, "Modeling the Onset of Gas Entrainment From a Stratified Two-Phase Region Through Branches on a Curved Surface," ASME J. Fluids Eng., **128**, pp. 717–725.
- [18] Reimann, J., and Khan, M., 1984, "Flow Through a Small Break at the Bottom of a Large Pipe With Stratified Flow," Nucl. Sci. Eng., **88**, pp. 297–310.
- [19] Smoglie, C., and Reimann, J., 1986, "Two-Phase Flow Through Small Branches in a Horizontal Pipe With Stratified Flow," Int. J. Multiphase Flow, **12**, pp. 609–625.
- [20] Maciaszek, T., and Micaelli, J. C., 1990, "CATHARE Phase Separation Modeling for Small Breaks in Horizontal Pipes With Stratified Flow," Nucl. Eng. Des., **124**, pp. 247–256.
- [21] Schrock, V. E., Revankar, S. T., Mannheimer, R., Wang, C. H., and Jia, D., 1986, "Steam Water Critical Flow Through Small Pipes From Stratified Upstream Regions," *Proceedings of the Eighth International Heat Transfer Conference*, San Francisco, CA, Vol. 5, pp. 2307–2311.
- [22] Yonamoto, T., and Tasaka, K., 1991, "Liquid and Gas Entrainment to a Small Break Hole From a Stratified Two-Phase Region," Int. J. Multiphase Flow, **17**, pp. 745–765.
- [23] Kowalski, J. E., and Krishnan, V. S., 1987, "Two-Phase Flow Distribution in a Large Manifold," *Proceedings of the AIChE Annual Meeting*, New York.
- [24] Schetz, J. A., and Fuhs, A. E., 1996, *Fundamentals of Fluid Mechanics*, Vol. 1 (Handbook of Fluid Dynamics and Fluid Machinery), Wiley, New York.

Swimming and Flying in Nature—The Route Toward Applications: The Freeman Scholar Lecture

Promode R. Bandyopadhyay

Fellow ASME
Department of Autonomous and Defensive Systems,
Naval Undersea Warfare Center,
Newport, RI 02841
e-mail: promode.bandyopadhyay@navy.mil

Evolution is a slow but sure process of perfecting design to give a life-form a natural advantage in a competitive environment. The resulting complexity and performance are so sophisticated that, by and large, they are yet to be matched by man-made devices. They offer a vast array of design inspirations. The lessons from swimming and flying animals that are useful to fluids engineering devices are considered. The science and engineering of this subject—termed “biorobotics” here—are reviewed. The subject, being of dynamic objects, spans fluid dynamics, materials, and control, as well as their integration. The emphasis is on understanding the underlying science and design principles and applying them to transition to human usefulness rather than to conduct any biomimicry. First, the gaps between nature and man-made devices in terms of fluids engineering characteristics are quantitatively defined. To bridge these gaps, we then identify the underlying science principles in the production of unsteady high-lift that nature is boldly using, but that engineers have preferred to refrain from or have not conceived of. This review is primarily concerned with the leading-edge vortex phenomenon that is mainly responsible for unsteady high-lift. Next, design laws are determined. Several applications are discussed and the status of the closure of the gaps between nature and engineering is reviewed. Finally, recommendations for future research in unsteady fluids engineering are given. [DOI: 10.1115/1.3063687]

Keywords: biorobotics, fluids engineering, fluid dynamics

1 Introduction

The goal of this review is to discuss how fluids engineering is benefiting by learning from the march of biology. Fluids engineering has normally taken physics as its fountain of inspiration—and with remarkable successes that dot our life today. Looking at biology for inspiration therefore is a departure. It is thought that the physics discipline is matured, and its return on investment is declining with time. By and large, swimming and flying platforms are visually the same today as they were decades ago, and the efficiency of motors—the most common electromechanical device—remains low, with most of the input energy being wasted and with their operation remaining noisy. Turbulence models, as they are accounting for more and more of flow complexities, are becoming ever so narrowly applicable. There is a need to understand why, while we have more in-depth information about fluid dynamics, the impact on performance is not proportionately as high. Truly predictive capabilities are still scarce. One could list many examples to show that today's engineering—fluids engineering, in our case—has matured to a great extent.

If we look at the march of natural history, one would expect such mature engineering to converge with biology. Therefore, a useful starting point is to quantify the gap between biology and engineering. Understanding the reasons why this gap exists should then be a target of queries and a means to advance. The reason why one should look for convergence of engineering with biology is as follows. Both biology and engineering are designs; they are tradeoffs of many competing mechanisms with sometimes different optimization and cost criteria [1]. If there are gaps between the

two, the approach should be to study the underlying mechanisms that are in play and determine whether those in nature should be inducted into engineering. This review examines such approaches and outlines successes.

A relative distinction between science and design, or basic and applied research, can be carried out in the following manner. In an elementary sense, from the point of view of basic and applied research, the broad rationale for biological inspiration in engineering may be viewed as shown schematically in the layered model in Fig. 1 [1]. Physics, which deals with fundamental forces and uncovers the laws of nature, is the core of science. All other layers deal with application in one form or another. The first adjacent layer is chemistry, which can be described as applied molecular physics. The next outer layer is biology, which is nature's application of physics and chemistry into self-contained, autonomous systems. We assign the next outer layer to engineering, which is man's application of physics and chemistry. The disciplines are relatively treated as more basic as we approach the core and more applied as we move to the outer layers. Biology and engineering are then both basically design. The degrees of freedom, number of actuators and sensors, redundancy, and autonomy generally decline in engineering systems compared with biological systems. All this echoes Engineer Fuller, who said that “In nature, technology has already been at work for millions of years” [2]. Biological systems have higher degrees of freedom and, yet, are reliable over many cycles of operation. Cost and reliability, on the other hand, have deterred engineers in the past from building systems based on unsteady principles of aerodynamics or hydrodynamics. Therefore, it is essential that biology-inspired designs have large performance gains, and the induction of new materials, sensors, and power and control technology should help to improve reliability. Appropriate integration of these subsystems is also a key to the technology transition of the principles of swimming and flying

Contributed by the Fluids Engineering Division of ASME for publication in the JOURNAL OF FLUIDS ENGINEERING. Manuscript received October 14, 2008; final manuscript received: October 15, 2008; published online February 9, 2009. Review conducted by Joseph Katz.

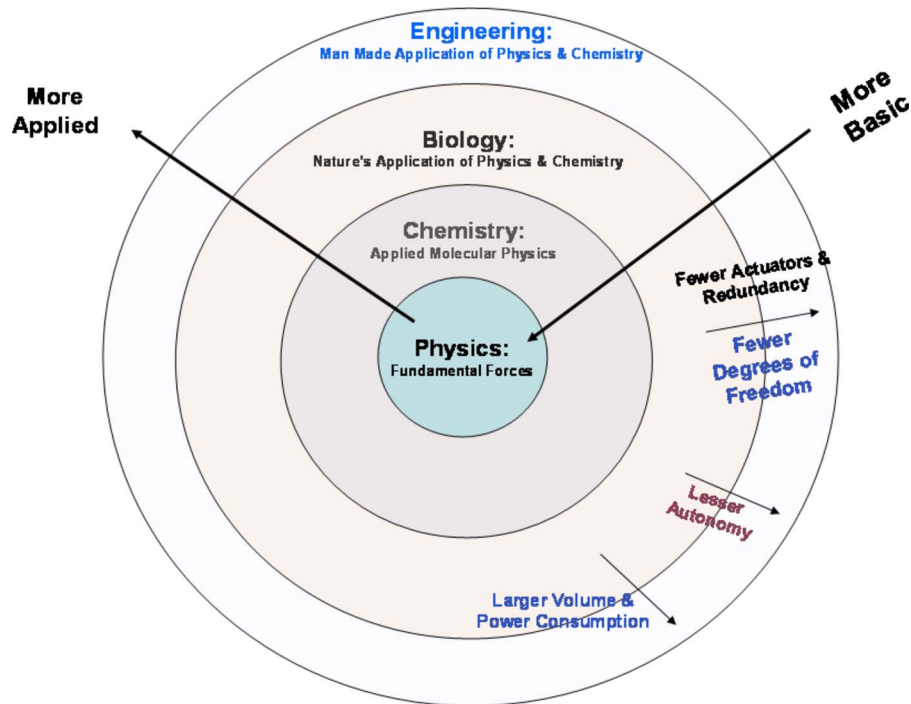


Fig. 1 Schematic of close relationship between biology and engineering [1]

animals. Because both biology and engineering are the subjects of design, the starting questions should be formulated carefully: What basic principles are in play? or, How is it built? The former is rooted in science, while the latter is in biomimicry.

If the goal of new approaches to fluids engineering is to improve performance, the first question that should be asked is as follows: How much improvement should we aim for? For example, if the hydrodynamic efficiency of a lifting surface improves from 50% to 75%, is that a large improvement? We argue below that such an absolute scale is misleading. The answer has to be sought in a systems context, and that is why there is a need to be cognizant of the component sciences that are integrated to build a device with durable advantage. Consider an elementary example. Imagine a person paddling a boat. What would be the impact on the overall efficiency if the hydrodynamic efficiency of the paddle was improved from 50% to 75%? An engineering alternative would have the paddler replaced with motor drives for electromechanical conversion and an engine converting chemical/nuclear fuel to electromotive energy. A well-built electric motor is 30% efficient, and an engine is 20% efficient. So, the result would be a system efficiency improvement of 3–4.5%. This is a sobering finding. We also take this opportunity to note that if the world is faced with a dwindling supply of hydrocarbon-based energy, then clearly addressing the gargantuan energy losses might well be more telling, although less glamorous, than drilling deeper into Earth's crust. One alternative is to bypass the inefficient engine and go directly from fuel to electromotive energy, which is what a fuel cell does. The best practical fuel cell efficiency is below 50–60% due to waste heat, purity and system requirements. Another alternative is to improve the electromechanical efficiency of motors, and for this we need to delve into polymer- and carbon-based artificial muscles. Such muscles are even more efficient when they are in a bath of chemical fuel. So, in principle, biology does provide a design paradigm for impacting not only fluids engineering per se, but also the entire fluids engineering-based system if we are willing to integrate such nature-based hydrodynamic mechanisms with artificial muscles.

There is growing paleontologic evidence for the notion that all living birds of today—from ostriches to hummingbirds to ducks—

trace their lineage to those that once lived by the shore. In other words, aquatic birds led to modern birds, and swimming and flying animals have a common ancestry. However, both in nature and in man-made devices, swimming and flying cover a large range of Reynolds numbers and mass, and conflicting requirements of required lift and thrust forces need to be met. Therefore, their design varies considerably. Here, Reynolds number is defined as a ratio of inertia to viscous forces usually in the form $Re = UL/v$, where U is the forward speed, L is the length scale, and v is the kinematic viscosity of the fluid medium.

The interest in high-lift arose among biologists in a bid to explain how flying animals can keep themselves aloft in a low-density medium such as air, which is 840 times lighter than water. Many aquatic animals can control buoyancy, which is not practical in air. Some birds certainly have a very large wing span—the wandering albatross has a wingspan of 3.4 m; an extinct vulture-like bird called the giant teratorn (*Argentavis magnificens*) is estimated to have weighed 75 kg and to have had a wingspan of 8 m. Also, early fossils show insect wing spans of 10–710 mm. Thus, high-lift in animals is certainly an intriguing issue. Since both swimming and flying animals range from the tiniest to very large species, the high-lift mechanism is utilized over a very large Reynolds number range.

At the other end of the spectrum, flying insects weigh from 20 μg to 3 g and span Reynolds numbers from 10 to 10,000. Insects produce far more lift forces than thrust compared with their bodyweights. (For swimming animals, the demand is the opposite, as buoyancy mechanisms are used to support gravity and aquatic animals tend to have a large percentage of saline water in their body making them nearly neutrally buoyant.) Low Reynolds number wings use the fling and clap method of high-lift. But insects of higher Reynolds numbers use a leading-edge vortex for high-lift. In fling and clap, the wings clap above the insect body. While flinging open, they create suction and a high-lift vortex is produced. Although fling and clap produces higher-lift forces than leading-edge dynamic stall vortex, the clap process tends to damage the wings. Not much is known at the lowest Reynolds number of 10, where thrips fly. Thrips have bristled wings. Measurements

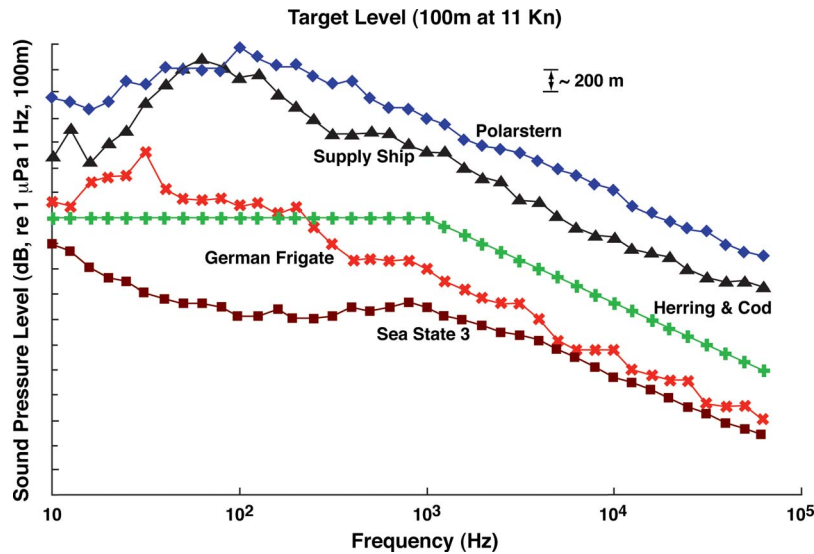


Fig. 2 International Council for the Exploration of the Sea (ICES) data on relative noise in ship and fish. The German frigate is quieter than fish. Fish are slightly noisier than the ambient at Sea State 3. Commercial ships are noisier than fish.

on geometrically scaled bristled and smooth wings show that the former produces lower levels of forces—not higher—during cruise or maneuver [3]. More research is needed on hairy appendages at low Reynolds numbers. Much of academic biorobotics is focusing on replicating the function and motion of animals. This effort is driven by curiosity and the hope for discoveries, inventions, and practical applications. One practical impetus is to keep man out of harm's way—for example, as in hazardous underwater salvage operations.

There are two distinct approaches to biorobotics. One seeks to understand the science principles first and then apply them, while the other merely mimics biology. Biology is not always superior to engineering. While turtles can navigate from the Florida coast to Africa and return to the same location within 100 m, undersea vehicles can roam around the globe and dock at their home pier within <1 m. While insect flight muscles have an efficiency of <10% [4], the efficiency of motors can be ~30%. While evolution took millions of years, the laboratory or numerical “genetic” simulation of fin efficiency [5] and eel kinematics [6] can take minutes to hours, respectively. Thus, there is no guarantee that mimicry will fill a need. For these reasons, in this review, we identify the mechanisms and function in animals and their appendages first. Then, we discuss the successes in the practical renderings of the mechanisms. The focus is on leading-edge vortex formation by unsteady wings—a mechanism extensively used in swimming and flying animals and now being explored for engineering renditions.

2 Performance Gaps Between Nature and Engineering

How can the integration of unsteady hydrodynamics with different disciplines help close the gaps between the performance of animals and that of current similar man-made vehicles and devices? There is a need to conduct careful measurements in the natural environment because they best show how energy storage, sensory inputs, stability, and navigation are integrated in one system. Future animal flight research is proceeding toward controlled experiments in simulated natural environments where different disciplines are integrated [7]. Biorobotics also needs to do the same for rapid success in application. To make a case for animal-inspired fluids engineering, it is useful to quantify the gaps between the performance of current man-made vehicles and those of animals. The performance gaps in several variables in the under-

water context have been determined in a series of investigations [5,8,9]. The variables considered are the turning radius of underwater vehicles, efficiency, radiated noise, sonar characteristics, and suction adhesion.

Figure 2 compares underwater noise for several ships and fish, with sea state 3 as a baseline. The vertical axis is in increments of 200 m and is not in dB. While ships are noisier than fish, the German frigate carried out noise abatement modifications to contain or absorb noise, leading to a remarkable improvement. The goal is to explore means of reducing noise and vibration at the source—i.e., at the propulsor and the power drives. Possible solutions include reducing propulsor rotational rates, which can be accomplished by implementing higher-lift hydrofoils, and improving the electromechanical efficiency of drives and power trains [10]. Profiles of new hydrofoils digitized from cadavers of swimming animals are discussed in a later section of this review. The hydrodynamic characteristics of these hydrofoils are worth exploring for improvement in propulsor performance.

One method of quantifying the performance gap between man-made vehicles and animals is to focus on underwater sound levels. The sound level under water is equivalent to the sound level in air plus 62 dB. A large airliner has a sound level of 120 dB (noise level at 1 m). This is equivalent to 182 dB in water. A cargo ship/tanker of sound level 190 dB is noisier than a large airliner. Even a tug and barge at 10 kn produces 170 dB. The onset of whale and dolphin avoidance response to industrial noise is at 120 dB, the ambient level in calm seas is 100 dB, and the coastal bay with snapping shrimp produces a noise level of 70 dB. Obviously, propulsion in man-made commercial vehicles is poorly designed compared with even large transcontinental swimming animals.

The variation in turning radius for constant normal acceleration between fish (such as bluefish and mackerel) and underwater vehicles of 1950s vintage and 1980s vintage shows gaps of several orders of magnitude [11,12]. Bluefish and mackerel are endowed with both speed and maneuverability. The fish data were generated from trajectories of fish navigating about obstacles in a laboratory environment. The vehicle data are from unmanned underwater vehicles traversing a figure-eight trajectory of scale on the order of kilometers in the ocean. The same trajectory curvature algorithm was used in both data sets. The comparison shows that for constant acceleration, fish make shorter radii turns. The gap in turning ability has been narrowed over time, although a factor-

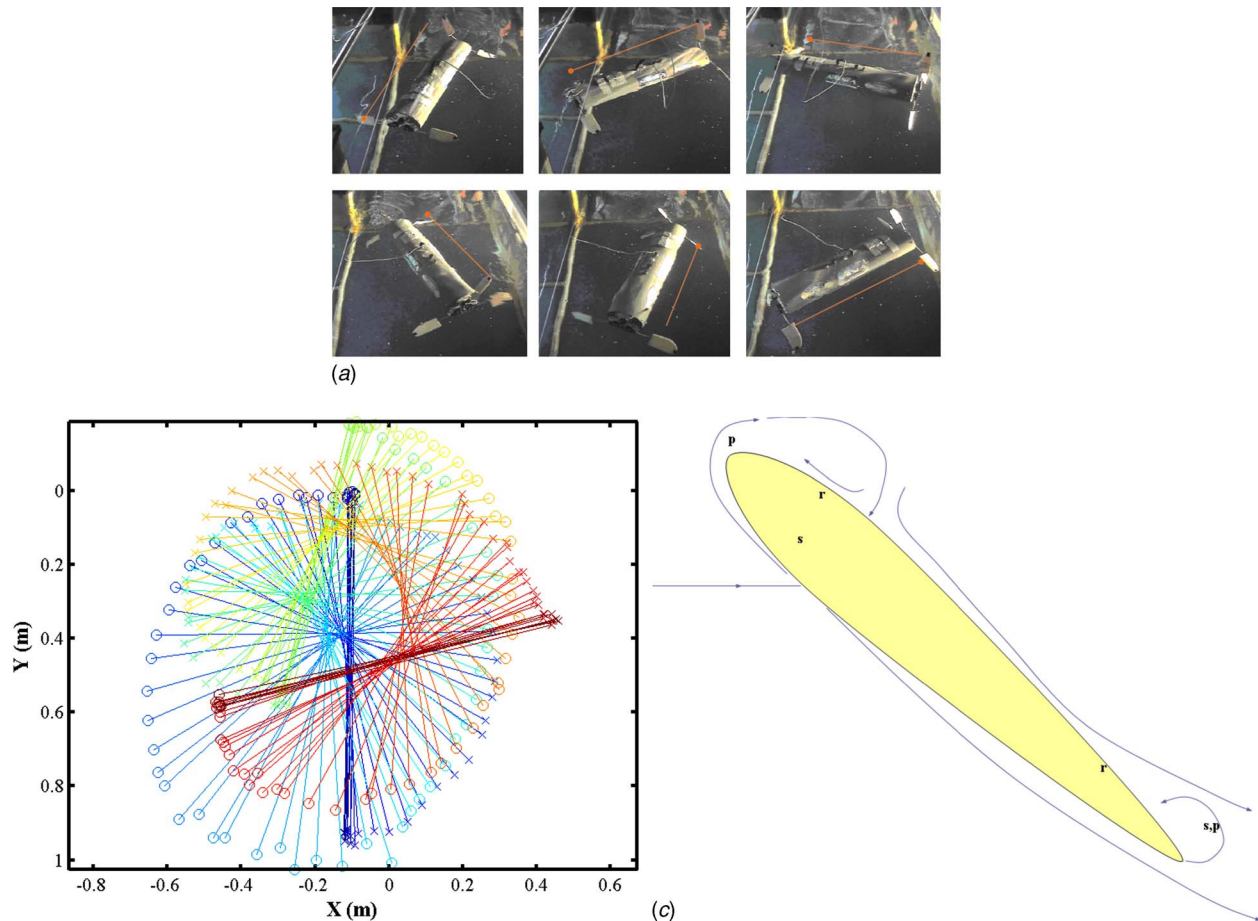


Fig. 3 (a) Sequence of photographs from a video showing clockwise zero-radius turning achieved by the NUWC BAUV. Time increases in (a) from left to right by 2.17 s. (b) Digitization of vehicle yaw showing accuracy of zero-radius turning [13]; vehicle (160 cm long) axis positions with time are plotted; color changes from blue to green as the vehicle makes one turn and then to red as it makes a counter turn. (c) Schematic of dynamic stall on the flapping fins based on dye and surface hot-film sensors; s: stagnation point, r: reattachment point, and p: point of separation.

of-10 gap remains. The narrowing is attributable to improvements in digital controllers and not to any hydrodynamics. Below, we discuss how the high-lift principles of swimming and flying animals have helped to close the gap completely.

A biorobotic autonomous underwater vehicle (BAUV) has been fabricated at the Naval Undersea Warfare Center implementing the dynamic stall high-lift principles of swimming and flying animals [5,8,13]. The cylindrical hull vehicle has six penguinlike fins that roll and pitch at the same frequency, with a 90 deg phase difference in between (Fig. 3). The kinematics of each fin is independently controlled. The fins undergo dynamic stall and produce higher-lift than is possible in steady flow. Figure 3(a) shows that it is now possible to take a cylinder and make it turn at zero radius. Figure 3(b) shows the digitized vehicle position at different times, with the vehicle undergoing clockwise and counterclockwise turns. The length of each line represents the vehicle axis. It is shown that the center of the vehicle moves little in comparison to the radius of turning or the length of the vehicle. This is a clear demonstration that the high-lift principles of swimming and flying animals have helped not only to match the turning abilities of fish but perhaps even to surpass them [11,12].

The distribution of propulsion power density of man-made underwater vehicles and that of swimming animals for which muscle energy density data are available have been compared [8]. The comparison shows propulsive power versus vehicle or fish volume. For cruise, there is a remarkable convergence between the two groups from nuclear submarines down to the tiny bonito—a

stretch of eight decades of power and displacement. The animal-inspired BAUV vehicle (Fig. 3) is in excellent agreement with shark of similar size. Tactical-scale man-made maneuvering vehicles from the open literature are not generally speaking well designed, perhaps for lack of reference. Smaller and more maneuverable vehicles are likely to gain in performance from comparison with animals.

What is the gap in efficiency between swimming and flying animals and man-made fins and vehicles inspired by such animals? The answer to this question is shown in Fig. 4. Different kinds of efficiencies are shown. There is a dearth of reliable efficiency data on animals. These general trends may be tentatively discerned. Man-made unsteady fins can now be as highly efficient as those in animals as long as the leading-edge vortex high-lift sources are generated by appropriate rolling and pitching motions. However, in both animals and man-made vehicles comprising a multitude of single actuators, efficiency is much lower. In the two generations of man-made vehicles with animal-inspired high-lift actuators, efficiency has improved, although it is still lower than that in flying insects. The efficiency of insect flight muscle is quite low—less than 10% [4]. Good quality electric motors have an efficiency of ~20% or higher. So, what could explain the lower efficiency of man-made vehicles where the individual fins are just as efficient as those in swimming and flying animals? The answer may be frictional losses and the lack of a resonant design, and these possibilities are considered below.

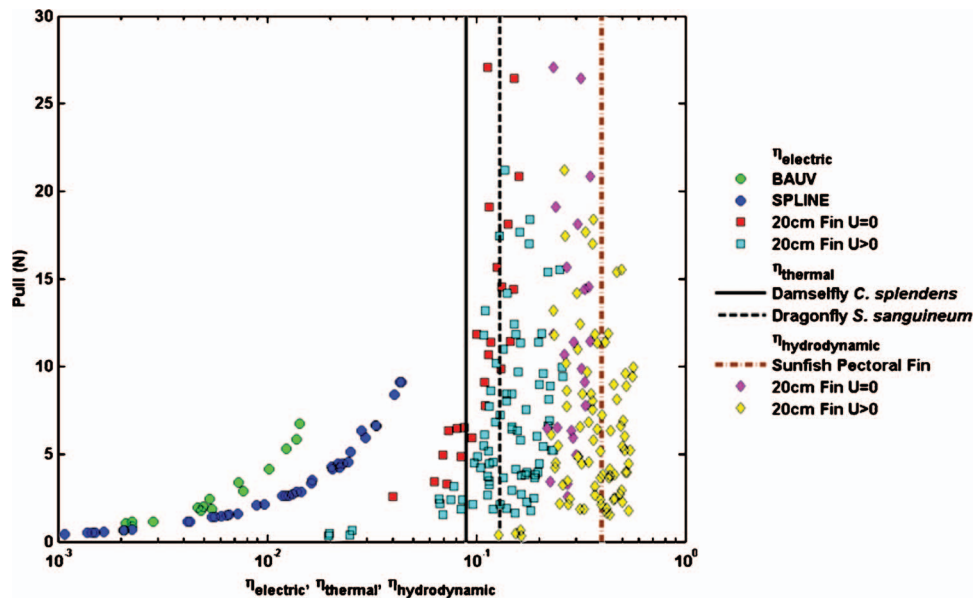


Fig. 4 Efficiencies due to flapping foils. Comparison of the efficiency of man-made vehicles and fins with those of swimming and flying animals [8]. The thrust of the biorobotic vehicles (BAUV and SPLINE) is measured as a pull (N) applied to a string and induced flow velocity is modeled. Single fin: 20 cm span, 10 cm chord. The limited animal data show efficiency only and are not versus pull. The sunfish data are from Lauder and Madden [93] and the insect data are from Wakeling and Ellington [46]. The sunfish pectoral fin hydrodynamic efficiency is taken as the ratio of added downstream kinetic energy to the total fluid kinetic energy when only the pectoral fins are active. The biorobotic fin hydrodynamic efficiency is taken as the ratio of the product of the cycle-averaged force in the forward direction and tow speed, and the input hydrodynamic power. The latter is equal to the sums of the products of torques and angular velocities for roll and pitch motions. The electric efficiency of vehicles and thermal efficiency of insects include power required to oscillate the fins. Thermal efficiency of insects is taken as the ratio of mechanical power output (=mechanical power for flight) to metabolic power input to muscles (=heat production immediately after flight).

In insects, wings operate in a narrow frequency band and a resonant oscillator design is employed. The quality Q of an oscillator in the neighborhood of resonance is defined as [14]

$$Q = 2\pi \frac{E_p}{E_d} \quad (1)$$

where E_p is peak kinetic energy of the oscillator and E_d is the energy dissipated per cycle. Sometimes, the numerator is taken to be the total kinetic energy stored in one cycle. The Q factor can be taken as the number of cycles it takes for the kinetic energy to dissipate to $1/e^{2\pi} = 1/535$ of its original value. A resonant system can be considered critically damped ($Q=0.5$), overdamped ($Q < 0.5$), or underdamped ($Q > 0.5$). The Q factor is 6.5 for the fruit fly, 10 for the hawkmoth, and 19 for the bumblebee. For biological systems, these values are “impressive.” In other words, the bumblebee wings resonate at higher amplitude at the resonant frequency than fruit fly wings do and their amplitude drops off more rapidly as well when the frequency moves away from resonant frequency. Flapping machines should also be designed as resonant systems. The controllers of underwater vehicles employing flapping fins do not have a resonant design, and the actuator drives have higher frictional losses.

Finally, a dolphin-inspired interaural time differencing sonar for underwater ranging at distances on the order of 100 m has been fabricated [15]. Emitter sound frequencies and the interaural spatial gaps are in the range of those in dolphins. It was found that the angular resolution can be about 1 deg—similar to that of dolphins, but higher than that of human beings. However, apparently much more energy needs to be input into the water for pinging than that used by dolphins, which employ short-duration, nonlinear chirps. The engineered sonar requires very little processing

compared with conventional sonars; it is lightweight in air, neutrally buoyant in water, low powered in comparison, and fits biorobotic vehicles, which tend to be on the scale of 1 m. In these criteria, the biology inspiration did lead to some advantageous performance. However, a large gap in performance exists, and a better understanding of how dolphins process acoustic returns and create three-dimensional images of their surroundings could lead to greater benefits.

3 Understanding From Biology

3.1 Origin and Mechanism. The mechanisms of insect flight/fish swimming and the mechanics of animal-inspired control surfaces have been reviewed earlier [16–20]. The reader might also like to refer to the special journal issues on biology-inspired engineering [1,5,21]. Engineers can find a summary of the aspects of the fluid dynamics of swimming and flying animals that biologists think are of relevance in Ref. [22]. They may also see how gravity, jets, pumps, friction, and waves are being dealt with by swimming and flying animals and the diversity of boundary conditions and solutions for the same problem statement—after all, there are 1000 species of bats and 28,000 species of fish. While engineers may shudder to openly speculate, biologists consider speculation an extremely useful tool for research. Biologists, who in general are strong in observation and intuition, tend not to be adept in the mathematical tools of fluids engineers. A teaming of engineers and biologists could be very fruitful in bringing rigor to the evaluation of mechanisms and reigning controversies, such as follows: Are rotational effects or wake capture new phenomena? Are they present in flying animals? Is the leading-edge vortex spiraling and stable?

One can go farther by swimming and flying than by walking. So, swimming and flying have given a vast opportunity for diversity to animals. The biomechanics of swimming and flying are treated in Ref. [23]. A comprehensive account of what is known about insect flight and the directions of future research is also available [24]. The reader should also be on the lookout for a coming treatise on the biomechanics of flying by Ellington.

Our understanding of the mechanisms of high-lift in swimming and flying animals is based on scaling laws and models (such as physical and analytical models), but largely on physical models. Scaling laws have been mostly based on experimental observations of live animals. Physical modeling has been based primarily on experiments with model wings (in the case of flight) and on live animals (in the case of swimming). Computational fluid dynamics and quasisteady modeling have provided verification and clarification of the physical models to some extent. The quasisteady models provide design laws for scaling. The models have provided checks on internal consistencies in measurements and on our understanding. Controversies between physical models and differences between robotic models and live animals have helped to advance our understanding. In what follows, the understanding from these various approaches is first treated separately and then synthesized. Caution needs to be exercised in linking biorobotics to animal mechanics too sanguinely. For example, sometimes the leading-edge vortex (LEV) has been likened to the delta wing LEV. However, the delta wing has a detached vortex lift, whereas the flapping wing has an attached vortex lift. Of course, neither is shed and both are stable.

The high-lift mechanism of swimming and flying animals has been examined from several different perspectives. The emphasis has been on vorticity production on solid surfaces, the spatial distribution of vortices in the wakes, and measurement and modeling of the forces produced. The approaches may be likened to observers trying to decipher what an animal is like based on its footprints. One group of observers has managed to collect the information from under the foot while the animal was in the process of treading on the surface, while another group is examining the footprints after the animal has already left. Some researchers have looked for evidence of the mechanism on the control surface but on scaled models of dragonfly, fruit fly, and abstracted penguin wings. Others have extensively explored the behavior of vorticity in the near wake using the particle image velocimetry (PIV) technique with live fish in controlled laboratory flows. The notable results are summarized as follows. Ellington and Dickinson showed that dynamic stall is the primary high-lift mechanism in insect flying. Dynamic stall has been implicated for high hydrodynamic efficiency of propulsion [5,8]. Direct evidence that fish exploit vortex flow properties for minimization of the cost of locomotion comes from the PIV work, where it was found that trout slalom between Kármán vortices with lowered muscle activity [25]. It has been shown that fish caudal fins have a universal dominant Strouhal number of 0.25–0.35, and they produce a reverse Kármán vortex train of thrust jets [26].

In science, new diagnostics have led to new understanding, new data, and new product development. The use of digital particle image velocimetry (DPIV) for free-swimming animals in a controlled laboratory environment has allowed the development of new hydrodynamics models of fish swimming mechanisms for cruise and turning [27]. Forces and moments produced by free-swimming fish can be estimated from DPIV wake vortex traverse [28]. Fish with similar morphologies, such as superperch and sunfish, were found to use vortex dynamics differently. For this reason, one could argue that investigation of muscles and actuators is inherently linked to unsteady hydrodynamics and should be carried out in an integrated manner for comprehensive understanding. Some authors have focused on the near-wake vortex structures and not on the flow over the control surfaces. The following modern measurement techniques, if used for flow over the control surfaces, might fill this gap and lead to further developments. A

projected comb fringe method of tracking the deformation of the transparent wings of a dragonfly in real time in free flight has been developed [29]. This method allows identification of a body-centered coordinate system using the natural landmarks on the dragonfly. The comb fringe pattern is projected onto the wing with high intensity and sharpness, and images of the distorted wing are then recorded using a high-speed camera. (The only assumption is that the leading edge is rigid.) The instantaneous attitude of the fly is also measured. This method needs to be explored in water. One method that might be useful in the list of contexts mentioned below is multi-exposure digital holographic cinematography. Such a portable instrument in fluids engineering context has been developed [30]. Over a depth of field on the order of 1 mm–1 cm, one can compare scanning planar systems with holograms, both with similar resolution. Measurement of velocities instantaneously over a larger depth of field is the advantage of the holographic method. The holographic method produces a large amount of data, and one tends to analyze only a small fraction of the data. Further development is expected to focus on the improvement of the quality of holograms and automation of analysis of holograms. Fluid velocity diagnostics based on digital imaging techniques have matured. They have been widely used by biologists and fluids engineers to examine wake vortex structures. However, this technique has not been used to examine the boundary layer flow on the lifting surfaces, which is the origin of the vorticity. This region is thin, particularly in animals, so measurement there is challenging. Movements of surfaces are further complications. But how to combine the above fringe method of measuring the movement of flexible, solid lifting surfaces with a diagnostic of the LEV roll-up in a live animal is perhaps the ultimate measurement challenge in biorobotics. Another area where high-resolution surface movement and flow velocity diagnostics would be useful is in exploring the mechanism and function of small surface roughnesses and irregularities that are widely found in the control surfaces of animals. Limited scaled-up experiments do not indicate what the value of these surface irregularities is and, in fact, suggest deterioration in performance. Swimming animals have mucus, so surface hot films cannot be used on such flexible surfaces. The holographic technique could be useful in such flow problems and could also be useful in investigating octopus suckers from behind roughened Plexiglas walls to understand if suckers are more active than they are credited with being [9]. For example, to determine if sucker adhesion to a porous surface is actively controlled, it would be useful to track the suckers' nerves, the motion of their microscopic surface irregularities, control of mucus surface tension, and flow rate with cup pressure, simultaneously. Such experiments would utilize advanced measurement techniques with animal-inspired active control to explore their fluids engineering value. The fringe method can give micrometer-level resolution in real time and, thus, could prove useful to fluids engineering investigations of intricate lifting surfaces of small swimming and flying animals. We have emphasized the importance of free-flight and free-swimming experiments in animals. These are difficult to conduct. High-speed photography of insects in free flight has been carried out [31]. A projection analysis technique that measures the orientation of the animal with respect to the camera-based coordinate system is used. The wing kinematics and body axes can be obtained from single frames.

3.2 Origin of High-Lift as Gleaned From Flight of Insects.

In this section, we examine the wings of flying animals and pectoral fins of swimming animals as siblings, but treat the caudal fins of swimming animals differently. Also, with practical transition in mind, among vortex-based mechanisms we focus more on LEV, reverse Kármán vortex streets, and traveling waves, and leave others as tentative. For example, in flapping fins, there is general agreement regarding dynamic stall as a high-lift mechanism. However, there is some controversy regarding rotational effects and wake capture to be of general relevance.

3.2.1 Clap and Fling Mechanism of High-Lift. We first consider the rather uncommonly observed clap and fling mechanism in flying animals. In clap and fling, a pair of lift- and thrust-producing control surfaces is subjected to antiphase rotational oscillation and translation and the angle of attack constantly changes. With this mechanism, it is essential to have the surfaces in pairs. The earliest systematic investigation of insect high-lift and physical modeling [32] was followed by the analytical two-dimensional and inviscid modeling of the clap and fling mechanism [33]. A series of experiments and physical modeling [34–38] clarified the mechanism and set in motion a torrent of interest. LEV was implicated in high-lift and soon became the focus of investigations and applications that continue today. Flow visualization experiments with a pair of scale-model wings of wasps were carried out in an attempt to explain how they sustain their weight in flight in a low-density medium such as air—something that is difficult to account for by several factors with classical aerodynamics [32]. The clap and fling lift enhancement mechanism denoting the 0–180 deg and 180–360 deg phases of the wing motions was proposed. During clap, the leading edges of the two wings first come closer, producing two LEVs, which are the sources of high-lift. Then, the trailing edges rotate to close, ejecting the intervening fluid as a jet and augmenting the thrust. Subsequently, the leading edges rotate apart, again forming two LEVs. This is followed by the trailing edges rotating and translating apart, which again rushes in fluid as a jet and augments the vortex lift. During both the clap and fling phases, vortices do not form at the trailing edges. The LEVs form first during both clap and fling, which probably inhibits the formation of the trailing edge vortices. Other explanations for the absence of trailing edge vortices also appear in literature. The problem with this model of high-lift has been that many insects never clap, even though 25% higher-lift is produced compared with conventional wing beat [39]—probably because clapping damages the wings or because the wings have higher drag during forward flight. Because the clap and fling mechanism is not widely prevalent in nature, Ellington and co-workers resumed the search for the ubiquitous mechanism of high-lift. The stable attached LEV is the subsequent discovery implicated in high-lift, attributed to Ellington, which has withstood the pressure of time. It is presented below in various manifestations in flight and in swimming, also spurring novel applications. This review is built on this kernel. High-speed photography of many different insects in free flight shows that there are many variations of the clap and fling mechanism [31]. How much the two wings touch and how far they stay apart vary between species and during maneuvering. It may be that the separation distance provides a fine control of the lift forces produced [31]. The insect lift enhancement research shows two kinds of insect and bird wing beats—clap and fling (which is less prevalent) and conventional wing beat. LEV is produced in the latter. Maximum lift per unit flight muscle mass is 54–63 N kg⁻¹ in those with conventional wing beats and 72–86 N kg⁻¹ in those with clap and fling [39]. Insects using conventional wing beats and birds and bats had the same former limiting muscle-lift characteristic, implying evolutionary convergence in performance but not in morphology, which remains diverse. In other words, each animal has retained its specialized wings and kinematics while achieving a universal level of efficiency characteristic of the type of their wing beat. The present review implicates the near-universality of LEV for conventional wing beat.

3.2.2 Leading-Edge Vortex Mechanism of High-Lift. The LEV mechanism is the most commonly observed wing kinematics in flying and swimming animals. In contrast to the clap and fling mechanism, with LEV a single control surface simultaneously heaves and pitches at the same frequency with a preferred phase difference between the two, whereby the angle of attack constantly changes. In addition to heave and pitch, or roll and pitch, twist may also be present in the wing/fin. Insect and bird flights have been modeled on the lines of propellers and rotating disks

[34–36,40]. The rate of change in momentum flux in the downward jet is equated to the weight. This analytical approach remains the foundation of experiments and of physical models. Experiments and numerical simulations have focused on circulation in the wake. For many insect wings, the spanwise variation in chord can be described by a beta function, implying universal wing loading behavior [41]. The presence of LEV on *Menduca sexta* has been shown [42]. Keeping these vortices attached for as long as possible is a strategy that insects probably use. Such studies on actual full insects are rare and difficult. The strategies that animals use to keep the stall vortices attached to their wings are open research topics. Research on the high-lift of animal control surfaces treats hovering and cruise separately. Biologists tend to conduct biomechanics experiments both on real animal wings and on models of animal control surfaces that are accurate to minute details. In hovering animals, in the Reynolds number range from 1100 to 26,000 and for aspect ratios of 4.53–15.84, aspect ratio has little effect on force coefficients [43,44]. The cause is attributed to the presence of clear LEVs. On the other hand, in conventional propellers (including wind turbines), delayed stall occurs only near the wing root. In the above, the fin aspect ratio is given by $AR=s/c$, where s is the span and c is the chord of the fin. The plate geometry ratio $R=c_{tip}/x_{tip}$ has been used to compare rectangular and triangular approximations of insect wings, such as butterfly wings, where c_{tip} is the chord at the tip and x_{tip} is the distance to the tip from the axis of rotation [45]. Dragonflies align their stroke plane normal to the thrust in contrast to what was previously thought [46]. Measurements of thermal changes after flight show that their mechanical efficiency is between 9% and 13%. The maximum muscle specific power is 156–166 W/kg.

Much controversy exists in our understanding of animal flight mechanisms or scaling laws. If dynamic stall is such a great boon from nature, then are there any system limitations in scaling up? The traditional view has been challenged [47]. It was thought that mass specific power from flight muscles varies as $m^{-1/3}$, where m is the body mass. In other words, less power is available with increasing mass, and different animals can fly in narrower and narrower speed ranges. Instead, it can be argued that lift production deteriorates with increasing size at lower speeds and mass specific power is not an intrinsic criterion [47]. Force and moment coefficients can be of instantaneous values of forces and moments or of averaged values over several cycles. Force (F) such as thrust or lift and drag is expressed as a coefficient, based on fin planform area or the swept area of the trailing edge, the former of the form as $C=F/1/2\rho U^2cs$, where c is the fin chord and s is the fin span.

3.2.2.1 Wing interactions. The dragonfly uses fore and hind wings to fly. Wing sets can interact strongly. Even minor changes in wing kinematics can lead to dramatic changes in the forces produced. The effects of all four wings can be modeled as a single actuator disk [46]. The vortex interactions of a pair of two-dimensional upstream and downstream wings, cylinder and wings [48], and also the interactions of fish swimming with upstream Kármán vortices [25] are considered later. The flight muscle efficiency of insects is less than 10%, and their muscles have a good elastic storage of the inertial energy to oscillate their wings [4]. How insects manage wing rotation during turning has been examined [49]. Direct evidence of active control of timing between the left and right wings shows that this is done at the ends of strokes when the wing flips. The flip control in flying insects is then a method of executing maneuvers. Measurements of lift and drag and flow visualization on impulsively started two-dimensional flapping insect wings at an intermediate Reynolds number of 10–1000 have been carried out [50]. Studies on impulsively started wings are instructive for insect flight biomechanics. Several experiments have reported that, in impulsively started bluff bodies, the peak transient forces lag wing acceleration [51–56]. The aerodynamics during wing flip (i.e., rapid wing rotation during upstroke-to-downstroke transition), which is more prevalent in in-

sects, has been investigated [57] using two-dimensional wings. It has been observed that the generation of maximum lift is increased if the wing travels through the wake of previously generated vortices, and a lift coefficient as high as 4 has been reported. Force measurements and flow visualization have been carried out with tethered fruit flies [58]. Each cycle was found to produce one vortex loop. No shedding of wing tip vorticity has been observed. The circulation of the vortex loop has been estimated and an unsteady high-lift mechanism confirmed, and a small but observable phase lag in the force time history relative to the wing stroke has been reported—the measured forces are generated after some delay from what one would expect from a visualization of the vortex patterns. The reasons are not definitively known. This delay could be related to Wagner effects, which are treated later [5,17]. A large data set of time histories of forces produced for a large parameter range of fin oscillation is available [59]. The Reynolds number is 115. Stroke plane deviation between the left and right wings of insects is suggested as a control scheme for turning. The authors also present a quasisteady model. The inadequacies of their model, particularly for drag, have led them to question past estimates of mechanical power based on wing kinematics. From examining the forces on a hovering, flapping, mechanical wing starting from start, it can be concluded that force production is influenced by vortices produced in previous cycles [51]. This is known as wake capture and is thought to be an acceleration-reaction force caused by the downwash from vortices formed in the previous cycles acting on the fin [60].

Two-dimensional computations have been compared with measurements on three-dimensional robotic foils simulating fruit fly wings [61]. For hovering, pressure forces make a dominant contribution to fluid forces—something that would escape PIV diagnostics. Interestingly, the disagreements between computations and measurements become more obvious during the periods when the foil decelerates and accelerates at the ends of strokes. We note that circulation does not vary along the span in a two-dimensional foil, and tip losses of finite span are absent. It is unclear what lessons can be unambiguously learned by comparing two-dimensional computations with three-dimensional foil measurements where it is known that spanwise flow plays an important role in LEV stabilization.

The presence of the LEV due to flapping foils at low Reynolds numbers of 120 and 1400 has been confirmed [62]. In the past, LEVs were not seen clearly below a Reynolds number of 5000. Further, it has been shown that at the lowest Reynolds numbers the LEV is stable and spirals from the root to the tip of the foil. However, the severity of the tip-ward flow is Reynolds number dependent. There is a large unexplored area of theoretical research in flapping foils—namely, the Reynolds number dependent stability of leading-edge dynamic stall vortices.

The quasisteady model originally developed for hovering flight has been modified and extended for forward flight [63]. Measurements indicate that added mass effects make a small but measurable contribution to the forces produced. Detailed measurements of the velocity field around dynamically scaled flapping wings of insects have been carried out [64]. It was found that there is a stable pair of counter-rotating vortices at the leading edge, rather than a single vortex. Extensive smoke visualization of the flow around free and tethered flying dragonflies has been carried out [65]. The work largely confirms the attached stable LEV model of insect flight. Spanwise flow is found to be present in both directions but is not thought to be dominant. The LEV is formed when the angle of attack increases rapidly. Qualitative differences are found between model studies and those of live dragonflies. Both the formation and shedding of LEVs are controlled during extreme changes in angles of attack. The mean farfield around flying insects has been related with the nearfield wing kinematics, and semi-empirical theory has been developed [66,67]. The mean induced flow is approximately a function of flapping frequency and stroke amplitude, and the remaining effects are accounted for by a

calibration factor that is wing shape dependent.

In addition to LEV, there can be other mechanisms in insect flight, such as wing-wing interactions and wing-wake interactions [17]. Traditional aerodynamic theories predict that performance improves with aspect ratio and stiffness. Swimming and flying animals have a vast diversity in aspect ratio and flexibility of their lifting surfaces. Unsteady potential flow analysis shows that aspect ratio and the proportion of wing area in the outer span determine the optimal wing form. Traditional notions apply only to low frequencies of wing motions and when the wings are stiff and tapered. Further work is needed to incorporate the nearfield unsteady wing kinematics into theoretical models of wing shape optimization.

Measurements of time histories of forces produced by a flapping wing of a fruit fly show that most of the lift force is attributable to two spikes produced near stroke reversal [68]. One of the spikes correlates with wing rotation, and the other occurs after the rapid wing rotation during stroke reversal. Combes and Daniel [68] attributed the rotation-dependent first peak in lift to a rotational mechanism similar to the well-known irrotational (inviscid) Magnus lift that is produced by the flow past a rotating cylinder. They attributed the rotation-independent second peak to wake capture, which is an interaction with the vortex formed during a previous cycle. These notions have been challenged [69]. An alternative explanation is that the first peak is due to vorticity produced because of wing rotation, and the second peak is because of reaction to accelerating an added mass of fluid [70]. Finite element computation of the forces produced by a fruit fly wing has been carried out [71]. The results are qualitatively similar to the measurements [68]. Some 50% of the forces are generated by the outer 25% of the wings. Advancing the phase of wing rotation with respect to stroke reversal was found to enhance force production, and the combination of translational and rotational mechanisms was thought to be important. A spiraling spanwise flow in the LEV was not found [72]. Also, the flow due to a maneuvering fruit fly has been simulated [73]. Both the wings and thorax, albeit in abstracted forms, were considered. There is a dearth of animal or biorobotic data on maneuvering to allow simulations to be compared accurately. Experimentally observed wing kinematics was used to show that turning (a sudden turning called *saccade*) involves a phase difference of 13 deg in the stroke angle between the left and the right wings, and the angle of attack in the inner wing is smaller by 6 deg. It was found that the leading edge and the tip vortex form a loop that is shed as a lambda-like vortex. It may be that the wake vortex loops for maneuvering animals, compared with the “simple” ring or elliptical vortices due to straight motion, have higher azimuthal modes of distortions. The role of vorticity structure harmonics in flight control is unknown. As synthesized in the section on LEV classification, each animal might have its own characteristic wake vortex topology produced during typical turning.

3.2.2.2 Effects of camber. Camber deformation in insect flight has minor effects [50,74]. But, some show otherwise [29]. Measurements on free-flying dragonflies have been carried out in the laboratory at a Reynolds number of 4×10^4 . Positive camber deformation of the hind wing during the downstroke generates a vertical force for supporting weight, and negative camber deformation of the wing during the upstroke generates a thrust force. Some have speculated that the time-varying camber deformation is a strategy for delaying the formation and shedding of LEVs and enhancing the delay of dynamic stall [29].

3.2.2.3 How sinusoidal is the wing motion in insect flight? Photographs of insects in free flight show that, as a first approximation, the wing motion may be considered sinusoidal [31]. However, there is an unmistakable presence of durations of higher accelerations and decelerations at either end of the wing beat, with constant velocities in the middle of half stroke. The second and

third moments of angular accelerations are, respectively, 4% and 9% lower than those in simple harmonic oscillations.

3.2.2.4 Generalized wake vortex model for bird flight. Experiments with bird flight in a very large wind tunnel have been carried out in an effort to develop a universal model of the wake vorticity pattern [75]. For one species (thrush nightingale), the entire speed range up to 11 m/s was covered. For birds, the mean flow speed can vary over 1–20 m/s and the mean chord over 1–10 cm. Thus, the Reynolds number can vary by a factor of 200. The work is a description of the Reynolds number effects on the wake vorticity. At low Reynolds numbers, the wake may appear to be dominated by elliptical vortices and, at high Reynolds numbers, the wing tip trailing vortices dominate the wake. However, the wake pattern is basically universal—it consists of a train of a pair of elliptical vortices followed by a rectangular vortex, the two being interconnected. The elliptical vortex is formed during the upstroke, while the rectangular vortex is formed during the downstroke. The vortex structures have sufficient momentum to support the weight of the bird. Note that dragonflies produce significant lift forces during the downstroke and thrust during the upstroke [29]. It may be that the elliptical vortex represents lift forces and the rectangular vortex represents thrust force; the former is more obvious at lower Reynolds numbers and the latter at higher Reynolds numbers.

3.2.2.5 Classification of leading-edge vortices. How many kinds of LEVs have been reported? The preliminary answer is two or three or four based on their topology. It is unclear if the variations are attributable to the differences in the sources, namely, the insect species [76]. The LEV descriptions and their variations are based on flapping mechanical models of a wasp [37] and of a tethered hawkmoth and dragonflies [77], and on tethered hawkmoths [72,76] and fruit fly models [7]. All descriptions of LEVs satisfy Kelvin's theorem that all vortices either form continuous loops or end on the surface. Based on Kelvin's theorem, there are two classes. The LEVs are differentiated largely based on whether the two LEVs from the two wings are connected at their roots over the thorax to form one continuous vortex, or whether the two LEVs attach to the solid surface at the root. If the two vortices connect at the thorax, then they inflect downstream to do so. Otherwise, there is no inflection and they attach to the surface at the root.

What about spanwise flow in the LEV? Maxworthy [37] pointed out that the spanwise core flow is necessary for stability, that is, for the LEV to remain on the near surface. In its absence, the LEV would continue to be fed with new vorticity generated at the leading-edge stagnation point and grow and, given enough time, would eventually be shed. Maxworthy [37] and Ellington et al. [72] clearly indicated spanwise core flow in their LEVs. Dickinson et al. [7] indicated spanwise flow but downstream of the LEV and not in the core. Dickinson et al. [7] reported a spiraling flow and a conical LEV with a root focus situated near the root. Therefore, a spanwise core flow can be expected. Dickinson et al. [7] observed that a boundary layer fence did not lead to the shedding of the LEV and suggested that the spanwise core flow is not essential for stability even in a conical LEV. Luttges [77] claimed two-dimensional flow and did not show any spanwise flow at any phase of wing motion. A synthesis of results shows that the Strouhal number, time period of flapping, and circulation can probably be tuned so that a vortex can grow in the absence of spanwise core flow, but not enough to be shed into the wake during the time period of flapping [76].

Insect LEVs are conical, blooming from the thorax outboard, but much less so in the case of the tethered hawkmoth and dragonfly LEV [77]. The tethered hawkmoth [72] and fruit fly model [7] LEVs are about 30% of the chord at midspan, and the tethered hawkmoth and dragonfly LEVs are higher. However, the tethered hawkmoth [76] LEV is in a class by itself, bearing some commonality with all of the above. This LEV is uniform from wing tip to

wing tip through the thorax, with core thickness being about 10% of the chord and hardly any spanwise core flow. The LEV supports 10–65% of the bodyweight.

What about in water? Surface shear measurements in a penguin wing model flapping below 2 Hz in water have been carried out [78]. It was shown that the leading-edge stagnation point oscillates in space about the mean location sinusoidally in synchrony with the flapping waveform. This would mean that the LEV and the spanwise flow also oscillate in space with time. In other words, the LEV is quasistable and not steady. Surface sensor array and complementary dye flow visualization clearly identify two nodes—the forward stagnation point and the reattachment point. Including the rear stagnation point, there are three nodes. Arguing conversely, it can be asserted [79] that the LEV probably has a saddle at the wing base outside the wing. Future work should focus on stability analysis to determine if spanwise core flow in the LEV is essential for LEV stability. *The evidence so far seems to be that every swimming and flying animal has its own kind of LEV critical point topology.* Ideally, one needs to do experiments with live animals rather than robotic models if one seeks to understand the mechanism of animal flight or swimming. A close-scaled replica of the entire animal would be the second choice. However, for primary effects (such as whether the LEV is present or not and its contribution to forces and efficiency), the value of studies on robotic models of the control surfaces of animals has been vindicated.

3.2.2.6 Scaling law of flight. The variation in wing kinematics of birds with body size has been examined [80]. It was found that the common Strouhal number for direct fliers is 0.21, and intermittent fliers are at 0.25. Strouhal number is defined as fA/U , where f is the wing beat frequency, A is the stroke amplitude, $b \sin(\theta/2)$, where b is the wing span and θ is the stroke angle, and U is forward speed. The stroke angle follows the empirical power relationship $\theta = 67b^{-0.24}$. Direct measurements of propulsive efficiency are lacking. It is believed that the propulsive efficiency reaches maximum values at these Strouhal numbers. Currently, animals are thought to oscillate their wings or tails in the Strouhal number range of 0.2–0.4. Future research should examine if the optimized Strouhal values vary with cruise and different kinds of maneuvering, such as hovering and constant-radius turning. Optimization experiments have been carried out on a two-dimensional translating and rotating flat plate to show that in the absence of rotation a stable LEV is not formed [81]. The ratio of the horizontal distance traveled by the plate to the projected chord is believed to be a key parameter for the formation of the LEV.

3.2.2.7 Bat flight: Effects of variable camber, droop, and membrane tension. Bat flight, which is dominated by large camber, droop, and the use of a thin membrane in tension, is being examined [82]. The downstroke consists of abduction, stretching of the wing, and large cambering and droop, while the return upstroke consists of adduction and retraction of the wing, resulting in loss of camber, droop, and membrane tension. During the downstroke, a wing tip vortex is shed. Stall occurs at higher angles of attack and is gentler compared with a similar wing with nondeforming membrane. A qualitative model of the compliant membrane is given, proposing that aerodynamic load is proportional to membrane tension. Direct evidence of the existence of any LEV and high-lift is yet to be available.

3.2.2.8 Vortex method. Simple models for analyzing the force production due to the wing beats of insects have been proposed [32,41]. Also, a vortex method of calculating the pressure distribution of insect wings has been developed. The forces and moments from these three methods have been compared with measurements [45]. The methods are in good agreement when the nondimensional plate geometry ratio R is less than 0.5. The simple models are not accurate when $R \sim 1$ (low-aspect-ratio wing). It is also not possible to take into account the interference between the

two wings in these methods. The vortex method is accurate when R is ~ 1 or is large (>2) and can take into account the interference of two wings. It is important to calculate the added mass effect accurately—particularly in the case of three-dimensional multi-wing insects [45].

The vortex method has been used to analyze the takeoff flight of the butterfly [74]. To do that, the time histories of normal force and moment on a pair of finite triangular plates rotating symmetrically about an axis have been computed [45]. The potential flow method is used to compute the pressure field around the plates. The total velocity potential is divided into two components—noncirculatory and circulatory. The noncirculatory part of the velocity potential satisfies the wall boundary condition and Kutta condition at the edge. It does not shed vortices into the flow and is expressed by sources and sinks. The circulatory part does not affect the boundary condition on the plate and is generated by the vortices shed into the flow. The noncirculatory part of the velocity potential satisfies Laplace's equation, which is solved using the vortex lattice method. The total velocity potential is also obtained from Laplace's equation. Flow visualization is used to identify the outer edges where dominant vortices are formed that induce higher velocities and greater effect on pressure distribution on the plate. The wake is a sum of these vortices shed from the outer edge. These vortices reside on a surface extending to the triangular plate. The strength of this vortex sheet is calculated from the circulation at the four corners of elements of numerical calculation. In this manner, the velocity induced by the vortex sheet is calculated. Unsteady Bernoulli's equation is used to calculate the total normal force and moment from dynamic and impulsive pressures. The noncirculatory part of the normal force has two components—one is proportional to the angular acceleration, including the added mass and added moment of inertia effects; and the other is proportional to the square of the angular velocity. Expressions of shape factors are given that are proportional to the added mass and added moment of inertia, which are calculated by both numerical and experimental methods [74]. The added mass and added moment of inertia are functions of the opening angle between the two plates or wings and are constant in the case of one plate. The shape factors are also functions of the plate shape and separation distance of the plates. A similar method has been given where the flow is taken to be the summation of distributed singularities of sources and sinks on the solid surface and the shedding of discrete vortices. However, instead of using a panel method for numerical solution, Dickinson and Gotz [50] gave an unsteady analytical solution where the unsteady Laplace equation is solved to satisfy the Kutta condition at the leading and trailing edges. The method is used in a two-dimensional, rigid flat plate only. Comparison is made with measurements. It is concluded that the forces originate from added mass effects that act immediately and from the delayed effects of the shedding of leading and trailing vortices and body image vortices.

3.2.2.9 Potential flow theory of unsteady wings. An analytical method based on potential theory has been developed for the calculation of aerodynamic forces due to two-dimensional wings that are slightly cambered and are undergoing heaving, surging, and feathering motions [83]. The suction force at the leading edge of steady airfoils is obtained using Blasius's formula. Polhamus's leading-edge suction analogy of vortex lift is used to treat the flow separation at the leading edge. An analytical inviscid method has been given for calculating forces produced by two-dimensional models of fruit fly wings [84]. The wing is thin, rigid, and uncambered. A potential reference is developed in which the wing is at rest, whereby Blasius's theorem is applicable. The model includes bound circulation and also a LEV circulation that is stationary with respect to the plate. The Kutta–Joukowski condition is then applied at both edges. To allow comparison with measurements where the wings are three dimensional and the velocity changes along the span, a method simpler than the blade element method is used. The velocity used to evaluate forces is taken as the wing tip

velocity times the square root of the nondimensional second moment of the wing area. Good agreement is obtained with the measurements [59]. It is proposed that because the stabilization of the LEV is attributable to flow three-dimensionality, wing camber might be an essential requirement.

3.3 Origin of High-Lift as Gleaned From Swimming Animals. Flying animals need to support their body mass against gravity, but swimming animals such as penguins do not very much need to. (Buoyancy devices are not considered here). Therefore, differences in the wings of swimming and flying animals can be expected. A golden eagle has nearly the same mass (4.7 kg) as a Humboldt penguin (4.2 kg). However, the planform area of the eagle wing is 38 times larger than that of the penguin [85].

Fish that use their body and caudal fins to move are fast swimmers. Those that use fins are good at maneuvering but are not fast swimmers. In this review, we concentrate on high-lift that comes primarily from the control surfaces (such as fins), and we focus, in particular, on the pectoral fins of sunfish, boxfish, bird wrasse, dolphins, and penguins, which include a range of decreasing flexibility (increasing rigidity) and increasing aspect ratio. In large-aspect-ratio wings, a substantial part of the lift force is produced in the outer part of the wing. Therefore, interesting questions can be raised. Are flexibility and aspect ratio two sides of the same coin? Is flexibility an extreme means for producing the results of large aspect ratio in low aspect ratio?

Many of the principles of fish swimming that are still with us date back to critical observations of long ago [86]. For motion, a fish generally uses its body to apply lateral forces in the water that cancel in the time mean but produce a net forward thrust. Body motion is in the form of a wave called a flexion. The form of this wave along the body is used to classify fish into three or four categories. Anguilliform swimming, named after eels, has been studied much less. In eels, the flexion amplitude remains unchanged, nose to tail. There is no discernable jet in the wake of an eel [87]. Sharks, which are also of the anguilliform, swim constantly and are suspected to be efficient. In carangiform and subcarangiform swimming, the flexion amplitude increases toward the tail, and more of the front part of the body is rigid. Lighthill used his elongated body theory to propose that this form of swimming is most efficient because there is the least amount of body motion and thrust is produced only in the tail. Carangiform swimming produces a jet in the wake. Most fish fall in this category and have been widely studied. In thunniform swimmers, only the caudal fin and a small part of the tail body move. The tuna fish, with an active crescent-shaped caudal fin, is an example.

Due to viscous friction, swimming is thought to require more power than is required by human-engineered land vehicles [88]. But aquatic animals are frugal in oxygen consumption as a result of breath holding. For example, the aerobic capacity of emperor penguins is lower than that of an emu or dog of the same mass [89]. This apparent paradox, which is akin to Gray's paradox [105], can be resolved by proposing that aquatic animals resort to drag reduction techniques and need to produce such minimal thrusts. However, aquatic animals may not only be lowering their drag but may also be lowering their abdominal temperature to lower metabolic rates for energy saving [90]. This possibility points out the importance of systems approach rather than a purely fluids engineering approach, when it comes to understanding the mechanisms of swimming and flying animals and their application.

3.3.1 Classification of Aquatic Propulsion. A survey of aquatic propulsion, followed by an analysis based on elongated body theory [91], has led to the classification of swimming in terms of Reynolds number (low and high), efficiency (greater than or less than 0.5), the variation in body undulation with length, and where in the body length the undulation starts. The theoretical hydrodynamic reasons for the distinctions between anguilliform and carangiform swimming can be deduced. In the former, the

mass of water energized by the anterior part is not in phase with the trailing edge motion, resulting in a lower efficiency. In the latter, the amplitude of the basic undulation grows toward the trailing edge and the energized water is in phase with the trailing edge, resulting in a higher efficiency. The explanation seems to be that the distribution of total inertia along the length, a combination of fish body mass and the virtual mass of water, is optimized to minimize “recoil,” resulting in high thrust and efficiency. The evolution in several different lines to the common final result—namely, the lunate tail, which is a pair of highly-swept-back wings, for the enhancement of speed and efficiency—has been examined [92]. The need to reduce caudal fin area in relation to depth to reduce drag without significant loss of thrust leads to this planform. The hydromechanical advantages of lifting surfaces require leading or trailing edges to bow forward. This last remark may bear some relevance to the convoluted form that flexible pectoral fins (such as those of sunfish) undergo [93].

3.3.2 To Flap or to Row? Many fish use their pectoral fins for propulsion, and this is known as labriform locomotion. Swimming with pectoral fins has been described by biologists in their two extremes—namely, drag-based (i.e., rowing) and lift-based (i.e., flapping) [22,94]. In rowing, which is used at low speeds, the fin moves forward and backward and there is little flow over the fin. In flapping, which is efficient at higher speeds, there is flow over the fin. Therefore, over a range of speeds, both types can be expected to be in use. The kinematics and related muscle activity of aquatic animals, focusing on the three-dimensional aspects of aquatic flight, have been examined [95]. Bird wrasse, for example, primarily use the lift-based mechanism—the fin twists, thereby changing the angle of attack along the span. In the abducted position, the bird wrasse pectoral fin planform is similar to that of insect wings. Six muscles actuate the fin motion in antagonistic groups. A simplified linkage model of the fin has been proposed. A blade element model has been used to compare the mechanical efficiency and thrust produced by an idealized fin undergoing elementary sinusoidal rowing or flapping motion [96]. In rowing, the fin rotates backward and forward about a vertical axis; in flapping, the fin moves up and down about a horizontal axis. Flapping fins are wing shaped and they taper away from the root, while paddle-shaped fins expand away from the root. Better performing pectoral fins of fish that rely on them for propulsion have a higher aspect ratio and a longer leading edge (compared with the trailing edge), and the center of the fin area is located closer to the root [97]. Efficiency is found to be higher in flapping, while thrust is higher in rowing, and it is suggested that rowing is useful in low-speed maneuvering, while flapping is useful in power-conserving cruising. These classifications receive some support from measurements [98,99].

Experiments show that as the frequency of flapping is increased, a foil no longer produces drag but starts to produce thrust attributable to a clear reverse Kármán vortex street [100]. Boundary layer thickness on the foil and Reynolds number do not play strong roles. It has been observed that fish and cetaceans flap their tails in a Strouhal number (fA/U) range of 0.25–0.35 [26]. A thrust-producing jet is convectively unstable, with a narrow range of frequencies of oscillation [101]. There is no modal competition between the natural mode (the absolutely unstable mode) and the forced mode, unlike that in bluff bodies. The flapping fin wake acts like a frequency-selective amplifier. Thrust reaches a maximum per unit of input energy at the frequency of maximum oscillation. The authors point out that saithe is an exception to the rule of preferred Strouhal number in nature and has a lower Strouhal number.

Flow visualization at a Reynolds number of 1100 and measurements of force and power at 40,000 on a two-dimensional heaving and pitching foil have been carried out [102]. Propulsive efficiency as high as 87% was reported, which is similar to the 85% claimed theoretically for whale flukes [103]. The following parameters were found to lead to optimum efficiency: a Strouhal

number of 0.25–0.40, heave-to-chord (h/c) ratio of ~ 1.0 , angles of attack between 15 deg and 25 deg, and a phase angle of 75 deg between heave and pitch. For two-dimensional foils, the h/c ratio is important because maximum efficiency is achieved for $h/c = 0.75–1.0$.

Based on flow visualization, it is concluded that the vortex dynamics responsible for high efficiency involves the formation of a LEV in every half-cycle, which amalgamates with the trailing edge vortex to form a reverse Kármán vortex street. More careful later measurements [104] have tended to lower earlier efficiency measurements made in the same laboratory [102]. Efficiencies as high as 71.5% were reported, and the optimum phase angle between heave and pitch was found to be 90 deg for best thrust and efficiency. Therefore, the high efficiencies and the low angles of phase difference between heave and pitch for optimum efficiency and thrust in Ref. [102] are not supported. It has been shown [104] that a higher harmonic should be introduced to the heave motion to make the angle-of-attack time history sinusoidal. This produced a higher thrust coefficient at higher Strouhal numbers. Impulsively started foils are shown to produce mean force coefficients of up to 5.5 and instantaneous lift coefficients of up to 15.0, which could be useful for maneuvering.

3.3.3 Early History of Fish Biomechanics. The principles of swimming known to us are based on the early works of Gray [105], followed by Bainbridge [106,107], and Lighthill [91]. The historical milestones of modeling, scaling, measurement techniques, and debates on the 50th anniversary of Bainbridge’s works on scaling laws of fish swimming have been recounted [108]. Gray’s modeling work [105] on energetics and maximum speed focused attention on the relationship between fish speed and size. Bainbridge [106,107] carried out measurements in circular channels, which were replaced later with water tunnels, allowing more accurate measurements. He showed that tailbeat frequency controls speed, and he proposed a universal relationship of size, tailbeat frequency, and stride length (distance traveled per beat), $U/L = 0.25[L(3f-4)]$, where U , L , and f are speed, length, and frequency, respectively. This is reminiscent of the advance ratio in propeller theory, $J = V/2\phi nR = (V/(nR))/2\phi$, which is translational speed divided by the product of rotational rate and diameter, where V is the flight velocity, ϕ is the peak-to-peak wing beat amplitude in radians, n is the wing beat frequency, and R is the wing length [109]. In other words, advance ratio is forward speed in wing lengths per wing beat divided by 2ϕ . Note that this analogy leads to the representation of speed in terms of body length per second—a legacy from Bainbridge [106,107] that survives today. Gray’s work [105] indicated paradoxes of unexplained differences between available and apparent power, and Bainbridge’s [106,107] representation of speed showed that large fish swim faster, but that their relative speeds in terms of body length are lower. The works of Gray [105] and Bainbridge [106,107] influenced the slender body model of Lighthill [110,111] and gave a framework for estimating power and efficiency.

3.3.4 Interaction of Body and Pectoral Fin in Swimming. The steady swimming and rising or sinking of sturgeon and shark have been compared, which determine where large vertical forces are produced—in the main body or in the pectoral fins [112]. These are long, slender fish with pectoral fins. With their long body aspect ratio, these fish tilt their body in a manner similar to what is used in the underwater hydrodynamics of cylinders at lower speeds ($L/D \sim 10$, where L and D are length and diameter, respectively)—larger angles of attack at lower speeds to generate lift. This is one clue that pectoral fins are not needed to produce lift in such fish. The technique of near-wake traverse using DPIV was used to indirectly estimate the forces and moments produced. During steady swimming, the pectoral fins produce no lift; instead, the positive angle of the body produces lift and the two balance moments. However, sinking or rising is initiated by the pectoral fins to produce a starting vortex whose central jet thrust

helps alter the pitch of the body. The rear half of the pectoral fin is used as a flap to do this. The authors point out that two-dimensional simplification of pectoral fins can be grossly in error. The interaction of the body and the pectoral fin is strong in sturgeon. The leopard shark also uses its body and pectoral fin interaction in much the same manner to control moments for cruise and maneuvering, such as initiation of rising and sinking [113]. It further uses the dihedral angle between its body and its two pectoral fins to control roll motion. How does the bamboo shark control the morphology of its body and its slightly flexible pectoral fin for station-keeping near a floor, and how does it rise or sink [113]? The behavior is compared with that during steady horizontal swimming. This shark basically promotes maneuverability over stability. It uses a combination of body angle of attack (positive or negative angles and their amplitude) and the concavity of the pectoral fin (concavity upward or downward and the amplitude of the resulting dihedral angle) to produce the required vectored vortex jets.

3.3.5 Heterocercal Fish Tail: Why Is It Asymmetric? High-speed photography and DPIV have been used to understand the role of heterocercal tails of free-swimming sturgeon [114]. Long, slender fish such as sturgeon and shark have such tails. Homocercal fins are symmetrical, but heterocercal fins are asymmetrical and have unequal lobes—the vertebral column turns upward into the larger lobe. This question is too complex and there is a need to know the force distributions along the body of free-swimming sturgeon and shark [114]. This topic is well suited to computational analysis and should consider maneuvering to reveal the mechanism.

3.3.6 Finlets and Caudal Fins: Are They Like Strakes and Delta Wings? A synthesis of literature suggests that we should discuss finlets and caudal fins jointly because they might be working in a synergistic manner, although they do not seem to have been examined jointly in the emerging context of high-lift. Fish such as chub mackerel, bonito, and tuna have several small non-retractable triangular fins in the body margin between the main dorsal/anal fins and the caudal fins—that is, on both sides of the tail end of the body margin in the vertical plane. Some of them are rigid and flat, while others are flexible. It is unclear if the finlets are actively controlled. The total surface area of the finlets is only 15% of the caudal fin area. What is their role? It is hypothesized that these finlets direct the flow in the vicinity of the body toward the caudal fin to augment the vortex jet in the tail [115]. This hypothesis receives some support from visualization—the finlets produce a combination of longitudinal converging flow and a counter-rotating flow with axial vorticity [116]. The fish wake consists of a linked array of tilted, elliptical vortex rings with induced central jets [117]. The minor axis of the elliptical rings remains equal to the span of the caudal fin irrespective of speed, while the major axis in the axial direction scales with speed.

The finlets and the caudal fins are closely located and produce vortex-dominated flows. Are they related? Some have thought that the finlets control turbulence or drag or cancel vortices [118–121]. The suggestion [122] that the finlets produce longitudinal flow to augment caudal fin lift has been both partially supported and criticized [123] based on morphology. It is suggested that vortex enhancement is marginal [123]. While different biologists have focused on different species with variations in morphology, it would be useful to find any universal mechanism. None of the authors appear to have dwelled explicitly on vortex-based high-lift as the universal mechanism of finlets and caudal fins. We synthesize the available understanding to suggest the following vortex lift hypothesis to spur investigations. We draw analogy to the Swedish Viggen fighter jet's high-lift aerodynamics. The Viggen aircraft has two small strakes upstream of the main delta wing; these strakes both operate at high angles of attack, whereby they both produce LEV and high-lift. The strake vortex enhances the delta wing lift. In a similar manner, we speculate that the

finlets and the caudal fin work in unison to produce vortex thrust for propulsion. The finlets enhance the main thrust jet by producing a pair of counter-rotating vortices with an intervening jet converging toward the tail, and they are formed alternately along the left and right vertical surfaces of the fish body. The finlet vortices rest on the low-pressure side of the caudal fin and enhance its lift force and augment the jet. It would be useful to conduct computational evaluation of this hypothesis.

3.3.7 Lateral Lagged Oscillation of Symmetric Fish Tail Fins. The caudal fins of homocercal species such as mackerel have extremely symmetrical caudal fins, and the symmetry extends to internal musculature. However, it has been shown that the posterior part of the caudal fin has fine motor control and the tail moves laterally as an acutely angled blade [124–126]. During the tail beat, tail height and area expand and contract. Lateral cyclic motion is lagged—the dorsal lobe (the upper part of the tail fin) leads the ventral lobe (the lower part of the tail fin)—and it undergoes a 15% greater lateral excursion. It has been suggested that such asymmetric motion produces upward lift during steady swimming [126]. The role of this fine control is not definitively known. This precision lateral tail fin actuation problem might benefit from computational investigation.

3.3.8 Multiple-Fin Propulsion in Fish. Some insects have a pair of wings for propulsion and lift. By and large, fish probably use multiple fins more commonly to cruise or maneuver. Wake traverse using PIV visualization has been done to determine the forces produced by various fins in bluegill sunfish [127]. For cruise, 50% of the thrust is produced by the pectoral fins, 40% of the thrust is produced by the caudal fin, and 10% is produced by the soft dorsal fins. For one example of turning, 65% of the force was produced by the pectoral fin and 35% was produced by the soft dorsal fin. The dorsal and caudal fin vortices interact to reinforce circulation, and they partition the force production among the fins. The control of moment may be an important determinant of multiple fin propulsion and their relative budgeting.

3.3.9 Production of Asymmetric Forces by Pectoral Fins for Turning. Fish spend a significant amount of time in turning compared with cruising. DPIV experiments on sunfish have been carried out to understand how asymmetric forces are produced by the pectoral fins that result in turning [127]. The fins modulate the pectoral fin stroke timing and wake momentum. The pectoral fin on the side from which the fish is turning away produces a lateral force that is four times the force it normally produces during cruising. The pectoral fin on the side of the fish toward which it is turning produces a thrust force that is nine times the force it normally produces for cruising. The result of the former is *rotation of the body*, while the result of the latter is *linear translation of the body* toward the center of turning. Fish obviously have a controller, yet to be discovered, that can partition or resolve the force and moment vectors instantaneously and assign monochromatic tasks (forces or moments) to independent fins. It may be that force production in fish for maneuverability and cruising is apportioned in such a manner that the net ability is conserved [128]. The hydrodynamics of bluegill sunfish and black superperch, which have similar fin morphology and are assumed to have similar reserves of energy, have been compared. Superperch have about twice the maximum speed, but sunfish are more maneuverable. They both use their pectoral fins to swim at low speeds and combine pectoral fins with the caudal fin at higher speeds. Pectoral fins are implicated in maneuvering. The superperch pectoral fin wake at all speeds consists of two vortex rings per fin cycle detached from the body. The sunfish pectoral fin wake consists of one detached vortex ring per fin cycle at low speeds and two vortex rings per fin cycle, with one attached to the body, at higher speeds. The orientation of the vortex rings is, however, characteristically different in the two—the sunfish pectoral fin rings always predominantly lie in the lateral plane, while the superperch rings predominantly lie in the horizontal plane. The orientation of the

central jet in the vortex rings explains why sunfish are marvels at maneuvering and superperch excel in speed.

3.3.10 Maneuverability and Flexible Pectoral Fins. Fish that swim in circles work harder than those that swim straight [129]. Power consumption density for propulsion based on red and white muscles, as well as that for underwater vehicles, is higher during maneuvering than during cruise [8]. Fish having flexible pectoral fins are highly maneuverable. The sunfish's pectoral fins are highly flexible, three dimensional, and have a low aspect ratio [130]. PIV studies show that attached vortices are formed at both edges of their fin [5]. A proper orthogonal decomposition of this fin's kinematics shows the fin modes with the proportion of forces that are produced [131]. The approximate three-dimensional vortex structure around an entire sunfish in steady swimming in the laboratory has been constructed from two-dimensional PIV measurements of velocity fields [132]. Longitudinal vortex structures found near the tips of all fins are reminiscent of wing tip vortices of three-dimensional bodies in a uniform flow—the signatures of induced drag. The maneuverability of rigid-bodied fish, such as box fish, propelled by multiple flexible fins, has been examined [133]. The results could help the design of autonomously stable underwater vehicles and automobiles. Most of the body of the box fish is made of inflexible bones, and its rigid body is restrictive of motion. Consequently, the fish has developed a set of fins to oscillate in a phase sequence to produce exquisite maneuvering ability in narrow confines. Flow visualization shows that large-scale tip vortex pairs are created at the sharp ventrolateral keels, and their trajectories relative to the body are manipulated to control stability autonomously. The body performs like a delta wing at a high angle of attack that has a detached LEV. One could conclude that the box fish is using its keel to produce the LEV, although largely to stabilize itself in a pre-existing stream. As a starting point to understanding fish motion, one could create a portfolio of the kinematics of pectoral fins, dorsal/anal fins, and caudal fins that fish (such as box fish, bird wrasse, etc.) use to produce braking, acceleration, spinning, cruising, hovering, and reversing [134]. Generally, for maneuvering, fish control the phase synchronization of several fins to produce a maneuvering motion. Sunfish are an exception; they use their pectoral fins only for station-keeping. Further research is needed on the controllers that manipulate the phase between a set of fins, or the dynamic flexibility of one set of fins to achieve the same result, and on how sensors such as lateral lines are integrated with controllers to close the loop.

3.3.11 Jets or Fins?. Primarily, fish use fins and squid use jets for propulsion. What is more efficient and what is worth considering for application? Squid typically have five to seven times higher oxygen consumption than fish [135], which suggests that jet propulsion is inefficient in comparison. There are squid, however, that use a mix of the two, apparently to compensate for the deficiency [136]. The limitation of jets comes from the fact that the rate of momentum transfer to water is greater with fins than with jets—the size of the bladder expelling fluid is limited and higher jet velocity costs more energy (=velocity squared). Jets due to ring vortices underpredict thrust, and entrained fluid also needs to be taken into account [137]. Environments, nozzle surface quality, active control, and appendages can all affect entrainment. In jet-dominated creatures, their effects on entrainment need closer scrutiny.

3.3.12 Conclusions on Pectoral Fin Mechanism. The hydrodynamic control surfaces on swimming animals have been categorized as passive and active [20]. Leading-edge tubercles of whale flippers and riblets on the skins of shark are passive devices that act as a boundary layer fence and viscous drag-reducing surface elements, respectively. Examples of active devices would include the flexible sunfish pectoral fins or penguin wings. Based on PIV measurements (made largely on station-keeping sunfish in a labo-

ratory environment and not on maneuvering), the major conclusions for the biomechanics of the sunfish pectoral fin are as follows: The fin produces thrust throughout the movement cycle during steady swimming and does so by a combination of changes in the fin kinematics, which include (1) spanwise and chordwise flexibilities, which act to stabilize the upper edge vortex and orient the surface pressure force in the forward direction even during the outstroke; (2) active camber control of the fin surface; (3) an increase in surface area during the in-stroke to increase thrust; (4) surface deformation (cupping shape) to reduce within-stroke oscillation in lift (vertical forces) by producing dual simultaneous LEVs of opposite sign; and (5) a bending wave from root to tip to increase downstream (thrust) momentum. The penguin wing is much less flexible in comparison to the sunfish pectoral fin. The chordwise flexibility of the penguinlike wing increases its hydrodynamic efficiency from a maximum of 0.62 for rigid wings to 0.86 for an optimized wing, while the thrust coefficient remains unaffected [18].

3.4 Flexibility. The formation and evolution of vorticity from the wings and the body suggest that aquatic animals (such as sunfish) use their highly flexible fins to control the loading along the span, and the convolution is a dynamic optimization in synchrony with the unsteady high-lift mechanism. Recall that fish use lateral lines to sense the pressure field, and such a convoluted vortex sheet that might evolve into more than one vortex ring could offer a greater moment for stability control. But there is no evidence yet that the sunfish wake produces more than one vortex ring. Time-domain panel computation of flexible wings, whose planform is similar to that of whale flukes, has been carried out [138]. It was shown that passive operation of the wing degrades propulsive efficiency. However, if the phase of the spanwise flexibility is carefully controlled with respect to the wing motion kinematics, propulsive efficiency can be enhanced. The wing tip should be moved in the same direction of the overall wing. An attached flow is assumed, so future work needs to account for what we now know about LEVs, appropriately scaled for aquatic simulation. A pneumatically operated flexible microactuator made of silicon rubber, circumferentially reinforced with fibers, has been used to build a flexible fin for underwater use [139]. Shore stiffness is varied along the length by varying the density of the fiber reinforcement. Higher curvature is produced by increasing internal pneumatic pressure. A feathering motion has been produced.

3.5 Power. Because of the main role played by unsteady mechanisms, existing aerodynamic theories that use steady-state lift and drag coefficients cannot be used for estimating the induced power of swimming and flying [40]. Yet, fundamentals relating circulation and lift are applicable. Vorticity is produced only on the solid surface of the wings and body. One could track the trajectories of points on the surfaces during a wing stroke and arrive at the vorticity sheet. For a sunfish, this sheet is going to be highly convoluted. During hovering, the vortex sheet is simpler than during maneuvering. The presence of this sheet is a result of force generation—loading of the wings and the body. The sheet quickly rolls into ring vortices to arrive at a more stable configuration. The work done to create the rings can be used to estimate the induced power (the force produced is the reaction of the vortex ring momentum per stroke period). Thus, accurate measurement of the ring vortices in the near-wake and of circulation is an indirect but practical tool for determining the induced power of swimming and flying animals. Many researchers devoted much effort to using dye, smoke, and PIV visualization to document the formation and roll-up of vorticity on the wing surfaces and also of its roll-up into large ring vortices in the near-wake of swimming and flying animals.

3.6 Understanding of Mechanism From Computational Fluid Dynamics. Insect flight covers a Reynolds number range of $10-10^5$ [140]. Swimming animals tend to fall in the lower part of the range—the lower range of the limit drops to 10^{-2} for swimming sperm. The distribution of Reynolds numbers for swimming animals and man-made vehicles appears in Fig. 10 in Ref. [19]. A comprehensive theory of force production in swimming and flying animals is not available. Measurements, modeling, and numerical simulation are filling the void in bits and pieces. Numerical and analytical simulations of fruit flies of wing planforms that are slightly smaller than those in earlier works have been carried out [70]. The computed time histories are similar to those measured [49,59], but with a constant shift to higher values. The claim in Ref. [72] that there is an attached dynamic stall vortex formed at the leading edge is supported; the vortex does not get shed and there is no stall. In agreement with other works [72,141], wake capture [59,68] does not exist apparently because the LEV is not shed. The Magnus effect as the origin of one of the peaks in lift has also been questioned [68]. Note that lift produced by a surface at an angle of attack is Magnus-like, but it is unclear how a Magnus-like force can be attributed directly to the rotation of the wing about its span. In any case, a Magnus effect is irrotational, but a peak in drag accompanies the peak in lift attributed to a Magnus effect. Instead, added mass effects and vortex formations are the causes of the two lift peaks before and after the stroke reversal. It has been shown that the unsteady oscillation of the wings can indeed support the weight of hovering flies as measurements show [32]. Wing kinematics that is yet unexplored might produce higher lift forces. The drag of fruit flies is estimated to be 1.27 times the lift force required to sustain the fly's weight. The body mass specific power is 28.7 W/kg, the muscle-mass specific power is 95.7 W/kg, and the muscle efficiency is 17%. This drag-to-lift ratio is higher compared with those in large fast birds or in hovering helicopters. Computational methods [70,141] have been used to study dragonfly wing interactions, and very little of any interaction is found [142]. Both fore and aft wings produce lift peaks during their downward strokes. During those times, they produce vortex rings with downward momentum.

Navier–Stokes computation has been carried out on a full bird wrasse swimming underwater using an adaptive mesh grid [143]. The pectoral fins are flexible, although the dynamic geometry is not as detailed as that in later investigations of sunfish pectoral fins. Also, detailed time histories of forces produced on a bird wrasse are not available, and an accurate comparison of the computation is hindered. The authors in any case show that in the flexible fin swimming under water the LEV is large, is not of the spiraling type, there is no strong spanwise flow, and the LEV is shed during the upstroke. The flexible pectoral fin is dominated by a strong axial flow and not a spanwise flow. The forces produced by fish-inspired pectoral fins attached to a 30-cm-long and 10-cm-diameter rigid cylinder have been computed [144]. The unsteady Navier–Stokes solver with automatic adaptive remeshing had an unstructured grid. Station-keeping at 1.5 m/s could be possible with these parameters: 20 deg angle of attack at the root of the fin, 2 Hz flapping frequency, and a 114 deg flapping amplitude. The mean power required is 1.573 W, which is 0.79 J/cycle. Numerical simulation of flexible fins has been carried out [131]. Photographs of sunfish pectoral fins swimming in a constant-speed stream in a controlled laboratory environment were digitized to determine the variation in fin topology with time. The flow around the moving boundaries was simulated using Cartesian-grid-based, immersed boundary algorithm pioneered earlier [145] for flows in hearts and lungs [146]. The large-eddy simulation method was used to compute the forces produced by the fin. The method of proper orthogonal decomposition was used to determine the modes of the fin topology and determine their contributions to the thrust produced. Mode-1, which visually appears to capture most of the cupping shape of the fin, produces 45% of the total mean thrust, the glaring omission being the peak during the second half of the

cycle. The addition of Mode-2 raises the contribution to 63%, and the second peak is partially generated. Although the further addition of Mode-3 generates 92% of the thrust, reproduction of the second peak remains elusive. Videography shows (simplistically, to this reviewer) that there may be at least two distinct kinds of deformations—those that are of the scale of the chord and span, resulting in cupping of the fin, and those that are distinctly smaller and extend over only a part of the fin. It would be worthwhile to examine the nonlinear interaction of these two scales of deformations, particularly in the augmentation of force peaks over a part of the cycle.

Numerical simulation of the flow due to flapping, rigid ellipsoids with varying aspect ratio has been carried out [147]. The relevance of freely flapping, rigid ellipsoids to the flapping fins of fish is unclear. The authors show that the gains in thrust and efficiency remain confined to aspect ratios of 2–3, and this is claimed to be the reason why such aspect ratios are commonly found in the pectoral fins among labriform swimmers. The fin wake is found to consist of vortex loops that convect downstream in two oblique directions to the flow, and their intervening angle is inversely proportional to the aspect ratio of the ellipsoid. Numerical simulation of a pair of rigid and finite flapping fins in tandem in the absence of a body has been carried out. As to be expected, certain spatial gaps between the fins can augment thrust and efficiency. However, the relevance of the two-dimensional rigid fin results to the hypothesis on the interaction between the dorsal and caudal fins of sunfish is tenuous [28]. The value of the vortex interaction and moment distribution due to fins around a body to the control of the whole animal/vehicle could be more important than thrust augmentation. The biomechanics works of biologists and biology-inspired hydrodynamics are yet to focus on the relationship of hydrodynamic properties and control.

3.6.1 Analysis. Vortex theory rests on the presence of concentrated regions of vorticity in the flow. The earliest vortex theory of insect and bird flights, developed to firmly supplant the momentum jet theory of continuous wake generation, is due to Rayner [40,148]. Both hovering and forward flights are considered. In hovering, the wake vortices are a stack of horizontal, coaxial, and circular rings. In forward flight, the rings are elliptical, but neither horizontal nor coaxial. Power reduction motivates the choice of flight style. This is illustrated by a comparison of the mallard and pheasant, which are large birds (>1 kg) that are not good in all conditions, such as hovering and fast flights. The mallard has large-aspect-ratio, thin, pointed wings, and the pheasant has low-aspect-ratio, broad, rounded wings. The mallard has lower power per unit mass and lower aerodynamic power at higher speeds. This explains why the mallard patters long before takeoff, while the pheasant can take off vertically if need be. Also, the mallard is one of the fastest flying birds, while the pheasant has a labored flight and rarely flies for long duration. The author gives a good discussion of the theoretical methods for estimating induced power. A theoretical model of how wing kinematics affects induced flow over insect bodies and the far-wake shows that wing beat frequency, stroke amplitude, and wing shape affect induced flow [66]. Navier–Stokes computations of a flapping wing at a low Reynolds number of 100 show the spanwise pressure gradient that prevents the LEV from being shed [149]. For the accurate determination of locomotive forces from wake traverse, both velocity and pressure field information are required [150].

3.6.2 Computation of Flow Due to Biorobotic Vehicles. Finite volume simulation of the inviscid forced-motion hydrodynamics of the MIT Robotuna vehicle has been carried out [151]. The Navier–Stokes equations are expressed in arbitrary Lagrangian–Eulerian form, and a mesh movement algorithm based on a modified form of the Laplace equation is developed to handle moving boundaries. The computed mean power compares with measurements within 10–15%, and the mean thrust compares with the

nonlinear potential method [152] within 12%. There is an intriguing phase difference in force and power time histories between the two computations.

3.7 Differences Between Rigid and Flexible Fins. Low-aspect-ratio, flexible fins produce LEVs that do not spiral, and the flow is dominated by axial flow and shedding of vortices. Large-aspect-ratio, rigid fins have strong LEVs that spiral spanward, creating vortex stability. We have preferred to demarcate, as above, in terms of flexibility rather than in terms of swimming and flying. Highly flexible, low-aspect-ratio wings do not seem to be used in flying where flapping frequencies need to be very high ($\times 10$ to 100) and, apparently, it is difficult to flex simultaneously at such high frequencies. Avian flight analysis suggests that large-aspect-ratio wings are more suitable for high-speed sustained flight, while low-aspect-ratio wings are better suited for hovering.

3.8 Wagner Effects. The Wagner effect is one of the unsteady effects that need to be considered in the mechanism of force production in swimming and flying animals. It is known that there is a time delay in the production of forces in impulsively started lifting surfaces. This delay is called the Wagner effect, and it has been experimentally elucidated [153]. Due to viscous effects, there is a delay in the development of the asymptotic value of the circulation around the lifting surface, that is, a delay in the establishment of the Kutta condition. The proximity of the starting vortex near the trailing edge in the early stages also affects this delay. The reduction in lift and drag can be estimated using the simple Wagner function, accounting for the distance traveled during stroke reversal [154]. Some have suggested that this effect might not be strong in insect flight [50,68], although others think differently [69,96]. Force measurements have been carried out in an abstracted penguin wing at chord Reynolds numbers of up to 125,000 at tow speeds up to 1.25 m/s [5]. During hovering and at low speeds ($\rightarrow 0$), a hysteretic effect reminiscent of the Wagner effect has been observed in the wing kinematics and forces measured. Because the accuracy of the estimation of the representative induced speed during hovering is somewhat doubtful, instead of relying only on lift coefficients, torque sensors were also used to determine if the observed hysteresis was genuine. The torque sensor measurements showed that some amount of hysteresis is definitely present, although it is not as large as given by the force coefficient plots. In addition, the hysteresis dropped as Reynolds number increased. A correlation of the motion of the stagnation point and lift forces also shows a phase difference reminiscent of the Wagner effect.

In the insectlike motion of wings, the wing mostly has steady kinematics except near the end, where the flip is rapid [59]. A time delay in forces has been observed during rapid wing flips at the end of wing travel, and it has not been examined if this happens when the flip is more gradual, as is the case in underwater experiments [8]. Models and numerical simulations do not compute lift and drag forces accurately during the rapid flips that are characteristic of insects, although they are otherwise accurate during the remaining phase of oscillation [59,61]. This is an area that needs further investigation. Also, future work is needed on the origin of the time delays found in the kinematics relevant to swimming and flying animals.

3.9 Added Mass Effects. When a lifting surface accelerates through a fluid, it experiences a reactive force due to the accelerated fluid. This is known as the added mass effect. It has also been termed “acceleration reaction” [60] and “virtual mass” [41,92], reflecting the authors’ emphasis on the domination of acceleration or virtual mass for force generation. Due to the simultaneous presence of circulatory forces, it may be difficult to calculate forces due to added mass. Added mass components can be estimated using empirically derived coefficients measured for various bodies [155]. For fish, added mass coefficients for an entire fish are 0.405 and 0.9255 in the fore-aft and up-down directions, respectively, and 1.0 for the pectoral fin sections [134]. An expression for cal-

culating the force due to the inertia of the added mass of the fluid has been given [156]. For a three-dimensional wing, it is calculated for each blade element and then is integrated along the span of the wing. In a pair of wings undergoing the “fling” motion, the interference of a pair of plates can increase the added mass of each plate, but only when the opening angle between the plates is small [45]. A method is available for estimating forces produced by swimming animals from the PIV measurements of velocity and added mass in the animal wake [157].

3.10 Effects of Twisting. High-speed photography of insects in free flight shows that the wing profile twists and flexes [31]. The wing is twisted along its span—the angle of attack being higher at the root. A theoretical model has been compared with measurements on a flapping foil that was passively twisting along its span [99]. The mechanical efficiency depended on advance ratio and wing twist, the maximum reaching a value of 0.83. This reviewer and co-workers have conducted measurements on twisting penguinlike fins, which show that twist affects efficiency ($\sim 5\%$) and thrust ($\sim 24\%$).

3.11 Flagellar Swimming: EEL Swimming. Here, we consider the swimming of eels and spermatozoa. Their kinematics and relationship to performance are summarized. Eels can swim thousands of kilometers and they have enough fat to undertake such a journey [158]. We consider eel swimming particularly because a robotic eel has been built and is an example of one of the earliest examples of robotic fish. The gait and low frequencies are amenable to shape memory alloys. Unlike fish, eels do not have a downstream pointing jet that is a reverse Kármán vortex [159]. However, they produce transverse jets. PIV measurements show that the drag and thrust vorticities in eels are not differentiated spatially as clearly as in carangiform fish, and the result is that the thrust jet is not discernable [87]. The cost of producing the wake increases with speed to the power of 1.48 and not 2.0. Eel propulsion efficiency is reported to be 0.43–0.97 [160]. Because of such wide disagreements, direct measurements of thrust forces produced are required and accurate measurements of efficiency are needed. Numerical simulation of eel swimming has been carried out where the kinematics for efficient swimming is obtained using a “genetic” algorithm to understand the relationship between body movement and forces produced [6]. It is unclear how comprehensively the technique has been validated, and claims of differences in flow physics with those observed experimentally are subjects of future studies. For example, an optimized Strouhal number in the range 0.6–0.7 has been reported, whereas it is known to be 0.2–0.4 for swimming and flying animals. However, while the condition of optimization of efficiency has been rigorously prescribed in the numerical simulations, most experiments have reported the Strouhal number of fin oscillation but have made no accurate measurements of efficiency. High efficiency is implicit in the popular Strouhal number—but this is not a rigorously established fact. Therefore, the questions are as follows: What is the efficiency of eel swimming? What is the optimized Strouhal number? Eels have two swim modes of kinematics; one is for efficient but slow swimming, and the other is for fast but inefficient swimming [161,162]. In the former, eels, nematodes, lamprey, or spermatozoa—whatever the flagellating animal may be—the animals undulate side to side down the length. In the latter, the front part of the body is kept straight and the thrust is generated in the rest of the body. In both kinds, ring vortices are shed and jets are produced. In any case, the reported work clarifies the vorticity composition of the wake. The lateral jets observed by experimenters [87,159] are shown to be due to ring vortices that are shed by the eel, two per cycle. One could then say that eels generate two lateral Kármán vortex streets and not one, and that they are vectored to the direction of motion. In this sense, their swimming is a variation in fish swimming. The experimenters also show that eel kinematics produces significant secondary flow, and the body undulation appears to interact with that. Producing too many vortices

per cycle and draining energy to the secondary flows might seem counterintuitive to efficient (or fast) swimming, as some indeed believe eel swimming to be. The interaction of the undulating body with the secondary flow might seem to be of higher order importance unless there is an exquisite nonlinear fluid and structure interaction. These are intriguing fluid-structure interactions in eel that require further investigation.

3.11.1 Flagellar Propulsion: Spermatozoa Swimming. Like eels, spermatozoa also use flagellar propulsion [6]. Swimming sperms have probably the lowest Reynolds number ($\sim 10^{-2}$) among swimming animals. A typical sperm is $1\ \mu\text{m}$ in diameter and $25\text{--}55\ \mu\text{m}$ in length—the head length is $5\ \mu\text{m}$, the remaining part being the flagellum (the tail). The helical flagellum is rotated at about 100 Hz by molecular motors embedded in the cell membrane. Its linear speed is reported to be between 0 and $160\ \mu\text{m/s}$ [163]. It is estimated to consume $2 \times 10^{-18}\ \text{W}$ of power, which can be obtained from the hydrolysis of a single adenosine triphosphate (ATP) molecule; this is considered to be efficient. ATP is like a “molecular currency” of intracellular energy transfer; it transports chemical energy within cells for metabolism. An exception to high-lift swimming and flying is the swimming of bacteria using the traveling wave of a rotating helical filament. The molecular drive is similar to that of a motor, with clearly identifiable stators and rotors. The stator has torque-generating units, and the rotor is made of ten rings of 45 nm diameter. The torque is generated in steps. The electrochemical gradient of sodium ion causes the stator to move or change shape, thereby imparting a torque to the rotor to which the filament is attached. The gradient could be used to slow down the filament rotational rate. The assembly of the molecular motor and the filament is called the flagellum. This is probably an example of the smallest rotary propulsor in nature.

3.11.2 Flagellar Motion. Typically, bacteria use four helical filaments to swim, rotating their body and the filaments. Depending on the direction of rotation (counterclockwise or clockwise), the filaments either bundle or disperse. Bundling allows propulsion. When the filaments disperse, the bacteria tumble and change direction. Experimental simulation has been carried out on a scale-model of bacterial flagellar bundling [164]. In the absence of the body, the bundling phenomenon was found to be purely mechanical—attributable to hydrodynamic interactions, bending and twisting elasticities, and geometry.

3.12 Propulsion of Microscopic Swimming Animals. The marine environment is teeming with microscopic animals swimming and feeding, while being constantly in motion. They swim in the transition range between Stokes ($Re \ll 1$) and Oseen ($Re \sim 1$) flows. An ocean-going, submersible, three-dimensional, digital, holographic system has been developed for tracking the motion of such small animals in their similarly scaled, naturally seeded surroundings [30]. The animals investigated are copepods of scale 1 mm, nauplii of scale 0.1 mm, and dinoflagellates of scale $10\text{--}30\ \mu\text{m}$. It is shown that the copepod has two kinds of motion—a periodic 0.5 mm upward jump to a point that is just short of the (lower) stagnation point of the previous recirculation zone, and a slower propulsion between jumps that partially counters the terminal sinking speed, thereby allowing the animal to see the same fluid as it slowly sinks. During the latter stage, the copepod develops a recirculation bubble spanning its extremities. When the recirculation bubble is fully explored or used for feeding, it initiates a jump to an as yet unexplored volume of fluid. The mechanism by which the feeding appendages produce the propulsive jet is not fully understood.

3.13 Limitations of Current Biomechanics Studies. The limitations of current biomechanics studies are discussed here from the point of view of engineering implementation. Fin kinematics is related to force production. Because application is system-based, the question is what kinematics can a fin produce

under all circumstances from system point of view, and not what we observe it to have in a narrow, controlled environment. Although animal studies may seem to be closer to the biological world than the studies on their robotic appendages, tethered animal flight, for example, could still not be representative of untethered flight. For example, fruit flies clap their wings during tethered flight, but not in untethered flight [17]. Apparently, the tethered animal flies in desperation to escape trying to maximize wing roll and lift production. It may be that, counter to researchers' best intentions, stressed animals have more mechanisms in their portfolios and are, in fact, harder animals to conduct controlled experiments with than their untethered brethren. For example, it is known only from “genetic” algorithm-based numerical simulation that anguilliform animals have two modes of swimming—a leisurely but efficient swimming and a fast but inefficient swimming [6]. Most biological studies are limited in their range of flight or swim styles and, therefore, may not be representative of insect flight or aquatic swimming in general [46]. So, measurements of animal swimming or flying in a controlled laboratory stream cannot always be generalized.

If we want to truly understand the mechanisms of swimming and flying animals, it is important to study animals in free flight and those that are freely swimming. Free-flight experiments have been carried out in the laboratory [31,75]. Experiments on fish freely swimming around obstacles have been carried out, albeit in captivity [11]. There might be differences in the free swimming and free flight of animals in the wild and those in captivity. Engineers would find that the uncertainties in the measurements of forces, moments, and efficiency in biological studies can be higher than what they are accustomed to—that is, those in laboratory biorobotic model studies conducted in controlled environments. Direct measurement of variables such as forces or efficiency is difficult with animals. Biological databases can consequently be sparse, too. But, these data gaps have sometimes led biologists to come up with insightful hypotheses that have contributed greatly to our understanding.

3.13.1 Limitations of Biological Studies: Production of Cycle-Averaged Versus Instantaneous Forces. The current biological studies on hydrodynamics or aerodynamics are not closely related to studies on controllers. Why should this integration be important? Animals have evolved as a complete system. The force mechanism is intimately related to what kinematics the animal uses for control. Many studies—both with live animals and with their biorobotic renditions—have studied cycle-averaged, hydrodynamic characteristics. However, this averaging smears the phase information and the large instantaneous amplitudes that can be of value to maneuvering. Engineering controllers would normally utilize cycle-averaged values [13]. It is much more difficult to develop a controller that makes use of the instantaneous force vectors [165]. If a controller works on instantaneous force vectors, then what is the best phase in a cycle when the kinematics should be altered? Instantaneous force vectors produced by one flapping fin (an abstracted biorobotic penguin wing) are not in a spherical pattern [8]. The pattern is rather beautiful and has a preferential direction. This suggests that many fins on a hull are required to allow body motion fully in all quadrants. Vectorially, the fins are specialized, rather than generalized.

3.13.2 Limitations of Biological Studies: Anatomical and Hydrodynamic Mechanisms. How do swimming and flying animals operate their pectoral fins to produce the desired kinematics in an efficient manner? In flying insects, a resonant mechanism is used to produce the motion in a narrow range of frequency. In swimming animals, it is not known if the same is true, although anatomical studies of dead animals have been carried out. It would be useful to carry out spring-mass damping analysis of the linkage and muscle mechanism simultaneously with fluid dynamics simulation. Experimentally, it would be useful to make measurements of kinetic energy in the pectoral fin and of damping while the

forces are being produced. Such studies would help the implementation of the high-lift mechanism in an efficient manner.

3.14 Summary. In a simple statement of summary, research on flying has focused on the aerodynamics of the flow over the wing, while research on swimming has mostly focused on the hydrodynamics gleaned from wake studies, and not as much from the hydrodynamics of the flow over the control surfaces. Both flying and swimming involve the production of a leading-edge vortex in the pectoral appendages of various topological complexities. Fish swimming involves the shedding of ring vortices in the near-wake, and the orientation of these vortices and the vector of the central jet determine the mode of swimming—straight or turning, or sinking or rising. There is a close relationship between the kinematics of the body and appendages and performance. In the flagellar swimming of eels or spermatozoa, there are two modes—low speed but high efficiency and high speed but low efficiency. In the former, a wave travels down the body; in the latter, flagellar swimming resembles caudal fin oscillation, which involves simultaneous heaving and pitching motions. The latter is reminiscent of high-lift actuation. It might be possible to design new turbomachines by implementing the mechanisms with appropriate drive systems. For example, low-speed, quiet, and energy-efficient ventilation of mines, tunnels, or buildings [199], or long-endurance swimming could be target application areas.

4 Understanding From Fluids Engineering: Modeling, Experiments, and Optimization

4.1 Science Questions

4.1.1 Origin of Force Generation. In this section, we review the nature of high-lift force generation in flapping foils. Vortex dynamics (such as the formation of LEVs) and flow bifurcations (such as at the stagnation and reattachment points) have been revealed from dye and surface hot-film array studies. The results are synthesized in Refs. [5,8]. The formation of the LEV is shown both by dye and hot-film array diagnostics. Hot-film surface array and force measurements have shown a correlation between unsteady force generation and movement of the stagnation point. The flapping foil has unsteady kinematics. The first contact of the solid surface with the surrounding unsteady pressure field is at the stagnation points. How unsteady, therefore, is the point of stagnation? How is its motion related to the unsteady forces produced? The wall-shear sensor signals are interpreted from the surface hot-film time traces in the following manner. At the forward stagnation points and at the flow separation and reattachment points of the surface, streamline patterns diverge, causing a minimum in wall shear and heat transfer. A surface array of wall-shear sensors was used to mark the oscillating forward stagnation line in a rolling and pitching hydrofoil [8]. Note that lift and the angle of attack are nearly linear in both steady and unsteady flapping foils. The location of the stagnation point is a measure of the local angle of attack and this can be calibrated to lift forces. In this manner, it is confirmed that in steady flow—and, indeed, in unsteady flow as well—the angle of attack and the lift forces are linearly related. There is a slight phase difference (~ 30 deg) between the two, attributable to the delay between the kinematics and the forces produced due to Wagner effects.

4.1.2 Scaling Laws of Swimming. In bodies producing thrust jets, the frequency of wing oscillation can be expressed as a Strouhal number or as a reduced frequency [166]. In avian biology, the reduced frequency of a full animal is given as $\sigma = \omega c / U$, where ω is the radian frequency (2π Hz), c is mean chord (wing area/maximum length), and U is forward speed [167]. If σ is far below 0.50, then quasisteady flow can be assumed; otherwise, the lift enhancement due to unsteady flow needs to be accounted for. The lift coefficient typically is 0.2–1.3 [5,8] and, therefore, strong unsteady effects can be expected, which were indeed found to be the case. In avian biology of wings, the nondimensional angular ve-

locity $\hat{\omega} = \omega \bar{c} / U_i$, where ω is the angular velocity, \bar{c} is the mean chord, and U_i is the wing tip velocity [31]. Sometimes, wing tip velocity is expressed as a ratio of the chordwise components of forward velocity at the fin tip due to translation and revolution, $\mu = U \cos(\phi) / R \dot{\phi}$ [63]. In model fruit fly experiments, $\hat{\omega}$ is in the range 0–0.374 [156]. Later investigations have shown that the Strouhal number is a more relevant parameter for unsteady kinematics of appendages because there is largely a convergence in its value among swimming and flying animals, albeit with some variation. In aquatic biology and aquatic biorobotics, in the case of a flapping caudal fin or pectoral wing, reduced frequency is also known popularly as the Strouhal number, although strictly speaking this is a misnomer [18], and is given by $St = fA / U$, where f is the flapping frequency (unlike natural frequency in vortex shedding behind bluff bodies), A is the width of the jet downstream of the flapping foil or the excursion of the trailing edge of the fin, and U is the average jet speed or forward or flow speed. The difference between St and σ is in the choice of the length scale—it is flow aligned in the former and across the flow in the latter. These two length scales directly signify the difference between steady flow and unsteady flow. The former length scale is a legacy of classical steady aerodynamics as in a flow-aligned aircraft wing. The latter length scale denotes how much momentum is being put into the fluid at the same frequency. A feathering parameter is also used to express the wing oscillation. It is given as $\chi = (U \alpha_m) / (\omega h)$, where α_m is the maximum angle of attack in the wing beat cycle, ω is radian frequency (2π Hz), and h is one-half of the wing beat amplitude. When α_m is large, $\chi = \alpha_m / \arctan(h_0 \omega / U)$. The feathering parameter is closer to St than σ is. In a two-dimensional heaving and pitching fin, the Strouhal number based on heave amplitude is $St = 4\pi h_0 \omega / U$, where h_0 is the heave amplitude in two-dimensional fin works, ω is the circular frequency in rad/s, and U is the forward or towing speed (or maximum heave velocity if hovering), $h(t) = h_0 \sin(\omega t)$, and $\theta(t) = \theta_0 \sin(\omega t + \psi) + \theta_{\text{bias}}$. Here, ψ is the phase angle between heave and pitch, usually set to 90 deg for best efficiency. In finite size fin rolling and pitching about a pivot point, the Strouhal number is given as $St = 2f \phi_0 R_{\text{av}} / U_\infty$, where $R_{\text{av}} = \sqrt{r_o^2 + r_i^2} / 2$, and where r_o and r_i are the outer and inner radii in reference to the roll axis, respectively. Foil motion is determined by roll amplitude ϕ_0 , frequency $\omega = 2\pi f$, pitch amplitude θ_0 , pitch bias θ_{bias} , and the phase between roll and pitch (which, unless stated otherwise, is set to 90 deg). Also, $\phi(t) = \phi_0 \sin(\omega t)$, $\dot{\phi}(t) = \omega \phi_0 \cos(\omega t)$, and $\theta(t) = \theta_0 \sin(\omega t + \psi) + \theta_{\text{bias}}$.

Measurements of forces, moments, and torque have been carried out in a penguin-inspired flapping fin under water in hover and cruise [8]. The results were similar for 20-cm- and 30-cm-span fins. These relationships have been observed for hover. Thrust direction depends on pitch bias and the phase difference between pitch and roll, that is, +90 deg or –90 deg. The magnitude of the thrust is proportional to the squares of roll angle and frequency of oscillation. Power depends on pitch amplitude. The first harmonic of thrust and lift changes little with pitch bias, while the second harmonic depends on mean force. These trends can be used in the modeling of the laws of a controller. During cruise at 0.42–1.25 m/s, these relationships have been observed. In the mean sense, the advantage over steady fin diminishes as speed increases. For the same pitch bias of, say, 10 deg, increasing tow speed produced higher maneuvering forces. Sensitivity to foil profile was low—switching the leading and trailing edges produced no large discernable difference in the time traces of thrust, lift, pitch, or roll power.

4.1.2.1 Scaling laws of Strouhal number of tail fin oscillation and efficiency. Triantafyllou and co-workers [18,26] examined the scaling laws of fish swimming and of oscillating fins. Drag-producing flow past a rigidly held obstacle produces an alternating Kármán vortex train, with an intervening jet pointing upstream. A

Strouhal number defined as $St = fd/U$ of 0.21 describes the universal vortex shedding process in the Reynolds number Ud/ν range of 60 to 2×10^5 [168]. On the other hand, the thrust-producing flapping tail of a fish produces a reverse Kármán vortex train of alternating vortices, with an intervening jet pointing downstream at a universal Strouhal number fA/U of 0.25–0.35, probably in the length Reynolds number range of 10^2 – 10^7 [16,18,26]. Here, the Strouhal number is defined with f (the flapping frequency of the caudal fin), A (the peak-to-peak flapping amplitude at the tip of the caudal fin), and U (the stream velocity). The instability process leading to the two Kármán streets is different—in the rigidly held obstacle, drag-producing case, it is an absolute instability; in the thrust-producing flapping fin case, it is a convective instability [18]. For this reason, it has been argued that it is more appropriate not to call both universal frequencies Strouhal numbers, and “reduced frequency” might be a better name for the thrust-producing wake. But we saw earlier that Lighthill’s reduced frequency has a different combination. So, a more appropriate name is “flapping number.” As in the recent trends in medical sciences, it is useful to give informational names rather than eponyms.

4.1.2.2 Other scaling laws of fish swimming. Other scaling laws of fish and fishlike swimming include the wavelength/wave speed ratio of fish tail oscillation and fin stiffness [18]. Some authors have argued that thrust is produced not only by the various fins, but also by the fish body. In the flow over a wavy surface, one expects pockets of trapped, separated flow and high attendant drag. So, how do fish minimize drag and produce thrust to match that level? The ratio of the phase speed of the fish tail and the stream speed $c_p/U = f\lambda/U > 1$ for thrust production ranges between 1.29 and 1.37 in cod, and for saithe it is 1.19. Here, λ is traveling wavelength. For two-dimensional surfaces, $C/U > 1.0$ leads to drag reduction. In a robotic fish, turbulence in the boundary layer reaches a minimum at $C/U = 1.2$. Thus, there is convergence in the various studies regarding the kinematics of the body. But, how much is known about the fluid-structure interaction of the body? Experiments show that, compared with a stiff foil, chordwise flexibility (measured by Shore toughness) can increase efficiency from 0.62% to 0.86%. Theoretical studies accounting for the unsteady effects are needed to understand why flexibility is more widely prevalent in the fins of swimming animals that have lower aspect ratio, the sunfish pectoral fin being one example.

Measurements of force and the motions of the wake vortices in an axisymmetric cylinder equipped with seal-inspired flapping caudal fins, using a phase-matched laser Doppler technique, have been carried out [169]. The authors examined the effects of interaction of the fins and the main body and between fins. The generation of the wake was classified as natural or forced. In the former, Reynolds numbers are low, a continuous sheet of vorticity is produced by the wake, and an instability process leads to wrapping into discrete vortices. Higher-order effects appear in the axial force coefficients when the Strouhal number is > 0.15 . The axial force coefficient is bounded between two asymptotes—the natural distribution given by inviscid theories at the lower end and an asymptote given by the characteristics of a forced and discrete shedding process at the higher end. In between, the nature is not universal, but transitional, where details such as the mode and frequency of flapping and the number of flaps are influential. Measurements of force and of vorticity-velocity vector maps in the axial and cross-stream planes show the region of the axial thrust jet. The efficiency of axial force production reached a peak below the Strouhal number range of 0.25–0.35. The Strouhal number of tail flapping does emerge as an important parameter governing the production of net axial force and efficiency, although it is by no means the only one; other parameters include flapping frequency and mode of flapping. The efficiency of thrust production, when the two caudal fins move in phase (waving), which is analogous to one caudal fin of fish, is higher than when

they are in the opposite phase (clapping). The importance of induced drag has been traced to the flapping mode and the attendant interaction of the flap-tip axial vortices. The phase variation in simulated and minute head swaying can modulate axial thrust produced by the tail motion, within a range of $\pm 10\%$, with no significant thrust improvement. This precision indicates that the phase relationship of vortex shedding from various discrete vorticity-generating surfaces is an effective tool of maneuvering in a fish. The general conclusion is that the mechanism of discrete deterministic and phased vortex shedding produces large, unsteady force vectors, which makes it inherently amenable to active control and suitable for precision maneuvering.

It is commonly thought that fish caudal fins have a Strouhal number of 0.25–0.35, because this is the predicted range for maximum efficiency, thereby uniquely relating Strouhal number to efficiency [12,26,169]. However, measurements of propulsion efficiency in animals are few and their accuracy is questionable, and efficiency may be dependent on other factors as well, whereby peak efficiency may occur at Strouhal numbers that are slightly different from the popular values of 0.25–0.35. Other factors may include the angle-of-attack range, amplitude-to-chord ratio, and the phase angle between roll and pitch motions [12,102,170]. Indeed, later measurements [171] show that these effects can cause a 20% reduction in the popular Strouhal number from that for the maximum efficiency. The Strouhal number of captive cetaceans—not their efficiency—has been measured. While the average Strouhal number of each species falls in the accepted range, the numbers vary over a large range within species and among individuals. 74% of Strouhal numbers fall in the range 0.20–0.30 and not in the range 0.25–0.35—the range predicted for maximum efficiency; only 54% of the values fall in the maximum efficiency range. Furthermore, in cetaceans, it is not just the Strouhal number that occurs in a narrow range, but the constituent variables f and A also do. Thus, it is not fully satisfying to claim that the Strouhal number captures the physics of thrust generation.

In the biorobotic work on a cylinder with attached caudal fins, efficiency depends on Strouhal number and another yet unidentified variable [169]. Measurements of efficiency have been carried out on a single abstracted penguin fin in water. The fin was undergoing rolling and pitching motions, and torque sensors were used on roll and pitch motors to measure efficiency. In the non-hovering case when pitch bias is set to zero, the data offered an opportunity to determine the effects of Strouhal number and fin kinematics on efficiency. It is shown that efficiency (η) can be as high as between 0.5 and 0.6 at Strouhal numbers of 0.25–0.70—a range higher than commonly given [26] for fish, which is 0.25–0.35. Here, the Strouhal number is defined with fin motion amplitude equal to the arc length traversed by the point on the fin that divides the swept area in two. Furthermore, for the single fin, efficiency has a peak distribution with Strouhal number and also with pitch amplitude. Pitch amplitude was varied in the range of ± 15 deg to ± 65 deg, and efficiency was found to peak ($\eta > 0.55$) in the pitch amplitude range of ± 25 deg to ± 45 deg in the Strouhal number range of 0.28–0.55. Peak efficiency occurred at higher Strouhal numbers at higher pitch amplitudes and at lower Strouhal numbers at lower pitch amplitudes.

Because Strouhal number and efficiency have not been measured simultaneously in any species, it would be more accurate to conduct a direct numerical simulation of animal (fish/dolphin) swimming and calculate propulsive efficiency and Strouhal number to resolve this issue definitively. Perhaps the MIT Robotuna or other emerging biorobotic fish could also be used in a biorobotic experimental work to validate the simulations. In any case, the Strouhal number captures the bulk of the unsteady effects and is useful in the development of control laws. Pitch amplitude can offer more accurate tuning of the laws.

4.2 Modeling of Animal-Inspired Swimming. Penguin thrust has been modeled using experimental data on the drag of a

wingless carcass cast and the forces produced by flapping wings [85]. The flapping frequency was measured from swimming penguins. A blade element analysis was used to compute wing beat thrust. In blade element analysis, the wing along the span is divided into many segments, and quasisteady two-dimensional flow is assumed over each segment. The forces on the segments are summed to obtain the total force on the wing. The blade element analysis was found to be more reliable because it showed close agreement between the thrust and drag estimates, in the parameter range of penguin swimming studied. An unsteady modeling on the other hand did not give close agreement between thrust and drag, and future work is needed. The submerged and surface swimming powers (N m/s) are modeled, respectively, as $P_{T\text{-sub}}=3.71U_b^{3.0}$ and $P_{T\text{-sur}}=5.88U_b^{3.6}$, where U_b is the mean forward speed of the swimming or animal. LEV-based unsteady actuator flows do not have strong effects of Reynolds number, and inviscid effects dominate. A closed-form expression—a rarity—of forces and moments produced by a general two-dimensional Joukowski foil in arbitrary motion is available [172]. The theoretical hydrodynamic method of conformal transformation and point vortices is used in the inviscid analysis. Thrust-producing foil oscillation parameters reproduce a nonsinusoidal force time history that is beyond the scope of linear theory. The work shows that the effects of added mass and vortices are independent.

4.2.1 Modeling of Penguin Swimming as a Pendulum. The thrust jet wake vorticity patterns of fish swimming and fluttering objects bear similarity [12,19]. A simple plunging plate also produces the detailed features of flow seen in dragonflies [65]. This result can be used to model dolphin swimming as a pendulum. The fluid-structure interaction of a dolphinlike animal is used to produce the relationship between Strouhal number, speed, and the kinematics of the caudal fin (frequency and amplitude of oscillation). The natural frequency of oscillation is the inherent frequency in the Strouhal number because the body oscillates like a pendulum. The natural frequency is given by the body length, as in the law of the pendulum. The variation in frequency with body length and speed is described by this relationship.

4.2.2 Methods for Calculating Lift Over Wings Due to LEVs

4.2.2.1 Leading-edge suction analogy: Nonflapping wings. Before we consider biology-inspired, unsteady high-lift, it is instructive to recall what relevant matter is known from steady-state classical aerodynamics. A two-dimensional or large-aspect-ratio steady wing separates at high angles of attack and stalls when lift forces precipitously drop. On the other hand, delta-shaped main or canard wings that have a low aspect ratio and sharp leading edges are deliberately operated at high angles of attack and are partly separated near the leading edge in steady flow. The pressure distribution around the sharp leading edge produces suction, and a large detached LEV ensues. However, instead of approaching stall, the wing lift is nonlinearly augmented substantially above the potential lift. The steady flow vortex lift can be accurately calculated using computational methods, such as nonlinear panel methods or Euler or Navier–Stokes methods. The steady flow vortex lift component of the total lift has been modeled by assuming that the low pressure in the vortex core in the detached flow originates from the leading-edge suction effects in attached flow. The vortex produces a force that is normal to the chord, whereby it also has a small drag component. Another steady flow method, even simpler, is to add the component of drag due to a normal velocity to the delta wing to the lift direction.

4.2.2.2 Cross-flow drag vortex analogy: Flapping fins. The LEV due to three-dimensional rolling and pitching fins is analogous to the cross-flow drag vortices of the fin when normal to flow, as in a bluff body. The cross-flow drag vortices of a static fin placed normal to a steady flow are similar to the dynamic stall vortices of the unsteady fin [5,8]. It has been proposed that the rolling and pitching motions constantly change the angle of attack

and keep the vortices attached to the fin. In this manner, stall is prevented and the steady behavior of lift and drag applies and one needs to know only the instantaneous angle of attack from the fin kinematics. Excellent agreement with instantaneous and time-averaged forces and power in flapping fins has been obtained. In delta wings, in the presence of a strong, adverse pressure gradient, the LEV bursts. When this happens, vortex lift is lost. No such vortex bursting and loss of lift have been reported in swimming and flying animals or in flapping wings.

4.2.3 Quasisteady Modeling. The difference between quasisteady modeling and unsteady modeling of forces produced by flapping wings has been examined [36]. The work reflects great physical insight. It was proposed that, if the mean lift coefficient required for hovering exceeds the maximum lift produced in steady state, then the assumption of quasisteady state is not valid. However, if the mean required lift coefficient is below the maximum measured steady lift coefficient, then the assumption might be valid. Literature survey indicated that the mean value of lift coefficient required for hovering is higher than the maximum measured steady-state values. This meant that unsteady models and not quasisteady models are required to compute insect flight. However, earlier works [36] did not benefit from accurate measurements of mean forces on isolated wings and of the time histories of forces [156]. Such measurements show that the maximum mean value of the lift coefficient of the wing is much higher than previously thought, and quasisteady modeling might be applicable. Sane and Dickinson [156] gave such a model with remarkably good general agreement with the measurements of time histories of forces. Total instantaneous force on the wing is considered to be the sum of inertia force due to added mass, instantaneous translational force, rotational force, and force due to wake capture. The first term is calculated using blade element analysis. The second term is obtained from the measurements of lift and drag. The rotational forces are determined at times when inertia and wake capture forces are small, by differencing the estimates of translational forces from the measurements of total forces. This type of quasisteady models is useful in understanding the mechanism budget. However, the model in Ref. [156] might benefit from further improvement. For example, during the short periods when upstrokes and downstrokes switch from one to the other, the spikes in the measured lift and drag values are not reproduced by their revised quasisteady model. But note that the wing kinematics used is not a simple harmonic—the translational and rotational velocities are constant during most of the stroke and abruptly change near the ends of the strokes. In previous sections on vortex methods and potential theories, the contributions based on conventional aerodynamic theories are given for modeling the forces produced by the wings of flying insects. The extension of the quasisteady model in Ref. [156] to flexible fins has not led to good agreement with the measurements of lift, thrust, or power for fish [134].

4.3 Efficiency. For aquatic propulsion, η , the hydrodynamic efficiency of propulsive flexural movements, has been defined as similar to Froude efficiency of a propeller as $\eta=U\bar{P}/\bar{E}$, where U is the mean forward velocity, \bar{P} is the mean thrust required to overcome what viscous drag the fish would sustain for forward velocity U if it remained rigid and symmetrical, and \bar{E} is the mean rate at which flexural movements work against the surrounding water [91]. For heaving and pitching fins, propulsion efficiency is defined as $\eta=C_T/C_P$, where C_T is the coefficient of thrust, C_P is the coefficient of power, and η_{thermal} , η_{electric} , and $\eta_{\text{hydrodynamic}}$ are electric, thermal, and hydrodynamic efficiencies, respectively (Fig. 4). The thermal efficiency refers to the mechanical efficiency of a flying insect based on the measurements of heat produced after flying [46,173,174]. The hydrodynamic efficiency is based on measurements of roll and pitch torques in the case of single fins [5]. In the case of the entire sunfish, the hydrodynamic effi-

ciency has been defined as the ratio of added downstream kinetic energy to the total fluid kinetic energy [131]. Efficiency in rolling and pitching fins of finite size is defined as $\eta = \bar{T}U_\infty / \bar{P}_{\text{hydro}}$. It can be shown that $\bar{P}_{\text{hydro}} = -\tau_\phi(t) \cdot \dot{\phi}(t) - \tau_\theta(t) \cdot \dot{\theta}(t)$, where τ is torque—roll (ϕ) or pitch (θ). In PIV wake traverse of the entire fish, the hydrodynamic efficiency has been defined as $\eta = (\text{added downstream kinetic energy}) / (\text{total fluid kinetic energy})$.

Measurements of propulsive efficiency of animals are extremely valuable but sparse. The output power of penguins has been measured from drag estimates [85,175]. The input power was measured from oxygen consumption. The ratio of these powers (called the energetic efficiency) varied with speed U as $\eta_0 = 0.103U$ (m/s)^{2.8}. The maximum efficiency η_0 measured at 1.26 m/s was 0.192. If the maintenance metabolism is subtracted from the input power, the propulsive efficiency is about 0.247. Literature has reports of considerably high estimates of propulsion hydrodynamic efficiency of penguins, dolphins, and other swimming animals that are indirectly obtained via hydrodynamic modeling, and they should be treated with caution. Measurements of forces and input power are not carried out with a tethered fish—a technique used with flying insects. Instead, an indirect method of estimation is from a balance model that measures the movement of the center of mass, which is body acceleration, of fish swimming in a flow tank [134]. The fish move back and forth over a cycle. It is estimated that the mechanical efficiency of the pectoral fins (i.e., the cycle-averaged thrust measured $\times U$ / power measured) of three spine stickleback fish, a very small fish that has flexible fins, is between 0.13 and 0.29. The hydrodynamic efficiency of an abstracted penguin fin for hover and cruise has been measured [5]. These matrix (flow and fin kinematics) based conventional style measurements took nearly 18 months to carry out and were parametric in approach. Subsequently, a “simplex” and annealing based methodology was developed to search for the best efficiency at a given coefficient of thrust. The efficiency envelope was reproduced typically in a few minutes, starting from any randomly selected set of kinematic parameters. No explicit knowledge of hydrodynamics was used. However, selective input of hydrodynamic insight further accelerated the optimization process. In principle, this approach might allow vehicles to perform outside the design envelope. Fish swim in a way that all side forces are zero over time, drag is minimal, and thrust equals drag. Most studies have examined biomechanics from this point of view. For maneuvering, such budgeting for nonzero side forces has not yet been carried out. How animals match fluid-structure impedance to maneuver efficiently or increase thrust is an open question. The design laws that account for the fluid-structure interaction are not known.

4.4 Flapping Foils and Traveling Wave Propulsion. Flow visualization shows the wake structure of a low-aspect-ratio (span/chord=0.54) flapping plate at Strouhal numbers below and above 0.25 [176,177]. Below a Strouhal number of 0.25, the wake consists of single horseshoe vortices of alternating sign shed twice per cycle, which is termed “2S type” [178]. Above 0.25, a pair of vortices is shed in each half of the cycle, which is termed “2P type.” Not all fish roll and pitch their pectoral fins for propulsion. For example, sting rays are thought to have enlarged pectoral fins, and undulatory waves pass down the fins to generate thrust—a form of propulsion called *rajiform*. The variation in the kinematics of the fin and the muscle motor pattern with speed has been examined [179]. Velocity increases with fin-beat frequency, wave speed, and the duty factors of the pectoral muscles. However, fin amplitude and the duration of muscle activity do not change with velocity. There is a clear delineation between muscle groups that do positive and negative work. Experiments on the oscillating fin model of a ray fish show that a wave travels downstream while the fin rolls [180]. The fin produces thrust during both the upward and

downward strokes. The maximum efficiency is estimated to be 0.40, which occurs at a Strouhal number of 0.25, based on the spanwise average deflection of the trailing edge, and not on the wake width [101].

4.5 Real-Time Optimization of Leading-Edge Vortex. An optimization algorithm for moving bodies called the covariance matrix adaptation evolution strategy has been developed [162]. It relates the body kinematics with the cost function in an efficient manner. The property of the algorithm is that it identifies many minima rather than a single optimum point. In the numerical investigation of the optimization of the drag reduction in a cylinder, the algorithm converged after 260 iterations, and a Cray J90 computer took 4 h of CPU time. This can be compared with the experimental flapping foil optimization [5] of 4 min and 40 iterations for optimization of efficiency using a Pentium 2 personal computer, where the CPU time is less. The number of iterations required is probably a somewhat fairer basis for comparison than the CPU time because the flow is “free of time cost” in the experiments. The code is available as a patch that might facilitate future use in other simulations [162]. The value of the code appears to be in the optimization of computationally intensive problems. Real-time optimization and the control of the hydrodynamics of one or the assembly of many fins are exciting new areas of research where both cycle-averaged and instantaneous approaches are being pursued [13,165].

5 Applications of Understanding

There are lessons learned by comparing biological locomotion designs, their biorobotic implementations, and their conventional engineering implementations [19]. Gaps between biological designs and their biorobotic renditions remain. The differences are spread over many layers of underlying science principles/mechanisms, sensor characteristics, energy sources/handling, philosophy/architecture of controllers, and materials. Biological systems use analog processing and are adept at computing a vast number of events via nonlinear algorithms for actuator control, a process that is beyond the capability of digital technology today. Transitions from biology to engineering can be seen as a structure-function relationship where fabrication difficulties come across as the most important impediments to such transitions [181]. While we have focused on the hydrodynamics and aerodynamics of swimming and flying animals that lie external to the body (such as the formation of LEVs), less attention has been paid to how animals produce the observed wing kinematics. Engineers have been hesitant to apply unsteady fluid dynamics mechanisms of high-lift due to concerns regarding performance cost (penalty) and reliability. Therefore, it is instructive to understand how fish mechanically produce the intricate fin motions and hold them appropriately under load.

Generalized biomechanical models of the muscle, tendon, and bones of fish have been developed [182]. Physical models show the existence of strain energy storage under bending [183]—a system that can be used to store energy during deceleration of the control surface and that can be used during acceleration to enhance electromechanical efficiency. Fish that cruise over long distances have a fiber matrix that criss-crosses at 45 deg to the vertebral axis. This fiber architecture, along with twisted spines, is a candidate for such energy storage. The importance of energy storage systems in swimming and flying animals and their impact on unsteady fluid-structure interaction need further research. The oblique tandem arrangement of fish has been used to provide force transmission pathways to the backbone and gain mechanical advantage to bend the body. In nature, parts have broad application but poor performance in a narrow range, while it is just the opposite in man-made parts. For this reason, man-made assemblies of biorobots are unlikely to closely match animals. In other words, a hybrid system would require a judicious mix of architecture in nature and man-made components.

Theoretical analysis and experiments with two-dimensional flapping foils agree well in thrust in a wide range except for the case of zero forward speed [184]. A 7.5 m/s shallow-draft boat of 900 kg payload was designed. The conclusion was that oscillating foils can provide efficient propulsion with a high degree of maneuverability. For feasibility, hydrodynamics is not a limitation, and the mechanical drive system was considered a challenge in 1968, which may not be the case today.

5.1 Transitioning the Evolved Hydrofoils to Engineering.

The tables of cross sections of National Advisory Committee on Aeronautics (NACA) profiles have played a seminal role in the development of aerodynamic and hydrodynamic turbomachinery blades, aircraft wings, and submarine sails. But they are meant to be used where dynamic stall is undesirable. So, the first question is as follows: How close are animal fin or wing cross sections to NACA profiles? Probably, a more useful question is the following: What can we learn from their flexible profiles and three-dimensional nature? The first question calls for a careful documentation of animal fins and dissemination of such fundamental data of nature's legacy to us. This was realized by this reviewer while heading the Biorobotics Program at the Cognitive and Neurosciences Division of the Office of Naval Research. Professor Frank Fish of Westchester University was commissioned to organize a team, in collaboration with the Smithsonian Institution and others, to collect CAT scans at 1 mm intervals. (The data set is contained in seven DVDs, which are in the public domain in the United States of America and may be obtained from Professor Fish of the University of Westchester, Westchester, PA.) Animals whose control surfaces were scanned are whales, seals, sea lions, manatee, penguins, sea turtles, rays, shark, and tuna. The data set remains largely unexplored. The highlights of the animal control surfaces are long, thin trailing edges particularly near the wing tips, wing-hull juncture cross sections, and thick leading edges. Because the scans also reveal the inner bone structure, the mass distribution can be gleaned as a clue to the elastic property of the dynamic wings. Measurements of the bodies and flukes of cetaceans have been reported, although they are not comprehensive. The cross sections and planforms of the flukes are thought to be related to performance. A systematic study of the relationship of these sections with those of the NACA profiles is worth undertaking. In particular, unlike the two-dimensional NACA profiles, the above data sets might give us benchmarks of what three-dimensional nature has optimized into. Measurements of humpback flippers show that the cross section resembles NACA 63₄-021 and NACA 0020 profiles [185,186]. The humpback flipper leading edge has been claimed to delay stall while increasing lift and decreasing drag. The experiments, however, were carried out in steady flow. Quasisteady modeling [5] suggests that the dynamic stall delay characteristics are an extension of the steady-state lift and drag characteristics. It is useful to know of steady behavior, but this should be considered to be only a precursor of more that needs to be known in unsteady flows. Furthermore, the six-series NACA profile was developed with an emphasis on laminar flow. At high angles of attack, such foils are less likely to reattach because the low kinetic energy fluid near the wall succumbs to the increasing pressure energy in the streamwise direction. So, how can the cross section of whale wings with their bulbous leading edge closely resemble the six-series in the mean? The answer might lie in the high Reynolds numbers of flippers. Even for steady flows, there is a need to focus on high Reynolds numbers where the flow might naturally become turbulent and allow reattachment of stall vortex while retaining the low-drag advantage of laminar flow in many regions of the flipper. What the close NACA cousins of the flipper cross sections are is an important question because the cross section presupposes similar characteristics.

5.2 Underwater Vehicles. Underwater vehicles implementing pectoral and caudal fins inspired by swimming and flying animals

have been reviewed [19]. The research originating at the Office of Naval Research received focus and the need to integrate the high-lift mechanism with neuroscience-based control and artificial muscle was put forward to allow "instantaneous" phase synchronization of many actuators. The need to focus on science principles instead of biomimicry was also emphasized. The biorobotics progress made at the Naval Undersea Warfare Center in Newport, RI, up to the year 2000, has been reviewed [12]. The work pointed out the value of fish-inspired robotics to low-speed maneuvering, rather than to straight high-speed propulsion where propulsor efficiency has reached a high level of perfection. The value of artificial muscle in the context of active camber control of propulsor blades was explored.

5.3 Seal-Inspired Vehicle. Bull elephant seals have dual flapping caudal fins. Inspired by them, an experimental model was built with a pair of flapping foils at the tapered tail end [169]. The foils could clap (out of phase) or wave (in phase). A divider plate was placed between the foils to enhance the clap and fling effects. Efficiencies as high as 0.60 of the flapping foils and as high as 0.40 of the combined cylinder and foils were measured. For the waving foil motion (which mimics a fish's caudal fin motion), the dominant Strouhal number was close to that found in fish but only in a narrow frequency range [26]. A sliding protrusion was also incorporated near the nose to simulate the formation of any vortices due to the head swaying of animals. It was found that this modulated the thrust within $\pm 10\%$.

5.4 Biorobotic High-Lift Vehicles. A flapping wing producing a LEV of high-lift is an intelligent structure—not in the cognitive sense, but in the sense of efficient and flexible use of structures. "Challenge is not simply to replicate an insect wing, but to create a mechanism that flaps it just as effectively" [181]. Figure 3(a) shows a six-finned BAUV built at NUWC by the author's team, whose hull is cylindrical and rigid [8,13]. The fins are abstracted penguin wings. Two generations of vehicles, the BAUV and SPLINE (Fig. 4), have been built, the latter with motors of higher torque and efficiency but fewer degrees of freedom. The fins are simplified rigid versions of penguin wings [5]. Both open-loop and closed-loop controllers have been developed [13]. An olivocerebellar nonlinear controller has also been developed to produce instantaneous phase synchronization of the fins or give them any desired phase shifts [165]. Each fin is capable of operating at its own kinematic settings—such as frequency, roll, pitch angle, and phase difference between roll and pitch. The result is a vehicle with multiple degrees of freedom. The following examples of precision maneuvering have been accomplished: practically zero-radius turning (Fig. 3), alternate pitching, crabbing, entering, parking in and leaving a small side chamber in a channel, precision depth and thrust control, and sideways motion between two narrow parallel walls. The vehicle's displacement is similar to that of shark, and its propulsive power is similar as well. The vehicle produces very low levels of radiated noise, which is a global measure of the absence of conventional sources of propulsor noise such as ingested turbulence, blade tonals, and trailing edge vibration. At MIT, several versions of a Lycra and foam sheathed robotic vehicle (the Robotuna) have been built that are very similar to a bluefin tuna. The goal was to build a propulsor that is better than the conventional propulsors, remaining faithful to fish form but to only the zeroth order. The drive system resided outside the fish. The Robotuna is a useful exercise in the synthetic integration of our understanding of caudal fin-based fish swimming, kinematics, scaling, control architecture, design, fabrication, and practicality. The Robotuna has allowed the direct confirmation of Gray's paradox [105]. It is indeed true that the drag of the swimming fish, constituted of an undulating body and an oscillating caudal fin, is lower than that of the rigid body, where the body is not undulating and the caudal fin is not oscillating. However, while Gray's paradox [105] implies a sevenfold reduction in drag, the reduction in the Robotuna is about half. The Robotuna work has succeeded in

creating a great deal of popular and professional interest in biorobotics and has been an invaluable training ground. Modern underwater propulsors are highly efficient (>80%), and it is unlikely that any fish-based mechanism would have significant impact on the design. Realizing this, it has been more fruitful to focus attention on the high-lift mechanism of pectoral fins and on maneuvering rather than on cruising [19,169]. However, at low speeds (<5 kn), propulsors could be supplanted by biology-inspired propulsion systems. The pectoral fin kinematics of the black bass on a rigid cylinder has been implemented [98]. Three motor and gear drives are used to roll the rigid fins forward and backward, upward and downward, and for rotation about the span. It is unclear if any high-lift LEV is being utilized or what the efficiency is. A rule-based fuzzy controller has been developed. A ± 90 deg phase difference between pitch and roll between the left and right fins is used for turning [13]. Maneuvering in a quiescent tank has been demonstrated.

5.5 Biorobotic Rendition of Propellers. Inspired by the fanned wing tips of soaring birds, winglets have been successfully incorporated into modern aircraft. The fanned wing mechanism of breaking up induced drag vortices for drag reduction has been used to design a novel propeller that has no wing tip [187]. A three-bladed propeller, for example, has the wing tips joined in a convoluted ring. Quiet and efficient performance is claimed.

5.6 Vortex Energy Extraction and “Free-Ride”. Behavioral observations indicate that flocks of birds and schools of fish (or fish behind obstacles) orient in a way that suggests they are utilizing the energy in the incoming vortex to enhance propulsion efficiency. These hypotheses receive support from synthetic laboratory experiments [48] and the controlled experiments with fish swimming in a laboratory stream behind an obstacle [25]. Flow visualization at a low Reynolds number of 550 and complementary force and torque measurements have been carried out at a high Reynolds number of 20×10^3 on a two-dimensional foil heaving and pitching behind an obstacle in a stream. The effects of the phase relationship between the incoming Kármán vortex stream and the foil oscillation on the resulting vortex street in the wake of the two interacting bodies and on the efficiency of the foil’s propulsion have been examined. The foil in this synthetic arrangement may be likened to a fish keeping station behind an obstacle shedding Kármán vortices in a stream. Three types of vortex streets may form. In the noninteracting case, the counter-rotating Kármán vortices from the two bodies remain distinct in the resulting wake. In the other two types, the vortices from the body and the foil interact destructively and constructively and, although measurements are not available, it is believed that circulation of the vortices in the resulting wake is diminished and enhanced, respectively. The peaks in efficiency and, therefore, in vortex-energy extraction are associated with destructive interaction, and the troughs in efficiency are associated with constructive interaction. Echoing these results, the PIV technique has been used to show that a trout alters its body undulation to match the Kármán gait [25]. Electromyogram time traces show that muscle activity is reduced during such favorable interaction. It was not investigated if the Kármán vortices are also weakened behind the trout when their energy is apparently extracted. A budgeting of the vortex circulation in the resulting wake would provide a quantitative validation of the hypothesis of energy extraction and destructive interaction. A foil rigidly held to a boat experiences thrust due to surface waves [188]. The wave changes the foil’s angle of attack, which effectively undergoes heaving and pitching motions. The streamwise turbulent intensity in the wake of a pitching foil can be canceled by another pitching foil downstream by proper control of the relative phase and amplitude of the pitching [189]. It has been shown that a passively mounted high-aspect-ratio foil located behind a vortex shedding bluff body resonates in the natural mode with the incoming Kármán street [25,190]. In the process, the foil can extract energy from the vortices and propel itself

upstream. The energy extracted is sufficient to overcome the foil’s drag. Energy extraction by the large-aspect-ratio foil is apparently higher than that in fish, whose aspect ratio is lower. It appears that the foil in this experiment may have been extracting a very small amount of the available vortex energy. It would be useful to explore the parameter space further in this experiment to increase energy extraction. It would also help if we could separate what the foil accrues from energy extraction and the thrust that it self-generates because the vortex imposes heaving and pitching motions. In other words, the dynamic and kinematic contributions of the incoming vortex street are worth separating. Practical devices for energy extraction from Kármán streets in water have been attempted where a polyvinylidene difluoride (PVDF) “eel” is freely excited by a Kármán vortex street behind a bluff body [191]. PVDF is a polymer that has a ten times larger piezoelectric property than other polymers and may be suitable for capacitive buildup and trickle charging of power storage devices. This work focused on Reynolds number effects of the membrane. A resonance between the imposed Kármán perturbation and, ideally, a damping-free membrane is most desirable to maximize strain energy and mechanical power. It was possible for a membrane to oscillate at the same frequency as that of the Kármán vortex, with identical amplitude and wavelength—a desirable “lock-in” condition. Modeling of the membrane as an Euler–Bernoulli beam gives the condition for lock-in. Work is needed to demonstrate energy harvesting over a range of Reynolds numbers. Extraction of energy from shed vortices is enticing to fluids engineers. However, the dynamics of drag varies richly with Reynolds number and the nature of the bluff body and how rigidly it is held. Matching electroactive materials over such a wide dynamic range is a challenge. Demonstration of a meaningful reliable net benefit remains elusive.

5.7 Flagellar Motion-Inspired Mixer. Pumping fluid in small systems efficiently is a challenge because the flow has a low Reynolds number that is viscosity dominated, and it has small scale. Chaos-based systems have not been successful. Low concentrations (<0.5% by volume) of bacteria and their flagellar motion have been used to enhance mixing in microchannels [192]. In a Y-shaped microchannel, using a fluorescing technique, the authors show that the diffusion coefficient rises markedly when motile *E. coli* bacteria are inserted into a stream of Dextran, which has high molecular weight. Direct visualization of bacterial motion and pressure drop, together with wall-shear measurements, would throw more light on the nature of flagellar mixing, efficiency, and their practical value.

5.8 Flagellar Swimming Robot. A single, helical, rigid flagellum has been built and its thrust has been compared with the measurements given by resistance force theory [193]. The experiments were carried out in silicone oil (350 cS viscosity) and the Reynolds number was comparable to that of microorganisms. The head of the swimmer was a 14.5-mm-diameter, 16.5-mm-long, two-phase stepper motor. The flagellum consisted of 1.23-mm-diameter steel wires, and it had a helical diameter and pitch of 14.8 mm. The frequency range was 5–15 Hz. The measurements of thrust are in near agreement with those calculated using resistive force theory. Thrust force varies linearly with frequency. A small swimming robot with a single helical rigid flagellum has also been built [193]. It weighs 1.85 g and is 16 mm in diameter and 46 mm long. It swims in silicone oil of viscosity 100 cS. The body of the robot is a brushless dc motor covered with Styrofoam for buoyancy control. The flagellum is made of a 0.42-mm-diameter steel wire. The wavelength is 13 mm, the wave amplitude is 23.5 mm, and the length of the flagellum is 20 mm. Linear swimming at predicted velocities was achieved.

5.9 Lateral Line-Inspired Sensors. Seal whiskers, the hairs on spider legs, the lateral lines of fish, and the tiny hairy cells in the human inner ear are a clustering of sensors that are used to

detect predators or preys. These sensors detect, amplify, and convert sound waves or vibration/pressure fluctuations or distributions. The clustering, filtering process, motion, and stereoscopic differencing give these sensors directional ability and three-dimensional ranging. They act as a substitute for vision. "Hair sensors" have been shown to detect flow speeds of 1 mm/s, although sensor noise is an issue. Rapid signal processing to allow the cognition of the spatial patterns of the surroundings is also a challenge. Controllers that make use of the sensory feedback also need to be developed. Micromachining of polymer has been used to build cantilever arrays that act as strain gauges or hot-film arrays. "Lateral line sensor arrays" have been shown to be effective in detecting dipole sources [194].

5.10 LEV-Based Flapping Machines. Insects stay aloft and propel themselves by pushing air downward and tilting the plane of their wing beat. During hovering, most insects move their wings back and forth in a horizontal plane, and this plane is tilted more and more as the insect moves forward at higher speeds [34]. Observing the similarity with rotor craft, the insect flow field has been modeled using the theoretical foundation of propeller aerodynamics [148,195]. Insect-inspired flapping machines have also been designed [14]. However, rotor craft blades are dominated by rotation, while insect flight wings are dominated by oscillatory motion. Differences in the mechanism and inaccuracies in modeling can be expected, although they both have the ability to hover if they are modeled in a similar manner. Animals use an elastic storage system to oscillate wings [4]. Biorobotic designs of such systems are yet to be carried out and could be attempted with artificial muscles. It has been proposed that the LEV dynamic stall mechanism be used for the micro-air vehicle design, rather than the fling and clap mechanism [14]. Design laws are given, and it is suggested that the preliminary design be based on hovering not only for simplicity but also because if the vehicle hovers well it is likely to support its mass and have adequate power at all practical speeds.

5.11 Micro-Air Vehicles. The micro-air vehicle (MAV) is an application where the old and new approaches to practical flight compete. In modern flying vehicles that are large, lift generation and propulsion are treated separately. However, in insect flying, no such separation is made. The MAV design, based on traditional fixed-wing aerodynamics, is more mature than that of flapping wings. MAVs are roughly the size of the palm of our hand. The current state-of-the-art is given in Ref. [196]. The link between the aerodynamic design and the insect high-lift mechanism of LEV and the appropriate wing kinematics that produce and sustain the LEV with MAVs have been discussed [197]. The microflying insect (MFI) is an example of the implementation of the high-lift principle of insect flight [198]. The MFI is remarkable in its closeness to fruit flies. Laboratory tethered flight has been demonstrated to show that adequate lift forces are produced. Further progress has been limited by the availability of energy sources.

5.12 Performance Enhancement of Existing Devices. In one of the most innovative applications of the high-lift principle, a novel delayed-stall propulsor has been patented [199]. Normally, propulsor designers strive to achieve azimuthal uniformity of flow. However, in the delayed-stall propulsor, there is a variable pitch in the upstream stator blades, whereby the downstream, rotating, conventional rotor blades experience a variable gust that simulates the heaving and pitching motions of flying insects. In other words, instead of oscillating the blades, Usab et al. [199] produced an oscillating flow and subject the rotor blades to that flow, which constantly changes the angle of attack as the blade moves circumferentially. The rotor blades are set at higher angles of attack than normal for effective delayed-stall vortices to form. Furthermore, the diametrically opposite blades are given an opposite but equal pitch about a mean value to cancel the noise sources. The design leads to an increase in total pressure rise across the fan stage compared with the baseline case, the maxi-

um increase being 50%. Alternatively, in a propulsor at the same forward speed, a reduction in rotational rate is possible, potentially leading to a reduction in noise of 4 dB, which is measurable.

5.13 Fishlike Tail Articulation of Propulsor Blades for Wake Momentum Filling. In a propulsor where a rotor is located behind a stator, the wake velocity defect of the stator causes a lift gradient on the rotor blades, which is a source of noise. Because of the well-defined periodicity of rotation and blades, the noise produced appears as a spike in the noise spectrum and is called a blade tonal. Observing that fish tail articulation produces a jet, this reviewer had proposed that the tails of the stator blades in an underwater propulsor be articulated appropriately to exactly fill the wake deficit. Preliminary theoretical and experimental investigations indicated that some reduction in noise might be possible [10]. More extensive experimental investigations were subsequently carried out at realistic Reynolds numbers and in the Strouhal number range found commonly in fish, although not in a full-scale propulsor [200]. A net noise reduction of 3–5 dB is indicated although difficulties in scaling remain. Future work should focus on accurate simulation of flow and noise and the use of artificial muscles for active tail actuation.

5.14 Octopus-Inspired Suction Cups. Aquatic animals such as octopus, limpets, and echeneid fish are reported to have the ability to adhere to other animals with rough skins for feeding and riding. These animals notably utilize suction cups and hooks. Do animals produce higher levels of suction (that is, lower differential pressures) in their suction cups and how do they attach to rough host surfaces under water without any seeming continuous suction cost to overcome leakage [9]? In laboratory measurements of the differential pressure inside the suction cup and in the ambient until the cup was released, the release force—expressed as tenacity (release force per unit area of adhesion)—was found to be similar to that in animals. However, it was found that when the host surface was rough and/or porous, the suction pump had to be left on for the man-made cups to remain attached. Is this a disadvantage in terms of energy consumption and complication over what animals do? Animals do not have any central pump or plumbing connecting their suction cups. They have a radial and circumferential muscle architecture that expands to create lower internal pressure. However, they have a microfine beaded cup-lip construction with radial grooves. Observing the matching of host surface (sharkskin riblet) topology in echeneid fish suckers, it was found that biorobotic sealed contact over rough surfaces is also feasible when the suction cup makes a negative copy of the rough host surface. However, for protracted, persistent contact, the negative topology would have to be maintained by active means. Energy has to be spent to maintain the negative host roughness topology to minute detail, and protracted hitch-riding on a shark for feeding may not be free for echeneid fish. Further work is needed on the mechanism and efficiency of the densely populated tiny actuators in fish suckers that maintain leak-proof contact with minimal energy cost and the feasibility of their biorobotic replication.

6 Research Recommendations

Biology-inspired unsteady fluids engineering has untapped pay-offs in efficiency, noise reduction, and performance—such as lower pressure drop/increased mass flow and lightweight, low-power passive sensor technologies. To succeed in the transition of the sciences and the design principles gleaned from biology, it is recommended that some benchmarks be identified—the benchmarks could be from existing performers. It is best to apply the principles to gain in function rather than mimic any animal in morphology or function because human needs are optimized for different functions than those in animals. The end product is likely to have a greater practical impact if the unsteady hydrodynamics or aerodynamics is integrated with appropriate control methodologies right from the beginning. Although electroactive polymers

are not yet developed as actuator materials, integration of the hydrodynamics with such polymers would usher in many successful transitions. The laws of probability tell us that integration of disparate disciplines is problematic, but such integration also offers the opportunity for significant payoffs. Caution needs to be exercised in slavishly mimicking nature. For example, it is known that the porpoising behavior of the penguin, where it builds up speed and then spreads bubbles around its body, reduces drag and helps it leap in the air. Recent embedded data loggers indicate that penguins traverse only 3.8% of the total distance traveled during the porpoising cycle [201]. They “porpoise” only at the beginning and end of their trip, presumably to avoid predators. It may be that this method of drag reduction is on the whole costly and should be used only in spurts. There are important differences between the performance characteristics of wild animals and those in captivity. The following are specific recommendations for future research, categorized in terms of mechanism (general, two-dimensional versus three-dimensional effects, interaction of hydrodynamics and control, and jets), computation and modeling, experimental methods, and application.

6.1 Mechanism: General. Any given high-lift mechanism should be investigated over a broad range of Reynolds numbers to determine generalities and scaling potential. The wake vortices need to be dissected in terms of lift and thrust vortices and their typical topology. The importance of energy storage systems in swimming and flying animals and their impact on unsteady fluid-structure interaction need further research. A budgeting of the vortex circulation in the resulting wake behind a trout in a Kármán stream would provide a quantitative validation of the hypothesis of energy extraction and destructive interaction. It will be useful to examine the nonlinear interaction, if any, between the different modes of flexible fins and determine if such interaction augments the force peaks over a part of the cycle. In particular, the modes that sprawl over the entire fin and those that are confined over a much smaller part may have some root in what animals seem to resort to. What are the distinguishing aspects of the mechanisms of eel swimming for speed and efficiency?

6.2 Mechanism: Two-Dimensional and Three-Dimensional Effects and Rigid Versus Flexible Fins. NACA profiles are two dimensional. On the other hand, we now have the profiles of the entire three-dimensional lifting surface and even of the entire animal. It would be worth exploring if nature is implementing any new principle of three-dimensional body and system optimization. Rigid, large-aspect-ratio, three-dimensional, and two-dimensional fins both have a maximum efficiency of about 0.60. Therefore, the question is the following: Do flexible fins have higher efficiency than rigid flapping fins? Related questions are as follows: Do jumbo squid, sunfish pectoral fins, and lamprey wings—all of which have visually similar fin cupping—have similar modes of folding/cupping? Do they all produce LEVs? Is a flexible fin the ultimate in efficient propulsion? Unsteady control surfaces produce redundant forces instantaneously which average to zero over the time period of oscillation of the surface. How can the production of such forces be minimized?

6.3 Mechanism: Interaction of Hydrodynamics and Control. It will be useful to determine the relationship between the unsteady hydrodynamics of the pectoral fins of fish with their neuromotor characteristics and spring-mass damper models. This could give us a clue as to how strain energy storage is controlled by the muscles and how the mechanism can be applied to engineering. The works of biologists and biology-inspired hydrodynamics have yet to focus on the relationship of hydrodynamic properties of the lifting surfaces and the control of the entire animal or hull. In this sense, the price of abstraction of the lifting surfaces in animals needs to be explored. During flapping, what is the best phase during which fin kinematics should be changed?

6.4 Mechanism: Jets. In jet-dominated creatures, the effects of environment, nozzle surface quality, active control, and appendages on entrainment need closer scrutiny. If any fluids engineer is attracted to complication, then one needs to go no further than the squid. After all, what other animal has a critical velocity above which it swims tail first? What other animal combines both jet and fin propulsion? It will be very interesting if we discover the interaction between the unsteady flow around a squid and its body that automatically causes the switch from head-first to tail-first at the critical speed. Is jet propulsion and maneuvering less efficient compared with LEV-based flapping fins?

6.5 Modeling and Computation. The quasisteady models need to be successfully extended to flexible flapping foils, such as the pectoral fins of fish. An accurate modeling of the induced velocity during hovering would be useful. The modeling of Wagner effects and added mass effects during fin flip would be useful. An accurate computational investigation of fish swimming freely would help resolve questions regarding (1) the role of tail fins in homocercal and heterocercal species, (2) interactions of body and pectoral fins, (3) the role of fine lateral and lagged motor control of the posterior part of the tail fins, and (4) the role of the interactions between finlets and caudal fins.

6.6 Experimental Methods. The fringe pattern method needs to be extended to water; for example, it needs to be used on the pectoral fins of fish. The combination of a fringe method for tracking the movement of the flexible control surfaces of animals and a holographic method of velocity measurement would open a new avenue of research of the mechanisms that animals are utilizing. Due to advances in sensors and computers, biomechanics measurements of swimming and flying in natural environments are more feasible today and might lead to new discoveries.

6.7 Application. Improving the efficiency of devices where pressure drop, mixing, and noise production are involved would have practical impact. Devices that can produce suction by deforming the cup (without any pumping or plumbing, as in the octopus) would be useful. Success in application would be influenced by our ability to integrate the disparate disciplines. Because this review is multidisciplinary in nature, cultures in biology and engineering could have an impact on how this research is carried out. For biorobotics to succeed, it is implied that engineers and biologists know of each others' professional cultures. This is a thorny issue, and one can only give a personal opinion. Biologists tend to diversify and account for multiple variables, and many disciplines are integrated in their work. Engineers tend to simplify, minimize the number of variables, and preferably integrate disciplines that are well developed. Biologists in the United States tend to name their laboratories after themselves, but engineers do not. Biologists, while they deal with multidisciplinary products, such as life, still use the science principle of stripping the problem to a bare minimum and developing a hypothesis. A narrow focus plays an important role in the advancement of both science and engineering. We have chosen to review primarily the emerging science and technology of the animal-inspired high-lift mechanism and its application. The more familiar animal-inspired research in fluids engineering, such as riblets, compliant coating, bubble injection, mucus secretion, and surface curvature, have not been considered.

7 Remarks

Consider these questions. Why is it that we can now build frigates that can cruise more quietly than schools of fish (Fig. 2), but we cannot yet build quiet hair dryers or lawn mowers? Why is it that massive cruising vehicles (such as nuclear or diesel submarines) follow the same energy scaling law as the red muscles of fish, which are used for cruising, and yet smaller maneuvering vehicles consume proportionately more energy than the scaling law given by white muscles of fish, which are used for maneuver-

ing [8]? Why is it that engineering is proficient in cruising as stated above over eight decades of scales in both length and shaft horsepower, but is incompetent in maneuvering compared with animals over a scale of less than four decades? Why is it that there exists such a wide gap in turning ability between fish and underwater vehicles and how can this gap be closed?

It is possible to understand the above observations if we realize that, in certain situations, there is convergence in the evolution of the biological world and engineering because we have understood the underlying physics principles and have optimally implemented them in design. It is useful that we can quantify several situations where convergence exists and those where a gap exists. But where convergence or progress is eluding us, we need to look for new science principles and seek new inspirations for design. The latter conscious departure from conventional teachings of hydrodynamics has led to engineering gains, and two demonstrated results are worth citing. In one, substantial power saving is possible due to heaving and pitching actuators compared with conventional propulsors. In the other, by departing from the age-old hydrodynamic gospel that we should strive for axisymmetry in inflows to propulsors, it has now been possible to enhance pressure recovery in fan ducts. In other words, the rotational rates of axisymmetric pumps or propulsors can be lowered for the same discharge or forward speed, leading to quieting. Implementation of such principles can reduce the number of blades required in fan jets, while producing the same amount of thrust. These tangible benefits are the result of a biology-inspired, multidisciplinary fluids engineering approach. When one strives to understand the physics principles first, and biomimicry is not resorted to, the Reynolds number variation between the world of swimming/flying animals and engineering is not necessarily a barrier to implementation.

In closing, the unsteady high-lift mechanism is widely prevalent in nature. It may be that all flying animals (such as birds and insects) and all swimming animals (such as fish and penguins) that have flapping pectoral wings or fins in one form or another implement the mechanism in its most universal form, which is the production of a LEV. The flapping of the pectoral fin produces and sustains a LEV, which is a major source of force. Other mechanisms, such as rotational effects and wake capture, have largely been discounted, although further work is necessary to comprehensively do that in many species. While in man-made flying vehicles, propulsion and lift are separately produced, in nature, they are produced together. In nature, flying animals need a large control surface to stay aloft and propel themselves, while swimming animals have relatively smaller control surfaces (relative to their bodyweight in air) that are used primarily for propulsion and maneuvering. The topology of the LEV in swimming and flying animals varies widely, depending on aspect ratio, flexibility, and the thorax or main body. LEVs can be straight or curved, two or three dimensional, and conical or cylindrical; they can originate from the thorax or the wing root; they can have large or negligible spanwise spiraling flow; and they can even be highly convoluted. It may be that all swimming and flying animals that have flapping (simultaneously rolling and pitching) appendages have their own unique form of LEV, if we are willing to account for the differences in critical points in their flow topologies. It is perhaps more important to investigate, model, measure, visualize, and accurately compute the LEVs, which are the source of force production, than it is to dwell on the wakes, although the latter is easier. The LEV is a sink of vorticity and its dynamics is key to the force production and stability of the animal or the vehicle. It is most desirable to investigate the LEV on an actual swimming and flying animal, rather than on any robotic scaled model. While that is the task of biologists, engineers are in a more enviable position of "getting away" with investigations on models, bearing in mind the implied departure from the biological inspiration that might entail. One of the most fascinating topics that is ripe for fluids engineering investigation is flexible wings. The spectrum of flexible wings or pectoral fins waiting to be examined is enormous. At one end is

the three-dimensional, highly convoluted, and beautiful thin pectoral fins of sunfish, and the other is the spanwise twisting, thick penguin wing or bending bird wing. Their hydrodynamic mechanism—namely, the nature of their LEVs—and their active optimization of oscillation parameters both need attention.

If in the ultimate analysis energy consumption is the Achilles heel, then efficiency is the most important variable that we need to pay attention to. However, most reports of efficiency of animal propulsion are unreliable to different extents, and even many engineering reports of efficiency are in error. This is remarkable because several mechanisms and preferred scaling laws are justified in terms of efficiency. More direct measurements of efficiency are needed. The modeling of unsteady thrust and drag needs to be improved. Accurate measurement and modeling of efficiency are important opportunities for fluids engineers. The effects of active cambering of wings on unsteady fluid dynamics are unclear. Wing kinematics and control strategies for turning need to be explored and compared with those for forward motion. Two-dimensional modeling is useful if it is analytical and complements experimentally derived physical models as in Refs. [32,33]. On the other hand, numerical simulation of two-dimensional wings is of little value for extension to measurements with robotic models or live animals. Numerical fluid dynamics simulation and theoretical modeling of flapping foils receive lower priority among biologists. With their mathematical skills, fluids engineers should be able to fill in a timely need. But works should preferably deal with three-dimensional foils, and extension of results from two-dimensional heaving and pitching foils is fraught with questions than it is helpful. Eel swimming might be ripe for investigations of the fluid-structure interaction. Why should eels resort to such seemingly inefficient swimming that produces significant secondary flows and two widely separated lateral streams of ring vortices for propulsion? Is there any subtle nonlinear mechanism that allows eels to swim to far-off places? One area where there is very little fluid dynamics information either from biologists or from engineers is the nature of the interaction of the unsteady appendage with the hull or thorax or main body. The main body may or may not be deforming with time as well. The effects on drag or stability are not known. Another area in which we have little information is the nature of vorticity roll-up at the oscillating wing tip. At extremely low Reynolds number flights, the limited measurements on the effects of surface furs on wings are counterintuitive and need closer inspection. An intriguing aspect is the rarity of cavitation in underwater LEVs or at the fin tip even in shallow water, although one would think that the fins/wings are more loaded than in steady swimming. Noise measurements or noise modeling of flapping foils are also rare. Unsteady fluids engineering is inherently amenable to emerging artificial muscle technologies and requires the development of new control theories. Much less work has been done on the integration of unsteady fluid dynamics inspired by swimming and flying animals with either artificial muscle technology or the development of control theories, although there are indications that such work is going to be rewarding. In fact, the very success in the implementation of high-lift mechanisms such as LEVs might depend on such integration. Because much work remains to be done in such ideal integration, accelerated progress might seem to happen if conventional technologies are used instead in the implementation of LEV, although lower performance than the full potential might thwart continued interest. Supplanting conventional motor drives with artificial muscle technologies that have higher electromechanical efficiency would favorably impact the overall system efficiency—the key to success. The development of controllers that first use cycle-averaged hydrodynamic force and moment characteristics and then produce unsteady main body behaviors throws away the key strengths in unsteadiness of swimming and flying animals [13]. Neuroscience-based nonlinear control would allow instantaneous control of fluid forces, thereby allowing the full potential of LEV-based unsteady fluid dynamics to be truly realized [165].

Acknowledgment

The author is grateful to the Cognitive and Neurosciences Program of the Office of Naval Research for the support of his biorobotics research over many years. Work with the following co-workers from the Naval Undersea Warfare Center in Newport, RI is acknowledged: Dr. David N. Beal, Dr. Alberico Menozzi, Dr. John Castano, Mr. William Nedderman, Mr. Henry Leinhos, Mr. Stephen Forsythe, Mr. J. Dana Hrubes, Mr. Dan Thivierge, Mr. Albert Fredette, Mr. Thomas Fulton, Mr. William Krol, and Mr. James Rice. The author also acknowledges collaboration with the Visiting American Society of Engineering Education (ASEE) Distinguished Summer Faculty—Professor Anuradha Annaswamy of the Mechanical Engineering Department of the Massachusetts Institute of Technology and Professor Sahjendra Singh of the Computer Sciences and Electrical Engineering Department of the University of Nevada at Las Vegas. He also wishes to acknowledge collaboration with Dr. William Macy of the University of Rhode Island Graduate School of Oceanography and with Naval Research Enterprise Internship Program (NREIP) visiting summer graduate students Michael Boller and Sarah Warren of the University of Rhode Island Biology and Ocean Engineering Departments, respectively. Finally, S. Schael of Wehretechnische Dienststelle 71, BWB, Koblenz, Germany is thanked for providing Fig. 2. Professor George Lauder and Dr. Peter Madden of the Harvard University Biology Department are thanked for the sunfish data in Fig. 4.

References

- [1] Bandyopadhyay, P. R., 2004, "Guest Editorial: Biology-Inspired Science and Technology for Autonomous Underwater Vehicles," special issue of IEEE J. Ocean. Eng., **29**(3), pp. 542–546.
- [2] Editorial, 2005, "Fly Guys," IEEE Spectrum, **42**(11), p. 10.
- [3] Sunada, S., Takashima, H., Hattori, T., Yasuda, K., and Kawachi, K., 2002, "Fluid-Dynamic Characteristics of a Bristled Wing," J. Exp. Biol., **205**, pp. 2737–2744.
- [4] Ellington, C. P., 1985, "Power and Efficiency of Insect Flight Muscle," J. Exp. Biol., **115**, pp. 293–304.
- [5] Bandyopadhyay, P. R., Beal, D. N., and Menozzi, A., 2008, "Biorobotic Insights Into How Animals Swim," J. Exp. Biol., **211**, pp. 206–214.
- [6] Kern, S., and Koumoutsakos, P., 2006, "Simulations of Optimized Anguilliform Swimming," J. Exp. Biol., **209**, pp. 4841–4857.
- [7] Dickinson, M. H., Farley, C. T., Full, R. J., Koehl, M. A. R., Kram, R., and Lehman, S., 2000, "How Animals Move: An Integrative View," Science, **288**, pp. 100–106.
- [8] Bandyopadhyay, P. R., Beal, D. N., Leinhos, H. A., Thivierge, D. P., and Mangalam, A., 2009, "Biomechanics of High Lift to Swim Better," J. Fluid Mech., under review.
- [9] Bandyopadhyay, P. R., Hrubes, J. D., and Leinhos, H. A., 2008, "Biorobotic Adhesion in Water Using Suction Cups," Bioinsp. Biomim., **3**, p. 016003.
- [10] Krol, W. P., Annaswamy, A., and Bandyopadhyay, P. R., 2002, "A Biomimetic Propulsor for Active Noise Control," Technical Report No. 11,350, Naval Undersea Warfare Center, Newport, RI.
- [11] Bandyopadhyay, P. R., Castano, J. M., Rice, J. Q., Philips, R. B., Nedderman, W. H., and Macy, W. K., 1997, "Low-Speed Maneuvering Hydrodynamics of Fish and Small Underwater Vehicles," ASME J. Fluids Eng., **119**, pp. 136–144.
- [12] Bandyopadhyay, P. R., 2002, "Maneuvering Hydrodynamics of Fish and Small Underwater Vehicles," Integr. Comp. Biol., **42**, pp. 102–117.
- [13] Menozzi, A., Leinhos, H., Beal, D.N. and Bandyopadhyay, P.R., 2008, "Open-Loop Control of a Multi-Fin Biorobotic Underwater Vehicle," IEEE J. Ocean. Eng., **33**, pp. 59–68.
- [14] Ellington, C. P., 1999, "The Aerodynamics of Insect-Based Flapping Machines," 14th Bristol International UAV Conference, pp. 37.1–37.12.
- [15] Forsythe, S., Leinhos, H. A., and Bandyopadhyay, P. R., 2008, "Dolphin-Inspired Maneuvering and Pinging for Short Distance Echolocation," J. Acoust. Soc. Am., **124**, pp. EL255–EL261.
- [16] Triantafyllou, M., Triantafyllou, G. S., and Yue, D. P. K., 2000, "Hydrodynamics of Fish-Like Swimming," Annu. Rev. Fluid Mech., **32**, pp. 33–53.
- [17] Sane, S., 2003, "The Aerodynamics of Insect Flight," J. Exp. Biol., **206**, pp. 4191–4208.
- [18] Triantafyllou, M. S., Hover, F. S., Techet, A. H., and Yue, D. K. P., 2005, "Review of Hydrodynamic Scaling Laws in Aquatic Locomotion and Fish-like Swimming," Appl. Mech. Rev., **58**, pp. 226–237.
- [19] Bandyopadhyay, P. R., 2005, "Trends in Biorobotic Autonomous Undersea Vehicles," IEEE J. Ocean. Eng., **30**, pp. 109–139.
- [20] Fish, F. E., and Lauder, G. V., 2006, "Passive and Active Flow Control by Swimming Fishes and Mammals," Annu. Rev. Fluid Mech., **38**, pp. 193–224.

- [21] Beal, D. N., and Bandyopadhyay, P. R., 2007, "A Harmonic Model of Hydrodynamic Forces Produced by a Flapping Fin," Exp. Fluids, **43**, pp. 675–682.
- [22] Vogel, S., 1996, *Life in Moving Fluids*, 2nd ed., Princeton University Press, Princeton, NJ.
- [23] Azuma, A., 1992, *The Biokinetics of Flying and Swimming*, Springer-Verlag, New York.
- [24] Dudley, R., 2003, *The Biomechanics of Insect Flight: Form, Function, and Evolution*, Princeton University Press, Princeton, NJ.
- [25] Liao, J. C., Beal, D. N., Lauder, G. V., and Triantafyllou, M. S., 2003, "Fish Exploiting Vortices Decrease Muscle Activity," Science, **302**, pp. 1566–1569.
- [26] Triantafyllou, G. S., and Triantafyllou, M. S., 1995, "An Efficient Swimming Machine," Sci. Am., **272**(3), pp. 64–71.
- [27] Lauder, G. V., 2000, "Function of the Caudal Fin During Locomotion in Fishes: Kinematics, Flow Visualization, and Evolutionary Pattern," Am. Zool., **40**, pp. 101–122.
- [28] Drucker, E. G., and Lauder, G. V., 1999, "Locomotor Forces on a Swimming Fish: Three-Dimensional Vortex Wake Dynamics Quantified Using Digital Particle Image Velocimetry," J. Exp. Biol., **202**, pp. 2393–2412.
- [29] Wang, H., Zeng, L., Liu, H., and Yin, C., 2003, "Measuring Wing Kinematics, Flight Trajectory and Body Attitude During Forward Flight and Turning Maneuvers in Dragonflies," J. Exp. Biol., **206**, pp. 745–757.
- [30] Malkiel, E., Alquaddoomi, O., and Katz, J., 1999, "Measurements of Plankton Distribution in the Ocean Using Submersible Holography," Meas. Sci. Technol., **10**, pp. 1142–1152.
- [31] Ellington, C. P., 1984, "The Aerodynamics of Hovering Insect Flight. III. Kinematics," Philos. Trans. R. Soc. London, Ser. B, **305**, pp. 41–78.
- [32] Weis-Fogh, T., 1973, "Quick Estimates of Flight Fitness in Hovering Animals, Including Novel Mechanisms for Lift Production," J. Exp. Biol., **59**, pp. 169–230.
- [33] Lighthill, M. J., 1973, "On Weis-Fogh Mechanism of Lift Generation," J. Fluid Mech., **60**, pp. 1–17.
- [34] Ellington, C. P., 1978, "The Aerodynamics of Normal Hovering Flight: Three Approaches," *Comparative Physiology: Water, Ions and Fluid mechanics*, K. Schmidt-Nielsen, L. Bolis, and S. Maddrell, eds., Cambridge University Press, Cambridge, pp. 327–345.
- [35] Ellington, C. P., 1980, "Vortices and Hovering Flight," *Stationare Effekte An Schwingende Fluegeln*, W. Nachtigall, ed., F. Steiner, Wiesbaden, pp. 64–101.
- [36] Ellington, C. P., 1984, "The Aerodynamics of Hovering Insect Flight, IV—Aerodynamic Mechanisms," Philos. Trans. R. Soc. London, Ser. B, **305**, pp. 79–113.
- [37] Maxworthy, T., 1979, "Experiments on the Weis-Fogh Mechanism of Lift Generation by Insects in Hovering Flight. Part 1. Dynamics of the 'Fling,'" J. Fluid Mech., **93**, pp. 47–63.
- [38] Spedding, G. R., and Maxworthy, T., 1986, "The Generation of Circulation and Lift in a Rigid Two-Dimensional Fling," J. Fluid Mech., **165**, pp. 247–272.
- [39] Marden, J. H., 1987, "Maximum Lift Production During Takeoff in Flying Animals," J. Exp. Biol., **130**, pp. 235–258.
- [40] Rayner, J. M. V., 1979, "A Vortex Theory of Animal Flight. Part 2. The Forward Flight of Birds," J. Fluid Mech., **91**, pp. 731–763.
- [41] Ellington, C. P., 1984, "The Aerodynamics of Hovering Insect Flight. II. Morphological Parameters," Philos. Trans. R. Soc. London, Ser. B, **305**, pp. 17–40.
- [42] Ellington, C. P., 1995, "Unsteady Aerodynamics of Insect Flight," Symp. Soc. Exp. Biol., **49**, pp. 109–129.
- [43] Usherwood, J. R., and Ellington, C. P., 2002, "The Aerodynamics of Revolving Wings—I. Model Hawkmoth Wings," J. Exp. Biol., **205**(11), pp. 1547–1564.
- [44] Usherwood, J. R., and Ellington, C. P., 2002, "The Aerodynamics of Revolving Wings—II. Propeller Force Coefficients from Mayfly to Quail," J. Exp. Biol., **205**(11), pp. 1565–1576.
- [45] Sunada, S., Kawachi, K., Watanabe, I., and Azuma, A., 1993, "Fundamental Analysis of Three Dimensional 'Near Fling,'" J. Exp. Biol., **183**, pp. 217–248.
- [46] Wakeling, J. M., and Ellington, C. P., 1997, "Dragonfly Flight I—Gliding Flight and Steady-State Aerodynamic Forces," J. Exp. Biol., **200**, pp. 543–556.
- [47] Ellington, C. P., 1991, "Limitations on Animal Flight Performance," J. Exp. Biol., **160**, pp. 71–91.
- [48] Gopalkrishnan, R., Triantafyllou, M. S., Triantafyllou, G. S., and Barrett, D., 1994, "Active Vorticity Control in a Shear Flow Using a Flapping Foil," J. Fluid Mech., **274**, pp. 1–21.
- [49] Dickinson, M. H., and Lehmann, F. O., 1993, "The Active Control of Wing Rotation by Drosophila," J. Exp. Biol., **182**, pp. 173–189.
- [50] Dickinson, M. H., and Gotz, K. G., 1993, "Unsteady Aerodynamic Performance of Model Wings at Low Reynolds Numbers," J. Exp. Biol., **174**, pp. 45–64.
- [51] Birch, J. M., and Dickinson, M., 2003, "The Influence of Wingwake Interactions on the Production of Aerodynamic Forces in Flapping Flight," J. Exp. Biol., **206**, pp. 2257–2272.
- [52] Hamdani, H., and Sun, M., 2000, "Aerodynamic Forces and Flow Structures of an Airfoil in Some Unsteady Motions at Small Reynolds Number," Acta Mech., **145**, pp. 173–187.
- [53] Odar, F., and Hamilton, W. S., 1964, "Forces on a Sphere Accelerating in a

- Viscous Fluid," *J. Fluid Mech.*, **18**, pp. 302–314.
- [54] Sarpkaya, T., 1982, "Impulsively-Started Flow About Four Types of Bluff Body," *ASME J. Fluids Eng.*, **104**, pp. 207–213.
- [55] Sarpkaya, T., 1991, "Non-Impulsively Started Steady Flow About a Circular Cylinder," *AIAA J.*, **29**(8), pp. 1283–1289.
- [56] Sarpkaya, T., 1992, "Brief Reviews of Some Time-Dependent Flows," *ASME J. Fluids Eng.*, **114**(3), pp. 283–298.
- [57] Dickinson, M. H., 1994, "The Effects of Wing Rotation on Unsteady Aerodynamic Performance at Low Reynolds Numbers," *J. Exp. Biol.*, **192**, pp. 179–206.
- [58] Dickinson, M. H., and Gotz, K. G., 1996, "The Wake Dynamics and Flight Forces of the Fruit Fly *Drosophila Melanogaster*," *J. Exp. Biol.*, **199**(9), pp. 2085–2104.
- [59] Sane, S. P., and Dickinson, M. H., 2001, "The Control of Flight Force by a Flapping Wing: Lift and Drag Production," *J. Exp. Biol.*, **204**(15), pp. 2607–2626.
- [60] Daniel, T. L., 1984, "Unsteady Aspects of Aquatic Locomotion," *Am. Zool.*, **24**, pp. 121–134.
- [61] Wang, Z. J., Birch, J. M., and Dickinson, M. H., 2004, "Unsteady Forces and Flows in Low Reynolds Number Hovering Flight: Two-Dimensional Computations Versus Robotic Wing Experiments," *J. Exp. Biol.*, **207**, pp. 449–460.
- [62] Birch, J. M., Dickson, W. B., and Dickinson, M. H., 2004, "Force Production and Flow Structure of the Leading Edge Vortex on Flapping Wings at High and Low Reynolds Numbers," *J. Exp. Biol.*, **207**, pp. 1063–1072.
- [63] Dickson, W. B., and Dickinson, M. H., 2004, "The Effect of Advance Ratio on the Aerodynamics of Revolving Wings," *J. Exp. Biol.*, **207**, pp. 4269–4281.
- [64] Poelma, C., Dickson, W. B., and Dickinson, M. H., 2006, "Time-Resolved Reconstruction of the Full Flow Field Around a Dynamically-Scaled Flapping Wing," *Exp. Fluids*, **41**, pp. 213–225.
- [65] Thomas, A. L. R., Taylor, G. K., Srygley, R. B., Nudds, R. L., and Bomphey, R. J., 2004, "Dragonfly Flight: Free-Flight and Tethered Flow Visualizations Reveal a Diverse Array of Unsteady Lift Generating Mechanisms, Controlled Primarily Via Angle of Attack," *J. Exp. Biol.*, **207**, pp. 4299–4323.
- [66] Sane, S. P., 2006, "Induced Airflow in Flying Insects, I: A Theoretical Model of This Induced Flow," *J. Exp. Biol.*, **209**, pp. 32–42.
- [67] Sane, S. P., and Jacobsen, N., 2006, "Induced Airflow in Flying Insects, II: Measurement of Induced Flow," *J. Exp. Biol.*, **209**, pp. 43–56.
- [68] Combes, S. A., and Daniel, T. L., 2001, "Shape, Flapping, and Flexion: Wing and Fin Design for Forward Flight," *J. Exp. Biol.*, **204**(12), pp. 2073–2085.
- [69] Walker, J. A., 2002, "Rotational Lift: Something Different or More of the Same?," *J. Exp. Biol.*, **205**, pp. 3783–3792.
- [70] Sun, M., and Tang, J., 2002, "Unsteady Aerodynamic Force Generation by a Model Fruit Fly Wing in Flapping Motion," *J. Exp. Biol.*, **205**, pp. 55–70.
- [71] Ramamurti, R., and Sandberg, W. C., 2005, "A Three-Dimensional Computational Study of the Aerodynamic Mechanisms of Insect Flight," *J. Exp. Biol.*, **205**, pp. 1507–1518.
- [72] Ellington, C. P., van den Berg, C., Willmott, A. P., and Thomas, A. L. R., 1996, "Leading-Edge Vortices in Insect Flight," *Nature (London)*, **384**, pp. 626–630.
- [73] Ramamurti, R., and Sandberg, W. C., 2007, "A Computational Investigation of the Three-Dimensional Unsteady Aerodynamics of *Drosophila* Hovering and Maneuvering," *J. Exp. Biol.*, **210**, pp. 881–896.
- [74] Sunada, S., Kawachi, K., Watanabe, I., and Azuma, A., 1993, "Performance of a Butterfly in Take-Off Flight," *J. Exp. Biol.*, **183**, pp. 249–277.
- [75] Spedding, G. R., Rosen, M., and Hedenstrom, A., 2003, "A Family of Vortex Wakes Generated by a Thrush Nightingale in Free Flight in a Wind Tunnel Over Its Entire Range of Flight Speeds," *J. Exp. Biol.*, **206**, pp. 2313–2344.
- [76] Bomphey, R. J., Lawson, N. J., Harding, N. J., Taylor, G. K., and Thomas, A. L. R., 2005, "The Aerodynamics of *Manduca sexta*: Digital Particle Image Velocimetry Analysis of the Leading-Edge Vortex," *J. Exp. Biol.*, **208**, pp. 1079–1094.
- [77] Luttges, M. W., 1989, "Accomplished Insect Fliers," *Frontiers in Experimental Fluid Mechanics*, Springer, Berlin, pp. 429–456.
- [78] Bandyopadhyay, P. R., Beal, D. N., and Mangalam, A., 2008, "Experiments on the Mechanism of Force Production in Rolling and Pitching Foils," *J. Fluid Mech.*, to be submitted.
- [79] Lighthill, M. J., 1963, "Introduction to Boundary Layer Theory," *Laminar Boundary Layers, Part II*, L. Rosenhead, ed., Oxford University Press, Oxford, pp. 46–113.
- [80] Nudds, R. L., Taylor, G. K., and Thomas, A. L. R., 2004, "Tuning of Strouhal Number for High Propulsive Efficiency Accurately Predicts How Wingbeat Frequency and Stroke Amplitude Relate and Scale With Size and Flight Speed in Birds," *Proc. R. Soc. London, Ser. B*, **271**, pp. 2071–2076.
- [81] Milano, M., and Gharib, M., 2005, "Uncovering the Physics of Flapping Flat Plates With Artificial Evolution," *J. Fluid Mech.*, **534**, pp. 403–409.
- [82] Tian, X., Iriarte-Diaz, J., Middleton, K., Galvao, R., Israeli, E., Roemer, A., Sullivan, A., Song, A., Swartz, S., and Breuer, K., 2006, "Direct Measurements of the Kinematics and Dynamics of Bat Flight," *Bioinspir. Biomim.*, **1**, pp. S10–S18.
- [83] Azuma, A., and Okamoto, M., 2005, "Theoretical Study on Two-Dimensional Aerodynamic Characteristics of Unsteady Wings," *J. Theor. Biol.*, **234**, pp. 67–78.
- [84] Minotti, F. O., 2002, "Unsteady Two-Dimensional Theory of a Flapping Wing," *Phys. Rev. E*, **66**, p. 051907.
- [85] Hui, C., 1988, "Penguin Swimming. I. Hydrodynamics," *Physiol. Zool.*, **61**, pp. 333–343.
- [86] Breder, C. A., 1926, "The Locomotion of Fishes," *Zoologica (N.Y.)*, **4**, pp. 159–297.
- [87] Tytell, E. D., and Lauder, G. V., 2004, "The Hydrodynamics of Eel Swimming. I. Wake Structure," *J. Exp. Biol.*, **207**, pp. 1825–1841.
- [88] Schmidt-Nielsen, K., 1972, "Locomotion: Energy Cost of Swimming, Flying, and Running," *Science*, **177**, pp. 222–228.
- [89] Kooyman, G. L., and Ponganis, P. J., 1994, "Emperor Penguin Oxygen Consumption, Heart Rate and Plasma Lactate Levels During Graded Swimming Exercise," *J. Exp. Biol.*, **195**, pp. 199–209.
- [90] Green, J. A., Butler, P. J., Woakes, A. J., and Boyd, I. L., 2003, "Energetics of Diving in Macaroni Penguins," *J. Exp. Biol.*, **206**, pp. 43–57.
- [91] Lighthill, M. J., 1969, "Hydromechanics of Aquatic Animal Propulsion," *Annu. Rev. Fluid Mech.*, **1**, pp. 413–446.
- [92] Lighthill, M. J., 1970, "Aquatic Animal Propulsion of High Hydromechanical Efficiency," *J. Fluid Mech.*, **44**, pp. 265–301.
- [93] Lauder, G. V., and Madden, P. G. A., 2006, "Learning From Fish: Kinematics and Experimental Hydrodynamics for Robotists," *Int. J. Autom. Comput.*, **3**, pp. 325–335.
- [94] Blake, R. W., 1983, *Fish Locomotion*, Cambridge University Press, Cambridge.
- [95] Westneat, M. W., 1996, "Functional Morphology of Aquatic Flight in Fishes: Kinematics, Electromyography, and Mechanical Modeling of Labriform Locomotion," *Am. Zool.*, **36**, pp. 582–598.
- [96] Walker, J. A., and Westneat, M. W., 2000, "Mechanical Performance of Aquatic Rowing and Flying," *Proc. R. Soc. London, Ser. B*, **267**, pp. 1875–1881.
- [97] Walker, J. A., and Westneat, M. W., 2002, "Performance Limits of Labriform Propulsion and Correlates With Fin Shape and Motion," *J. Exp. Biol.*, **205**, pp. 177–187.
- [98] Kato, N., 1999, "Hydrodynamic Characteristics of Mechanical Pectoral Fin," *ASME J. Fluids Eng.*, **121**(3), pp. 605–613.
- [99] Archer, R. D., Sapuppo, J., and Betteridge, D. S., 1979, "Propulsion Characteristics of Flapping Wings," *Aeronaut. J.*, **83**, pp. 355–371.
- [100] Kadlec, R. A., and Davis, S. S., 1979, "Visualization of Quasiperiodic Flows," *AIAA J.*, **17**, pp. 1164–1169.
- [101] Triantafyllou, G. S., Triantafyllou, M. S., and Grosenbaugh, M. A., 1993, "Optimal Thrust Development in Oscillating Foils With Applications to Fish Propulsion," *J. Fluids Struct.*, **7**, pp. 205–234.
- [102] Anderson, J. M., Streitlien, K., Barrett, D. S., and Triantafyllou, M. S., 1998, "Oscillating Foils of High Propulsive Efficiency," *J. Fluid Mech.*, **360**, pp. 41–72.
- [103] Bose, N., and Lien, J., 1989, "Propulsion of a Fin Whale (*Balaenoptera Physalus*): Why the Fin Whale is a Fast Swimmer," *Proc. R. Soc. London, Ser. B*, **237**, pp. 175–200.
- [104] Read, D. A., Hover, F. S., and Triantafyllou, M. S., 2003, "Forces on Oscillating Foils for Propulsion and Maneuvering," *J. Fluids Struct.*, **17**, pp. 163–183.
- [105] Gray, J., 1933, "Studies in Animal Locomotion. III. The Propulsive Mechanism of the Whiting (*Gadus Merlangus*)," *J. Exp. Biol.*, **10**, pp. 391–400.
- [106] Bainbridge, R., 1961, "Problems of Fish Locomotion," *Symp. Zool. Soc. Lond.*, **5**, pp. 13–32.
- [107] Bainbridge, R., 1962, "Training, Speed and Stamina in Trout," *J. Exp. Biol.*, **39**, pp. 537–555.
- [108] Webb, P., 2006, "Bainbridge Sets the Stage on Scaling in Fish Swimming," *J. Exp. Biol.*, **209**, pp. 1789–1790.
- [109] Ellington, C. P., 1999, "The Novel Aerodynamics of Insect Flight: Applications to Micro-Air Vehicles," *J. Exp. Biol.*, **202**, pp. 3439–3448.
- [110] Crocker, M. J., 1999, "Sir James Lighthill and His Contributions to Science," *Keynote Lecture, Sixth International Congress on Sound and Vibration*, Technical University of Denmark, Lyngby, Denmark.
- [111] <http://www.iiav.org/sirjameslighthill.pdf>.
- [112] Wilga, C. D., and Lauder, G. V., 2000, "Three-Dimensional Kinematics and Wake Structure of the Pectoral Fins During Locomotion in Leopard Sharks *Triakis semifasciata*," *J. Exp. Biol.*, **203**, pp. 2261–2278.
- [113] Wilga, C. D., and Lauder, G. V., 2001, "Functional Morphology of the Pectoral Fins in Bamboo Sharks, *Chiloscyllium Plagiosum*: Benthic vs. Pelagic Station-Holding," *J. Morphol.*, **249**, pp. 195–209.
- [114] Liao, J., and Lauder, G. V., 2000, "Function of the Heterocercal Tail Fin in White Sturgeon: Flow Visualization During Steady Swimming and Vertical Maneuvering," *J. Exp. Biol.*, **203**, pp. 3585–3594.
- [115] Nauen, J. C., and Lauder, G. V., 2001, "Three-Dimensional Analysis of Finlet Kinematics in the Chub Mackerel (*Scomber Japonicus*)," *Biol. Bull.*, **200**, pp. 9–19.
- [116] Nauen, J. C., and Lauder, G. V., 2001, "Locomotion in Scombird Fishes: Visualization of Flow Around the Caudal Peduncle and Finlets of the Club Mackerel *Scomber Japonicus*," *J. Exp. Biol.*, **204**, pp. 2251–2263.
- [117] Nauen, J. C., and Lauder, G. V., 2002, "Hydrodynamics of Caudal Fin Locomotion by Chub Mackerel, *Scomber Japonicus* (*Scombridae*)," *J. Exp. Biol.*, **205**, pp. 1709–1724.
- [118] Wardle, C. S., 1977, "Effects of Size on the Swimming Speeds of Fish," *Scale Effects in Animal Locomotion*, T. J. Pedley, ed., Academic, New York, pp. 299–313.
- [119] Aleev, Y. G., 1969, *Function and Gross Morphology in Fish*, Keter, Jerusalem.

- [120] Helfman, G. S., Collette, B. B., and Facey, D. E., 1997, *The Diversity of Fishes*, Blackwell Scientific, Malden, MA.
- [121] Lindsey, C. C., 1978, "Form, Function, and Locomotory Habits in Fish," *Fish Physiology*, Vol. VII, W. S. Hoar and D. J. Randall, eds., Academic, New York, pp. 1–100.
- [122] Magnuson, J. J., 1970, "Hydrostatic Equilibrium of *Euthynnus Affinis*, A Pelagic Teleost Without a Gas Bladder," *Copeia*, **1**, pp. 56–85.
- [123] Nauen, J. C., and Lauder, G. V., 2000, "Locomotion in Scombrid Fishes: Morphology and Kinematics of the Finlets of the Chub Mackerel *Scomber Japonicus*," *J. Exp. Biol.*, **203**, pp. 2247–2259.
- [124] Bainbridge, R., 1963, "Caudal Fin and Body Movements in the Propulsion of Some Fish," *J. Exp. Biol.*, **40**, pp. 23–56.
- [125] Webb, P. W., 1975, "Hydrodynamics and Energetics of Fish Propulsion," *Bull. - Fish. Res. Board Can.*, **190**, pp. 1–159.
- [126] Gibb, C., Dickson, K. A., and Lauder, G. V., 1999, "Tail Kinematics of the Chub Mackerel *Scomber Japonicus*: Testing the Homocercal Tail Model of Fish Propulsion," *J. Exp. Biol.*, **202**, pp. 2433–2447.
- [127] Drucker, E. G., and Lauder, G. V., 2001, "Wake Dynamics and Fluid Forces of Turning Maneuvers in Sunfish," *J. Exp. Biol.*, **204**, pp. 431–442.
- [128] Drucker, E. G., and Lauder, G. V., 2000, "A Hydrodynamic Analysis of Fish Swimming Speed: Wake Structure and Locomotor Force in Slow and Fast Labriform Swimmers," *J. Exp. Biol.*, **203**, pp. 2379–2393.
- [129] Weihs, D., 1981, "Effects of Swimming Path Curvature on the Energetics of Fish," *Fishery Bulletin*, **79**, pp. 171–176.
- [130] Lauder, G. V., Anderson, E. J., Tangorra, J., and Madden, P. G. A., 2007, "Fish Biorobotics: Kinematics and Hydrodynamics of Self-Propulsion," *J. Exp. Biol.*, **210**, pp. 2767–2780.
- [131] Mittal, R., Dong, H., Bozkurtas, M., Lauder, G. V., and Madden, P., 2006, "Locomotion With Flexible Propulsors: II. Computational Modeling of Pectoral Fin Swimming in Sunfish," *Bioinspir. Biomim.*, **1**, pp. S35–S41.
- [132] Tytell, E. D., 2006, "Median Fin Function in Bluegill Sunfish Loomis Marchers: Streamwise Vortex Structure During Steady Swimming," *J. Exp. Biol.*, **209**, pp. 1516–1534.
- [133] Bartol, I. K., Gharib, M., Webb, P. W., Weihs, D., and Gordon, M. S., 2005, "Body-Induced Vertical Flows: A Common Mechanism for Self-Corrective Trimming Control in Boxfish," *J. Exp. Biol.*, **208**, pp. 327–344.
- [134] Walker, J. A., 2004, "Kinematics and Performance of Maneuvering Control Surfaces in Teleost Fishes," *IEEE J. Ocean. Eng.*, **29**, pp. 572–584.
- [135] O'Dor, R. K., and Weber, D. M., 1986, "The Constraints on Cephalopods: Why Squid Aren't Fish," *Can. J. Zool.*, **64**, pp. 1591–1605.
- [136] Bartol, I. K., Mann, R., and Patterson, M. R., 2001, "Aerobic Respiratory Costs of Swimming in the Negatively Buoyant Brief Squid *Lolliguncula Brevis*," *J. Exp. Biol.*, **204**, pp. 3639–3653.
- [137] Krueger, P., 2001, "The Significance of Vortex Ring Formation and Nozzle Exit Overpressure in Pulsatile Jet Propulsion," Ph.D. thesis, California Institute of Technology, Pasadena, CA.
- [138] Liu, P., and Bose, N., 1997, "Propulsive Performance From Oscillating Propulsors With Spanwise Flexibility," *Proc. R. Soc. London, Ser. A*, **453**, pp. 1763–1770.
- [139] Ando, Y., Kato, N., Suzuki, H., Suzimori, K., Kanda, T., and Endo, S., 2006, "Elastic Pectoral Fin Actuators for Biomimetic Underwater Vehicles," *Proceedings of the 3rd International Symposium on Aero. Aqua Biol.-Mechanisms, ISABMEC, Ginowan, Okinawa, Japan, Jul. 3–7*, pp. 1–8.
- [140] Dudley, R., 2000, *The Biomechanics of Insect Flight*, Princeton University Press, Princeton, NJ.
- [141] Mao, S., and Hamdani, H., 2001, "High-Lift Generation by an Airfoil Performing Unsteady Motion at Low Reynolds Number," *Acta Mech. Sin.*, **17**, pp. 97–144.
- [142] Sun, M., and Lan, S. L., 2004, "A Computational Study of the Aerodynamic Forces and Power Requirements of Dragonfly (*Aeschna Juncea*) Hovering," *J. Exp. Biol.*, **207**, pp. 1887–1901.
- [143] Ramamurti, R., Sandberg, W. C., Löhner, R., Walker, J. A., and Westneat, M. W., 2002, "Fluid Dynamics of Flapping Aquatic Flight in the Bird Wrasse: Three-Dimensional Unsteady Computations With Fin Deformation," *J. Exp. Biol.*, **205**, pp. 2997–3008.
- [144] Ramamurti, R., and Sandberg, W. C., 2006, "Computational Fluid Dynamics Study for Optimization of a Fin Design," *AIAA Paper No. 2006–3658*.
- [145] Peskin, C., 1972, "Flow Patterns Around Heart Valves: A Numerical Study," *J. Comput. Phys.*, **10**, pp. 252–271.
- [146] Mittal, R., and Iaccarino, G., 2005, "Immersed Boundary Methods," *Annu. Rev. Fluid Mech.*, **37**, pp. 239–261.
- [147] Dong, H., Mittal, R., and Najjar, F. M., 2006, "Wake Topology and Hydrodynamic Performance of Low-Aspect-Ratio Flapping Airfoil," *J. Fluid Mech.*, **566**, pp. 309–343.
- [148] Rayner, J. M. V., 1979, "Vortex Theory of Animal Flight, I—Vortex Wake of a Hovering Animal," *J. Fluid Mech.*, **91**, pp. 697–730.
- [149] Lan, S. L., and Sun, M., 2001, "Aerodynamic Properties of a Wing Performing Unsteady Rotational Motions at Low Reynolds Number," *Acta Mech.*, **149**, pp. 135–147.
- [150] Dabiri, J. O., 2005, "On the Estimation of Swimming and Flying Forces From Wake Measurements," *J. Exp. Biol.*, **208**, pp. 3519–3532.
- [151] Smith, R.W., and Wright, J.A., 2004, "Simulation of RoboTuna Fluid Dynamics Using a New Incompressible ALE Method," *AIAA Paper No. 2004–23–2347*.
- [152] Zhu, Q., Wolfgang, M. J., Yue, D. K. P., and Triantafyllou, M. S., 2002, "Three-Dimensional Flow Structures and Vorticity Control in Fish-Like Swimming," *J. Fluid Mech.*, **392**, pp. 183–212.
- [153] Walker, P. B., 1931, "Experiments on the Growth of Circulation About a Wing and an Apparatus for Measuring Fluid Motion," *Rep. Memo. Aeronaut. Res. (Great Britain)* 1402.
- [154] Fung, Y. C., 1993, *An Introduction to Aeroelasticity*, Dover, New York.
- [155] Brennen, C.E., 1982, "A Review of Added Mass and Fluid Inertial Forces," Report No. CR82,010, Naval Civil Engineering Laboratory, Port Hueneme, CA.
- [156] Sane, S. P., and Dickinson, M. H., 2002, "The Aerodynamic Effects of Wing Rotation and a Revised Quasi-Steady Model of Flapping Flight," *J. Exp. Biol.*, **205**, pp. 1087–1096.
- [157] Peng, J., Dabiri, J. O., Madden, P. G., and Lauder, G. V., 2007, "Non-Invasive Measurement of Instantaneous Forces During Aquatic Locomotion: A Case Study of the Bluegill Sunfish Pectoral Fin," *J. Exp. Biol.*, **210**, pp. 685–698.
- [158] van Ginneken, V. J. T., and van den Thillart, G. E. E. J. M., 2000, "Eel Fat Stores Are Enough to Reach the Sargasso," *Nature (London)*, **403**, pp. 156–157.
- [159] Müller, U. K., Smit, J., Stamhuis, E. J., and Videler, J. J., 2001, "How the Body Contributes to the Wake in Undulatory Fish Swimming: Flow Fields of a Swimming Eel (*Anguilla Anguilla*)," *J. Exp. Biol.*, **204**, pp. 2751–2762.
- [160] Tytell, E. D., 2004, "The Hydrodynamics of Eel Swimming, II. Effect of Swimming Speed," *J. Exp. Biol.*, **207**, pp. 3265–3279.
- [161] Blackburn, L., 2006, "Swimming Secrets," *J. Exp. Biol.*, **209**, pp. i–ii.
- [162] Milano, M., and Koumoutsakos, P., 2002, "A Clustering Genetic Algorithm for Cylinder Drag Optimization," *J. Comput. Phys.*, **175**, pp. 79–107.
- [163] Katz, D. F., and Dott, H. M., 1975, "Methods of Measuring Swimming Speed of Spermatozoa," *J. Reprod. Fertil.*, **45**(2), pp. 263–272.
- [164] Kim, M., Bird, J. C., Avan Parys, J., Breuer, K. S., and Powers, T. R., 2003, "A Macroscopic Scale Model of Bacterial Flagellar Bundling," *Proc. Natl. Acad. Sci. U.S.A.*, **100**, pp. 15481–15485.
- [165] Bandyopadhyay, P. R., Singh, S. N., Thivierge, D. P., Annaswamy, A. M., Leinhos, H. A., Fredette, A. R., and Beal, D. N., 2008, "Synchronization of Animal-Inspired Multiple High-Lift Fins in an Underwater Vehicle Using Olivo-Cerebellar Dynamics," *IEEE J. Ocean. Eng.*, **33**(4), pp. 563–578.
- [166] Lighthill, J., 1975, *Mathematical Biofluidynamics*, Society for Industrial and Applied Mathematics, Philadelphia, PA.
- [167] Lighthill, M. J., 1975, "Aerodynamic Aspects of Animal Flight," *Swimming and Flying in Nature 2*, T. Y. Wu, C. J. Brokaw, and C. Brennen, eds., Plenum, New York, pp. 423–492.
- [168] Schlichting, H., 1979, *Boundary-Layer Theory*, 7th ed., McGraw-Hill, New York, pp. 31–32.
- [169] Bandyopadhyay, P. R., Castano, J. M., Nedderman, W. H., and Donnelly, M. J., 2000, "Experimental Simulation of Fish-Inspired Unsteady Vortex Dynamics on a Rigid Cylinder," *ASME J. Fluids Eng.*, **122**, pp. 219–238.
- [170] Wang, Z. J., 2000, "Vortex Shedding and Frequency Selection in Flapping Flight," *J. Fluid Mech.*, **410**, pp. 323–341.
- [171] Rohr, J. J., and Fish, F. E., 2004, "Strouhal Numbers and Optimization of Swimming by Odontocete Cetaceans," *J. Exp. Biol.*, **207**, pp. 1633–1642.
- [172] Streitlien, K., and Triantafyllou, M. S., 1995, "Force and Moment on Joukowski Profile in the Presence of Point Vortices," *AIAA J.*, **33**, pp. 603–610.
- [173] Wakeling, J. M., and Ellington, C. P., 1997, "Dragonfly Flight II—Velocities, Accelerations, and Kinematics of Flapping Flight," *J. Exp. Biol.*, **200**, pp. 557–582.
- [174] Wakeling, J. M., and Ellington, C. P., 1997, "Dragonfly Flight III—Lift and Power Requirements," *J. Exp. Biol.*, **200**, pp. 583–600.
- [175] Hui, C., 1988, "Penguin Swimming, II. Energetics and Behavior," *Physiol. Zool.*, **61**, pp. 344–350.
- [176] Buchholz, J., and Smits, A. J., 2005, "Vortex Structures in the Wake of a Flapping Plate," *Phys. Fluids*, **17**, p. 091102.
- [177] Buchholz, J. H. J., and Smits, A. J., 2006, "On the Evolution of the Wake Structure Produced by a Low Aspect-Ratio Pitching Panel," *J. Fluid Mech.*, **546**, pp. 433–443.
- [178] Williamson, C. H. K., and Roshko, A., 1988, "The Hydrodynamics and Eel Swimming, II: Effects of Swimming Speed Vortex Formation in the Wake of an Oscillating Cylinder," *J. Fluids Struct.*, **2**, pp. 355–381.
- [179] Rosenberger, L. J., and Westneat, M. W., 1999, "Functional Morphology of Undulatory Pectoral Fin Locomotion in the Stingray *Taeniura Lyman* (Chondrichthyes: Dasyatidae)," *J. Exp. Biol.*, **202**, pp. 523–5359.
- [180] Clark, R. P., and Smits, A. J., 2006, "Thrust Production and Wake Structure of a Batoid-Inspired Oscillating Fin," *J. Fluid Mech.*, **562**, pp. 415–429.
- [181] Dickinson, M. H., 1999, "Bionics: Biological Insight Into Mechanical Design," *Proc. Natl. Acad. Sci. U.S.A.*, **96**(25), pp. 14208–14209.
- [182] Westneat, M. W., 2001, "Mechanical Design for Swimming: Muscle, Tendon, and Bone," *Fish Physiol.*, **19**, pp. 271–311.
- [183] Wainwright, S. A., 1983, "To Bend A Fish," *Fish Biomechanics*, P. W. Webb and D. Weihs, eds., Praeger, NY, pp. 68–91.
- [184] Scherer, J. O., 1968, "Experimental and Theoretical Investigation of Large Amplitude Oscillating Foil Propulsion System," Technical Report No. 662–1, Hydronautics Inc., Laurel, MD.
- [185] Fish, F. E., and Battle, J. M., 1995, "Hydrodynamic Design of the Humpback Whale Flipper," *J. Morphol.*, **225**, pp. 51–60.
- [186] Miklosovic, D. S., Murray, M. M., Howle, L. E., and Fish, F. E., 2004, "Leading Edge Tubercles Delay Stall on Humpback Whale (Megaptera Novaeangliae) Flippers," *Phys. Fluids*, **16**, pp. L39–L42.
- [187] Bannasch, R., 2001, "From Soaring and Flapping Bird Flight to Innovative Wing and Propeller Constructions," *Fixed and Flapping Wing Aerodynamics*

- for *Micro Air Vehicle Applications*, T. J. Mueller, ed., Prog. Astro. Aero., Vol. 195, AIAA Publishers, Reston, VA, pp. 453–472.
- [188] Isshiki, H., and Murakami, M., 1984, “A Theory of Wave Devouring Propulsion,” *J. Soc. Nav. Archit. Jpn.*, **156**, pp. 102–114.
- [189] Koochesfahani, M. M., and Dimotakis, P. E., 1988, “A Cancellation Experiment in a Forced Turbulent Shear Layer,” AIAA Paper No. AIAA-88-3713.
- [190] Beal, D. N., Hover, F. S., Triantafyllou, M. S., Liao, J. C., and Lauder, G. V., 2006, “Passive Propulsion in Vortex Wakes,” *J. Fluid Mech.*, **549**, pp. 385–402.
- [191] Allen, J. J., and Smits, A. J., 2001, “Energy Harvesting Eel,” *J. Fluids Struct.*, **15**, pp. 629–640.
- [192] Kim, M. J., and Breuer, K. S., 2007, “The Use of Bacterial Carpets to Enhance Mixing in Microfluidic Systems,” *ASME J. Fluids Eng.*, **121**, pp. 319–324.
- [193] Behkam, B., and Sitti, M., 2005 “Modeling and Testing of a Biomimetic Flagellar Propulsion Method for Microscale Biomedical Swimming Robots,” IEEE Advanced Intelligent Mechanotronics Conference, Monterey, CA, Jul. 24–28.
- [194] Chen, J., Fan, Z., Zou, J., Engel, J., and Liu, C., 2003, “Two-Dimensional Micromachined Flow Sensor Array for Fluid Mechanics Studies,” *J. Aerosol Eng.*, **16**(2), pp. 85–97.
- [195] Ellington, C. P., 1984, “The Aerodynamics of Hovering Insect Flight, V—A Vortex Theory,” *Philos. Trans. R. Soc. London, Ser. B*, **305**, pp. 115–144.
- [196] Wootton, R., 2000, “From Insects to Microvehicles,” *Nature (London)*, **403**, pp. 144–145.
- [197] Zbikowski, R., 2002, “On Aerodynamic Modeling of an Insect-Like Flapping Wing in Hover for Micro-Air Vehicles,” *Philos. Trans. R. Soc. London, Ser. A*, **360**, pp. 273–290.
- [198] Yan, J., Avadhanula, S. A., Birch, J., Dickinson, M. H., Sitti, M., Su, T., and Fearing, R. S., 2001, “Wing Transmission for a Micromechanical Flying Insect,” *J. Micromechatronics*, **1**(3), pp. 221–238.
- [199] Usab, W. J., Hardin, J., and Bilanin, A. J., 2004, “Biology-Inspired Delayed Stall Propulsor,” *IEEE J. Ocean. Eng.*, **29**, pp. 756–765.
- [200] Opila, D. F., Annaswamy, A. M., Krol, W. P., and Raghu, S., 2004, “Biomimetic Reduction of Wake Deficit Using Tail Articulation at Low Reynolds Number,” *IEEE J. Ocean. Eng.*, **29**, pp. 766–776.
- [201] Yoda, K., Sato, K., Niizuma, Y., Kurita, M., Bost, C.-A., Le Maho, Y., and Naito, Y., 1999, “Precise Monitoring of Porpoising Behaviour of Adélie Penguins Determined Using Acceleration Data Loggers,” *J. Exp. Biol.*, **202**, pp. 3121–3126.

Hot-Wire Anemometry for Velocity Measurements in Nanopowder Flows

Sergey P. Bardakhanov

Khrstianovich Institute of Theoretical and Applied Mechanics,
Novosibirsk 630090, Russia;
School of Mechanical Engineering,
Yeungnam University,
Gyongsan 712-749, Korea
e-mail: bard@itam.nsc.ru

Sang W. Joo¹

School of Mechanical Engineering,
Yeungnam University,
Gyongsan 712-749, Korea
e-mail: swjoo@yumail.ac.kr

A new technique for velocity-field measurements in fine granular systems is introduced. The hot-wire anemometry, mainly used for gaseous flows, is applied to nanopowders and is found to be a viable experimental method for flow measurements. A generic chute flow of aluminum oxide C and Aerosil A-90 and A-380 powders through a vertical channel is chosen as a test platform, and the results suggest that the hot-wire anemometry is a favorable option for nanopowder measurements. [DOI: 10.1115/1.3077140]

1 Introduction

Powders are widely used in many manufacturing processes as either final products or intermediate materials. They have been thus intensively studied for a long while, but predicting the dynamics of powders in motion is still a challenging problem due to the difficulties in theoretical modeling and experimental measurement. Although each individual particle is solid, powders collectively behave as a fluidlike material that requires complicated constitutive modeling or demanding simulations of the molecular-dynamics type. Many experimental methods available for conventional fluids are not directly applicable to powders, which in general are composed of opaque particles of varying shapes and sizes.

In a theoretical study of rapid powder flows, Jenkins and Savage [1] showed an analogy with the kinetic theory of gases, whose viscosity increases with temperature. Haff [2] treated a granular medium as an interstitial liquid with high density and viscosity. A fluid-mechanical approach for slow powder flows was proposed by Tardos [3], who designed a number of experimental devices to obtain data for the powders of comparatively large particles, and argued that these data can be applied to different flow situations with appropriate viscosity adjustments. By using fiber-optic probes, Savage [4] measured the velocity of 1.2 mm diameter polystyrene beads in a rectangular channel with two smooth glass sidewalls and two walls lined with rough rubber sheet. His experimental method for the powder velocity was, however, restricted to channels narrow enough to allow the fiber-optic-probe observations. For thick channels his method did not accommodate direct

velocity measurements in the interior region. Another experimental method for flow velocities of granular materials was introduced by Azanza et al. [5], who measured the velocity of the metal beads mixed with different color probes flowing in an inclined duct. In their experiment, there was an observation window, through which different color beads can be identified by a direct visual contact. The bead movement was filmed with a high-speed digital camera at a rate of 230 images per second, proving the sequential images of the colored probes with a double-flash light source. This method was also restricted to the measurement of the circumferential region of the bead flow. Green et al. [6] used electrodynamic tomography for axial velocity measurements close to the wall of a gravity drop conveyor. The method is applicable to pneumatically conveyed charged particles. More recent studies of powder flows, performed in a somewhat different context, included the use of X-ray penetration image analysis [7], laser Doppler anemometry (LDA) [8], and magnetic resonance imaging (MRI) [9], each with limited applicability.

The purpose of this brief is to propose the hot-wire anemometry as a viable option with relatively low cost and wide applicability for velocity measurement of fine powders. With recent developments in nanotechnology, more ultrafine powders are processed, and a convenient method of measurement is in high demand. The hot-wire anemometer, principally used in gas flow measurement, consists of an electrically fine-heated platinum or tungsten wire that is immersed into the flow. As the fluid velocity increases, the rate of heat flow from the heated wire to the flow stream increases. Thus, a cooling effect on the wire electrode occurs, causing its electrical resistance to change. In a constant-current anemometer, the fluid velocity is determined from a measurement of the resulting change in wire resistance. In a constant-resistance anemometer, fluid velocity is determined from the current needed to maintain a constant wire temperature and, thus, the resistance constant. Boerefijn et al. [10] reported that hot-wire anemometry used inside an air-fluidized bed of glass, called microscaled powder, allows the measurement of the time-resolved local heat transfer coefficient, but the length and diameter of the wire in their study were large so that the spatial resolution was low. The underlying idea of the investigation is that the particle velocity fluctuations are related to the extent of macro versus micro mixing of the solids in the emulsion phase under different fluidization regimes. With this consideration, the aim of the study is to arrive at a characterization of the quality of fluidization via the analysis of time series of local heat transfer coefficients measured by means of a hot-wire anemometer. Three different air/solid systems characterized by different fluidization patterns are investigated with the aim of establishing the prevailing length scales of particle recirculation. Bardakhanov and Kozlov [11] addressed that a hot-wire can be used to study the nonstationary nanopowder flow due to gravity.

In this brief a method for using hot-wire anemometry for fine powders is reported. The method, allowing velocity measurements for a wide range of flow regions, is verified by comparisons with previous theoretical and experimental results.

2 Experimental Setup

The experimental apparatus is sketched in Fig. 1(a). It consists of a funnel connected to a vertical calibrated glass pipe with an inner diameter of 9.5 cm, a height of 120 cm, and a scale clearly placed on its wall. In the closed position, the shutter allows the loading of the powder. The full loading of the powder can be up to 400 g, depending on powder properties, such as the bulk density. When the shutter opens, the powder goes down into the hopper, which has a few times larger capacity than the pipe. After a run the powder is extracted by a pump, and prepared to be loaded again to the pipe for the ensuing run. A cone valve moves up and down and functions as the main flow-rate controller. The valves and taps, located in the upstream and the downstream of the chan-

¹Corresponding author.

Contributed by the Fluids Engineering Division of ASME for publication in the JOURNAL OF FLUIDS ENGINEERING. Manuscript received February 8, 2008; final manuscript received December 21, 2008; published online February 4, 2009. Assoc. Editor: Juergen Kompenhans.

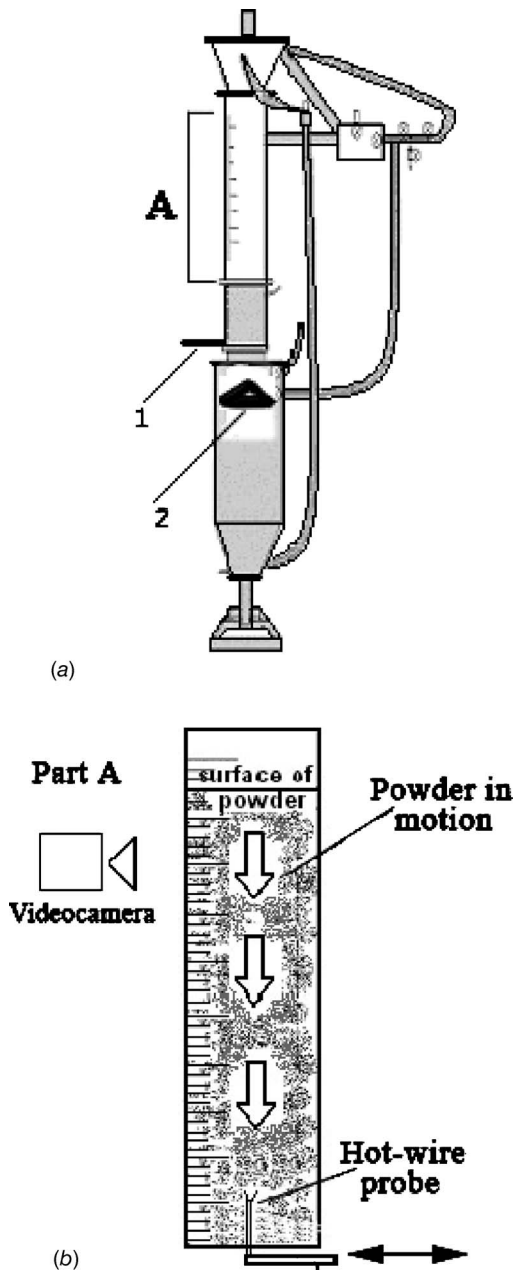


Fig. 1 Experimental apparatus: (a) full view and (b) part A magnified; (1) shutter and (2) cone controller

nel and in pipes connecting the funnel and hopper, allow precise control of the flow rate due to the regulation of air flow up and down the powder.

The flow scheme and the hot-wire probe installation are shown in Fig. 1(b). The standard hot-wire probe of DANTEC (Denmark) with a gold-plated tungsten wire with a diameter of $5 \mu\text{m}$ and a length of 1 mm is used. The standard probe support is installed in the coordinate mechanism, which is placed sufficiently above the exit into the hopper in order to avoid flow fluctuations. The hot-wire translates horizontally between the channel wall and the center, enabling velocity measurements in the entire channel cross section through voltage measurements in the powder flow. The hot-wire instrument is used in constant-temperature mode of operation. Powders of Aerosil series of silica A-90 and A-380 and of alumina aluminum oxide C are used as the flow medium, with average primary particle diameters of 20 nm, 7 nm, and 13 nm and specific surfaces of $S=90 \text{ m}^2/\text{g}$, $380 \text{ m}^2/\text{g}$, and $100 \text{ m}^2/\text{g}$,

respectively. Compared with the aluminum oxide C the silica powders require extra care with the flow control due to their fluffiness and stickiness. The influence of the wall friction also seems to penetrate further into the entire flow. It is notable that the probe wire endures even the largest local flow velocity of up to 1 m/s of solid particles without breakage.

An observation camera is mounted for monitoring the dropping height of the powders and to calibrate the hot-wire in the powder by measuring the powder free-surface speed at the centerline relative to the wall scale. Calibration of the same hot-wire probe was performed also in a wind tunnel with air, where the reference velocity is measured by a Pitot-Prandtl tube. Wire contamination is a potential problem for a hot-wire method because it leads to the change in calibration. But the contamination takes place with sticky organic dust. In the present experiment the nanopowders used are refractory, with melting point much higher than 1000°C , very pure ($>99.8\%$), and do not stick to the wire. The contamination thus did not take place, and the calibration is intact.

3 Measurement

Using the apparatus described above local velocity measurements are taken for nanopowders flowing down the cylindrical pipe due to gravity. It is to be expected that initially the nanopowders fall more or less like a solid column with almost no shear motion. After the shutter opens, this column accelerates quickly, reaching a maximum speed, until the bottom (downstream) front reaches the cone, as can be deduced from Fig. 2(a). The resistance due to the air pressure in the hopper is negligible initially. The cone then starts to play, the weight of the column decreases, air pressure resists, friction on the wall hinders the flow, and the free-surface speed decreases. An identical sequence can be observed from the hot-wire signal, shown in Fig. 2(b). Prior to powder motion the voltage is constant (region 1) because constant heat flux is provided to the hot-wire. The powder then is quickly accelerated (region 2). In regions 3 and 4, the average voltage decreases at the same rate due to the aforementioned effects. The break separating regions 3 and 4 is made by the initial pressing and quick depressing-pressing of the flexible pipe, exhausting the air-nanoparticle mixture from the hopper to the following valves and taps. It actually demonstrates the effectiveness of the flow control. Near the end of region 4 entire powders have passed through the probe. Region 5 thus is mostly air flow. The similarity in the two profiles shown in Fig. 2 would allow calibration of hot-wire using a video camera and free-surface measurement. It would be necessary, however, to achieve a steady flow with constant mean velocity. The flow control is not possible using the cone only except at a low speed. Different combinations of valve and tap control, height of the powder, and funnel cover opening need to be experimented to reach a constant powder-flow velocity for a chosen cone height (see label 2 in Fig. 1(a)) between the complete open and shut positions. Different time gaps between powder loading and measurement can also influence the flow rate due to densification of the powder and change in the friction between the powder and the wall. Ensemble-averaged voltage on the hot-wire and powder free-surface velocity on the digital camera are taken from minimum of ten different trials. For each case all the adjustments for flow control are performed until the free-surface velocity detected by the camera (and supported by view of hot-wire signal) shows a constant value within a definite range of time. Depending on flow speed, the length of an averaged signal ranges 0.2–0.5 s.

The calibration runs of the same hot-wire probe with air in a large wind tunnel and with aluminum oxide C powder flow in the pipe are shown in Fig. 3. With the nanopowder, the calibration is performed for the hot-wire located at the center of the channel. The velocity is plotted against voltage for seven different flow regimes, based on proper combinations of the cone and tap control. The cases for higher speed show multiple points, and the relationship between the voltage and the powder velocity is thus

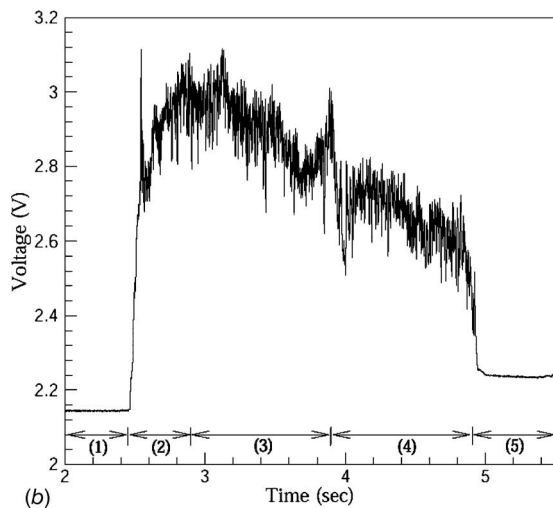
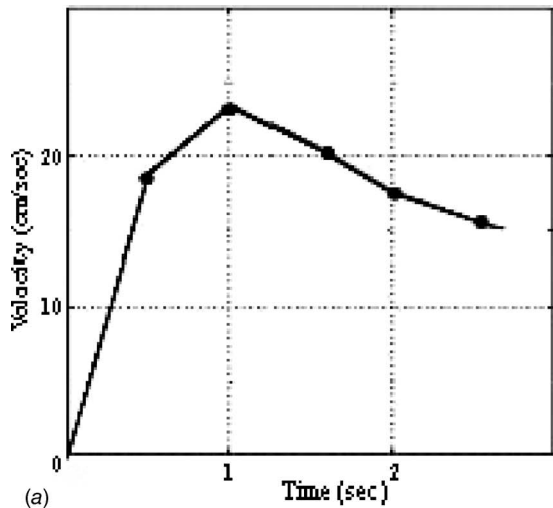


Fig. 2 (a) Free surface motion and (b) hot-wire signal of powder flow in the vertical pipe; the height of the powder is 100 cm and the hot-wire is located at the center

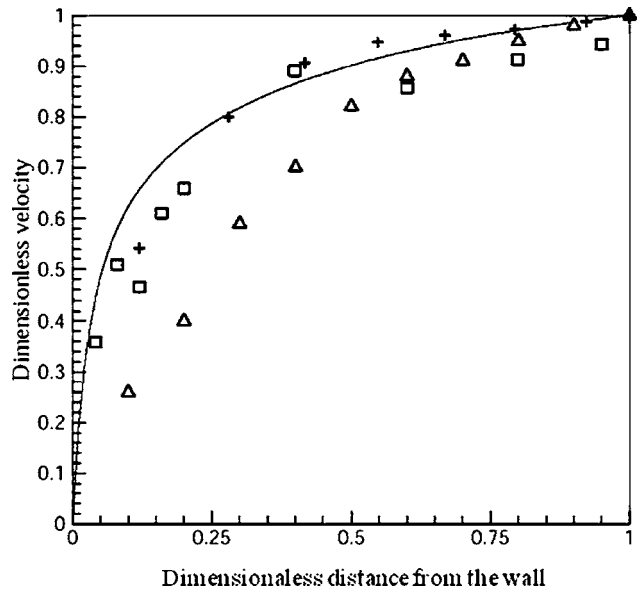
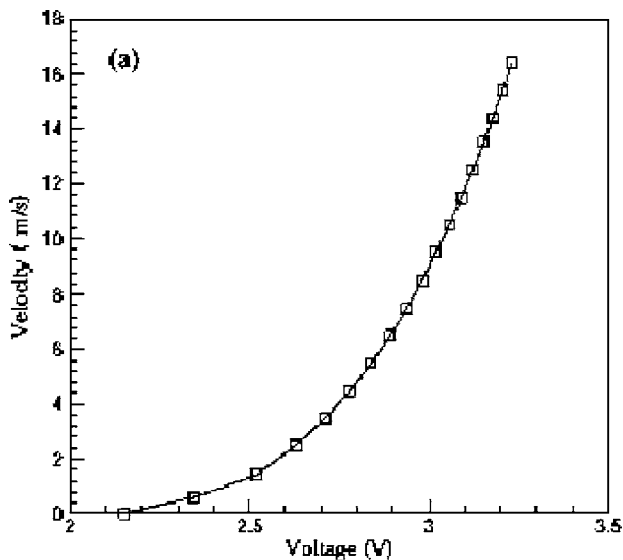


Fig. 4 Velocity profile of Savage [13] (solid line), Savage [4] (Δ), Gutfrand and Pouliquen [12] (+), and the present experimental result for case VII (\square)

obtained by a curve fitting of the ensemble-averaged data. As the flow velocity increases, the voltage increases monotonically for both air and nanopowders in a similar manner. It is noted, however, that the velocity scales for air and nanopowders are in the order of m/s and cm/s, respectively. The rate of heat transfer obviously is much higher in the nanopowder.

The hot-wire velocity measurements are performed rather extensively using the aforementioned method for various flow rates and cross-sectional locations. For relatively high flow rates, they are in general agreement with the discrete particle simulation of Gutfrand and Pouliquen [12], who identified a shear zone near the wall with large velocity gradient and a core plug-flow zone. In this brief, a representative case is presented with comparisons with previous analytical and experimental results.

Figure 4 shows the velocity profile for case VII with the theoretical result of Savage [13], the experimental result of Savage [4], and the simulation of Gutfrand and Pouliquen [12]. The horizon-

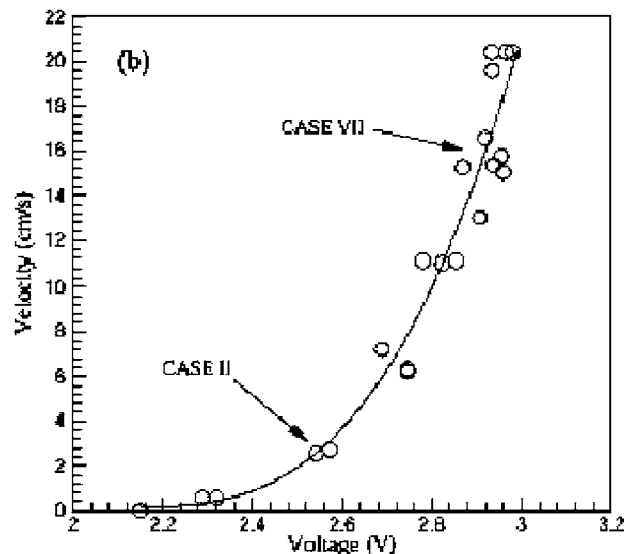


Fig. 3 Calibration curves of hot-wire probe: (a) air and (b) powder

tal and vertical axes are scaled by the channel radius and the maximum velocity at the center, respectively. The difference in the velocity gradient in the core and the shear zone is conspicuous except for the measurement of Savage [4], where the shear zone is extended to the entire radius. The present experimental result shows good agreement with theoretical and computational predictions in the shear zone near wall and the core zone. The computational result of Gutfraind and Pouliquen [12] shows more pronounced core plug-flow, and is in better agreement with the present experiment.

4 Concluding Remarks

It is shown that the hot-wire anemometry can be a viable option for flow measurements of fine powders. It is relatively easy to implement, and enables accurate measurements in the deep core region of opaque particles, where other advanced optical methods may fail. The experimental apparatus designed for the test problem of vertical granular flow of nanopowders allows precise and fluctuation-free control of the flow. Elaborate assessment of the accuracy of the method and applicability to a wider range of powder-flow problems are yet to be performed. This brief nevertheless suggests the hot-wire anemometry as an important candidate for further study in nanopowder flows.

Acknowledgment

This work was supported by the National Center for Nanomaterials Technology of Pohang through Yeungnam University. The authors thank Y.O. Han, D.Y. Lee, O.Y. Korkina, M.E. Juraeva, and V.V. Obanin for their invaluable contributions.

References

- [1] Jenkins, J. T., and Savage, S. B., 1983, "A Theory for the Rapid Flow of Identical, Smooth, Nearly Elastic, Spherical Particles," *J. Fluid Mech.*, **130**, pp. 187–202.
- [2] Haff, P. K., 1983, "Grain Flow as Fluid-Mechanical Phenomenon," *J. Fluid Mech.*, **134**, pp. 401–430.
- [3] Tardos, G. I., 1997, "A Fluid Mechanical Approach to Slow, Frictional Flow of Powders," *Powder Technol.*, **92**, pp. 61–74.
- [4] Savage, S. B., 1979, "Gravity Flow of Cohesionless Granular Materials in Chutes and Channels," *J. Fluid Mech.*, **92**, pp. 53–96.
- [5] Azanza, E., Chevoir, F., and Moucheron, P., 1999, "Experimental Study of Collisional Granular Flows Down an Inclined Plane," *J. Fluid Mech.*, **400**, pp. 199–227.
- [6] Green, R. G., Rahmat, M. F., Dutton, K., Evans, K., Goude, A., and Henry, M., 1997, "Velocity and Mass Flow Rate Profiles of Dry Powders in a Gravity Drop Conveyor Using an Electrodynamical Tomography System," *Meas. Sci. Technol.*, **8**(4), pp. 429–436.
- [7] Uchida, K., and Okamoto, K., 2006, "Measurement of Powder Flow in a Screw Feeder by X-Ray Penetration Image Analysis," *Meas. Sci. Technol.*, **17**(2), pp. 419–426.
- [8] Darelus, A., Rasmuson, A., Bjorn, I. N., and Folestad, S., 2007, "LDA Measurement of Near Wall Powder Velocities in a High Shear Mixer," *Chem. Eng. Sci.*, **62**, pp. 5770–5776.
- [9] Mantle, M. D., Sederman, A. J., Gladden, L. F., Huntley, J. M., Martin, T. W., Wildman, R. D., and Schattuck, M. D., 2008, "MRI Investigations of Particle Motion Within a Three-Dimensional Vibro-Fluidized Granular Bed," *Powder Technol.*, **179**, pp. 164–169.
- [10] Boerefijn, R., Poletto, M., and Salatino, P., 1999, "Analysis of the Dynamics of Heat Transfer Between a Hot Wire Probe and Gas Fluidized Beds," *Powder Technol.*, **102**, pp. 53–63.
- [11] Bardakhanov, S. P., and Kozlov, S. A., 2001, "Hot-Wire Measurements in Nanopowder Flow," *Eighth International Conference on Stability of Homogeneous and Inhomogeneous Liquids*, ITAM, Novosibirsk, pp. 16–17.
- [12] Gutfraind, R., and Pouliquen, O., 1996, "Study of the Origin of Shear Zones in Quasi-Static Vertical Chute Flows by Using Discrete Particle Simulation," *Mech. Mater.*, **24**, pp. 273–285.
- [13] Savage, S. B., 1998, "Analyses of Slow High-Concentration Flows of Granular Materials," *J. Fluid Mech.*, **377**, pp. 1–26.

Effects of Jet Obliquity on Hydraulic Jumps Formed by Impinging Circular Liquid Jets on a Moving Horizontal Plate

R. P. Kate

P. K. Das

Suman Chakraborty¹

e-mail: suman@mech.iitkgp.ernet.in

Department of Mechanical Engineering,
Indian Institute of Technology,
Kharagpur 721302, India

The present work attempts to investigate the effects of jet obliquity on the spatial patterns formed as a consequence of hydraulic jumps due to the impingement of circular liquid jets on continuously moving but nonaccelerating horizontal flat plates. Both the normal and the oblique impinging jets are considered, in order to characterize the contrasting features of the associated hydraulic jump mechanisms. Theoretical calculations are executed to obtain the locations of the jump, for different jet and plate velocities and jet inclination angles, using a depth-averaged momentum integral equation for shallow-free surface flows. Comparisons are subsequently made between the theoretical predictions and experimental observations reported in the literature, and a good agreement between these two can be observed. Special cases of a circular hydraulic jump when the target plate is stationary and the impinging jet is vertical, and elliptic hydraulic jumps when the target plate is stationary and the impinging jet is obliquely inclined, are also discussed. It is conjectured that flow due to impinging jets on a horizontal moving plate can be modeled as an equivalent flow due to an inclined impinging jet on stationary horizontal flat plates, with appropriate alterations in the jet velocity and the jet inclination angles. [DOI: 10.1115/1.3059583]

Keywords: hydraulic jump, impinging liquid jet, stagnation point

1 Introduction

Physics of flow patterns of hydraulic jumps associated with normal impinging jets on stationary flat surfaces have been extensively studied in the literature. Figure 1(a) qualitatively depicts such a typical circular hydraulic jump profile. Kurihara [1] was the first to derive a scaling law for the radius of the circular hydraulic jump as a function of relevant physical parameters purely from the theoretical studies. One of the earliest important contributions in the study of circular hydraulic jump is the work done by Watson [2]. He investigated the flow due to normal impinging jet by dividing it into several regions. Similarity and approximate solutions were developed for the radial position of the hydraulic jump based on the Reynolds number at the impingement point and the liquid film thickness outside the jump. Detailed quantitative estimations for the positions of the hydraulic jump, based on flow rate and viscosity of the liquid, were obtained by Bohr et al. [3]. Godwin [4] assumed that the jump occurs at a

point where the growing viscous layer touches the free surface and the flow becomes fully developed. Based on Godwin's conjecture Brechet and Néda [5] developed a scaling relation for the radius of the jump, taking the drop height (vertical distance of the nozzle tip from the plate) as an additional parameter. However, the effect of drop height on the jump radius turned out to be negligible. Bush and Aristoff [6] in their recent study demonstrated the influence of surface tension on the circular hydraulic jump. However, their experiments revealed that the influence of surface tension on the jump radius turned out to be rather small, and can therefore be neglected.

Oblique impinging jets, in comparison to normal impinging jets, have received relatively less attention in fluid mechanics literature. In the case of oblique impingement, the axial symmetry exists only up to the free jet region. The flow, in general, is three-dimensional elsewhere [7,8]. The impingement region is expected to change in its size and shape with an obliquity of the jet inclination. From the impingement zone onwards, the flow no longer remains axisymmetric, although, a partial symmetry in this regard is still postulated. An upstream shift of the stagnation point from the geometrical center of the noncircular impingement zone for oblique impinging jets has been reported in the literature [7,8]. Kate et al. [9], in a more recent investigation, analyzed the non-circular hydraulic jumps formed as a consequence of oblique impingement of circular liquid jets on stationary flat horizontal plates, both from experimental and theoretical perspectives. Such a typical scenario is qualitatively depicted in Fig. 1(b). As can be observed in Fig. 1(b), the profile of the hydraulic jump is more or less of an elliptic shape. The change in the profile of the jump from circular, in the case of normal impinging jets, to elliptic ones in the case of obliquely impinging jets, has been attributed to the progressive changes in the impingement or stagnation point zone due to obliquities in the jet inclination. However, these studies have been restricted to hydraulic jumps formed on stationary surfaces only.

Despite the practical importance associated with jet impingements on moving surfaces, very few studies in the literature have been specifically directed to investigate the associated flow and hydraulic jump mechanisms. Recently, Gradeck et al. [10] carried out experimental and numerical investigations on hydraulic jumps due to normal impingement of circular liquid jets on a moving surface for various jet and plate velocities, as well as for various nozzle diameters and drop heights (i.e., distance of the nozzle tip from the plate).

Aim of the present work is to develop a fundamental theoretical understanding of the geometrical features of the hydraulic jumps formed as a consequence of the impingement of circular liquid jets on moving horizontal plates, with different levels of jet obliquity. A comparative analysis is also presented with the hydraulic jumps due to normal impinging jets on moving plates, as well as hydraulic jumps due to both normal and oblique impinging jets on stationary surfaces, so as to depict the contrasting features of the pertinent spatial patterns formed, as a function of the plate velocity (U) and the jet inclination angle with the horizontal (ϕ).

2 Radial Locations of the Jump

A schematic depicting the interaction of an oblique impinging jet with a moving horizontal plate is represented in Fig. 2. In Fig. 2(a), a circular liquid jet of radius r_0 impinges on a steadily moving plate of a theoretically infinite extent. The speed with which the jet falls on the plate is assumed to be V_j . In the case of a stationary plate, the intersection of jet with the plate results in an elliptic impingement zone, with a major axis $r_0/\sin \phi$ and a minor axis r_0 [9]. The corresponding stagnation point (i.e., the source of a radial flow) shifts to a distance of $r_0 \cot \phi$ from the geometric center of the ellipse. It can be easily shown that the polar radius of the elliptic stagnation zone with respect to the stagnation point is given by [9]

¹Corresponding author.

Contributed by the Fluids Engineering Division of ASME for publication in the JOURNAL OF FLUIDS ENGINEERING. Manuscript received June 5, 2006; final manuscript received October 27, 2008; published online February 4, 2009. Assoc. Editor: Timothy J. O'Hern.

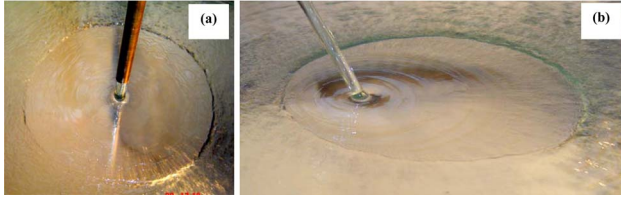


Fig. 1 Qualitative pictures of hydraulic jumps due to impinging circular liquid jets on a stationary smooth horizontal surface: (a) jet impinging normally on the plate and (b) jet inclined at an oblique angle with the plate

$$r_e = r_0 \left(\frac{\sin \phi}{1 + \cos \phi \cos \theta} \right) \quad (1)$$

In case of oblique impingement of a jet on a moving plate, the situation is further complicated by the fact that the deformation of the impingement zone is simultaneously influenced by the plate motion and the jet obliquity. A combined effect of these two can be taken into account by considering that the system is equivalent to the oblique impingement of another jet on a stationary horizontal plate, with an effective impingement velocity, V_e (refer to Fig. 2(b)), and an effective angle of inclination, α , such that

$$V_e = \sqrt{V_j^2 + U^2 + 2V_j U \cos \phi} \quad (2)$$

$$\alpha = \tan^{-1} \left\{ \frac{V_j \sin \phi}{(U + V_j \cos \phi)} \right\} \quad (3)$$

Accordingly, stagnation point shift, s (refer to Fig. 2(c)), and the polar radius of the elliptic stagnation zone, r_{em} , with respect to the stagnation point for the oblique impinging jet interacting with a horizontal plate moving with a velocity, U , can respectively be obtained as

$$s(U, V_j, \phi) = \frac{r_0(U + V_j \cos \phi)}{V_j \sin \phi} \quad (4)$$

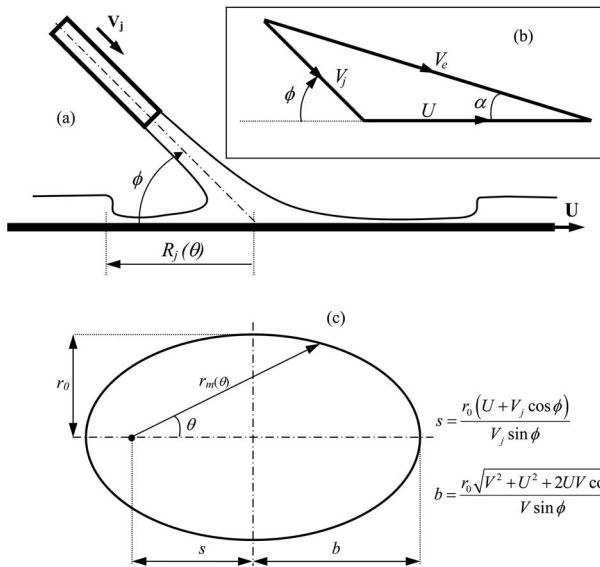


Fig. 2 (a) Schematic of an impinging jet on a horizontal moving surface, (b) jet impinging with velocity V and inclination angle ϕ on a plate moving with a velocity U can be considered equivalent to the jet impinging with a velocity V_e and inclination angle α , on a stationary horizontal plate, and (c) deformed impingement zone due to obliquely impinging circular liquid jet on horizontal moving surface

Table 1 Numerical value of constant c (Eq. (25)) for higher order velocity profiles

Velocity profile	Approximate value of c
$\frac{8}{3}\eta - \frac{4}{3}\eta^3$	0.76
$\frac{20}{9}\eta - \frac{5}{9}\eta^4$	0.83
$\frac{17}{7}\eta - \frac{3}{7}\eta^5$	0.85

$$r_{em}(U, V_j, \phi, \theta) = \left\{ \frac{V_j \sin \phi}{[(U + V_j \cos \phi) + (\sqrt{V_j^2 + U^2 + 2UV_j \cos \phi})] \sin \theta} \right\} \quad (5)$$

The volume flux distribution, $\psi(\phi, \theta)$, of the radially spreading flow (where θ is the polar angle specifying the azimuthal location of a point under concern in the plane of the surface, with reference to the stagnation point) can be accordingly obtained as

$$\psi = rhV_r(\theta) = \frac{r_0^2}{2} \left[\frac{(V_j \sin \phi)^3}{V_j^2 + U^2 + 2UV_j \cos \phi} \right] \left[1 + \left(\frac{U + V_j \cos \phi}{\sqrt{V_j^2 + U^2 + 2UV_j \cos \phi}} \right) \cos \theta \right]^2 \quad (6)$$

The radially spreading three-dimensional flow, in this case, can be modeled effectively as a pseudo-two-dimensional one by considering the coordinate r itself as a function of θ , and the radial locations of the jumps can be obtained as (the detailed analytical treatment can be obtained from [9])

$$R_j = \gamma = c \psi^{5/8} \nu^{-3/8} g^{-1/8} \quad (7)$$

Here, the constant c depends on the velocity profile chosen during the analysis [9]. For a parabolic profile, for example, c turns out to be approximately 0.73. For higher order profiles satisfying the requisite boundary conditions, the respective values of c turn out to be as those shown in Table 1. Finally, substituting the expression for ψ from Eq. (6) in Eq. (7), the radial locations of the jump, $R_j(\phi, U, \theta)$, for a given jet velocity, V_j , are obtained as

$$R_j(\phi, U, \theta) = c \left\{ \frac{r_0^2}{2} \left[\frac{(V_j \sin \phi)^3}{V_j^2 + U^2 + 2UV_j \cos \phi} \right] \left[1 + \left(\frac{U + V_j \cos \phi}{\sqrt{V_j^2 + U^2 + 2UV_j \cos \phi}} \right) \cos \theta \right]^2 \right\}^{5/8} \nu^{-3/8} g^{-1/8} \quad (8)$$

Equation (8) gives a generalized expression for radius of the hydraulic jump profiles on moving horizontal plates, formed with various levels of jet obliquity. Various simpler situations addressed in the literature, however, can be obtained as special cases of Eq. (8) by substituting appropriate values for U and ϕ . Thus, Eq. (8) provides us with a common basis of comparison of hydraulic jump profiles for different plate and jet velocities, and also with different levels of jet inclination.

Table 2 Summary of hydraulic jump profiles due to circular impinging jet of radius r_0 and velocity V_j on smooth horizontal flat plates

Jet inclination angle (ϕ)	Stationary plate ($U=0$)		Moving plate ($U \neq 0$)	
	Impingement zone	Hydraulic jump profile	Impingement zone	Hydraulic jump profile
$\phi=90$ deg	Approximately of the same dimensions as that of the jet. Stagnation point coincides with the geometrical center of the jet.	Circular	Elliptic: major axis, $\frac{2r_0\sqrt{V_j^2 + U^2}}{V_j}$, and minor axis $2r_0$. Stagnation point shifts at a distance of $\frac{r_0 U}{V}$ from the geometrical center of the ellipse.	Noncircular
$25 \text{ deg} \leq \phi \leq 90 \text{ deg}$	Elliptic: major axis, $\frac{2r_0}{\sin \phi}$, and minor axis $2r_0$. Stagnation point shifts by a distance of $r_0 \cot \phi$ from the geometrical center of the ellipse.	Noncircular	Elliptic: major axis, $\frac{2r_0\sqrt{V_j^2 + U^2 + 2UV_j \cos \phi}}{V_j \sin \phi}$, and minor axis $2r_0$. Stagnation point shifts at a distance of $\frac{r_0(U + V_j \cos \phi)}{V_j \sin \phi}$ from the geometrical center of the ellipse.	Noncircular in general, and circular in case $U = -V_j \cos \phi$

3 Results and Discussions

Since the present study offers with a generalization of hydraulic jump profiles formed as a consequence of the interaction between impinging circular jets and flat horizontal plates, a comparative summary of the various special cases following under this category can be of potential interest. This is illustrated in Table 2 for the different special situations mentioned earlier. It is also interesting to note here that although the jump profile is, in general, elliptical in nature for moving horizontal plates, under special circumstances one may obtain circular jump profiles even in such a complicated flow situation, in case U , V_j , and ϕ are related as follows:

$$V_j \cos \phi + U = 0 \quad (9)$$

The above is in accordance with the fact that a circle is a special case of an ellipse with equal major and minor axes.

In order to assess the quantitative predictive capability of the simple theoretical model presented in this work, experimental and numerical results from Gradeck et al. [10] are compared with the predictions from the present theory, with regard to the radial locations of the hydraulic jump of a normal impinging jet on a moving surface. The present theoretical predictions are found to agree well with the reported data, as depicted in Fig. 3. The deviation of the experimental results of Gradeck et al. [10] from our theory may be due to the following.

1. Gradeck et al. [10], in their experimental results, depicted a segment of the jump profile and not a complete jump profile. This might be due to the use of a plate with relatively smaller dimensions and a relatively large diameter nozzle. Under such circumstances, the liquid flowing along the direction of plate may get drained off before the formation of the complete hydraulic jump profile, and therefore only a segment of the jump would be visible.

2. In addition, due to smaller dimensions of the plate in one direction, drainage of the liquid will not be uniform. On the other hand, the present theoretical analysis assumes a target plate of infinite dimensions. Under these conditions, the profile of the hydraulic jump should be a closed one, resembling an elliptical shape.

Experimental results of Gradeck et al. [10], in that perspective, can be compared with the present theoretical predictions for only over a portion of that profile. In order to obtain a more complete picture on the close-shaped hydraulic jump profiles and the effects of nozzle inclinations, Fig. 4 is plotted in which typical hydraulic jump profiles, as obtained using Eq. (8), in the case of a plate of relatively larger dimensions are depicted. It is also important to mention here that our theoretical predictions match more accurately with the experimental results, as compared with the numerical results of Gradeck et al. [10] that were obtained by using a commercial computational fluid dynamics (CFD) code, as evident in Fig. 3.

It is interesting to note in the present context that for the case of normal impinging jets, a circular hydraulic jump becomes possible only when $U=0$, since it is only in that case that Eq. (9) is satisfied with $\phi=90$ deg. On the other hand, for $\phi \neq 90$ deg, a circular hydraulic jump becomes possible when $U = -V \cos \phi$. With $\phi=60$ deg, this occurs when $U = -0.845$ m/s for the case presented in Fig. 4(b). From Fig. 4, it is also evident that with $U > 0$, major axes of the jump profile get progressively more elongated and the minor axes get progressively more contracted with an increase in the value of U . The stagnation point also shifts progressively downwards with the same. These effects are much more prominent for the obliquely impinging jet. In fact, for $\phi = 60$ deg, almost the entire jump profile remains confined within

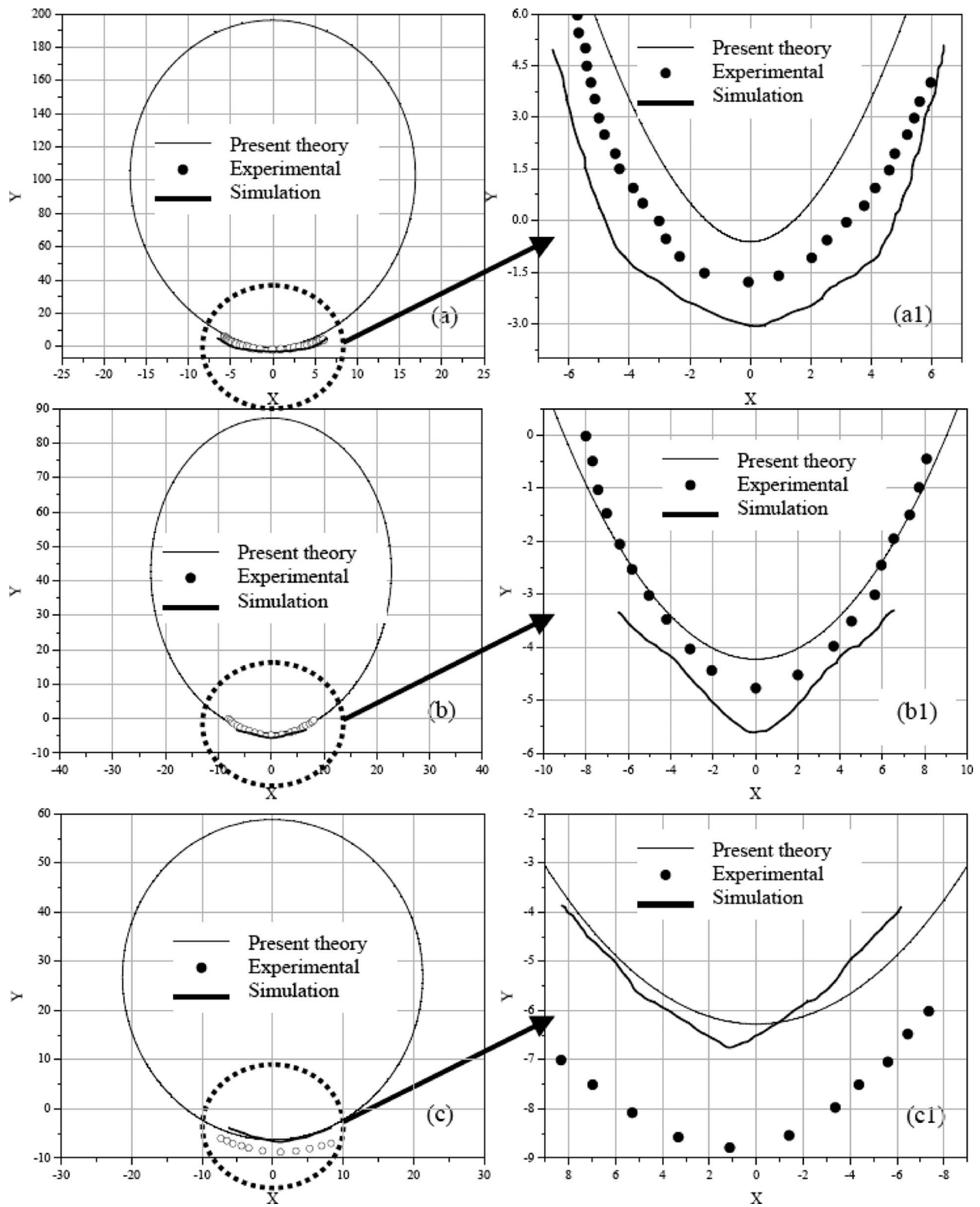


Fig. 3 Hydraulic jump profiles for different jet and plate velocities for normal impinging jets, as compared with the experimental and numerical results reported in Gradeck et al. [10]: (a) $V_j=0.41$ m/s, $U=2.04$ m/s, (b) $V_j=1.0$ m/s, $U=1.53$ m/s, and (c) $V_j=1.0$ m/s, $U=1.02$ m/s)

the lower quadrant for $U > 0$, as seen in Fig. 4(b). Figure 5 depicts the change in aspect ratio (ratio of major axis of the elliptical hydraulic jump to the minor axis) with the velocity ratio (ratio of plate velocity to the jet velocity) for different jet inclination angles. It can be seen from this figure that for the same nozzle inclination angle, two different conditions can lead to the same jet

aspect ratio, one with a negative V/U ratio and the other with a positive V/U ratio. However, the corresponding V/U ratios are not symmetrical with respect to a stationary jet and moving plate condition (i.e., $V/U=0$). In other words, the positive V/U ratio that gives rise to the same a/b ratio, for a particular value of ϕ , is not of the same magnitude as that of the corresponding negative

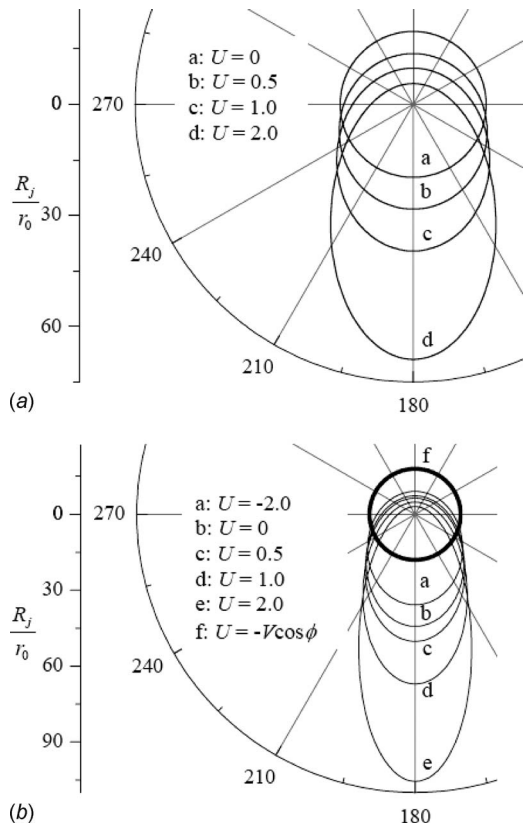


Fig. 4 Hydraulic jump profiles due to circular liquid jet impinging jets on a smooth horizontal moving surface, for (a) a normal impinging jet ($Q=3.33 \times 10^{-5} \text{ m}^3/\text{s}$, $r_0=4.4 \text{ mm}$) and (b) an oblique impinging jet ($Q=3.33 \times 10^{-5} \text{ m}^3/\text{s}$, $r_0=4.4 \text{ mm}$, $\phi=60 \text{ deg}$)

V/U ratio. For positive V/U ratios, progressively higher jump aspect ratios can be obtained by lowering the values of ϕ for a given value of V/U . Such dramatic changes in the jump aspect ratios cannot be affected by varying the nozzle inclination angle for negative V/U ratios. Special cases leading to circular hydraulic jumps can be obtained for $|V/U| < 1$ only, since the value of $\cos \phi$ is always restrained to be within -1 and $+1$.

4 Conclusions

Hydraulic jumps due to impinging jets on uniformly moving flat horizontal plates have been theoretically investigated under different jet inclination angles and plate velocities. It has been conjectured that flow due to impinging jets on a horizontal moving plate can be modeled as a flow due to an inclined impinging jet on stationary horizontal flat plates, with appropriate alterations in the jet velocity and the jet inclination angles. The predicted theoretical results are in good agreement with experimental results reported in the literature.

Regarding the restrictions under which the present theoretical model can be applied with confidence, it can be noted that the “regular” oblate shape of the jump profiles are likely to be disturbed and distorted considerably, in case the effective angle of

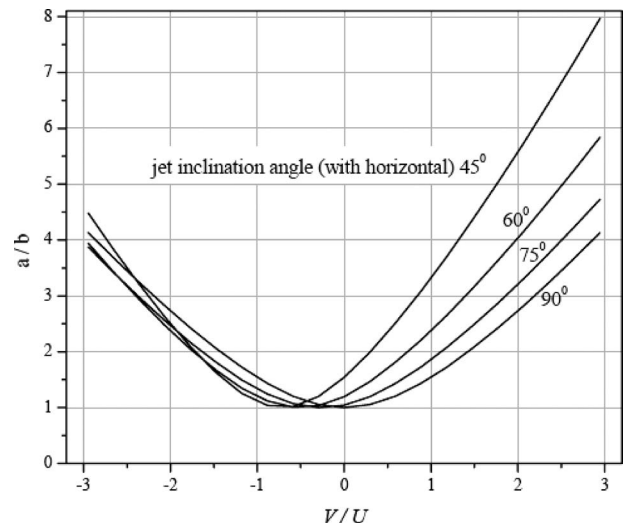


Fig. 5 Change in aspect ratio (ratio of major axis, a , to the minor axis, b , of the elliptical hydraulic jumps) with change in velocity ratio for different jet inclination angles

obliquity (α) falls below a critical limit (typically, in the tune of 25 deg) as observed under experimental conditions [10]. Such situations might confer a series of interesting flow patterns (such as the shape of a fish), including jumps with corners, which are markedly different from the regular elliptical (or oblate) jump profiles observed with higher values of jet inclination. Such irregularly-shaped jump profiles can be attributed to the changes in the spreading flow profile due to “jet-jump interaction,” at relatively lower jet inclination angles. These hydraulic jump profiles are analogous to regular reflection waves in compressible fluid flows, and fall beyond the scope of the present theory to be mathematically analyzed. Research investigations on the formation of such irregularly-shaped hydraulic jump profiles on moving horizontal plates are currently under way in our group.

References

- [1] Kurihara, M., 1946, “On Hydraulic Jumps,” Rep. Research Institute for Fluid Engineering (Kyusyu Imperial University, “Ryutai Kougaku Kenkyusho Kiyou”), 3, pp. 11–33 (in Japanese).
- [2] Watson, E. J., 1964, “The Spread of a Liquid Jet Over a Horizontal Plane,” *J. Fluid Mech.*, 20, pp. 481–499.
- [3] Bohr, T., Dimon, P., and Putkaradze, V., 1993, “Shallow-Water Approach to the Circular Hydraulic Jump,” *J. Fluid Mech.*, 254, pp. 635–648.
- [4] Godwin, R., 1993, “The Hydraulic Jump (“Shocks” and Viscous Flow in the Kitchen Sink),” *Am. J. Phys.*, 61, pp. 829–832.
- [5] Brechet, Y., and Néda, Z., 1999, “On the Circular Hydraulic Jump,” *Am. J. Phys.*, 67, pp. 723–731.
- [6] Bush, J. W. M., and Aristoff, J. M., 2003, “The Influence of Surface Tension on the Circular Hydraulic Jump,” *J. Fluid Mech.*, 489, pp. 229–238.
- [7] Rubel, A., 1981, “Computations of the Oblique Impingement of Round Jets Upon a Plane Wall,” *AIAA J.*, 19, pp. 863–871.
- [8] Sparrow, E. M., and Lovell, B. J., 1980, “Heat Transfer Characteristics of an Obliquely Impinging Circular Jet,” *Trans. ASME, Ser. C: J. Heat Transfer*, 102, pp. 202–209.
- [9] Kate, R. P., Das, P. K., and Chakraborty, S., 2007, “Hydraulic Jumps Due to Oblique Impingement of Circular Liquid Jets on Flat Horizontal Surface,” *J. Fluid Mech.*, 573, pp. 247–263.
- [10] Gradeck, M., Kouachi, A., Dani, A., Arnould, D., and Boreán, J. L., 2006, “Experimental and Numerical Study of the Hydraulic Jump of an Impinging Jet on a Moving Surface,” *Exp. Therm. Fluid Sci.*, 30, pp. 193–201.

Perspective: Validation—What Does It Mean?

Patrick J. Roache

Consultant

1215 Apache Drive,

Socorro, NM 87801

e-mail: hermosa@sdsc.org

Ambiguities, inconsistencies, and recommended interpretations of the commonly cited definition of validation for computational fluid dynamics codes/models are examined. It is shown that the definition-deduction approach is prone to misinterpretation, and that bottom-up descriptions rather than top-down legalistic definitions are to be preferred for science-based engineering and journal policies, though legalistic definitions are necessary for contracts. [DOI: 10.1115/1.3077134]

Keywords: validation, calibration

1 Introduction

“Validation: The process of determining the degree to which a model {and its associated data} is an accurate representation of the real world from the perspective of the intended uses of the model.”

Unfortunately, considerable disagreement exists on what this definition *means*, or should mean.

This definition of validation has been cited extensively in computational fluid dynamics (CFD) and other computational modeling fields, and is widely accepted. Despite the apparent clarity of this concise one-sentence definition using common terms, there is disagreement on its interpretation among scientists and engineers, who are habitually careful readers. There are at least three contested issues: whether *degree* implies acceptability criteria (pass/fail), whether *real world* implies experimental data, and whether *intended use* is specific or general (even by those who think it is needed at all). This gives $2^3=8$ possible interpretations of the same definition, without even getting into arguments about what is meant by *model*, i.e., computational, conceptual, mathematical, strong, and weak. The job of sorting out claims and arguments is further complicated by the fact that principals in the debates have sometimes switched sides on one or more of these three issues (myself included).

Before examining the definition of validation, we need to make a small distinction on what it is we are claiming to validate, i.e., between *code* and *model*. A model is incorporated into a code, and the same model (e.g., some Reynolds-averaged Navier–Stokes (RANS) model) can exist in many codes. Strictly speaking, it is the model that is to be validated, whereas the codes need to be verified. But for a model to be validated, it must be embodied in a code before it can be run. It is thus common to speak loosely of “validating a code” when one means “validating the model in the code,” and vendors like to claim they are providing a “validated code,” and legal and regulatory requirements may specify use of “verified and validated codes.” In theory, the same model would only have to be validated in one (verified) code to be accepted as validated in another (verified) code; in practice for RANS codes, this is unrealistic, so “validating a code” is usually meaningful in context.

Contributed by the Fluids Engineering Division of ASME for publication in the JOURNAL OF FLUIDS ENGINEERING. Manuscript received June 19, 2008; final manuscript received December 22, 2008; published online February 4, 2009. Review conducted by Joseph Katz.

2 History of the Definition

The definition was precisely stated in a 1996 (re-issued in 2003) U.S. DoD Instruction [1] (see also Refs. [2,3]), which referred to an earlier minisymposium that used almost the same wording. The DoD re-issue in 2003 [1] added the bracketed additional phrase “{and its associated data}” after the word *model*, which would suggest a strong-sense concept of model. The definition was adopted (without the bracketed term) in the AIAA Guide for V&V in CFD [4] and in the ASME V&V 10 [5], which was based in many aspects on Ref. [4].¹ The definition is widely used beyond these documents, and the observations herein should not be construed simply as criticisms of these sources, but rather as cautions that there are inherent problems with interpretation. The documents cited [1–5] are uneven in their stated interpretations on these issues, with V&V 10 [5] being specific and clear on all three issues. Unfortunately, while acknowledging that a range of definitions exist for validation and other V&V terms [5], it does not acknowledge that a range of interpretations exist for the same definition. Also, while citing Refs. [1–4] for its definition of validation, it does not acknowledge the fact that it differs from Refs. [1–4] in its interpretation, notably on the issue of inclusion of pass/fail criteria. It is also a fact that, for each publication, opinions on what the definition means differ even among members of the same committee that wrote the document. ASME V&V 20 [6] notes the definition but also its range of interpretations, adopting a more general descriptive approach. Likewise, neither the ASCE monograph on V&V for free-surface flows [7] nor my 1998 book [8] required the deductive top-down approach implied by legalistic definitions, using instead a descriptive bottom-up approach. It is noteworthy that, in spite of all the agonizing over interpretations, none of the specifics of the complete V&V methodology presented in V&V 20 [6] is affected by any of these choices. Furthermore, while consistent use throughout the computational communities is desirable, there is no necessity for this journal or others to accept a DoD or other definition as canonical, especially when it is easily shown that there are inherent problems with the definition and a wide range of interpretations. (Contracts present a different consideration; see below.)

Based on my contacts in the V&V community, including committee participation in the writing of Refs. [5–7], professional contacts with the principals of Ref. [4], and experience teaching 12 short courses on V&V, I believe that most professionals make the following interpretations of the definition upon first reading.

3 Issue No. 1: Acceptability Criteria (Pass/Fail)

Regarding the issue of whether acceptability criteria (or adequacy, or pass/fail criteria) are included in this definition of validation, initially people generally say “yes” without hesitation. This is due mostly to a correct recognition that pass/fail decisions must be made in any engineering project, and reinforced by the later phrase “from the perspective of the intended uses of the model,” which understandably seems to imply such project-specific criteria (see discussion below). However, people quickly see the value of the alternative view. Although pass/fail criteria are certainly project requirements, the requirements do not necessarily need to be included in the term “validation.” In fact, in the original DoD documents [1–3] the term “acceptability” was not used in regard to validation, but in regard to “accreditation” (and which has elsewhere been described as “certification”). From Ref. [1]:

“Acceptability Criteria (Accreditation Criteria). A set of standards that a particular model, simulation, or federation [system of interacting models] must meet to be accredited for a specific purpose.

¹Although Ref. [5] cited the 2003 version of Ref. [1], it did not include the bracketed term added to the original 1996 issue of Ref. [1].

Accreditation. The official certification that a model, simulation or federation of models and simulations and its associated data are acceptable for use for a specific purpose.”

However, acceptability for accreditation, as stated in Ref. [1], involved additional criteria besides validation accuracy, which supposedly was intended to be included in validation [9]. But close reading of the documents themselves [1–3] give no indication of this, and strongly suggest to me that the acceptability criteria reside under accreditation (or certification, or perhaps another project-related term) rather than validation. The AIAA Guide [4] is somewhat vague (and committee members disagree), and there is widespread misunderstanding of Ref. [4] on this point (see discussion in Sec. 5). But V&V 10 [5], even though inspired by the AIAA Guide [4], strongly includes pass/fail criteria, even to the point of insisting that the pass/fail criteria (validation requirements) be set firmly before the comparison to experiment in the description of intended use. No acknowledgment of this departure from Ref. [4] is given in Ref. [5] to the likely confusion of any user-engineer who happens to read both documents and who has other things on his mind. It would have been less confusing if the sources each had used different wording for the definition, which might alert the user-engineer, rather than use the same “definition” with different interpretations of the terms.

More important than what the documents state is the fact that people quickly see the advantage of not including a pass/fail tolerance while performing validation. Rather, one simply evaluates the agreement between computational results and experimental results (with their respective uncertainties—see below), and presents the difference as the level of validation. This recognizes the fact that the same validation level (e.g., 10% agreement for skin friction coefficient) may be adequate for one application and not for another. This is just the kind of validation exercises performed for many years for RANS turbulence models, for example.

There are two very distinct processes: first, comparison of model predictions with experimental values, leading to an assessment of model accuracy, and second, determination of acceptability or pass/fail of that accuracy level for a particular application. The methodologies employed in each process have virtually nothing in common. In some usage, a model whose results have been compared with experiments is labeled validated regardless of the agreement achieved. In this loosest use of the term, validated then is not a quality of the code/model per se, but just refers to the quality assurance (QA) process. Carried to an extreme, this viewpoint gives the designation validated even to very poor models. Celik [10] pointed out that it would be misleading to assign the inevitably value-laden term “validated” for a code that produces inarguably poor results (say, wrong qualitative trends, e.g., lift coefficient decreasing with angle of attack) just because it has gone through the validation QA process. I agree, and do not recommend this usage. A more moderate usage is to call the model validated, regardless of the agreement achieved, but to state explicitly that the model is validated to a specified level and within the validation uncertainties determined from following the procedures in Ref. [6] or others. This way, the validation statement provides a quantitative assessment, but stops short of a rigid pass/fail statement, since that requires consideration of the design, cost, risk, etc. This usage is well presented by Oberkampf et al. [11], p. 348. “Stating our view succinctly: validation deals with quantified comparisons between experimental data and computational data; not the adequacy of the comparisons.” The other extreme makes validation project-specific by specifying the error tolerance a priori, e.g., see Ref. [5]. This ties a code/model validation rigidly to a particular engineering project rather than to less specific science-based engineering (or worse, it neglects the fact that agreement may be acceptable for one application and not for another).

Since not all comparisons should result in a code being given the value-laden designation of validated, some minimal agreement should be required. As a reviewer has noted, since it is impossible

to avoid attaching a value to validated, it can be argued that it is preferable to attach a well defined criterion from the start. But on balance, I think this is outweighed by the disadvantages, as discussed (ephemeral pass/fail criteria, applicability of validation results to more than one project, and disparate methods for assessing fidelity and adequacy). The general (and necessarily vague) level of acceptable agreement must be determined by common practice in the discipline. The simulation results with their uncertainties are compared with experiments with their uncertainties, and if reasonable agreement, as determined by the state-of-the-art standards (including at least correct qualitative trends), is achieved, then the code/model can be termed validated. This does not necessarily mean that the model will be adequate for all applications. Such a project-specific pass/fail tolerance should be relegated to accreditation or certification [8]. The value of this pass/fail tolerance tends to vary over time with design decisions, product requirements, and economics; even though the objective results of the validation comparison itself have more permanent value.

Many discourage the use of the term “validated code” no matter how good the agreement with experiment because it might be misleading or even deliberately misused, e.g., in commercial code marketing. But it does not seem realistic to try to outlaw the past practice, and codes that have gone through validation will inevitably be referred to as “validated codes.” Nevertheless, as Tsang [12] (cited in Ref. [8], p. 26) noted, “almost by definition, one can never have a Validated computer model without further qualifying phrases.” The qualifications include knowledge of the experimental validation set points, the specific validation variables or metrics, what is included in model, and of course the degree of validation achieved, which requires stated uncertainties of both computations and experiments.

4 Issue No. 2: Necessity for Experimental Data

In the validation definition, most engineers read “real world” to imply *real world data*, i.e., what most people would call experimental data. Surprisingly, not everyone agrees with this interpretation. (In Refs. [1–3] the distinction was not specifically addressed; in Refs. [4,5] the requirement was clear and unequivocal, although some members of the committees disagreed.) The apparent motivation is to try to gain the approval implicit in “validation” without the onerous requirement for obtaining real experimental data. There are difficult problems, e.g., nuclear stockpile, for which further testing is outlawed. It is not always clear what these proponents would substitute. Some look for agreement between different models. As noted in Ref. [8], p. 276, if one code has been previously validated, it can be regarded as a repository of experimental information, a set of second-hand experimental data plus smoothing and interpolation/extrapolation to parameter values other than experimental set points. But, in general, code-to-code comparison is not validation. The recommended view, agreeing with Refs. [5–8], is uncompromising: no experimental data means no validation.

Regarding validation by comparison with a previously validated code, a reviewer has noted that, if a second code is being “validated” at a set point, the original data could be used, not the first code that has been validated at that same set point. In principle, this would usually be the preferred approach. However, for some practical situations the use of a previously validated code could be preferable and certainly more convenient and, I believe, acceptable. First, note that previous multiple validation experiments may not agree with each other, even within the experimental uncertainties (if indeed these have been presented), and they may not be at exactly the same set points. Second, suppose that a new model to be validated is not expected to be as accurate as previous models (but perhaps has an advantage of simplicity, computational speed, numerical stability, or lack of sensitivity to grid resolution and is therefore cheaper to run). Then it would make sense to compare the results of the new model with those of

a previously validated (but perhaps more complex, slower, less robust, or more expensive) model. (A ready example is a turbulence model using new wall functions, which could be validated against previously validated models employing integration to the wall.) It would be impossible to justify if the new model was intended to be more accurate than the old model taken as a benchmark, except as an interim validation exercise used to justify further validation work (perhaps with new and improved validation experiments).

5 Issue No. 3: Intended Use

The requirement for “intended use” sounds good at first, but it fails upon closer thought. Did Wilcox [13] need to have an “intended use” in mind when he evaluated the $k-\omega$ RANS turbulence models for adverse pressure gradient flows? He may very well have had uses in mind, but does a modeler need to have the same use in mind two decades later? If not, must the validation comparison be repeated? Certainly not.

The “intended use” phrase also bears on pass/fail criteria (Issue No. 1), seeming to indicate that pass/fail criteria are to be included in the definition of validation. There is widespread misunderstanding of the AIAA Guide [4] on this point, as acknowledged by Oberkampf et al. [11], a principal architect of Ref. [4]. He states that pass/fail criteria are not included: “We argue that this is what the words mean in the definition...” The fact that the authors must “argue” the interpretation indicates that the document is unclear, which is understandable given the phrase “from the perspective of the intended uses of the model.” Oberkampf insists that “intended use” applies not to a pass/fail tolerance but rather to the metrics involved. Although this observation is relevant, it is not complete because the same metrics might be applicable to different end uses, just as the same pass/fail tolerances might be. Although Refs. [1–4] are not emphatic about specificity of intended use, they are suggestive. V&V 10 [5] is admirably clear but unrealistically strong, even to the point of insisting on an a priori specification of validation criteria, which if taken seriously would effectively eliminate the possibility of validation in any basic research sense, in my opinion. All these documents [1–5] have a strong orientation to management of large engineering projects, which deters from their applicability to basic research, unlike V&V 20 [6].

Clearly, much of the confusion is the result of trying to use the same word for different needs. Project oriented engineers are more concerned with specific applications, and naturally tend to rank *acceptability* within validation (which is the term used more often than accreditation or certification). Research engineers and scientists tend to take a broader view, and often would prefer to use validation to encompass only the assessment of accuracy level, rather than to make decisions about whether that level is adequate for unspecified future uses. It is also significant to recognize that these project-specific requirements on accuracy are often ephemeral, so it is difficult to see a rationale for a priori rigid specifications of validation requirements [5,11] when the criteria so often can be renegotiated if the initial evaluation fails narrowly.

6 Recommended Interpretation and Alternative Description

My recommendations, consistent with V&V 20 [6], are that choices for the interpretation of the validation definition be made as follows.

Recommendation on Issue No. 1. Criteria for acceptability of accuracy (adequacy, pass/fail criteria, or accuracy tolerance) are not part of validation, but analysts performing validation exercises should be wary of appearing to bless a code as “validated” when it is clearly unsatisfactory for any reasonable application (e.g., it cannot even predict correct qualitative trends). In an engineering project, the acceptability of the agreement is part of the next

project step, variously called accreditation, certification, or others. It is an engineering management decision, not a scientific evaluation.

Recommendation on Issue No. 2. Experimental data are necessary for validation. Many have said unequivocally [5–8,11] that experimental data are the *sine qua non* of validation

no experimental data \Rightarrow no validation

Many other factors remain, of course, including the quality and quantity of the data, the necessity for uncertainty estimates for both modeling and experiments [6], the extent of the domain of validation (the range of parameter space in the set points of the experiments and the interpolation/extrapolation of experimental and computational results), whether previously validated codes can be used as a secondary database, whether scaled experiments are adequate, etc. But as a minimum, some experimental data are required. This data can include historical observations and already established scientific facts (especially obvious for invalidation), as pointed out by a reviewer, but it is noteworthy that Refs. [4,5] disagree, adopting a literal sense of temporal “prediction,” which is at odds with scientific practice.

Recommendation on Issue No. 3. Intended use, at least in its specific sense, is not required for validation. The common validation definition could be salvaged by redefining intended use to include very general intentions, but frankly this appears to be a hollow exercise. The fact is that a useful validation exercise does not necessarily require an intended use, specific or general. For example, the well-known data on turbulent backstep flow of Driver and Seigmiller [14] in the ERCOFTAC database can be used for code/model validation, with neither the experimenters in 1985 nor modelers in (say) 2008 having a specific use in mind. This is precisely the situation for the Lisbon III Workshop on V&V [15].

However, it is also true and very important that (as recommended strongly in Refs. [4–6,11]) experiments designed specifically for a validation exercise, with a specific application in mind and with collaboration between experimenters and modelers in the design of the experiments, are much more likely to produce data on the relevant metrics with relevant precisions than experiments designed without applications in mind.

Alternative description. Alternately, for science-based engineering, we can *describe* validation rather than rigidly define it. First (and virtually universally agreed upon [4–8,11]) is the distinction between verifications and validation. Verifications (first of the code and then of particular calculations or solutions) are simply matters of mathematics and address questions of correct coding and discretization accuracy of particular solutions, whereas validation involves comparison with reality, i.e., science (or physics, in its most general sense). In general terms, validation involves comparison of modeling results with experimental results. This has been used in the past, but I agree with Refs. [4–6,11] that it is too soft. The trouble (as noted in Ref. [11]) is that the difference between model result and experiment is too easily taken to be the accuracy when in fact the story is more difficult. It is time to improve standards somewhat on even the minimal requirements for the term validation.

The minimal required improvement is contained in one word: *uncertainty*. We can describe validation (legitimate minimal validation) as the comparison of model results *and their associated uncertainties* with experimental results *and their associated uncertainties*. A specific methodology for this comparison including interpretation of the answers is given in Ref. [6] using accepted well established quantitative techniques for every aspect of the entire process, and using definitions and statistical techniques that are consistent between experimental and modeling methodologies. I believe that such a descriptive approach is all that is needed for science-based engineering and for journal publication standards. In any case, the warning [12] still applies: it is meaningless to talk about “validation” without significant further qualifications.

7 Calibration is Not Validation

Whether one takes a definition-deductive approach or a less rigid descriptive approach, it is necessary to be clear that calibration, the adjustment or tuning of free parameters in a model to fit the model output with experimental data, is not validation. (This distinction is emphasized in each of Refs. [4–7], but earlier uses [8] often described calibration as just validation for a restricted range of physical parameters.) Calibration is a sometimes necessary component of (strong sense) model development. But this calibration is not to be considered as validation, which occurs only when the previously calibrated model predictions are evaluated against a set of data not used in the tuning [4–8]. There is no value in tuning free parameters to obtain a drag coefficient to match an experimental value, and then claiming code/model validation because the “prediction” agrees with the same experiment. Historically, this has been a common failing of free-surface flow modeling projects [7]. Of course, if all point values and functionals of interest are well matched using a small set of free parameters with physically realistic values, this will tend to be convincing in itself, but another data set not used in the tuning will be more so.

8 Implications for Contractual and Regulatory Requirements

Although bottom-up descriptions of validation may be adequate for research journals, rigid and legalistic definitions will be required for contract specifications and regulatory requirements. If a contract specifies that a “validated code” must be used in the modeling, then all parties must know what is meant by “validation” as well as verification, accreditation, etc. My preferences for the definition interpretations are given above, but whatever the contracting or regulating body decides, what is clear from the history of this controversy is the following. Although a rigid, legalistic definition may be required, it is not sufficient. As with questions of constitutional law, interpretations will differ. No matter how carefully the words are crafted, one cannot expect all readers to make the same interpretations.

To better ensure that the intent is correctly interpreted, the contract or regulation specifications should amplify the definitions used with specific interpretations. For example, if the above defi-

nition is adopted, the specifications should not just say “real world” and expect the analyst or contractor to know that experimental data is required. The bare legalistic definitions should be expanded to describe the definition, as done notably in V&V 10 [5]. The definition-deduction approach alone is not adequate; the human capacity for equivocation assures that no legalistic definition is inviolable.

Acknowledgment

The author gratefully acknowledges discussions with H.W. Coleman and S.S.Y. Wang, and improvements suggested by four reviewers. This work has been partially supported by Idaho National Laboratories, Battelle Energy Alliance Contract No. 54525.

References

- [1] Department of Defense, 1996, “DoD Modeling and Simulation (M&S) Verification, Validation, and Accreditation (VV&A),” DoD Instruction No. 5000.61.
- [2] Department of Defense, 1994, “DoD Modeling and Simulation (M&S) Management,” DoD Directive No. 5000.59.
- [3] Military Operations Research Society, 1994, Simulation Validation (SIMVAL) 1994, Mini-Symposium Report, Sept. 28–30.
- [4] AIAA, 1998, *Guide for the Verification and Validation of Computational Fluid Dynamics Simulations*, American Institute of Aeronautics and Astronautics, Reston, VA.
- [5] ASME Committee PTC-60, 2006, ANSI Standard V&V 10. ASME Guide on Verification and Validation in Computational Solid Mechanics.
- [6] ASME Committee PTC-61, 2008, ANSI Standard V&V 20. ASME Guide on Verification and Validation in Computational Fluid Dynamics and Heat Transfer.
- [7] ASCE/EWRI Task Committee, 2009, 3D Free Surface Flow Model Verification/Validation.
- [8] Roache, P. J., 1998, *Verification and Validation in Computational Science and Engineering*, Hermosa, Albuquerque, NM.
- [9] Pace, D. K., 2008, personal communication.
- [10] Celik, I., 2006, personal communication.
- [11] Oberkampf, W. L., Trucano, T. G., and Hirsch, C., 2004, “Verification, Validation, and Predictive Capability in Computational Engineering and Physics,” *Appl. Mech. Rev.*, **57**(5), pp. 345–384.
- [12] Tsang, C.-F., 1991, “The Modeling Process and Model Validation,” *Ground Water*, **29**(6), pp. 825–831.
- [13] Wilcox, D. C., 2006, *Turbulence Modeling for CFD*, DCW, La Canada, CA.
- [14] Driver, D. M., and Seegmiller, H. L., 1985, “Features of a Reattaching Turbulent Shear Layer in Divergent Channel Flow,” *AIAA J.*, **23**(1), pp. 163–171.
- [15] Eça, L., and Hoekstra, M., 2007, Announcement for the Third Workshop on CFD Uncertainty Analysis, Instituto Superior Técnico, Lisbon, Portugal, Oct. 23–24.